

Measurement of the inclusive $t\bar{t}$ cross section and search for additional scalars in $t\bar{t}$ final states at the CMS experiment

Dissertation

zur Erlangung des Doktorgrades
an der Fakultät für Mathematik, Informatik und Naturwissenschaften
Fachbereich Physik
der Universität Hamburg

vorgelegt von
Laurids Jeppe

Hamburg
2025

Gutachter der Dissertation:

Zusammensetzung der Prüfungskomission:

Vorsitzender der Prüfungskomission:

Datum der Disputation:

Vorsitzender Fach-Promotionsausschuss PHYSIK: Prof. Dr. Wolfgang J. Parak

Leiter des Fachbereichs PHYSIK: Prof. Dr. Markus Drescher

Dekan der Fakultät MIN: Prof. Dr.-Ing. Norbert Ritter

Abstract

Two key measurements and two phenomenological studies of top quark pair ($t\bar{t}$) production with the CMS experiment at the CERN Large Hadron Collider are presented. They include the first measurement of the $t\bar{t}$ cross section at the new energy frontier, a detailed analysis of the $t\bar{t}$ threshold culminating in the first observation of $t\bar{t}$ bound state effects, and searches for new physics in $t\bar{t}$ final states, such as heavy scalars, pseudoscalars or Axion-Like Particles.

The inclusive $t\bar{t}$ production cross section $\sigma_{t\bar{t}}$ is measured for the first time at the world-record energy of $\sqrt{s} = 13.6$ TeV, using 1.21 fb^{-1} of early LHC Run 3 data. By combining the dilepton and lepton+jets ($\ell+\text{jets}$) decay channels and constraining the lepton and b tagging efficiencies *in situ*, a precision of 3.4%, comparable to previous $\sigma_{t\bar{t}}$ measurements, is achieved. This constitutes the first measurement of proton-proton scattering at $\sqrt{s} = 13.6$ TeV worldwide.

Furthermore, a search for heavy spin-0 states decaying to $t\bar{t}$ using 138 fb^{-1} of LHC Run 2 data at $\sqrt{s} = 13$ TeV in the dilepton channels is presented. The invariant $t\bar{t}$ mass ($m_{t\bar{t}}$) is combined with spin correlation observables to gain sensitivity to the spin and \mathcal{CP} structure of possible new intermediate states. The analysis is supported by a detailed modeling study of off-shell $t\bar{t}$ production and of the interference between $t\bar{t}$ and tW production.

An excess of events over the $t\bar{t}$ continuum background is observed at low values of $m_{t\bar{t}}$, with spin correlations consistent with a pseudoscalar state. It is interpreted in terms of a pseudoscalar $t\bar{t}$ bound state η_t , and its cross section is measured to be $\sigma(\eta_t) = 8.7 \pm 1.1 \text{ pb}$ using a simplified model inspired by non-relativistic quantum chromodynamics. The excess is statistically significant at more than five standard deviations, constituting the first observation of $t\bar{t}$ bound state effects.

Other interpretations of the observed excess are similarly possible. In particular, scenarios with generic pseudoscalar or scalar bosons are explored, and exclusion regions on their coupling to the top quark are derived both for the dilepton channels alone as well as in a combination with a separate analysis of the $\ell+\text{jets}$ channels. In addition, Axion-Like Particles (ALPs) decaying to $t\bar{t}$ are considered in the case of vanishing tree-level ALP-gluon couplings, while the more generic case is investigated phenomenologically in simulation.

Zusammenfassung

Es werden zwei essentielle Messungen und zwei phänomenologische Studien zur Produktion von Top-Quark-Paaren ($t\bar{t}$) mit dem CMS-Experiment am CERN Large Hadron Collider vorgestellt. Sie umfassen die erste Messung des $t\bar{t}$ -Wirkungsquerschnitts bei der weltweit höchsten Schwerpunktsenergie, eine detaillierte Analyse der $t\bar{t}$ -Produktionsschwelle, die in die erste Beobachtung von einem gebundenen Zustand des $t\bar{t}$ -Systems mündet, sowie Suchen nach neuer Physik in $t\bar{t}$ -Endzuständen, wie etwa schwere Skalar- oder Pseudoskalarbosonen oder Axion-Like Particles.

Der inklusive $t\bar{t}$ -Produktionsquerschnitt $\sigma_{t\bar{t}}$ wird zum ersten Mal bei $\sqrt{s} = 13.6 \text{ TeV}$ gemessen, unter Verwendung von frühen LHC Run 3-Daten mit integrierter Luminosität von 1.21 fb^{-1} . Durch Kombination der Dilepton- und Lepton+Jets ($\ell+\text{jets}$)-Zerfallskanäle von $t\bar{t}$ und simultane Bestimmung der Lepton- und b-tagging-Effizienzen *in situ* wird eine Präzision von 3.4% erreicht, die mit früheren $\sigma_{t\bar{t}}$ -Messungen vergleichbar ist. Dies stellt die weltweit erste Messung von Proton-Proton-Streuprozessen bei $\sqrt{s} = 13.6 \text{ TeV}$ dar.

Darüber hinaus wird eine Suche nach schweren Spin-0-Zuständen, die zu $t\bar{t}$ zerfallen, in den Dilepton-Kanälen mit 138 fb^{-1} Daten von LHC Run 2 bei $\sqrt{s} = 13 \text{ TeV}$ vorgestellt. Die invariante Masse von $t\bar{t}$ ($m_{t\bar{t}}$) wird mit Spinkorrelations-Observablen kombiniert, um die Sensitivität gegenüber dem Spin und der \mathcal{CP} -Struktur möglicher neuer intermediärer Zustände zu erhöhen. Die Analyse wird durch detaillierte Studien zur Modellierung der Off-Shell- $t\bar{t}$ -Produktion sowie zur Interferenz zwischen $t\bar{t}$ - und tW -Produktion untermauert.

Ein Überschuss von Ereignissen gegenüber dem $t\bar{t}$ -Kontinuums-Hintergrund wird bei niedrigen Werten von $m_{t\bar{t}}$ und mit Spinkorrelationen konsistent mit einem pseudoskalaren Zustand beobachtet. Er wird als pseudoskalarer gebundener $t\bar{t}$ -Zustand η_t interpretiert, und dessen Produktionsquerschnitt wird mithilfe eines vereinfachten, von nichtrelativistischer Quantenchromodynamik inspirierten Modells zu $\sigma(\eta_t) = 8.7 \pm 1.1 \text{ pb}$ gemessen. Der Überschuss ist mit einer Signifikanz von mehr als fünf Standardabweichungen statistisch belegt und stellt somit die erste Beobachtung von gebundenen Zuständen im $t\bar{t}$ -System dar.

Weitere Interpretationen des beobachteten Überschusses sind ebenfalls möglich. Insbesondere werden Szenarios mit generischen pseudoskalaren oder skalaren Bosonen untersucht, und Ausschlussregionen hinsichtlich ihrer Kopplungen an das Top-Quark werden sowohl für die Dilepton-Kanäle allein als in Kombination mit einer separaten Analyse der $\ell+\text{jets}$ -Kanäle berechnet. Zusätzlich werden zu $t\bar{t}$ zerfallende Axion-Like Particles (ALPs) betrachtet: einerseits im Fall verschwindender ALP-Gluon-Kopplungen, andererseits im allgemeinen Fall, der phänomenologisch in Simulationen untersucht wird.

Eidesstattliche Versicherung

Hiermit versichere ich an Eides statt, die vorliegende Dissertationsschrift selbst verfasst und keine anderen als die angegebenen Hilfsmittel und Quellen benutzt zu haben.

Sofern im Zuge der Erstellung der vorliegenden Dissertationsschrift auf generativer Künstlicher Intelligenz (gKI) basierende elektronische Hilfsmittel verwendet wurden, versichere ich, dass meine eigene Leistung im Vordergrund stand und dass eine vollständige Dokumentation aller verwendeten Hilfsmittel gemäß der guten wissenschaftlichen Praxis vorliegt. Ich trage die Verantwortung für eventuell durch die gKI generierte fehlerhafte oder verzerrte Inhalte, fehlerhafte Referenzen, Verstöße gegen das Datenschutz- und Urheberrecht oder Plagiate.

Datum

Unterschrift des Doktoranden

Contents

1	Introduction	12
2	Theoretical framework	15
2.1	Standard Model	15
2.1.1	Quantum Chromodynamics	16
2.1.2	Top quark	17
2.1.3	Higgs mechanism	18
2.2	The $p p \rightarrow t\bar{t}$ process	19
2.2.1	Spin state of the $t\bar{t}$ system	21
2.2.2	Spin density matrix	24
2.3	Bound state effects in $t\bar{t}$	26
2.3.1	Properties of a $t\bar{t}$ bound state	26
2.3.2	Non-relativistic QCD calculations	28
2.3.3	Modeling in Monte Carlo simulation	31
2.4	Beyond the Standard Model	33
2.4.1	Heavy scalars in $t\bar{t}$ production	34
2.4.2	Two-Higgs Doublet Model	37
2.4.3	Axion-Like Particles	37
3	Experimental methods	40
3.1	The Large Hadron Collider	40
3.2	The CMS experiment	41
3.3	Object reconstruction	44
4	Monte Carlo event generation	47
4.1	Matrix Element generators	48
4.1.1	Higher orders in QCD	50
4.1.2	ME generators for $t\bar{t}$	51
4.2	Parton showers and matching	52
4.3	Multi-parton interactions	54
4.4	Hadronization	54
4.5	Pileup	55
4.6	Detector and trigger simulation	56
5	Statistical methods	57
5.1	Likelihood definition	57

5.2	Confidence intervals	58
5.3	Nuisance parameter diagnostics	60
5.4	Technical implementation	62
6	Measurement of the inclusive $t\bar{t}$ cross section at $\sqrt{s} = 13.6$ TeV	63
6.1	Introduction	63
6.2	Data sets and event selection	65
6.2.1	Data sets	65
6.2.2	Object definition	66
6.2.3	Channel definition	68
6.3	Corrections	70
6.3.1	Experimental corrections	70
6.3.2	Data-driven background estimation	76
6.4	Control distributions	81
6.5	Systematic uncertainties	85
6.6	Fit results	91
6.6.1	Statistical checks	91
6.6.2	Top quark mass dependence	94
6.7	Summary and Outlook	95
7	Simulation of on- and off-shell $t\bar{t}$ production with the Monte Carlo generator <code>bb41</code>	97
7.1	Introduction	97
7.2	The Monte Carlo generator <code>bb41</code>	98
7.2.1	Version differences	100
7.3	Other $t\bar{t}$ Monte Carlo generators	100
7.3.1	$t\bar{t} + tW$	100
7.3.2	<code>ttb_NLO_dec</code>	101
7.4	Technical setup	101
7.4.1	Parton shower matching	101
7.4.2	Same-flavor leptons	102
7.5	Results	103
7.5.1	Comparison between generators	103
7.5.2	Comparison of FSR matching settings	110
7.6	Summary and Outlook	112
8	Search for heavy scalar or pseudoscalar bosons in $t\bar{t}$ final states	113
8.1	Introduction	113
8.2	Analysis setup	114
8.2.1	Data sets	114
8.2.2	Object definition	117
8.2.3	Event selection	118

8.2.4	Experimental corrections	118
8.2.5	Reconstruction of the $t\bar{t}$ system	120
8.2.6	Sensitive observables	125
8.3	Higher-order corrections in $t\bar{t}$	125
8.3.1	NNLO QCD corrections	126
8.3.2	NLO EW corrections	127
8.4	Matrix element reweighting for A/H signals	129
8.4.1	Principle of the method	129
8.4.2	Combination of multiple origin samples	131
8.4.3	Validation	132
8.5	Systematic uncertainties	132
8.5.1	Theory uncertainties	132
8.5.2	Experimental uncertainties	135
8.5.3	Uncertainty smoothing	136
8.5.4	Differences between MC generators	138
8.6	Pre-fit distributions	141
8.7	Interpretation of the excess	146
8.7.1	Extraction of $t\bar{t}$ bound state effects	146
8.7.2	Parity of the excess	147
8.7.3	Checks of the result	149
8.7.4	Interpretation in terms of A and H	155
8.7.5	Comparison of η_t and A interpretations	156
8.8	Limits on A/H bosons	158
8.9	Combination with the $\ell+$ jets channels	164
8.9.1	Analysis strategy in the $\ell+$ jets channels	164
8.9.2	A/H limits	167
8.9.3	Simultaneous A+H exclusion contours	167
8.10	Comparison to other results	173
8.10.1	ATLAS $t\bar{t}$ threshold measurement	173
8.10.2	ATLAS A/H $\rightarrow t\bar{t}$ search	176
8.10.3	Other $t\bar{t}$ measurements	177
8.11	Summary and Outlook	178
9	Investigation of Axion-Like Particles decaying to $t\bar{t}$	182
9.1	Introduction	182
9.2	Translation of experimental limits	183
9.3	Phenomenological setup	183
9.4	Comparison of ALP and pseudoscalar A	186
9.5	Projected limits for ALPs	189
9.6	Summary and Outlook	191

10 Conclusions	193
10.1 Summary	193
10.2 Outlook	194
A Bibliography	196
B Acknowledgments	220
C Appendix	221
C.1 Sample normalizations in the matrix element reweighting	221

1 Introduction

It has always been the goal of high-energy physics to decipher the fundamental rules of nature. The most recent triumph in this journey was undoubtedly the discovery of the Higgs boson at the ATLAS and CMS experiments of the Large Hadron Collider (LHC) in 2012 [1–3], thus completing the Standard Model of particle physics (SM). Since then, the SM has been measured with ever-growing precision in the hope of finding and characterizing possible deviations from its predictions, and searches for new physics beyond the Standard Model (BSM) have been performed in various final states with complementary signatures. So far, no significant discrepancy has been found.

One promising avenue to search for new physics is the top quark, which is the most massive fundamental particle known today. Because of its high mass, it could be particularly connected to new phenomena. For example, it could be crucial in the search for new Higgs bosons, as they might exist in extended Higgs sectors, if their couplings to SM particles are Yukawa-like, i.e. proportional to the particle mass. In addition, the top quark is the only colored particle with a lifetime short enough so that it decays before it hadronizes. It therefore allows measurements of properties like spin and polarization that are significantly more difficult to access for all other quarks.

In this thesis, different aspects of top quark pair ($t\bar{t}$) production in proton-proton collisions at the LHC are studied at the Compact Muon Solenoid (CMS) experiment [4], which is one of the two large general-purpose LHC experiments. As a first test of top quark physics at the world record center-of-mass energy of $\sqrt{s} = 13.6$ TeV, a measurement of the inclusive $t\bar{t}$ production cross section is presented [5]. This energy was reached by the LHC for the first time in 2022 at the start of Run 3, after three years of shutdown and technical upgrades. The measurement performed here uses only 1.21 fb^{-1} of data, taken in July and August 2022. To achieve a precision on the $t\bar{t}$ cross section comparable with previous LHC measurements, experimental corrections such as lepton and b quark jet identification efficiencies have been estimated *in situ*, i.e. as part of the cross section measurement. The result was the first public result of LHC Run 3. It showed the high quality of the then-fresh collision data and provided a first confirmation of the SM at the new energy frontier.

Second, in measurements of top quark properties and for searches of new particles connected to the top quark, a reliable modeling of the $t\bar{t}$ production process is indispensable. For this purpose, the Monte Carlo (MC) event generator **bb4l** [6] is studied in great detail. It computes the full $\text{pp} \rightarrow b\bar{b}\ell\ell\nu\bar{\nu}$ matrix element for the

dilepton decay channel of $t\bar{t}$ and thus accurately models off-shell effects as well as the interference between $t\bar{t}$ and tW production. **bb41** is validated for the first time in the CMS simulation setup, and compared to other MC generators for $t\bar{t}$ production, preparing its use in future precision measurements at CMS [7].

Finally, a search for new spin-0 resonances decaying to $t\bar{t}$ is presented, utilizing the complete CMS Run 2 data set corresponding to an integrated luminosity of 138 fb^{-1} [8, 9]. The analysis focuses on the dileptonic decay channel. In addition to the invariant mass of the $t\bar{t}$ pair $m_{t\bar{t}}$, spin correlation observables derived from the kinematics of the leptons and top quarks are employed to probe the spin and \mathcal{CP} nature of potential new intermediate resonances.

Notably, a statistically significant excess over SM predictions is observed at low $m_{t\bar{t}}$, with features consistent with a pseudoscalar hypothesis. The excess is found to be consistent with a pseudoscalar $t\bar{t}$ (quasi-)bound state, which is expected to exist in the SM according to non-relativistic QCD calculations, though its modeling remains a challenge. This constitutes the first time such a $t\bar{t}$ bound state is experimentally observed.

Since the experimental analysis cannot exclude possible BSM contributions to the excess, other possible interpretations are investigated, such as the existence of additional scalar or pseudoscalar bosons as expected e.g. in a Two-Higgs-Doublet Model. The interference of these new bosons decaying to $t\bar{t}$ and SM $t\bar{t}$ production is taken into account, leading to complex signatures in the $m_{t\bar{t}}$ spectrum. In addition to an interpretation of the same low- $m_{t\bar{t}}$ excess, exclusion regions are derived for the presence of either one or two such new bosons in terms of their couplings to the top quark. For this purpose, the analysis of the dilepton decay channel of $t\bar{t}$ is further combined with a separate analysis of the lepton+jets decay channel.

As a third interpretation of the excess, heavy Axion-Like Particles (ALPs) decaying to $t\bar{t}$ are considered for the first time [10]. For the case that no explicit couplings between ALPs and gluons exist, experimental constraints on ALP couplings to top quarks are derived. For the case that ALP couplings to both top quarks and gluons exist, a phenomenological study of the discovery prospects of such heavy ALPs, as well as of the possibility to distinguish them from other pseudoscalars, is performed. These results are presented for the currently available luminosity as well as future projections.

The thesis is organized as follows. In Chapters 2 to 4, the framework used for the analyses is outlined. In particular, Chapter 2 describes aspects of the SM and BSM theories relevant for this work, Chapter 3 describes the LHC, the CMS detector, and object reconstruction methods, Chapter 4 discusses the machinery of Monte Carlo generators, and Chapter 5 briefly describes statistical inference techniques.

Following that, Chapters 6 to 9 each discuss one of the experimental or phenomenological results that comprise this work: the inclusive $t\bar{t}$ cross section measurement in Chapter 6, the study of off-shell $t\bar{t}$ production and $t\bar{t}/tW$ interference in Chapter 7,

1 Introduction

the search for spin-0 states in $t\bar{t}$, including its interpretation as a $t\bar{t}$ bound state, in Chapter 8, and the investigation of ALPs decaying to $t\bar{t}$ in Chapter 9. Finally, a short summary and outlook is given in Chapter 10.

Chapters 6 and 7 fully consist of work done as part of this thesis, while in Chapters 8 and 9 the major contributions from this thesis are summarized at the beginning of the chapters.

2 Theoretical framework

This chapter gives an outline of the theoretical concepts and models used in this thesis. It is split into two parts: First, the Standard Model of elementary particle physics is discussed, with an emphasis on the top quark. Secondly, several hypothesized extensions of the Standard Model, relevant for the searches presented in Chapters 8 and 9, are briefly introduced and compared.

2.1 Standard Model

The Standard Model of elementary particle physics, often simply called the Standard Model or SM, is, at the time of writing, the most successful theory describing the fundamental particles making up our universe [11, 12]. It is the result of a steady progression of increasingly complex models, starting with the introduction of quantum mechanics in the early 20th century and ending - for now - with the discovery of the Higgs boson at the LHC in 2012. The model has been extensively tested at many different experiments, most importantly the large collider experiments like PETRA, LEP, HERA, the Tevatron, and the LHC. So far, it has survived most of these tests with excellence, the biggest exception being the observation of neutrino masses (cf. Sec. 2.4).

The SM is formulated as a relativistic quantum field theory (QFT). That is, its most fundamental objects are fields acting on four-dimensional spacetime which, after a quantization procedure, yield physically observable particles as fundamental excitations. By the usual counting scheme, there exist seventeen different such fields, which can be classified into different groups, as schematically shown in Fig. 2.1.

The first group consists of the twelve fermions, which have spin $\frac{1}{2}$ and make up all visible matter. They are further split into the leptons, consisting of three electrically charged leptons - electron, muon, and tau lepton - and three corresponding electrically neutral neutrinos, as well as the quarks, of which there are six different flavors, called up, down, strange, charm, bottom, and top. The quarks have fractional electric charge, and in addition carry color charge as their defining property. Of note is that the fermions are also split into three generations, with each generation consisting of a charged lepton, a neutrino, and two quarks. The only fundamental differences between the particles of different generations are their masses, though the resulting physically observable properties, such as the lifetime, might be dramatically different.

The second group of particles are the bosons, which have integer spin. Here, the four gauge bosons with spin 1 act as the force carriers of the four fundamental

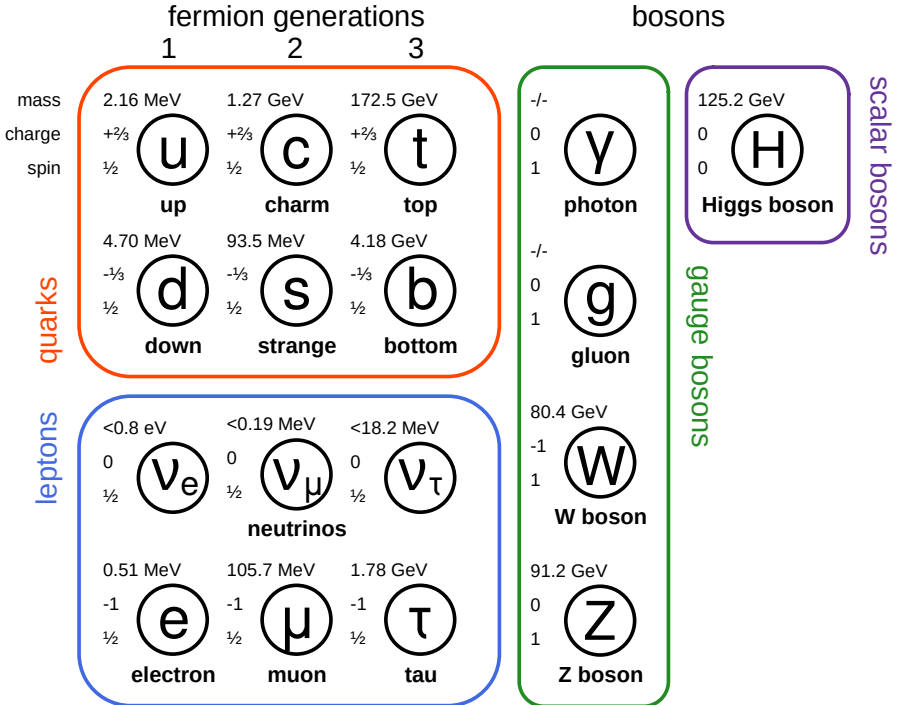


Figure 2.1: **The Standard Model.** A schematic depiction of the particle content of the SM, showing the seventeen fundamental particles, split into six quarks, six leptons, four gauge bosons, and the Higgs boson. The mass, electromagnetic charge, and spin of the particles is given next to the labels. Mass information is taken from Ref. [13].

interactions described by the SM: the photon, for the electromagnetic interaction with coupling strength α_{elm} ; the W and Z bosons, for the weak interaction with coupling strength α_W ; and the gluon, for the strong interaction with coupling strength α_S . At high enough energies, the electromagnetic and weak interaction unify into the electroweak interaction (coupling strength α_{EW}). The final particle is the Higgs boson, which has spin 0. Its most important role in the SM is to give mass to the fermions, as well as the W and Z bosons, through the so-called Higgs mechanism [14, 15], which is briefly outlined in Sec. 2.1.3.

2.1.1 Quantum Chromodynamics

The sector of the SM relating to the strong interaction is called *quantum chromodynamics* (QCD). It is a non-Abelian gauge theory with underlying gauge group $SU(3)$, the gluon as its gauge boson and coupling strength α_S as stated above [12, 16]. The charge under $SU(3)$ is called *color charge* and is carried by all quarks, as well as by the gluon itself, which is a consequence of the non-Abelian nature of the

$SU(3)$ group. Because of this, gluons can self-interact both through three-gluon and four-gluon vertices.

The self-interaction of gluons has drastic implications for the phenomenology of the theory. Because of it, the potential energy of two color-charged particles (i.e. quarks) rises with the distance between them. This is in contrast to the electromagnetic interaction, where the Coulomb potential between two charged particles, as mediated by the photon, approaches zero for large distances. Due to this behavior, when the distance between two quarks of opposite color increases, the energy stored in the gluon field similarly increases until it is large enough to form another quark-antiquark pair from the vacuum. In this simplified picture, the two quarks from this pair would then form two bound states with the original two quarks, giving two composite particles which are color-neutral on the outside [12].

This principle, called *confinement*, is fundamental to QCD: at low energies, no free colored particles can be observed. Because of this, quarks at low energies always form color-neutral bound states, which can be *mesons* consisting mainly of a quark and an antiquark, such as the pion, or *hadrons* consisting mainly of three quarks or three antiquarks, such as the proton and the neutron making up most visible matter.

Protons and neutrons in particular consist of three light quarks (the *valence quarks*, which are two up quarks and a down quark for the proton, and one up quark and two down quarks for the neutron) as well as a *sea* of further quarks and gluons, which arise from vacuum fluctuations. The details of the proton structure, like many low-energy QCD phenomena, are nonperturbative and cannot be computed analytically from the first principles of QCD (though some properties can be inferred using heavy numerical calculations in lattice QCD). They are quantitatively described by the *parton distribution functions* (PDFs), which can be seen as the probability to find a specific parton (gluon or quark) inside the proton at a given energy and momentum. More details about the description of protons in collider experiments is given in Sec. 4.1.

By contrast, at high energies, the potential between quarks reverts to the Coulomb potential, and the strong interaction slowly diminishes in strength. This behavior is called *asymptotic freedom* and makes perturbative calculations for collider experiments possible. This is further reflected in the *running* of the strong coupling α_S as a function of the energy scale of the process: it slowly decreases for high energies, while it tends towards infinity at the *Landau pole* located at $\Lambda_{\text{QCD}} \approx 250$ MeV. This marks the scale at which QCD becomes nonperturbative [16, 17].

2.1.2 Top quark

This thesis focuses on one particular strongly interacting fundamental particle: the top quark. As such, it will be described in further detail in this section.

The top quark was first discovered in 1995 at the Tevatron by the CDF and D0 experiments [18, 19]. With a rest mass of $m_t \approx 172.5$ GeV [20], the top quark is the

most massive known fundamental particle, and as a result it has unique properties compared to the other quarks: Its extremely short lifetime of $\sim 5 \times 10^{-25}$ s is lower than the typical time needed for a quark to hadronize under the strong interaction, making it the only bare quark — that is, the only quark which, via its decay products, is observable outside of hadrons. Among others, a consequence of this is that it fully preserves spin information during its decay, while such information is typically lost for other quarks during hadronization. More details on this are found in Sec. 2.2.2.

A second important property of the top quark that follows from its high mass is its large Yukawa coupling to the SM Higgs boson, which is of order one. As a result, the Higgs boson couples preferentially to the top quark of all SM fermions, and the study of both the SM Higgs boson and hypothetical additional Higgs bosons (see Sec. 2.4) is tightly connected to the top quark.

In the SM, the top quark decays to a bottom quark and a W boson with a branching ratio (BR) of almost 100% (to the degree that all other decays are commonly neglected). The W boson, in turn, can decay either to a charged lepton (e , μ or τ) and the corresponding neutrino with a BR of $\sim 32.6\%$, or to a pair of quarks (one up- and one down-type) with a BR of $\sim 67.4\%$. This results in different final states for top production processes, which are discussed more in Sec. 2.2.

2.1.3 Higgs mechanism

The Higgs boson is the most recently discovered particle of the SM. Its existence was confirmed in 2012 at the LHC by the ATLAS and CMS Collaborations [1–3], establishing the SM in its current form as the accepted description of elementary particle physics. In the SM, the Higgs boson is described by the so-called Higgs mechanism. It is briefly discussed in this section due to its relevance for many SM extensions involving additional Higgs bosons, as searched for in Chapters 8 and 9.

In the SM Lagrangian, the Higgs boson appears as a complex doublet ϕ in the form

$$\mathcal{L}_{\text{SM}} \subset (D_\mu \phi)^\dagger (D^\mu \phi) + V(\phi) \quad (2.1)$$

where D_μ is the covariant derivative, containing the minimal coupling to the gauge fields, and the Higgs potential $V(\phi)$ is

$$V(\phi) = \mu^2 \phi^\dagger \phi - \lambda (\phi^\dagger \phi)^2. \quad (2.2)$$

Here, μ^2 and λ are free parameters of the model. If both parameters are positive, this potential has a minimum at a non-zero value of

$$|\phi| = \frac{\mu}{\sqrt{2\lambda}} \equiv \frac{v}{\sqrt{2}} \quad (2.3)$$

with the vacuum expectation value $v = \mu/\sqrt{\lambda}$. This minimum, corresponding to

the vacuum state, is degenerate with respect to the three phases (i.e. the $SU(2)$ symmetry) of the complex doublet.

In the Higgs mechanism, this symmetry is now spontaneously broken in the transition from the high-energy state of the early universe (where the minimum is at $|\phi| = 0$) to the low-energy state observed today. The physical particles after symmetry breaking are then described by fluctuations around the new vacuum state. If the Higgs field were to be considered on its own, this would lead to one massive (corresponding to fluctuations in the $|\phi|$ direction) and three massless degrees of freedom (corresponding to the phases).

However, the interaction with the electroweak gauge fields encoded within D_μ leads to the massless degrees of freedom being absorbed into the gauge fields. This turns three of the four massless spin-1 gauge fields of the electroweak Lagrangian (with two degrees of freedom each) into massive fields instead (which have an additional longitudinal polarization, and thus three degrees of freedom). These three massive gauge fields are identified with the W and Z bosons, while the remaining massless field is identified with the photon. Finally, the leftover massive degree of freedom from the Higgs doublet ϕ is identified with the spin-0 boson observed at the LHC.

The resulting masses of the Z, W and Higgs bosons can be calculated as a function of μ^2 , λ and the electroweak couplings and thus used to test the Higgs mechanism. In addition to the electroweak bosons, the Higgs mechanism can also give masses to fermions (charged leptons and quarks) by including a Yukawa interaction term in the Lagrangian. This results in couplings between the SM Higgs boson and the different fermions that are proportional to the respective fermion mass.

In many possible extensions of the SM, the simple Higgs mechanism as presented here is extended or replaced by more complex theories. This can lead to modifications to the Yukawa couplings, making Yukawa coupling measurements attractive as tests of the SM. Two examples of such extensions are discussed in Secs. 2.4.2 and 2.4.3.

2.2 The $pp \rightarrow t\bar{t}$ process

In proton-proton collisions at the LHC, the dominant production mode of top quarks is the production of a top-antitop quark pair ($t\bar{t}$). The different parts of this thesis all focus on this process in different ways, and so this section gives a detailed overview of relevant effects.

At leading order (LO) in QCD, there are three diagrams (up to permutations of initial and final states) contributing to $t\bar{t}$ production, which can be seen in Fig. 2.2. They differ in their initial states: the first two diagrams are induced by gluon fusion, while the last one is induced by quark fusion (mostly from $u\bar{u}$ and $d\bar{d}$). The fraction of these is determined by the corresponding parton densities; at a center-of-mass energy of $\sqrt{s} \geq 13$ TeV, gluon fusion dominates with a fraction of roughly 90%.

At next-to-leading order (NLO) in QCD, many more diagrams become relevant,

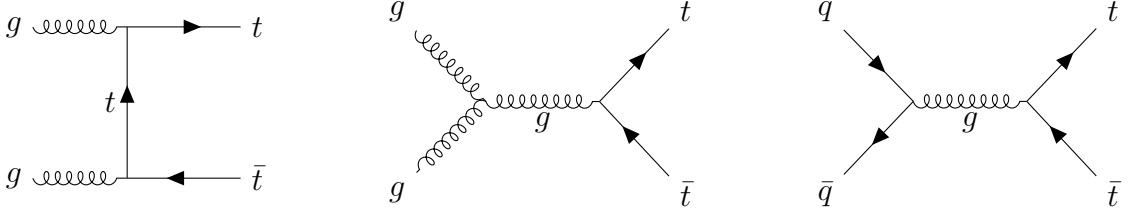


Figure 2.2: **Feynman diagrams for $pp \rightarrow t\bar{t}$.** The three diagrams (up to permutations) that contribute to the $pp \rightarrow t\bar{t}$ process at LO in QCD.

including those induced by the fusion of one quark and one gluon, while radiating a real quark. Similarly, real emissions of gluons can take place in gg or $q\bar{q}$ fusion diagrams. These effects change the kinematic properties of the produced top quarks, leading to NLO corrections for predicted distributions.

After production, both the top and antitop quark in the $t\bar{t}$ pair dominantly decay into a W boson and a b (anti)quark each. This leads to three different decay channels of the $t\bar{t}$ pair depending on the decays of the two W bosons, which are classified according to their number of leptons: The dilepton channel, with final state $b\bar{b}\ell\ell\nu\bar{\nu}$; the lepton+jets channel, with final state $b\bar{b}\ell\nu q\bar{q}$; and the all-hadronic channel, with final state $b\bar{b}qq\bar{q}\bar{q}$. Here, q stands in for any light quark (u, d, s or c).

The three channels differ greatly in their experimental challenges: The dilepton channel has the lowest branching ratio of $\sim 10.6\%$, which is further reduced to $\sim 6.4\%$ when excluding τ leptons decaying to hadrons due to then being experimentally hard to reconstruct. It also suffers from the fact that the two produced neutrinos escape the detector unobserved and are only measured as missing transverse momentum (cf. Sec. 3.3), losing both information in the forward direction as well as the ability to disentangle the two neutrinos. On the other hand, the final state of two opposite-sign charged leptons, two b jets, and missing transverse momentum does not have many other contributing processes in the SM, leading to very pure selections (particularly when the two leptons are an electron and a muon). All results in this thesis make use of this channel prominently.

By contrast, the lepton+jets channel has a large BR of $\sim 43.9\%$ ($\sim 30.4\%$ when excluding τ leptons decaying to hadrons), leading to high data statistics, and allows for easier interpretation of the missing transverse momentum due to only one neutrino. However, it can suffer from contamination by W+jets and multijet QCD background (the latter with non-prompt or fake leptons), from issues with combinatorics (i.e. the assignment of experimentally measured jets to the decay products) and from hadronic jet uncertainties, which can be large. This decay channel is employed for the result in Chapter 6 as well as in the combination in Chapter 8.

Finally, the all-hadronic channel, with a similar BR of $\sim 45.4\%$, is typically difficult to isolate from the background of QCD multijet production, and in addition suffers even more strongly from combinatorics and jet uncertainties than the lepton+jets

Term symbol	Spin multiplicity	\mathcal{P}	\mathcal{C}	\mathcal{CP}
1S_0	singlet	-1	+1	-1
3P_0	triplet	+1	+1	+1
3S_1	triplet	-1	-1	+1
1P_1	singlet	+1	-1	-1
3P_1	triplet	+1	+1	+1
3D_1	triplet	-1	-1	+1

Table 2.1: **Spin states of $t\bar{t}$.** Overview of the possible angular momentum states of the $t\bar{t}$ system with $J \leq 1$, including the spin multiplicity, the parity \mathcal{P} , the charge-parity \mathcal{C} , and their product \mathcal{CP} .

channel. As a result, it is in many cases the least precise of the three channels, and is not studied further in this work.

2.2.1 Spin state of the $t\bar{t}$ system

As fermions with spin $\frac{1}{2}$, top quarks have two possible spin states. As a result, the relative spins of the $t\bar{t}$ system can be either aligned, leading to a total vector state with spin $S = 1$, or anti-aligned, leading to a scalar state with spin $S = 0$. Furthermore, the $t\bar{t}$ system as a whole can have orbital angular momentum L , where L is a non-negative integer.

In analogy to atomic orbitals, the total angular momentum is then $\vec{J} = \vec{L} + \vec{S}$, and for any chosen basis the set of quantum numbers $\{S, L, J, J_z\}$ consists of conserved quantities. The angular momentum state is commonly written using a term symbol $^{2S+1}L_J$, where $2S + 1$ denotes the multiplicity of the spin state, and the orbital angular momentum L is written using spectroscopic notation (S for $L = 0$, P for $L = 1$, D for $L = 2$ etc). An overview of the lowest possible states ($J \leq 1$) is given in Tab. 2.1, including also the parities and charge-parities \mathcal{P} and \mathcal{C} , which can be inferred from the intrinsic parities of top and antitop as well as the orbital angular momentum. In proton-proton collisions, a mixture of all these states is produced, with the ratio depending on the production mode (gg , $q\bar{q}$ or gq), the energy, and the kinematics of the collision. Measurements of the spin and angular momentum state of the $t\bar{t}$ systems produced at the LHC thus give information about the details of the production mechanism, and can be attractive tests of the SM.

In practice, the spins of the top (anti)quarks cannot be observed directly, and instead must be inferred from their decay products. The way in which the spin information is passed to the decay products is determined by the maximally parity-violating nature of the weak interaction as well as by conservation of angular momentum. This is illustrated in Fig. 2.3 (left) for the leptonic decay of the top quark: Since the b quark is almost massless compared to the top quark, so that

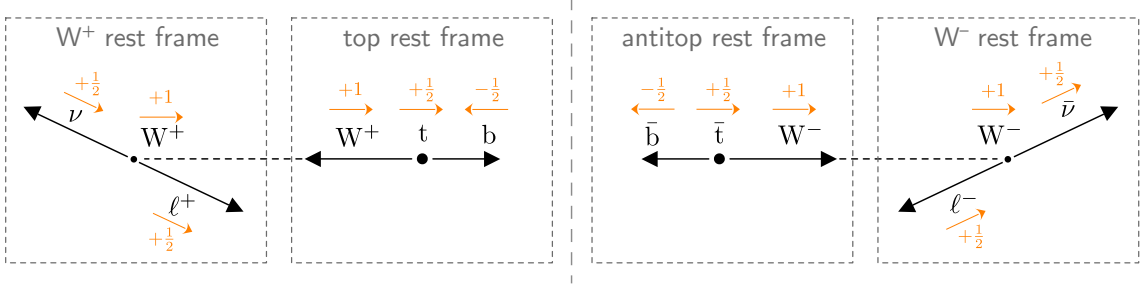


Figure 2.3: Helicity in top decays. Sketch of the allowed helicity configurations in a top (left) and antitop quark decay (right) to a lepton. The orange arrows and numbers illustrate the spin of the respective particles. The (anti)top decay is shown in the (anti)top rest frame, and the W boson decay in the W boson rest frame, as indicated by the gray boxes. It can be seen that, due to conservation of angular momentum and the parity-violating nature of the weak interaction, the ℓ^+ is preferred to be emitted in the direction of the t spin, while the ℓ^- is preferred to be emitted opposite to the direction of the \bar{t} spin.

$m_b = 0$ can be assumed in the following, it will be ultra-relativistic. Like for all fermions, its helicity is thus determined by its chirality. As a result, for the decay $t \rightarrow W^+ b$ the b quark — left-handed due to the weak interaction — has negative helicity (spin opposite to its direction of flight), leading to a longitudinally polarized W boson through conservation of angular momentum.

Since the decay of the W^+ into $\ell^+ \nu$ is again mediated by the weak interaction, and both decay products are nearly massless, the helicities of ℓ^+ and ν must be positive and negative, respectively. Boosting into the W^+ rest frame (leftmost box in Fig. 2.3), and again applying conservation of angular momentum, one then finds from the sketch that the charged lepton is emitted preferably in the direction of the top quark spin.

Repeating the same line of arguments for the decay of the antitop (Fig. 2.3 right), one finds that the opposite holds there: the charged lepton is emitted preferably opposite to the antitop spin. As a result, the direction of flight of the charged lepton in the center-of-mass system of its parent (anti)top can be used as a proxy for the (anti)top spin (or, equivalently, its polarization). It should be noted that this property of the top quark is unique among the quarks of the SM, since all other quarks hadronize via the helicity-ignorant strong interaction and thus lose the largest part of their spin information¹.

Returning to the full $t\bar{t}$ system, and applying the above observation to both top and antitop, one can now define observables to probe the $t\bar{t}$ spin state, or equivalently, the

¹See e.g. Ref. [21] for the greatly reduced possibilities of measuring spin correlations in $b\bar{b}$ or $c\bar{c}$ systems at the LHC.

spin correlation between t and \bar{t} . A simple such variable is the azimuthal difference $\Delta\phi_{\ell\ell}$ between the two leptons in a dileptonic decay. Assuming that the top and antitop are emitted back-to-back, a state with the top and antitop spins aligned (i.e. $S = 1$) will cause the two leptons to be emitted preferably in opposite directions, leading to large $\Delta\phi_{\ell\ell}$, while anti-aligned spins ($S = 0$) will lead preferably to parallel leptons and thus small $\Delta\phi_{\ell\ell}$. While this variable has the advantage of being easy to define and experimentally clean to measure, it is suboptimal in that it is also strongly affected by the kinematics of the $t\bar{t}$ production, including higher-order corrections in QCD, and is heavily sculpted when selecting certain areas of $t\bar{t}$ phase space. Thus, it is afflicted with large modeling uncertainties.

A more powerful variable can be defined by employing suitable reference systems as follows: the lepton and antilepton are first Lorentz boosted into the center-of-mass frame of the $t\bar{t}$ system, and then further boosted into the center-of-mass frame of their parent (anti)tops. Then, a correlation variable c_{hel} is defined as the scalar product of their direction unit vectors in these reference frames²:

$$c_{\text{hel}} = \hat{\ell}_t^+ \cdot \hat{\ell}_{\bar{t}}^- \quad (2.4)$$

It can be shown that, irrespective of the mode of production of the $t\bar{t}$ system and inclusive in the rest of the phase space, the distribution of this observable always follows a straight line [23], i.e.

$$\frac{1}{\sigma} \frac{d\sigma}{dc_{\text{hel}}} = \frac{1}{2} (1 - D c_{\text{hel}}). \quad (2.5)$$

The slope D depends on the spin and angular momentum of the produced $t\bar{t}$ state. At LO in QCD, it can be shown that $D = -1$ for pure singlet states (anti-aligned spins, e.g. 1S_0 , 1P_1) and $D = +\frac{1}{3}$ for pure triplet states (aligned spins, e.g. 3S_1 , 3P_0) [24, 25]. Higher-order corrections in QCD can slightly reduce these slopes through emissions of real gluons in the decay, which weaken the correlations, but these effects are of the order of 0.2% at NLO for leptons [26, 27].

In practice, any observed ensemble of $t\bar{t}$ pairs will be a mixture of the different spin states depending on the production mechanism and underlying theory, which can be probed by measuring the slope D . As will be discussed in Sec. 2.4, extensions of the SM can change the predicted slope, making measurements of D attractive tests for new physics. The value of D has been measured e.g. in Refs. [28–30], as well as more recently as a proxy variable in the context of measurements of quantum entanglement in $t\bar{t}$ production [31, 32].

²In this work, the naming convention from Ref. [22] is followed for c_{hel} . In e.g. Ref. [23], this variable is instead called $\cos\varphi$.

2.2.2 Spin density matrix

A more detailed way to quantify the spin properties of the $t\bar{t}$ system, respective to an arbitrary spin basis, is the production spin density matrix \mathbf{R} . When averaged over initial polarizations and colors, and summed over final colors but not over final polarizations, it can be written as [24, 25, 33]

$$\mathbf{R} = A \mathbb{1} \otimes \mathbb{1} + B_i^1 \sigma_i \otimes \mathbb{1} + B_i^2 \mathbb{1} \otimes \sigma_i + C_{ij} \sigma_i \otimes \sigma_j. \quad (2.6)$$

Here, $\mathbb{1}$ is the two-dimensional identity matrix, σ_i with $i = 1, 2, 3$ are the Pauli matrices, and the first and second components of the tensor product refer to the spin of the top and antitop quark, respectively. The scalar coefficient A describes the overall amplitude (i.e. the differential cross section as a function of the top and antitop kinematics) of $t\bar{t}$ production, the vectors \vec{B}^1 and \vec{B}^2 describe the polarization of the top and antitop quark, and the matrix \mathbf{C} describes the correlation between their spins. All of them are, in general, functions of the partonic center-of-mass energy and the scattering angle of the top quark relative to the incoming partons.

As explained in Sec. 2.2.1, in a dileptonic decay the spin information is transferred almost completely to the charged leptons. Defining the lepton directions of flight in their parent (anti)top rest frames $\hat{\ell}_t^+$ and $\hat{\ell}_{\bar{t}}^-$ as in Eq. (2.4), the resulting differential cross section in terms of the lepton angles, collectively denoted as Ω , is [33]

$$\frac{1}{\sigma} \frac{d\sigma}{d\Omega} = 1 + \vec{B}^1 \cdot \hat{\ell}_t^+ + \vec{B}^2 \cdot \hat{\ell}_{\bar{t}}^- + (\hat{\ell}_t^+)^T \mathbf{C} \hat{\ell}_{\bar{t}}^-. \quad (2.7)$$

By integrating out the remaining angles, it can be shown from this that, irrespective of the chosen basis, the slope D as defined in Eq. (2.5) can be recovered from the matrix \mathbf{C} as [23, 34]

$$D = \frac{1}{3} \text{Tr} [\mathbf{C}]. \quad (2.8)$$

As discussed in Sec. 2.2.1, D is maximally negative for pure singlet states (corresponding to a positive slope in c_{hel}). It is thus ideal for separating those in a mixed ensemble like the one provided by $pp \rightarrow t\bar{t}$ production, which contains all possible spin states (cf. Tab. 2.1).

One can define similar separating observables for other states using the spin density matrix by choosing a suitable spin basis. In this work, the so-called helicity basis proposed in Ref. [35] is used. The three axes of this basis, denoted \hat{k} , \hat{r} and \hat{n} , are defined as follows: \hat{k} is simply the direction of flight of the top quark in the center-of-mass frame of the $t\bar{t}$ system, such that the top quark spin with respect to \hat{k} is equal to the helicity. The second axis, \hat{r} , is orthogonal to \hat{k} in the scattering plane of the $pp \rightarrow t\bar{t}$ process. Finally, the third axis \hat{n} is orthogonal to both \hat{k} and \hat{r} , oriented such that the $\{\hat{k}, \hat{r}, \hat{n}\}$ system is left-handed. If \hat{p} denotes the beam axis and θ_t^* the top scattering angle with respect to this axis, the latter two axes are given by

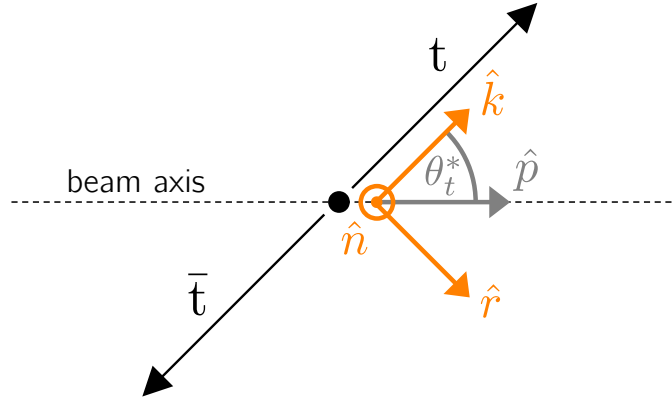


Figure 2.4: **Helicity basis.** Sketch of the helicity basis used to define the top and antitop quark spins. The unit vectors \hat{k} , \hat{r} and \hat{n} define the right-handed basis, while the beam axis is given by \hat{p} and the top quark scattering angle by θ_t^* .

$$\hat{r} = \frac{\hat{p} - \cos \theta_t^* \hat{k}}{|\hat{p} - \cos \theta_t^* \hat{k}|} \quad \text{and} \quad \hat{n} = \hat{r} \times \hat{k} = \frac{\hat{p} \times \hat{k}}{|\hat{p} \times \hat{k}|}. \quad (2.9)$$

This coordinate system is visualized in Fig. 2.4. It is used, among others, in Refs. [29, 30] to measure both the polarizations \vec{B}^1 and \vec{B}^2 and spin correlation coefficients C_{ij} ($i, j = k, r, n$). In this work, only the spin correlation is considered. Particularly, in addition to c_{hel} , the following observable is defined:

$$c_{\text{han}} = -(\hat{\ell}_t^+)_k (\hat{\ell}_{\bar{t}}^-)_k + (\hat{\ell}_t^+)_r (\hat{\ell}_{\bar{t}}^-)_r + (\hat{\ell}_t^+)_n (\hat{\ell}_{\bar{t}}^-)_n \quad (2.10)$$

where $(\hat{\ell})_i$, $i = k, r, n$ refers to the i -th component of the respective vector in the $\{\hat{k}, \hat{r}, \hat{n}\}$ basis. For comparison, using the same notation, c_{hel} can be written as

$$c_{\text{hel}} = +(\hat{\ell}_t^+)_k (\hat{\ell}_{\bar{t}}^-)_k + (\hat{\ell}_t^+)_r (\hat{\ell}_{\bar{t}}^-)_r + (\hat{\ell}_t^+)_n (\hat{\ell}_{\bar{t}}^-)_n. \quad (2.11)$$

The only difference between c_{hel} and c_{han} thus lies in the sign of the first term encoding the correlation in the \hat{k} direction, i.e. the top direction of flight. Like c_{hel} , c_{han} has the advantage of always being linear in the absence of phase space cuts, i.e.

$$\frac{1}{\sigma} \frac{d\sigma}{dc_{\text{han}}} = \frac{1}{2} (1 + D^{(k)} c_{\text{han}}) \quad (2.12)$$

where [24]

$$D^{(k)} = \frac{1}{3} (C_{kk} - C_{rr} - C_{nn}). \quad (2.13)$$

From Eq. (2.13), it can be seen that the slope is maximally negative, $D^{(k)} = -1$, when the top and antitop spins are anti-correlated along the top direction of flight ($C_{kk} = -1$) and correlated along the orthogonal directions ($C_{rr} = C_{nn} = +1$). The (unpolarized) state described by these correlations is a pure triplet state ($S = 1$) [24].

Particularly, the 3P_0 state of $t\bar{t}$ always corresponds to this spin state: It has no total angular momentum, so that its total spin and orbital angular momentum must be anti-aligned. Since the orbital angular momentum is always exactly zero in the direction of flight of the top quarks, the $t\bar{t}$ system must be in an orbital angular momentum eigenstate with $L_k = 0$, and thus also in a total spin eigenstate with $S_k = 0$. In other words, the spins in the \hat{k} direction are anti-aligned, corresponding to $C_{kk} = -1$. In order to arrive at $S = 1$, i.e. a pure triplet state, it is required that the other entries fulfill $C_{rr} = C_{nn} = 1$.

Thus, c_{han} is ideal for separating the 3P_0 state from a mixed ensemble of $t\bar{t}$ spin states, in the same way c_{hel} is for the 1S_0 state. Both c_{hel} and c_{han} will be used in Chapter 8 to search for new intermediate states in $t\bar{t}$ production; the theory behind this is briefly discussed in Sec. 2.4.1.

2.3 Bound state effects in $t\bar{t}$

When predicting distributions of observables for hard scattering processes such as $t\bar{t}$ production, one usually employs perturbative calculations at a fixed order in the strong coupling constant α_S , possibly matched to a parton shower (see Chapter 4). However, at low energy scales (or equivalently, long distances) the strong interaction becomes nonperturbative (cf. Sec. 2.1.1), leading to effects that cannot be captured in the usual perturbative expansion irrespective of the order in α_S (though they might or might not be captured in expansions or resummations with other parameter choices).

For quarks other than the top quark, long-distance effects are well known to lead to the formation of quark-antiquark bound states, called *quarkonia*. Examples for $c\bar{c}$ and $b\bar{b}$ production are J/ψ , η_c or Υ . An important question is now whether a similar bound state (“toponium”) exists for $t\bar{t}$ production, as well as what properties it would have. This will be discussed in detail in the following section.

2.3.1 Properties of a $t\bar{t}$ bound state

To begin, some simple properties of a possible toponium state are roughly estimated by adapting the simple picture of a non-relativistic bound state. The top quark and antiquark are, for now, seen as stable particles bound by QCD, in analogy how proton and electron are bound by the electric force inside the hydrogen atom. The QCD potential between quark and antiquark as a function of the radius r can be

approximated as³

$$V_{\text{QCD}}^{[1,8]}(r) = -\frac{C^{[1,8]}\alpha_S}{r} + \mathcal{O}(\alpha_S^2) \quad (2.14)$$

where the color factor is $C^{[1]} = 4/3$ for color-singlet and $C^{[8]} = -1/6$ for color-octet $t\bar{t}$ states. As a result, only $t\bar{t}$ systems in a color-singlet state feel an attractive force and can possibly form a bound state, while color-octet states are instead repulsed.

In analogy with the hydrogen atom, one can now estimate the ground state binding energy of a color-singlet $t\bar{t}$ bound state as [37–39]

$$E_b = -\frac{1}{2} \frac{m_t}{2} (C^{[1]}\alpha_S)^2 \quad (2.15)$$

and the Bohr radius of the bound state as

$$r_b = \frac{2}{C^{[1]}\alpha_S m_t}. \quad (2.16)$$

To evaluate this numerically, the scale at which α_S should be evaluated needs to be defined. An intuitive choice is the inverse of the Bohr radius $1/r_b$, corresponding to the typical energy scale of the (anti)quark [39, 40]. At one loop in QCD, the running of α_S is given by [12]

$$\alpha_S(Q^2) = \frac{\alpha_S(m_Z^2)}{1 + \beta_0 \alpha_S(m_Z^2) \ln\left(\frac{Q^2}{m_Z^2}\right)} \quad \text{with} \quad \beta_0 = \frac{33 - 2N_f}{12\pi} \quad (2.17)$$

where $N_f = 5$ is the number of active quark flavors and $\alpha_S(m_Z^2) = 0.118$ is the strong coupling constant at the reference scale of the Z boson mass, $m_Z = 91.2 \text{ GeV}$ [13]. Replacing α_S by $\alpha_S(1/r_b^2)$ in Eq. (2.16) yields a self-consistent equation with the numerical solution

$$\alpha_S(1/r_b^2) = 0.158 \quad \text{and} \quad r_b = 0.056 \text{ GeV}^{-1} \approx 0.01 \text{ fm}. \quad (2.18)$$

This extremely small radius would make a possible $t\bar{t}$ bound state the smallest known non-pointlike object [41].

Inserting $\alpha_S(1/r_b^2)$ into Eq. (2.15) finally gives the binding energy and “mass” of toponium:

$$E_b = -1.93 \text{ GeV} \implies M = 2m_t + E_b \approx 343 \text{ GeV} \quad (2.19)$$

where a value of $m_t = 172.5 \text{ GeV}$ was used for the top quark mass. Varying the

³In general, the potential also contains a linear term proportional to r parameterizing the self-interaction of gluons in QCD and the resulting confinement [36]. However, it is small for systems of sufficiently small size like toponium and thus neglected for the simple estimation in this section.

scale used to evaluate α_S up and down by a factor 2, as typically done, results in a variation of $\Delta E_b \approx \pm 0.5 \text{ GeV}$. A further useful quantity is the average velocity of the top (anti)quarks in the bound state, given simply by (in units of the speed of light) [39]:

$$v_0 = C^{[1]} \alpha_S = 0.21. \quad (2.20)$$

However, this simple picture is spoiled by the large width of the top quark of about $\Gamma_t = 1.4 \text{ GeV}$ [13] and resulting short average lifetime of $\tau_t \approx 5 \times 10^{-25} \text{ s}$. Since both the top quark and antiquark making up the bound state can in principle decay independently, the dominant decay of toponium will be through disassociation, i.e. through one of the constituent quarks decaying to Wb as usual [38]. The width and lifetime of toponium can thus be respectively estimated as $2\Gamma_t$ and $\frac{1}{2}\tau_t$. This can be compared to the formation time of toponium, estimated as the classical revolution time of the quark and antiquark and given by [39]

$$\tau_{\text{form}} = \frac{2\pi r_b}{v_0} \approx 1 \times 10^{-24} \text{ s}. \quad (2.21)$$

Since $\tau_{\text{form}} > \frac{1}{2}\tau_t$, either the top or the antitop quark will in most cases decay before toponium can form, so that the $t\bar{t}$ system does not form a stable bound state [37, 38]. One can still estimate the fraction of at-rest $t\bar{t}$ pairs that live long enough to form a bound state by approximating the lifetime of a $t\bar{t}$ system via an exponential distribution, which gives $\exp(-2\tau_{\text{form}}/\tau_t) \approx 1\%$. Based on this simple picture, $t\bar{t}$ bound state formation is expected to be a rather small effect.

2.3.2 Non-relativistic QCD calculations

A more quantitative picture of $t\bar{t}$ bound state effects is given by the framework of non-relativistic QCD (NRQCD) [40, 42–44]. In this approach, the partonic differential cross section for the production of a $t\bar{t}$ pair from two initial state partons i and j as a function of its invariant mass $m_{t\bar{t}}$ can be written in a factorized form as [40]

$$\frac{d\hat{\sigma}(ij \rightarrow t\bar{t})}{dm_{t\bar{t}}}(\hat{s}, m_{t\bar{t}}) = F_{ij \rightarrow t\bar{t}}(\hat{s}, m_{t\bar{t}}) \frac{1}{m_t^2} J(m_{t\bar{t}}) \quad (2.22)$$

where \hat{s} is the partonic center-of-mass energy squared⁴, $F_{ij \rightarrow t\bar{t}}(\hat{s}, m_{t\bar{t}})$ is the *hard function*, which contains the hard scattering matrix element for $pp \rightarrow t\bar{t}$, and $J(m_{t\bar{t}})$ is the *long-distance function* that encodes possible bound state effects. The hard function can be computed in the usual manner in relativistic perturbative QCD at a fixed order in α_S (cf. Sec. 4.1). The long-distance function is obtained from the solutions to the Schrödinger equation describing top quark and antiquark, analogously

⁴At LO in QCD, there is no additional radiation, and so $\hat{s} = m_{t\bar{t}}^2$.

to the hydrogen atom as discussed in the previous section. Here, it is assumed that the relative velocity of the top and antitop quark is small and they can thus be considered non-relativistic.

If the top quarks are considered stable, i.e. $\Gamma_t = 0$, there is a discrete set of solutions with masses $M_n = 2m_t + E_n$ as given by Eq. (2.15) and the long-distance function below the threshold is given by [40]

$$J(m_{t\bar{t}}) = \sum_n |\Psi_n(0)|^2 \pi \delta(m_{t\bar{t}} - M_n) \quad (2.23)$$

where $|\Psi_n(0)|^2$ is the squared wave function at the origin for solution n . This picture thus corresponds to a discrete set of cleanly separated, stable bound states described by δ functions, similar to $c\bar{c}$ and $b\bar{b}$ bound states.

In practice, the finite top width is of a similar order of magnitude as the binding energy (see previous section), and cannot be neglected. One can take the finite top width into account by replacing the long-distance function with [40]

$$J(m_{t\bar{t}}) = \text{Im } G(\vec{r} = 0; m_{t\bar{t}} + i\Gamma_t) \quad (2.24)$$

where $G(\vec{r} = 0; m_{t\bar{t}} + i\Gamma_t)$ is the *Green's function* of the non-relativistic Schrödinger equation, evaluated at zero distance ($\vec{r} = 0$) using a complex mass $m_{t\bar{t}} + i\Gamma_t$.

The long-distance function is shown numerically in Fig. 2.5 for both the stable top and finite width case, evaluated at LO in QCD using the expressions in Ref. [40]. The same scales and values of α_S as in Eq. (2.18) have been used for the evaluation. As discussed in the previous section, bound-state effects are only present for a color-singlet state, while for a color-octet state, the long-distance function is smaller than the long-distance function for free quarks, indicating a suppression of the cross section for color-octet states close to the threshold.

For color-singlet states, in the finite width case the bound state energy levels are no longer cleanly separated, but smeared together with the $t\bar{t}$ continuum by the finite top width (solid orange curve). The bound state and the $t\bar{t}$ continuum are thus in principle not separable, and bound state effects should be seen as a correction to the usual fixed-order $t\bar{t}$ continuum spectrum. Because of this, this effect is sometimes called a “quasi-bound state” or a “virtual bound state”.

Still, a peak in the long-distance function is clearly visible at $m_{t\bar{t}} \approx 2m_t - 2 \text{ GeV}$, coinciding with the binding energy estimated in the simple picture of the previous section. This location of the peak is confirmed by multiple independent full NRQCD calculations, taking into account also the hard function as well as higher orders of α_S in the QCD potential [40, 42–45]. The details of the line shape differ between some of the calculations, and should thus be considered uncertain. However, the experimental resolution of $m_{t\bar{t}}$ is expected to be much larger than the bound state width of order $\sim 2\Gamma_t$ (see Sec. 8.2.5), making the details of the spectrum irrelevant to an experimental search.

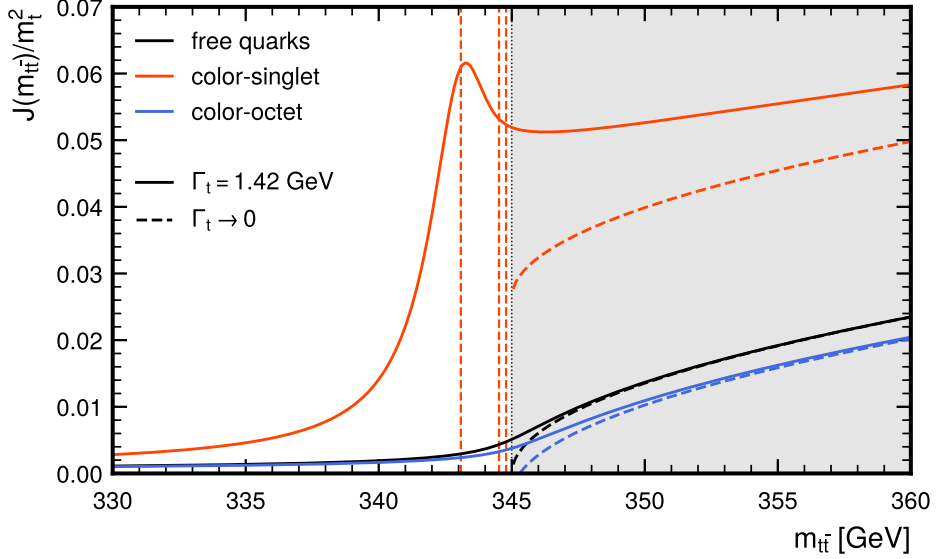


Figure 2.5: Long-distance function encoding $t\bar{t}$ bound state effects. The long distance function $J(m_{t\bar{t}})$ (Eq. (2.22)), normalized to the top mass squared, as a function of $m_{t\bar{t}}$ around the $t\bar{t}$ threshold. The free quark case (i.e. no interaction) is shown in black, and the color-singlet and color-octet cases are shown in orange and blue, respectively. Dashed lines correspond to stable top quarks ($\Gamma_t \rightarrow 0$, Eq. (2.23)), split into a discrete spectrum below and a continuous spectrum above the $t\bar{t}$ threshold (gray shaded area). Solid lines correspond to the case of a finite top width (Eq. (2.24)). All curves have been computed using the expressions in Ref. [40].

Besides the $m_{t\bar{t}}$ spectrum, one can infer the angular momentum state of the $t\bar{t}$ bound state from the available production mechanisms at the LHC. Since both of the top quarks have low velocity, states with orbital angular momentum $L \neq 0$ will be strongly suppressed (beyond NLO in NRQCD [40]). Furthermore, because $q\bar{q}$ systems are always color octets, $t\bar{t}$ bound states can at LO be produced only from gg initial states in proton-proton collisions. Close to the $t\bar{t}$ threshold, the gg initial state in $t\bar{t}$ production always has spin $S = 0$ (and thus total angular momentum $J = 0$), with $S = 2$ contributions suppressed by powers of the top velocity [25], Thus, the resulting $t\bar{t}$ system must be in the ${}^1S_0^{[1]}$ state. At NLO in QCD, also ${}^3S_1^{[1]}$ states can be produced; however, the contribution is very small (less than 0.1% of the total cross section [40]).

2.3.3 Modeling in Monte Carlo simulation

The existing NRQCD calculations for proton-proton collisions predict only certain differential distributions and cannot be directly compared to experimental data on a per-event level. Because of this, a simplified model for the $t\bar{t}$ bound state that can be used in MC simulation (cf. Chapter 4) is introduced following Refs. [24, 46–48]. Instead of a first-principles calculation, the bound state effects are modeled as an additional spin-0 state η_t , which is added to the conventional perturbative QCD (pQCD) calculation of $t\bar{t}$. η_t is defined to couple directly to gluons and top quarks via the interaction Lagrangian [24, 47]

$$\mathcal{L}_{\eta_t} = -\frac{1}{4}g_{gg\eta_t}\eta_t G_{\mu\nu}^a \tilde{G}^{a\mu\nu} - ig_{t\bar{t}\eta_t}\eta_t \bar{t}\gamma_5 t \quad (2.25)$$

where $G_{\mu\nu}^a$ is the gluon field strength tensor, $\tilde{G}_{\mu\nu}^a$ its dual, and $g_{gg\eta_t}$ as well as $g_{t\bar{t}\eta_t}$ are arbitrary coupling strengths. The resulting model has three free parameters: the binding energy $E_b = m(\eta_t) - 2m_t$, the total width $\Gamma(\eta_t)$ and the production cross section $\sigma(\eta_t)$ (the latter determining the couplings $g_{gg\eta_t}$ and $g_{t\bar{t}\eta_t}$). In Ref. [47], they are determined by fitting them to the NRQCD calculation from Ref. [43], yielding

$$E_b = -2 \text{ GeV} \implies m(\eta_t) = 343 \text{ GeV}, \quad \Gamma(\eta_t) = 7 \text{ GeV}, \quad \sigma(\eta_t) = 6.4 \text{ pb}. \quad (2.26)$$

The binding energy is again consistent with the simple estimation in Eq. (2.19). In the generation of events, the top quarks are now allowed to be fully off-shell by calculating the full amplitude $pp \rightarrow \eta_t \rightarrow W^+W^-b\bar{b}$, thus making sure that the phase-space region $m_{WWb\bar{b}} < 2m_t$ is populated. Furthermore, Ref. [47] recommends that the contribution of η_t should be restricted to the region $|m_{WWb\bar{b}} - m(\eta_t)| \leq 6 \text{ GeV}$ so that the bulk of the $t\bar{t}$ phase space, in which the pQCD calculation is expected to be accurate while the NRQCD calculation misses relativistic corrections, is not affected.

However, Refs. [46, 48] recommend instead

$$E_b = -2 \text{ GeV} \implies m(\eta_t) = 343 \text{ GeV}, \quad \Gamma(\eta_t) = 2\Gamma_t = 2.8 \text{ GeV} \quad (2.27)$$

and no cut on $|m_{WWb\bar{b}} - m(\eta_t)|$.

The resulting $m_{WWb\bar{b}}$ distribution for the combination of pQCD $t\bar{t}$ and η_t is shown in Fig. 2.6 at the level of hard scattering for both parameterizations, on its own as well as stacked on top of a pQCD prediction of the $t\bar{t}$ continuum at NLO in QCD. The stacked distributions are compared to an NRQCD prediction from Ref. [44]. At the level of hard scattering, the lower width of $\Gamma(\eta_t) = 2\Gamma_t$ agrees much better with the predicted NRQCD spectrum and avoids an unphysical discontinuity due to the $m_{WWb\bar{b}}$ cutoff. Thus, this parameterization will be used in this work wherever possible, i.e. in Secs. 8.7 and 8.8, though the parameterization of Eq. (2.26) is

2 Theoretical framework

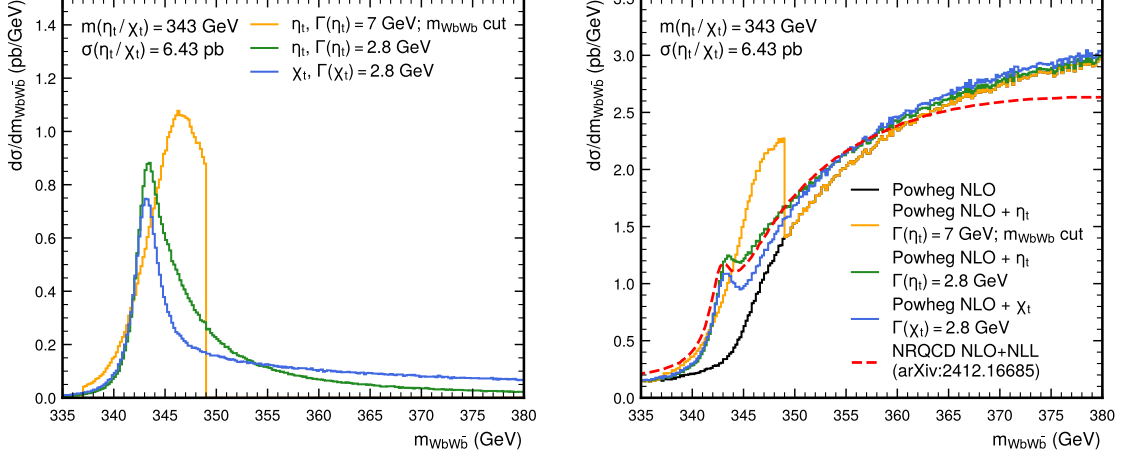


Figure 2.6: Line shape of η_t and χ_t . The $m_{WWb\bar{b}}$ distribution close to the $t\bar{t}$ threshold, as predicted by the η_t and χ_t models on their own (left) and stacked on top of a pQCD $t\bar{t}$ prediction from POWHEG NLO (right, see Sec. 4.1.2). For the orange line, the η_t width is chosen to be 7 GeV, and a cut on $|m_{WWb\bar{b}} - m(\eta_t)|$ is applied (Eq. (2.26)), while for the green line, the η_t width is chosen as 2.8 GeV, and no further cuts are made (Eq. (2.27)). The blue line shows χ_t for a width of 2.8 GeV. In the right plot, all models are compared to an NRQCD prediction from Ref. [44].

retained for the sake of consistency with other results in Sec. 8.9. For more details, see these sections.

In the final stages of this work, a more involved model for $t\bar{t}$ bound states was published in Ref. [49]. There, instead of simulating an additional pseudoscalar state η_t , the bound state effects are included in LO color-singlet $t\bar{t}$ production by directly reweighting produced events with the ratio of Green's functions. This model is in principle fully predictive, i.e. it does not require fitting parameters to external calculations. However, it could not be validated in time for inclusion in the results of Chapter 8, it does not explicitly distinguish between $t\bar{t}$ spin states, and it is also unclear on how to match it to the $t\bar{t}$ continuum. Because of this, it is not further considered here and its investigation left for future work.

While NRQCD predicts any possible $t\bar{t}$ bound state contribution in pp collisions to be dominated by the ${}^1S_0^{[1]}$ state, with contributions from excited states strongly suppressed, experimentally it will still be useful to compare this spin state to other possibilities. To this end, a second toy model, denoted χ_t , is defined in analogy to η_t by the interaction Lagrangian

$$\mathcal{L}_{\chi_t} = -\frac{1}{4} g_{gg\chi_t} \chi_t G_{\mu\nu}^a \tilde{G}^{a\mu\nu} - g_{t\bar{t}\chi_t} \chi_t \bar{t}t \quad (2.28)$$

where $g_{gg\chi_t}$ and $g_{t\bar{t}\chi_t}$ are again arbitrary couplings. This Lagrangian contains a \mathcal{CP} -even coupling to the top quark, compared to the \mathcal{CP} -odd coupling in Eq. (2.25). It thus produces $t\bar{t}$ systems in the ${}^3P_0^{[1]}$ state, which is the only other possible state with $J = 0$ (cf. Tab. 2.1). The free parameters of this model are again cross section, mass, and width; they are set here to the same values as for η_t in all cases⁵.

The resulting $m_{WWb\bar{b}}$ line shape is also seen in Fig. 2.6. It shows a small peak similar to η_t at ~ 343 GeV, though it exhibits a more pronounced tail at high $m_{WWb\bar{b}}$ since the 3P_0 state carries one unit of orbital angular momentum and thus favors higher top quark velocities. In Sec. 8.7.2, the χ_t model will be used in conjunction with η_t to probe the spin state of the observed excess. Other possible states, such as the vector state ${}^3S_1^{[1]}$, are not considered here and instead left for future work.

2.4 Beyond the Standard Model

The Standard Model, greatly successful as it is at describing the results of collider experiments so far, is nonetheless known to be incomplete. In fact, there exist several experimental results which cannot be explained by SM predictions, such as the observation of dark matter in many astrophysical contexts [52–54], the observed matter-antimatter asymmetry in the universe [55, 56], or the observed masses of the neutrinos [57, 58].

In addition, the SM is plagued by several theoretical challenges that will likely not be overcome without major modifications to the theory. Chief among these is the unification of the forces of the SM - the electroweak and strong interactions - with gravity as described by General Relativity, which is not included in the SM at all. Doing so has proven extremely challenging, and no fully consistent unified theory of all forces is known yet. Further open questions are, for example, the hierarchy or naturalness problem [59–61] or the strong \mathcal{CP} problem [62, 63].

In order to solve these problems in a satisfactory manner, a more general theory will have to be found, which should include the SM as its low-energy limit. In many cases, this will result in additional as of yet undiscovered particles. There is a multitude of such Beyond the Standard Model (BSM) extensions, each attacking different parts of the problems, and one of the major tasks of particle physics is to explore which parts of the parameter space of these models can be probed with the current experiments.

This work, in particular, aims to probe models predicting new, heavy spin-0 states coupling strongly to the top quark. Such models are interesting for several reasons:

⁵In Ref. [50], an estimation similar to the one in Sec. 2.3.1 at the stable-top level results in a ~ 3 GeV higher mass for a 3P_0 bound state than for a 1S_0 bound state. Similar arguments can be made based on analogies to $c\bar{c}$ and $b\bar{b}$ quarkonia [51]. However, it is unknown whether this would be noticeable even in the hard-scattering level spectrum due to the large smearing from the top width. It is anyway expected to be irrelevant within the experimental resolution.

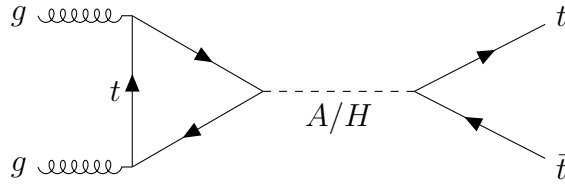


Figure 2.7: **Feynman diagram for $gg \rightarrow A/H \rightarrow t\bar{t}$.** Only the leading-order gluon fusion diagram is shown, with a top quark running in the loop.

extensions of the Higgs sector of the SM (cf. Sec. 2.1.3) are commonly proposed to solve e.g. the naturalness problem of the SM, and usually contain additional scalar particles with Yukawa interactions [64–66]. Additional scalars could also be mediators between the SM and dark matter [67, 68], and in certain cases could even solve the strong \mathcal{CP} problem ([69, 70], cf. Sec. 2.4.3).

In Sec. 2.4.1, the effect of additional scalars in the $pp \rightarrow t\bar{t}$ process are outlined in a generic fashion. Following that, two explicit realizations of such models are discussed, namely the Two-Higgs Doublet Model (2HDM) (Sec. 2.4.2) and Axion-Like Particle (ALP) models (Sec. 2.4.3).

2.4.1 Heavy scalars in $t\bar{t}$ production

Consider an unspecified BSM extension predicting (possibly among others) a massive spin-0 state Φ coupling to top quarks via a Yukawa interaction. In the absence of couplings to other particles, the Lagrangian of such a state can be written as [24]

$$\mathcal{L}_\Phi = \frac{1}{2}(\partial_\mu \Phi)(\partial^\mu \Phi) + \frac{m_\Phi^2}{2}\Phi^2 + g_{\Phi\bar{t}t}\frac{m_t}{v}\bar{t}\Phi(\cos\alpha + i\gamma_5 \sin\alpha)t. \quad (2.29)$$

where m_Φ is the mass of the new state and $g_{\Phi\bar{t}t}$ is a coupling modifier, scaled to the SM Higgs-top Yukawa coupling with the SM Higgs vacuum expectation value v . The phase α is a free parameter determining the \mathcal{CP} structure of the $\Phi\bar{t}t$ coupling: For $\alpha = 0$, the coupling is purely \mathcal{CP} -even or scalar, while for $\alpha = \pi/2$, the coupling is purely \mathcal{CP} -odd or pseudoscalar. Intermediate values for α will cause \mathcal{CP} -mixed couplings, which in general will result in \mathcal{CP} violation in processes involving top quarks. Possible experimental indicators of such \mathcal{CP} violation in $pp \rightarrow t\bar{t}$ are e.g. discussed in Ref. [34].

In the scope of this work, only the \mathcal{CP} -conserving cases of Φ are considered. For convenience, the pure pseudoscalar case will in the following be called A, while the pure scalar case will be called H.

Similar to the SM Higgs boson, the most important production channel of either state at the LHC will be through loop-induced gluon fusion, followed by associated production with either $t\bar{t}$ or a single top quark. Only the former is considered here; experimental searches for the latter case can be found e.g. in Ref. [71].

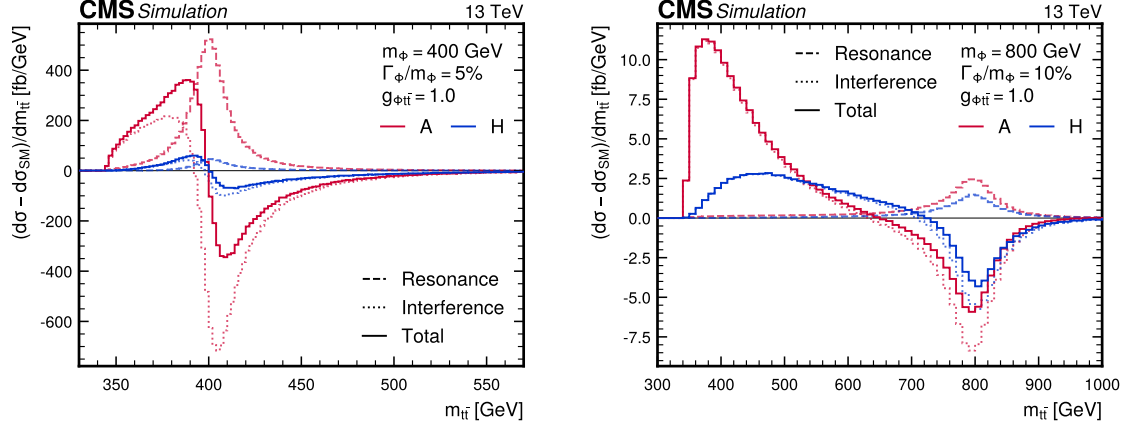


Figure 2.8: **Differential cross sections for $\text{pp} \rightarrow \text{A}/\text{H} \rightarrow \text{t}\bar{t}$.** The proton-proton differential cross section as a function of the invariant $t\bar{t}$ mass, with the SM prediction subtracted, for $m_{\text{A}/\text{H}} = 400 \text{ GeV}$, $\Gamma_{\text{A}/\text{H}}/m_{\text{A}/\text{H}} = 5\%$ (left) and $m_{\text{A}/\text{H}} = 800 \text{ GeV}$, $\Gamma_{\text{A}/\text{H}}/m_{\text{A}/\text{H}} = 10\%$ (right) as well as for A (red) and H (blue), at a coupling modifier of $g_{\text{At}\bar{t}/\text{Ht}\bar{t}} = 1$. The resonance and interference components as well as their sum are shown as dashed, dotted and solid lines, respectively [9]. They are calculated from the same Monte Carlo simulation samples described in Sec. 8.2.1.

The decay of the new state will depend on its mass: for low masses, the particle will decay either through loop-induced couplings to e.g. gg or $\gamma\gamma$ or, if present, through couplings to other SM or BSM particles than the top quark. For masses of $m_{\text{A}/\text{H}} > 2m_t$, however, the decay to $t\bar{t}$ is kinematically allowed and will in many cases be dominant due to the large Yukawa coupling. In this case, the process $gg \rightarrow \text{A}/\text{H} \rightarrow t\bar{t}$ will lead to the same final state as SM $t\bar{t}$ production, as illustrated in Fig. 2.7. This process will be considered in more detail in the rest of this chapter, and one of the main results of this thesis is an experimental search for such a signature (Chapter 8).

Fig. 2.8 shows the predicted differential cross sections of this model in terms of $m_{t\bar{t}}$, the invariant mass of the $t\bar{t}$ pair, for different A/H masses. The cross section is shown as the difference to the SM prediction at the level of the hard scattering and at LO in QCD. It can be seen that the total effect of A and H is a very distinct peak-dip structure around the A/H mass. This is because the $gg \rightarrow \text{A}/\text{H} \rightarrow t\bar{t}$ production channel interferes with SM $gg \rightarrow t\bar{t}$ production, which leads to deficits in certain regions of phase space due to destructive interference. For high A/H masses, there is an additional broad peak at low masses of $m_{t\bar{t}}$. This originates from the gluon PDF, which is steeply increasing for small parton momentum fractions, corresponding to low $m_{t\bar{t}}$, and thus compensates the suppression by the off-shell A/H at low $m_{t\bar{t}}$ for the A/H-SM interference.

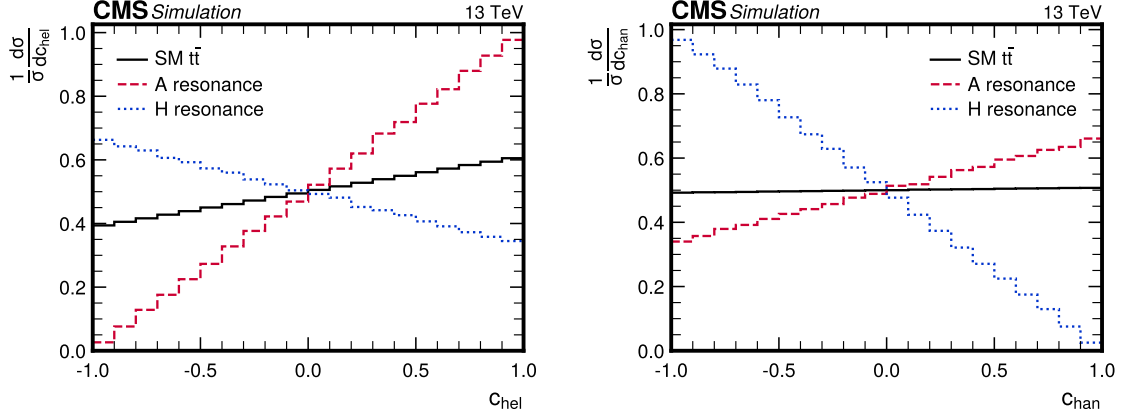


Figure 2.9: **Distributions of c_{hel} and c_{han} for $A/H \rightarrow t\bar{t}$.** The differential cross sections as a function of c_{hel} (left) and c_{han} (right) for A (red), H (blue) and the SM (black) for comparison [9]. They are calculated from the same Monte Carlo simulation samples described in Sec. 8.2.1.

A further consequence of the interference is that the differential cross section scales non-linearly with the coupling modifiers $g_{A t\bar{t}}$ and $g_{H t\bar{t}}$. The dependence (for arbitrary observables) can be parameterized as

$$d\sigma = d\sigma^{\text{SM}} + g_{A t\bar{t}/H t\bar{t}}^2 d\sigma^{\text{int}} + g_{A t\bar{t}/H t\bar{t}}^4 d\sigma^{\text{res}} \quad (2.30)$$

where the superscripts “SM”, “int” and “res” refer to the SM, SM-A/H interference, and resonant A/H contributions, respectively.

In addition to the $m_{t\bar{t}}$ spectrum, an A/H contribution is also expected to modify the spin state of the $t\bar{t}$ system. As a single spin-0 particle, an intermediate A/H resonance has neither spin nor orbital angular momentum. Due to conservation of angular momentum, this implies that the $t\bar{t}$ system will be produced in a state with $J = 0$, which leaves only the 1S_0 and 3P_0 states (cf. Tab. 2.1).

Furthermore, the spin-0 intermediate state has positive intrinsic parity and is charge-neutral. This implies that for H, whose interaction with the top quark is \mathcal{CP} -even, the $t\bar{t}$ system will be in the 3P_0 state ($\mathcal{CP} = +1$, cf. Tab. 2.1). For A, on the other hand, the interaction is \mathcal{CP} -odd, leading to the 1S_0 state ($\mathcal{CP} = -1$). As a result, the processes $gg \rightarrow A \rightarrow t\bar{t}$ and $gg \rightarrow H \rightarrow t\bar{t}$ always produce pure spin singlet and spin triplet states, respectively.

As explained in Secs. 2.2.1 and 2.2.2, the observable c_{hel} has maximal slope D for spin-singlet states, making it a good discriminator between A and the SM. Similarly, the observable c_{han} (Eq. (2.10)) has a maximal slope $D^{(k)}$ for the 3P_0 state and is a good discriminator between H and the SM. The distributions of both observables can be seen in Fig. 2.9, with the SM prediction shown as well for comparison. Both c_{hel} and c_{han} will be used in the experimental search for such states presented in Chapter 8.

2.4.2 Two-Higgs Doublet Model

A common class of models predicting additional scalars as discussed in Sec. 2.4.1 are Two-Higgs-Doublet Models (2HDMs) [64, 72]. In these models, there are two complex $SU(2)$ Higgs doublets with eight degrees of freedom in total (as opposed to a single doublet in the SM), which after electroweak symmetry breaking results in five physical states (compare Sec. 2.1.3). Such a structure for the Higgs sector arises, for example, in many supersymmetric models [73] or axion models [74].

In general, 2HDMs can include \mathcal{CP} -violating interactions (similar to Sec. 2.4.1) as well as flavor-changing neutral currents (FCNCs). Both of these phenomena are experimentally well constrained, and so it makes sense to restrict oneself to \mathcal{CP} - and flavor-conserving limits. Doing so leads to definite quantum numbers of the five physical scalar states of the 2HDM: two neutral scalar (\mathcal{CP} -even) states h and H , a neutral pseudoscalar (\mathcal{CP} -odd) state A , and two charged states H^+ and H^- . Usually, the state h is identified with the SM Higgs boson at a mass of 125 GeV. Then, the two other neutral states H and A , if massive enough, could play the role of additional Higgs bosons decaying to $t\bar{t}$ as discussed in Sec. 2.4.1.

Depending on the nature of the discrete symmetry that is used to impose flavor conservation, there can be different types of 2HDMs, which differ in the structure of the couplings to the SM. No particular 2HDM type is assumed in this work, and the results of Chapter 8 are instead presented in terms of the generic model of Sec. 2.4.1.

2.4.3 Axion-Like Particles

Another very generic class of BSM scalars relevant to the $pp \rightarrow t\bar{t}$ process are axions and Axion-Like Particles (ALPs), denoted here as a . Axions were originally conceived as solutions to the strong \mathcal{CP} problem [62, 63, 75, 76], which is a result of the non-trivial vacuum structure of QCD. When deriving the effective QCD Lagrangian, the presence of certain classes of topological solutions to the classical Yang-Mills equations leads to an additional \mathcal{CP} -violating term [77]

$$\mathcal{L}^{QCD} \supset \theta \frac{\alpha_S}{8\pi} G_{\mu\nu}^a \tilde{G}^{a\mu\nu} \quad (2.31)$$

where $G_{\mu\nu}^a$ is again the gluon field strength and $\tilde{G}_{\mu\nu}^a$ its dual. The coefficient θ of this term is a free parameter in the range $[0, 2\pi]$, with no particular value preferred from first principles. However, experimentally, no \mathcal{CP} violation in QCD has been observed, and θ is strongly bounded at $|\theta| \leq 10^{-10}$ (the strongest bounds coming from measurements of the electric dipole moment of the neutron [77–79]). The fact that *a priori* the angle θ can take any value, but is bounded this strongly from the experiment, is called the strong \mathcal{CP} problem.

A possible natural solution of this problem is to introduce a new spin-0 BSM particle a , called the axion [75, 76], with a Lagrangian [77]

$$\mathcal{L}^{\text{ax}} = \frac{1}{2}(\partial_\mu a)(\partial^\mu a) + \frac{\alpha_S}{8\pi} \frac{a}{f_a} G_{\mu\nu}^a \tilde{G}^{a\mu\nu} + \text{interaction terms} \quad (2.32)$$

where f_a is called the axion scale, and all other interaction terms with SM fields are required to be invariant under a shift $a \rightarrow a + \kappa f_a$ with arbitrary κ . It can be shown that this Lagrangian, when added to the SM QCD Lagrangian including the term in Eq. (2.31), leads to a global minimum at $a/f_a + \theta = 0$, so that after a field shift the \mathcal{CP} -violating term is absorbed in the axion-gluon coupling and no \mathcal{CP} violation is expected in QCD alone. This is known as the Peccei-Quinn mechanism.

In Eq. (2.32), the axion-gluon interaction term has dimension 5 and is thus non-renormalizable, with the cutoff scale given by f_a . The axion must thus necessarily be seen as a low-energy effective field theory (EFT) description of different physics at the higher scale f_a . Many different UV-complete models including axions exist [77, 80–83], which lead to different interaction terms with other SM particles such as photons, electroweak bosons or massive fermions.

In this work, a focus is placed upon models which predict couplings to SM fermions, particularly the top quark. The EFT Lagrangian is parameterized in a model-independent approach as [84]

$$\begin{aligned} \mathcal{L}^{\text{ALP}} = & \frac{1}{2}(\partial_\mu a)(\partial^\mu a) + \frac{m_a^2}{2}a^2 - c_G \frac{a}{f_a} G_{\mu\nu}^a \tilde{G}^{a\mu\nu} - c_B \frac{a}{f_a} B_{\mu\nu} \tilde{B}^{\mu\nu} \\ & - c_W \frac{a}{f_a} W_{\mu\nu}^a \tilde{W}^{a\mu\nu} - \sum_f c_f \frac{\partial^\mu a}{f_a} \bar{\Psi}_f \gamma_\mu \Psi_f \end{aligned} \quad (2.33)$$

where the index f runs over the SM fermions, Ψ_f are the fermion fields, $B_{\mu\nu}$ and $W_{\mu\nu}^a$ are the EW boson field strengths before symmetry breaking, and the free parameters are the scale f_a , the mass m_a , and the couplings to gluons c_G , to EW bosons c_B and c_W and to fermions c_f (where no flavor mixing was assumed). This Lagrangian, depending on the choice of the free parameters, might or might not correspond to a UV-complete model and solve the strong \mathcal{CP} problem. Because of this, the field a is here called an Axion-Like Particle. Even when it does not correspond to a true axion, it might be a physically well-motivated extension of the SM, e.g. as a dark matter candidate or mediator.

In the ALP-fermion interaction term in Eq. (2.33), the shift symmetry of a is directly manifest since it only depends on the derivative of a . However, by employing the equations of motion for a as well as the Higgs mechanism, one can rewrite Eq. (2.33) with a Yukawa-like interaction instead [85–87]. Dropping the EW bosons and fermions other than the top quark leads to

$$\mathcal{L}^{\text{ALP}} = \frac{1}{2}(\partial_\mu a)(\partial^\mu a) + \frac{m_a^2}{2}a^2 - c_{\tilde{G}} \frac{a}{f_a} G_{\mu\nu}^a \tilde{G}^{a\mu\nu} + i c_t m_t \frac{a}{f_a} \bar{t} \gamma^5 t. \quad (2.34)$$

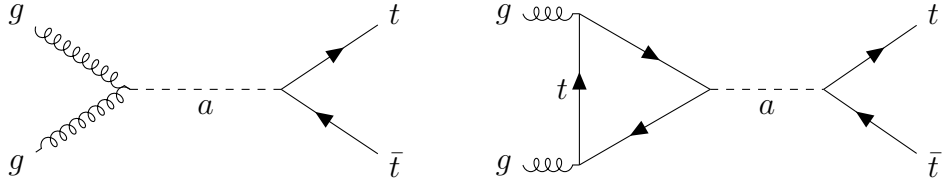


Figure 2.10: **Feynman diagrams for $gg \rightarrow a \rightarrow t\bar{t}$.** The left diagram corresponds to the gluon-ALP contact interaction and scales with $c_{\tilde{G}}c_t$, while the right diagram shows the top quark loop and scales with c_t^2 .

Performing this basis change induces an additional ALP-gluon coupling term (in general dependent on the other SM couplings), which was absorbed by redefining the Wilson coefficient from c_G to $c_{\tilde{G}}$ as [10, 86]

$$c_{\tilde{G}} = c_G + \frac{\alpha_S}{8\pi}c_t \quad (2.35)$$

where couplings to EW bosons and other fermions were again dropped. This basis will be used in the remainder of this work.

It can be seen by comparing Eq. (2.34) to Eq. (2.29) that the ALP-top coupling has the exact same structure as the generic \mathcal{CP} -odd boson introduced in Sec. 2.4.1. Thus, if the ALP is heavy enough to be produced at the LHC and decay to $t\bar{t}$, it can be searched for in $t\bar{t}$ final states similarly to the generic pseudoscalar A. Such heavy ALP masses can be reached naturally and serve as solutions to the strong \mathcal{CP} problem e.g. in UV models containing extra non-Abelian gauge groups, resulting in containing forces with large containment scales [69, 70, 88, 89].

If, in addition, the ALP couplings also satisfy $c_{\tilde{G}} = 0$, the two Lagrangians in Eqs. (2.29) and (2.34) are identical, and all conclusions drawn on A can be directly transferred to the ALP. On the other hand, if $c_{\tilde{G}} \neq 0$, an additional production diagram involving a gluon contact interaction becomes available, as depicted in Fig. 2.10 (left). A phenomenological study characterizing both cases in detail forms the core of Chapter 9 of this work.

3 Experimental methods

3.1 The Large Hadron Collider

At the time of writing, the Large Hadron Collider [90] at CERN is the largest and most powerful particle accelerator in the world. Located underground at the border of France and Switzerland close to Geneva, it consists of two circular beamlines of roughly 27 km circumference in which proton bunches are accelerated and collided. Superconducting magnets, cooled with liquid helium to temperatures of around 4 K, generate magnetic fields of over 8 T to keep the protons on their circular orbit, and similarly superconducting electromagnetic radio-frequency cavities accelerate the protons to beam energies up to 7 TeV. When operating as designed, around 2800 proton bunches per beam containing 3×10^{14} protons total are present in the beamline simultaneously, revolving with a frequency of about 11.245 kHz. From this, peak instantaneous luminosities of about 20 kHz pb^{-1} can be reliably reached. Alternatively, the LHC can also collide heavy ions, such as lead or oxygen, instead of protons.

There are four large experiments making use of the colliding beams at the LHC, located at the four interaction points. The two larger of these are ATLAS [92] and CMS [4], both of which are general-purpose experiments intended to study all aspects of the Standard Model in proton-proton collisions. The work of thesis was performed as part of the CMS Collaboration, and so the CMS experiment is described in Sec. 3.2 in more detail. The two smaller experiments, on the other hand, are specialized for certain tasks, namely the study of B physics and exotic hadrons for LHCb [93] and the study of heavy-ion collisions for ALICE [94].

The data taken at the LHC so far can be divided into three Runs. Run 1 lasted from 2010–2012, during which the LHC operated at center-of-mass energies of 7 and 8 TeV, significantly below the original target values, and yielded a total integrated luminosity of about 29 fb^{-1} . It is this data that led to the original discovery of the Higgs boson. Following this, after two years of pause, Run 2 resumed in 2015 with a center-of-mass energy of 13 TeV and lasting to 2018. Around 140 fb^{-1} of data was collected during this time. This complete data set, save for the small contribution from 2015, is analyzed in Chapter 8 of this thesis.

Then, Run 3 of the LHC started in 2022 after another three years of pause, and is planned to last until 2026 at the time of writing. The center-of-mass energy was again increased slightly to 13.6 TeV, and in the years 2022–2024 around 196 fb^{-1} have been recorded, already surpassing Run 2. In Chapter 6 of this thesis, the very

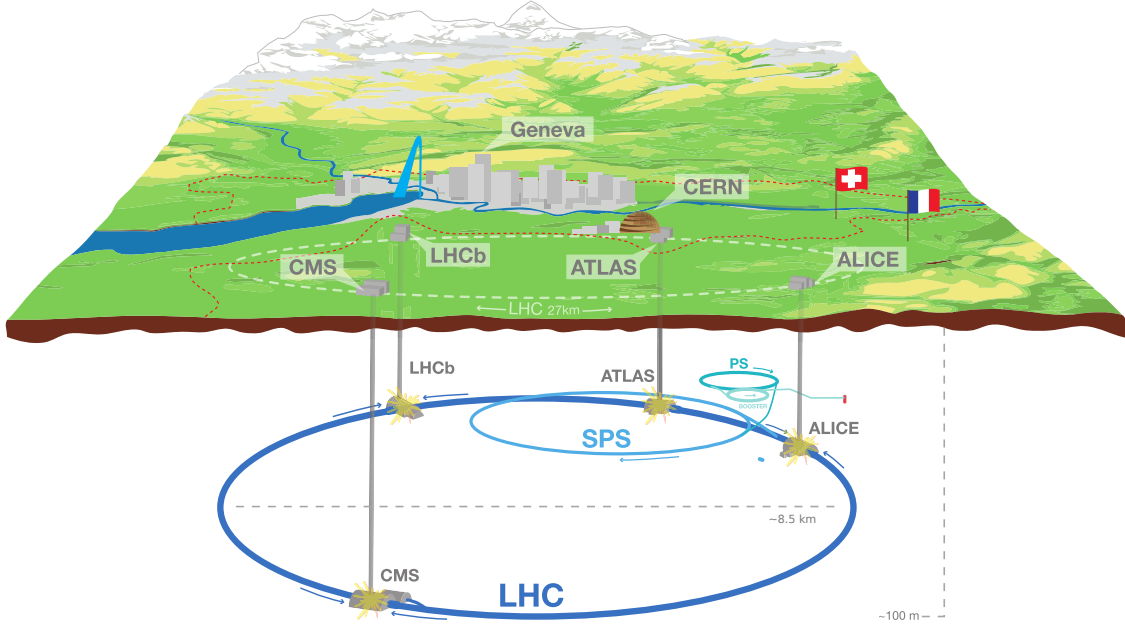


Figure 3.1: **The Large Hadron Collider.** A sketch of the LHC and its location in Geneva, Switzerland, including its two pre-accelerators PS and SPS as well as the four large experiments ATLAS, CMS, ALICE and LHCb. *Figure taken from Ref. [91].*

first data of Run 3, corresponding to 1.21 fb^{-1} taken in July and August 2022 at CMS, are analyzed in the context of a $t\bar{t}$ cross section measurement.

In the future, it is planned to upgrade the LHC to be able to run at higher instantaneous luminosities as well as a further increased energy of 14 TeV [95]. The CMS detector will similarly be upgraded to replace aging components and deal with the increased pileup conditions [96, 97], and a total integrated luminosity of around 3 ab^{-1} is expected to be collected. In Chapter 9, among others, sensitivity projections for this luminosity are made for Axion-Like Particles decaying to $t\bar{t}$.

3.2 The CMS experiment

The Compact Muon Solenoid experiment [4, 97], located at Interaction Point 5 of the LHC close to Cessy, France, is a general-purpose particle detector targeting a broad range of SM and BSM phenomena. Its main feature is a superconducting solenoid magnet creating a strong magnetic field of 3.8 T. CMS is a hermetic detector, covering almost the full solid angle in space, and is split into a *barrel*, covering a range of $|\eta| \lesssim 1.5$, and two forward *endcaps*, covering $|\eta| \gtrsim 1.5$. Here, $\eta = \sinh^{-1}(p_z/p_T)$ is the *pseudorapidity*, which is commonly used in collider experiments to quantify

3 Experimental methods

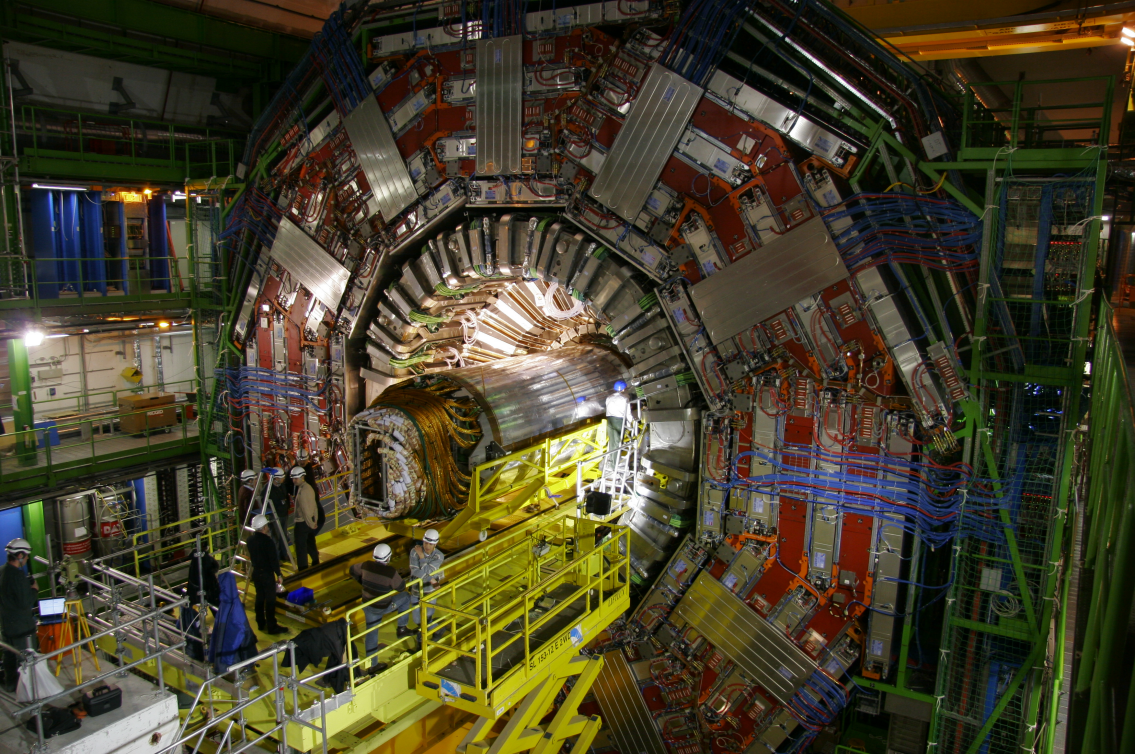


Figure 3.2: **Photo of the CMS detector.** A photograph of the opened CMS detector, taken during the installation of the tracker. *Figure taken from Ref. [98].*

the forward momenta p_z of particles relative to their transverse momenta p_T . CMS consists of several subdetectors, which are geared towards different particle types and properties.

Subdetectors The innermost part of CMS is the *tracker*, which is a silicon detector comprised of several layers of silicon pixel and strip sensors [99, 100]. These record interactions with particles (“tracker hits”) shooting outwards from the interaction point in the center in three-dimensional space. Through reconstruction of the particle tracks and fits of the curvature due to the magnetic field, the tracker thus allows for the measurement of particle momenta. Furthermore, extrapolating the tracks back to their origin allows for the determination of the point of interaction, and thus for discrimination between particles arising from different proton-proton interactions. Due to the presence of the beam pipe, the tracker covers only pseudorapidities of $|\eta| < 2.5$, enabling high precision momentum determination in this range only.

The second-to-innermost subdetector is the *electromagnetic calorimeter* (ECAL), which is intended to measure the energy of electrons and photons [102, 103]. It consists of transparent lead tungstate cells, in which incoming electrons or photons

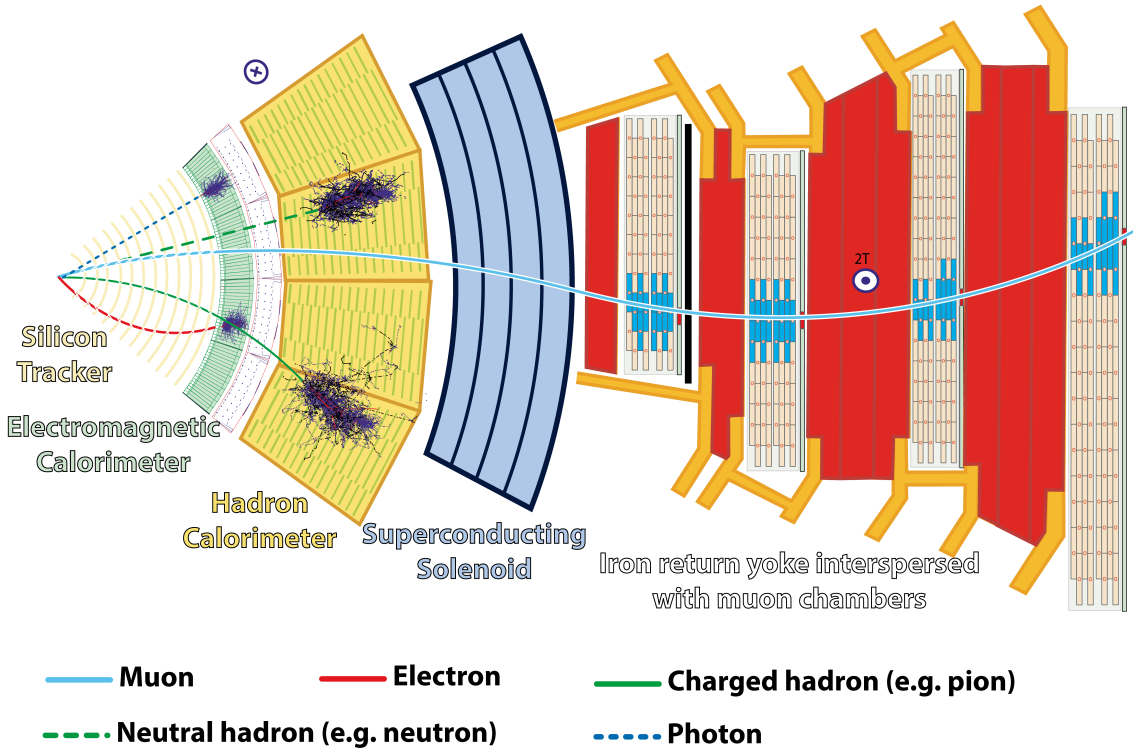


Figure 3.3: Sketch of the CMS subdetectors. A cross section view of the different CMS subdetectors, with the trajectories of example particles and their interactions. *Figure taken from Ref. [101].*

create electromagnetic showers leading to avalanches of electron-positron pairs and photon radiation. These are then recorded by photo diodes, and the energy of the incoming particle can be reconstructed from the amount of measured photons. Pseudorapidities of $|\eta| < 1.48$ and $1.65 > |\eta| < 3$ are covered for the barrel and the endcaps, respectively. The majority of electrons and photons are fully stopped in the ECAL and do not interact with the further subdetectors.

Following the ECAL, the *hadronic calorimeter* (HCAL) measures the energy of charged or neutral hadrons [104, 105]. It is a sampling calorimeter consisting of interleaved absorber plates, which initiate hadronic showers through the strong interaction with the nuclei of the material, and scintillators, which transmute the hadronic showers into photons to be detected by photodetectors. The HCAL covers $|\eta| < 1.4$ and $1.4 < |\eta| < 3$ for the barrel and endcaps, respectively, and additionally features a forward section ranging up to $|\eta| < 5$, though the latter is not used anywhere in this work.

Surrounding the HCAL lies the superconducting solenoid, further surrounded by the final subdetector: the *muon chambers* [106, 107]. They are interspersed with four layers of the iron return yoke of the magnet, which confines the magnetic field.

3 Experimental methods

Since muons interact only sparsely with matter, they escape the calorimeters and the solenoid unhindered, and are detected in four muon subsystems working in accord at different pseudorapidities: the drift tubes ($|\eta| < 1.2$), cathode strip chambers ($0.9 < |\eta| < 2.4$), resistive plate chambers ($|\eta| < 1.9$) and gas electron multipliers ($1.6 < |\eta| < 2.4$). All of them are gas detectors, which are sensitive to the ionization of a gas when a muon passes through it, and record hits of the muon trajectory, thus allowing for a momentum measurement similar to the tracker.

Trigger system Besides the different subdetectors, a crucial part of the CMS experiment is the *trigger system* [108]. It is necessary due to the large number of bunch crossings at the LHC, which, if they were all recorded, would produce data rates far in excess of the computational bandwidth and storage capacities available. To combat this, only events which are of physical interest should be recorded. It is the task of the trigger system to determine what these events should be.

The trigger system is split into two parts. The first is the low-level or level-one trigger (L1T) [109], which is a hardware trigger consisting of custom electronics and whose inputs are directly the output signals of several of the subdetectors. It is designed to trigger on signatures consistent with specific objects, such as electrons, muons or hadronic jets, with significant energy. Since it needs to take a decision for every collision event, it only has a time interval of around $4\text{ }\mu\text{s}$ to do so, requiring purpose-built low-latency electronics. Its target is an output event rate of 100 kHz, which can be adjusted by prescaling certain trigger paths so that only a fraction of passing events is recorded.

The second part of the trigger system is the high-level trigger (HLT) [110, 111]. It is a software trigger, running on a GPU-accelerated server farm directly in the CMS service cavern, on which a dedicated, speed-optimized version of the standard CMS object reconstruction algorithm is executed for each event passing the L1T. Specific triggers are then implemented as decisions based on these reconstructed trigger objects, allowing large freedom in selecting events based on the desired physics program. Typical triggers require, for example, the presence of different numbers or combinations of electrons, muons, photons, hadronic jets or missing transverse momentum. The transverse momentum thresholds and further requirements on these objects need to be adjusted so that the total trigger rate is reduced to an average of around 400 Hz. Only these events are then saved to hard drives, and kept for further analysis.

3.3 Object reconstruction

In order to interpret the physics behind a collision event, the outputs of the subdetectors have to be translated into physics objects which can be mapped to the underlying physical particles. At CMS, this is done with a single unifying method,

the Particle Flow (PF) algorithm [112], which is designed to combine the information from the several subdetectors to build physics objects (called PF candidates) as appropriate. The physics objects relevant to this work are listed in the following.

Charged particle tracks are obtained from the tracker by fitting recorded tracker hits using a χ^2 minimization, and their momentum and charge are estimated from their curvature as described above [99]. By extrapolating the tracks back to their origin, the position of vertices in space can also be determined.

From this, the *primary vertices* (PVs) can be found, which are the locations of the proton-proton interactions that caused the tracks in the first place. By contrast, secondary vertices arise from the decays of particles with long enough lifetime that they move a significant distance from the PV. PVs are determined by a likelihood fit to all tracks of sufficient quality [99]. In each event, the PV whose tracks show the largest p_T sum is designated the hard-scattering PV, assumed to correspond to the physical process of interest, while further PVs are due to soft-QCD pileup interactions. The number of PVs per event is thus a good measure of the amount of pileup.

The other main ingredient besides tracks and vertices are *calorimeter clusters* from either the ECAL or the HCAL. A clustering algorithm is required here because particles typically deposit their energy in more than one calorimeter crystal.

By matching the positions of calorimeter clusters and charged particle tracks, *electrons* (for the ECAL) and *charged hadrons* (for the HCAL) can be constructed. The combined measurements of the momentum (from the curvature) and the deposited energy (from the calorimeter) allows for the reconstruction of the mass, and thus the identification of the particle. For electrons, the effect of bremsstrahlung originating in the tracker volume has to be considered, usually resulting in multiple calorimeter clusters per electron (called a supercluster) which need to be combined together. Isolation criteria on the clusters are also required to veto electrons that are part of a hadronic jet (see below). By contrast, calorimeter clusters which do not have charged tracks are assigned to *photons* (for the ECAL) or *neutral hadrons* (for the HCAL). CMS furthermore employs algorithms to remove hadrons that are believed to originate from pileup instead of the hard-scattering vertex. In Run 2, the Charged Hadron Subtraction (CHS) method [112] was used for this purpose, while in Run 3, the better performing PUPPI method [113, 114] was used instead.

Muons interact only very rarely with the calorimeter, and are instead built by directly combining charged tracks with hits in the muon chambers. In this work, muons are only considered if they match to hits in both subdetectors.

From these definitions, further high-level objects can be built. The first are *hadronic jets*, which are clustered from all other PF candidates using the anti- k_T algorithm with a distance parameter of $\Delta R = 0.4$ [115] (referred to as AK4 jets). This algorithm is infrared- and collinear-safe, i.e. it is insensitive to soft and/or collinear radiation in QCD, which is nonperturbative [17]. It further has the advantage that the resulting jets are approximately circular in the φ - η plane, making them

3 Experimental methods

experimentally intuitive to handle. Since leptons or photons can be created from electroweak decays of hadrons, these also need to be included in the jet clustering; to ensure that they are not double-counted, leptons and photons that are included in jets are not further considered as standalone objects.

Hadronic jets can further be *b tagged*, that is, identified as originating from a B hadron. Since the strong interaction is flavor-conserving, the decay of B hadrons to hadrons of other flavors has to be mediated by the flavor-mixing in the weak interaction, leading to comparatively long lifetimes. B hadrons can thus be identified through secondary vertices corresponding to the B hadron decay, which can be displaced from the PV by several millimeters. In practice, machine learning-based classifiers like the DEEPJET algorithm [116] are used, which take more properties of the jet into account besides the displacement of the secondary vertex.

Finally, the *missing transverse momentum* \vec{p}_T^{miss} can be calculated as the negative of the vectorial sum of all transverse momenta in the event [117]. Since the initial state of a collision at the LHC has negligible transverse momentum, \vec{p}_T^{miss} represents the total transverse momentum of the particles that left the detector unobserved. In the SM, this is the case for neutrinos, but it could also be BSM particles such as e.g. dark matter candidates.

4 Monte Carlo event generation

In order to test the Standard Model or extract any of its parameters at the LHC, one requires a prediction of proton-proton scattering which can be directly compared to the experimental data recorded by the detectors in the form of collision events. This is, in general, a very complex task consisting of many different subprocesses and physical scales, which are illustrated in Fig. 4.1.

The generation starts with the hard parton scattering, then continues with the emission of additional gluon and quark radiation, effects of interactions of other partons in the colliding protons, the creation of color-neutral hadrons from gluons and quarks, interactions between other protons in the same bunch, and ends with the simulation of the different subdetectors and triggers. Many of these processes are not only probabilistic, but intractable through direct analytical or numeric integration due to the large phase space and the complexity of the problems involved. To compare to recorded events, one further requires a prediction that is fully differential in all variables explicitly and implicitly considered in an experimental analysis.

For this purpose, the Monte Carlo (MC) method is used. Here, it amounts to randomly sampling an event from the phase space of the starting distribution - in this case, the hard scattering - and then passing it through a chain of simulation tools for the remaining steps until one arrives at an event that is directly comparable to events recorded experimentally. This method is advantageous in that the numerical error in an arbitrary region of phase space always scales with $1/\sqrt{N}$, where N is the total number of events produced, independently of the dimensionality of the problem. Thus, eliminating the numerical error on a prediction is mostly a matter of producing a sufficient number of MC events.

In this chapter, the different tools used in the CMS simulation chain are discussed. A focus is laid on the hard scattering or matrix element generators (Sec. 4.1) as well as the parton showering (Sec. 4.2) since these are the focus of the studies presented in Chapter 7 and furthermore of relevance to Chapter 8, while interactions with other partons in the colliding protons (“multi-parton interactions”, Sec. 4.3), hadronization (Sec. 4.4), interactions between other protons in the same bunch (“pileup”, Sec. 4.5), as well as the detector and trigger simulation (Sec. 4.6) are only briefly touched upon.

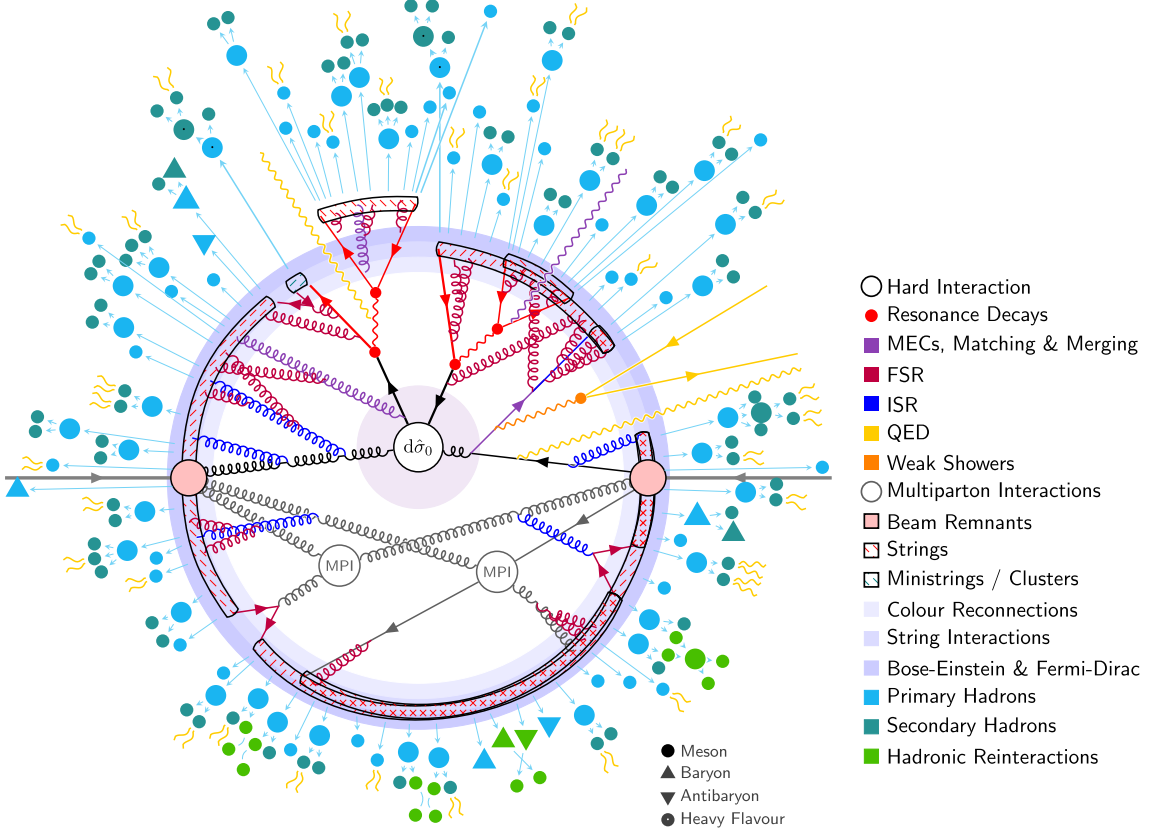


Figure 4.1: **Illustration of MC generation.** An illustration of the different subprocesses and scales involved in MC generation, starting from the hard scattering in the center (white circle) and ending with physical hadrons at the outside, for the example of a $pp \rightarrow t\bar{t}$ event with fully hadronic decays as simulated in PYTHIA. *Figure taken from Ref. [118].*

4.1 Matrix Element generators

At the LHC, protons are collided with large center-of-mass energies of multiple TeV. Because protons are not fundamental particles, but bound states of QCD consisting of quarks and gluons (partons) which cannot be perturbatively described from first principles (cf. Sec. 2.1.1), providing accurate predictions for proton-proton collisions is generally a very challenging task. For the specific case of hard scattering processes, i.e. processes in which the particles in the final state X have large transverse momenta, one can employ the factorization theorem of QCD [16]:

$$\sigma(pp \rightarrow X) = \int_0^1 dx_1 \int_0^1 dx_2 \sum_{a,b} f_a(x_1, \mu_F) f_b(x_2, \mu_F) \hat{\sigma}(a(x_1 P) + b(x_2 P) \rightarrow X) \quad (4.1)$$

where P is the incoming momentum of the protons, assumed to be purely longitudinal and thus $P = \sqrt{s}/2$, and the sum runs over all possible combinations a, b of initial state partons. This formula factorizes the total hadronic cross section into two parts: The partonic cross section $\hat{\sigma}(a + b \rightarrow X)$ describes the scattering of two partons at high energies, and can be computed perturbatively in α_S due to the asymptotic freedom of QCD. The functions $f_a(x, \mu_F)$ on the other hand are the parton distribution functions (PDFs) and describe the probability of finding a parton of type a with momentum fraction $p_a/P = x$ in the proton structure [16]. Since they probe low momentum scales where α_S is large, they cannot be computed perturbatively and instead need to be measured experimentally. In addition to x , they also depend on the factorization scale μ_F , which is the energy scale defining the separation between hard (perturbative) and soft (non-perturbative) QCD. It is typically set to be equal to the characteristic energy of the incoming partons, e.g. half the partonic invariant mass. In contrast to the dependence on x , the dependence on μ_F is a prediction of QCD and follows from the DGLAP equations [17, 119].

The partonic cross section can further be written differentially as [16]

$$d\hat{\sigma}(ab \rightarrow X) = \frac{1}{2\hat{s}} \left(\prod_f \frac{d^3 p_f}{(2\pi)^3} \frac{1}{2E_f} \right) |\mathcal{M}(ab \rightarrow X)|^2 (2\pi)^4 \delta^{(4)} \left(p_a + p_b - \sum_f p_f \right) \quad (4.2)$$

where $\hat{s} = x_1 x_2 s$ is the partonic center-of-mass energy squared, the term in the first pair of brackets refers to the integral over the final state phase space and depends only on the properties of the final state particles f , the δ function encodes energy and momentum conservation, and only the scattering matrix element \mathcal{M} depends on the details of the interaction mediating the considered process.

Events are now generated by drawing randomly from the full kinematically allowed final state phase space, as well as from the PDFs characterizing the initial state, and keeping them with a probability proportional to the corresponding hadronic cross section according to Eq. (4.1). The partonic cross section here is usually known analytically, though for complex processes (especially at NLO or higher) it usually leads to complicated expressions requiring the use of computer algebra. The PDFs, based on fits to experimental data, are usually tabulated and interpolated; in this work, the NNPDF 3.1 PDF set is most commonly used for this purpose [120]. In practice, codes usually employ an adaptive sampling algorithm to enhance the fraction of events that pass and thus speed up the calculation, see e.g. Ref. [121].

4.1.1 Higher orders in QCD

ME generators exist at LO, NLO, and (approximate) NNLO in QCD, all of which are used at different points in this work. For NLO and NNLO processes, care must be taken to cancel ultraviolet (UV) as well as infrared (IR) divergences that appear in the integration of the matrix element. The former is done in the framework of renormalization, which usually introduces a dependence on an additional scale, the renormalization scale μ_R . Similar to μ_F , it is typically set to the energy scale of the process, and, since the dependence is expected to vanish at infinite order in QCD, variations of μ_R and μ_F are often used to assess the size of uncertainties due to missing higher orders [12]¹.

IR divergences, on the other hand, arise in two circumstances: first, when the momenta of massless virtual particles in loop diagrams, such as gluons or light quarks, approach zero; and second, when a real massless particle is emitted such that it is soft or collinear with respect to the emitter. These two contributions from virtual and real IR divergences need to be canceled with each other to obtain a finite result. As a result, NLO calculations for the final state X will always need to also take into account the final state $X + j$, where j can be a gluon or light quark [123].

In an analytical (i.e. non-MC) fixed-order calculation, this cancellation can in principle be performed directly by summing the real and virtual contributions to an observable of interest before the numerical evaluation². This is not possible in MC simulations, since the real and virtual contributions, which correspond to different final states, need to be kept as separate events. Instead, subtraction methods are commonly used, where counterterms canceling the divergences are respectively added to and subtracted from the real and virtual contributions. When considering both real and virtual events in an analysis, the counterterms cancel with each other and the full amplitude is recovered [17]. A disadvantage of this method is that it can lead to negative weights for the events, since only the full amplitude, but not the real and virtual contributions on their own, are guaranteed to be positive definite. How significant this problem is in practice strongly depends on the method used and the process in question.

In this work, two different ME generators are used. The first is MG5_AMC@NLO, a general-purpose ME generator that can work both at LO and NLO [124]. It features fully automated computation of arbitrary processes in the SM or BSM, where the model is specified in the Universal FeynRules Output (UFO) format [125]. It is used

¹Using μ_R and μ_F variations as estimates of missing higher order uncertainties, while common, can only give a rough estimate of the magnitude of missing higher order contributions and does not truly give information about shape deficiencies in differential distributions. A recent, more thorough approach are *theory nuisance parameters* quantifying the uncertainty in specific parts of the theory calculation [122]. This method has however not yet been extended to $t\bar{t}$ production and is thus not considered here.

²In practice, subtraction methods are still commonly used for fixed-order calculations for numerical reasons, especially when the computation is automated for arbitrary processes [17].

in this work for both SM and BSM processes.

The second ME generator used is PowHEG Box (short for Positive Weighted Hardest Emission Generator), which is a generic framework for NLO and approximate NNLO generators [126–128]. In contrast to MG5_AMC@NLO, it is not automated, and requires the manual implementation of each process. Many processes are publicly available as part of the PowHEG Box collection, and several are used in this work. The two generators also differ in the scheme used to match to the parton shower, which is explained in Sec. 4.2.

4.1.2 ME generators for $t\bar{t}$

Throughout this work (Chapters 6 to 9), the $pp \rightarrow t\bar{t}$ process is mostly generated using the PowHEG Box subprocess `hvq` [129]. This generator employs the narrow-width approximation (NWA), which means that it treats the top quark as a stable particle with a fixed mass and zero width. It thus generates $pp \rightarrow t\bar{t}$ as a $2 \rightarrow 2$ process, with the top quarks in the final state, at NLO in QCD. As with all PowHEG Box processes, it is intended to be matched to a parton shower (cf. next section).

However, in practice the top quark is unstable, i.e. it has a finite width, and decays immediately to a W boson and a b quark (cf. Sec. 2.2). In `hvq`, the modeling of the decay is done approximately in a second step after the production of $t\bar{t}$. This proceeds as follows [130, 131]: for each event, generated at the level of stable $t\bar{t}$, the allowed decay phase space of the top (anti)quarks is randomly and uniformly sampled, i.e. random three-momenta are drawn in the top or antitop rest frame for the possible decay products ($b\ell\nu$ or $bq\bar{q}$). The full matrix elements for the $2 \rightarrow 6$ process including decays, e.g. $pp \rightarrow b\bar{b}\ell\ell\nu\bar{\nu}$ for a dilepton decay, are now evaluated at LO in QCD for the randomly drawn three-momenta of the decay products. The three-momenta are now kept with a probability proportional to the squared matrix element; otherwise, they are thrown away and the decay procedure is repeated.³

This algorithm is computationally efficient, since only the $2 \rightarrow 2$ production matrix element needs to be computed (i) at NLO and (ii) during the event generation process. It furthermore has the advantage that it includes $t\bar{t}$ spin correlations (cf. Sec. 2.2.1), at least at LO, since the decay of t and \bar{t} are treated simultaneously (as opposed to decaying t and \bar{t} independently).

However, it does not capture finite width effects since the top quarks are considered stable during event generation. In `hvq`, it is possible to alleviate this somewhat by reshuffling the momenta of the decayed $t\bar{t}$ events such that the invariant mass of the t and \bar{t} decay products follows a simple Breit-Wigner distribution [131]. This option is used in this work everywhere `hvq` is considered. It still represents an ad-hoc procedure with no guarantee to reproduce the true top quark line shape at any order

³A very similar algorithm is implemented in the code MADSPIN [131], and the algorithm is sometimes known as the MadSpin algorithm.

in QCD.

To improve on this, one needs to consider the full $2 \rightarrow 6$ process without explicitly splitting into production and decay. Among others, this is done at NLO in QCD for the dilepton final state by a different POWHEG Box subprocess called `bb41` [6]. In Chapter 7, `bb41` is discussed in detail and validated in the context of CMS simulation, and it is applied to the modeling of the $t\bar{t}$ production threshold in Sec. 8.5.4.

4.2 Parton showers and matching

The output of ME generators are events whose final states typically involve quarks and gluons with high momenta. Formally, such computations are accurate to some fixed order in α_S at which the calculation was performed, and all further emissions of gluons, as well as splittings of gluons into quark-antiquark-pairs, is suppressed by additional powers of α_S . However, the matrix elements for such splittings become singular in the limit that the emitted partons are soft and/or collinear to the emitting particle, leading to IR divergences, as discussed in Sec. 4.1. For initial state radiation, the divergences can be regulated by absorbing them in renormalized PDFs, from which the DGLAP equations can be derived [12, 17]. They still lead to large corrections for each additional soft or collinear splitting considered, proportional to $\alpha_S \log(\hat{s}/\Lambda_{\text{QCD}}^2)$, where $\Lambda_{\text{QCD}} \approx 250$ MeV is the scale at which QCD becomes nonperturbative. This term is of order 1 and thus spoils the convergence of the perturbative series if it is cut off at a fixed order in α_S [16, 17]. Physically, this corresponds to the emission of many further partons besides the one or two considered at NLO or NNLO, which are not captured by the matrix element at a fixed order in QCD.

A way to approximately incorporate these emissions is by using parton showers, the idea of which is sketched in the following. For a parton associated with some scale Q_0 , the probability for no splitting to occur above the scale Q (with $Q < Q_0$) is called the *Sudakov factor* $\Delta(Q_0, Q)$. Because the structure of the IR singularities in QCD is universal, i.e. depending only on the types of particles in the splitting but not the rest of the process, its leading-logarithmic behavior can be computed from the matrix elements of $q \rightarrow qg$ and $g \rightarrow q\bar{q}$ splittings (the *splitting kernels*). The parton shower algorithm now iteratively draws the scales Q at which splittings should happen from this random distribution, thus generating real emissions and splittings with successively lower scales down to Λ_{QCD} . In practice, the Sudakov factor usually contains additional terms beyond the leading-logarithmic behavior depending on the details of the algorithm [17].

The scale Q which determines in which order the splittings are performed is also called the *ordering variable*, and its form can be freely chosen as long as it correctly captures the soft and collinear singularities. Two common choices are the transverse momentum of the emission (p_T -ordered shower) or the emission angle respective to the emitting particle (angular-ordered shower). The result of either choice is an

effective resummation of the logarithms associated to each emission, which is why parton showers are said to be leading-log (LL) accurate for certain observables.

The main parton shower used in this work is a p_T -ordered dipole shower, included as part of the PYTHIA multi-purpose event generator [118, 132]. It works by collecting quark-antiquark pairs into color dipoles, which radiate gluons together so that the recoil is distributed between the quarks. Here, it is mostly used by matching it to the ME generators described in Sec. 4.1. This is usually trivial at LO: the parton shower simply starts from the final state as given by the ME generator.

At NLO or higher, however, care must be taken that there is no double-counting between the additional real emissions in the final state of the ME generator (e.g. MG5_AMC@NLO or POWHEG Box) and the emissions of the shower (e.g. PYTHIA), as well as between the virtual corrections that are exact in the ME generator and approximated in the shower [17]. Several matching schemes exist to solve this issue. In this work, the MC@NLO and POWHEG schemes are used and briefly explained in the following.

In the MC@NLO scheme [133], as implemented in MG5_AMC@NLO, the double-counting is corrected for using another subtraction scheme: During the generation of the real and virtual correction terms in the matrix elements, the approximate corrections that would be used in the parton shower are subtracted from the squared amplitude. When the events generated in this way are then showered, the approximate correction terms are effectively added back, so that formally the exact result is recovered at NLO accuracy. This strategy is conceptually simple and easy to generalize (and thus automatize, as done in MG5_AMC@NLO). However, at phase-space points where the approximate terms are larger than the exact ones, it inherently results in events with negative weights, which can greatly increase the MC statistics required.

In the POWHEG scheme [126, 127], as used in the POWHEG Box, the fraction of negative weights is greatly reduced by always generating the first real emission in the ME generator, so that the real emission term is already exact, and then only subtracting the approximate virtual correction term. The parton shower then needs to only generate the second-hardest and higher emissions, which is typically achieved by starting the shower evolution at the scale of the first, ME-level emission (sometimes called “wimpy shower”).

This approach assumes that the scale definitions in the ME generator and the parton shower are identical, which in general will not always be the case. In particular, for the important case of POWHEG matched to PYTHIA, used in this work for the simulation of $pp \rightarrow t\bar{t}$, there is a mismatch in the scales which might lead to double-counting. A more refined approach here is to use a vetoed shower: the shower evolution is started at the kinematically allowed limits and evolves downwards as usual, ordered by the scale as defined by PYTHIA. For the first emission the scale is then recomputed according to the POWHEG definition, and it is vetoed and re-showered if this scale is higher than the one in the ME. This approach is used for all

$pp \rightarrow t\bar{t}$ simulation in this work unless otherwise specified.

A further improvement in the accuracy of the MC prediction can be achieved by generating any number of additional partons in the matrix element at either LO or NLO, so that these partons are described exactly by the ME generator instead of approximately by the shower. This, however, requires complex matching procedures, such as MLM matching [134] for LO and FxFx matching [135] for NLO matrix elements. In this work, both schemes are only used tangentially for either background processes in Chapter 6 or an alternative $t\bar{t}$ prediction in Chapter 8.

More complicated procedures also have to be invoked in the case that the ME contains more than one real emission. This case is studied in detail for the ME generator `bb4l` in Chapter 7. Furthermore, besides PYTHIA, the multi-purpose generator HERWIG [136, 137] is considered in parts of Chapter 8, and briefly described there.

4.3 Multi-parton interactions

In addition to the hard scattering, additional soft QCD interactions might occur between the other partons in the two colliding protons. This is referred to as multi-parton interactions (MPI) or the underlying event (UE). It is handled by PYTHIA based on heuristic models, interleaved with the parton shower. In general, MPI parameters need to be tuned to experimental data. This was done by the PYTHIA authors, such as in the different versions of the Monash tune [138], and building on top of this by the CMS Collaboration in the form of the CP tune family, most prominently the CP5 tune [139]. Both tunes are based on a large data set of e^+e^- , ep , $p\bar{p}$, and pp collision data from many different experiments. The CP5 tune is used in all parts of this work.

4.4 Hadronization

In the course of the MPI-interleaved parton shower, the gluons and quarks gradually become softer until the parton shower is stopped at an arbitrary cutoff scale, which should lie slightly above the energy scale $\mathcal{O}(\Lambda_{\text{QCD}})$ at which QCD becomes non-perturbative. The physics below this scale, namely the hadronization of these quarks and gluons into hadrons as well as their subsequent decays, thus needs to be described heuristically.

For most of this work, this is done using the Lund string fragmentation model [140, 141], again implemented in PYTHIA. In this model, the strong force between a quark and an antiquark of opposite color is modeled as a string in space-time, standing in for a three-dimensional flux tube. The energy stored in the string is proportional to its length, consistent with the long-distance behavior of the QCD potential observed

e.g. in lattice QCD. Hard gluons can be accommodated in this model as kinks in the string, i.e. for a $q\bar{q}g$ state, the q and \bar{q} are connected through the gluon instead of directly.

As the quarks move apart, the energy stored in the string increases, until it is large enough that the string fragments by creating an additional $q\bar{q}$ pair from the vacuum (cf. Sec. 2.1.1). This repeats if the energy in the resulting strings is still large enough. Otherwise, the low-mass $q\bar{q}$ pair is considered a meson, based on the flavors of its constituents. This way, only color-neutral particles are present after hadronization, as required by confinement (cf. Sec. 2.1.1). In its purest form, this model has only two free parameters which parameterize the distribution of the momentum fraction of the $q\bar{q}$ pair in each fragmentation. However, in order to correctly describe e.g. flavor composition and p_T spectra of jets, many more parameters are usually needed. For more details on string fragmentation in PYTHIA, see e.g. Ref. [118]. Similar to MPI, hadronization parameters need to be tuned to data, and are also included in the Monash and CP5 tunes.

One shortcoming of the default MPI and hadronization models is that both work in the leading color approximation, i.e. in the limit of a large number of QCD colors ($N_c \rightarrow \infty$). This simplifies the models greatly because the chance of two unrelated color lines sharing the same color becomes infinitesimally small. Corrections to this approximation are typically of order $1/N_c^2 = 1/9$, and can be done via color reconnection (CR), for which different models exist, see e.g. Refs. [142, 143]. The difference between different models is often considered a source of uncertainty in measurements, such as in Secs. 6.5 and 8.5, and can be a limiting factor for some analyses (e.g. top quark mass measurements [144, 145]).

Finally, decays of produced unstable hadrons, including possible decay chains, are also handled by PYTHIA. Branching ratios are taken from experimental measurements where available, and predicted from heuristic models where not, see e.g. Ref. [118].

4.5 Pileup

At the currently achieved instantaneous luminosities, the proton bunches colliding at the LHC contain more than 10^{11} protons on average (cf. Sec. 3.1). Because of this large number, it is expected that a single collision event contains interactions between more than one pair of protons from the two colliding bunches. This is known as pileup. It differs from MPI, in which the different interactions are between multiple partons in the same proton and are thus correlated from a QFT perspective, while different pileup interactions are independent from each other. In Run 2, the average number of pileup interactions per bunch crossing ranged from 23-32 depending on the era of data taking [114], while it is 40 or higher in Run 3.

In simulation, pileup interactions are considered by mixing the generated hard interaction process with a dedicated sample of purely soft-QCD interactions, also gen-

erated in PYTHIA. The probability distribution of the number of pileup interactions is an input to this procedure, and is typically corrected after the generation is finished by reweighting in a suitable variable. In Sec. 6.3.1, an experimental approach to this problem is taken by correcting experimentally accessible pileup-related parameters directly to data. In Sec. 8.2.4, on the other hand, the distribution of the true number of interactions is instead reweighted based on a theory prediction, using the measured total inelastic cross section and integrated luminosity as inputs [146].

4.6 Detector and trigger simulation

After the simulation of the interaction processes, the resulting collection of particles produced in an event is propagated to a full detector simulation using the program GEANT4 [147]. The result is a set of detector information from all subdetectors as well as the outputs of different triggers, similar to true experimental data, and so it can be passed to the different object reconstruction algorithms (cf. Sec. 3.3) in the same way as the data. Events are then analyzed by comparing the reconstructed objects and quantities between data and simulation, ensuring a one-to-one comparison. Possible residual differences between data and simulation are often corrected for by applying calibration factors measured using well-known processes. The details of such calibrations will be explained in Chapters 6 and 8 where relevant.

5 Statistical methods

In experimental particle physics, results are typically extracted by directly comparing detector-level predictions, for example obtained using MC simulation as discussed in the previous chapter, to the observed data for suitably chosen observables. The measured data here are necessarily afflicted by statistical uncertainties, both due to the probabilistic nature of quantum mechanics and the inherent randomness of particle interactions in the detector. They should thus be seen as a sample drawn from a random distribution, and in order to extract underlying parameters of any model, statistical methods are required.

In this work, all statistical interpretation is performed in the framework of *binned profile maximum likelihood fits*. This method follows the Frequentist approach to statistics, in which probability is seen purely as a measure of the *frequency* for a random event to occur when a random experiment is repeated many times. Thus, physical properties that should be extracted are considered to be fixed, if unknown, quantities, which enter the random distribution of the observed data as parameters. In order to estimate the desired properties, the observed data points are sorted into orthogonal bins according to one or more sensitive observables, and each bin is treated as an independent counting experiment where the observed number of events is given by a Poisson distribution.

5.1 Likelihood definition

Denoting the set of physical properties to be estimated (the *parameters of interest* or POIs) collectively as $\vec{\mu}$, the likelihood of $\vec{\mu}$ for bin i , given that N_i events were observed, is [148]

$$L_i(\vec{\mu}, \vec{\theta}) = \text{Pois}\left(N_i | n_i(\vec{\mu}, \vec{\theta})\right). \quad (5.1)$$

Here, Pois refers to the Poisson distribution, and $n_i(\vec{\mu}, \vec{\theta})$ is the mean expected number of events in bin i as predicted by the physics model under consideration. The set of parameters $\vec{\theta}$ are *nuisance parameters* (NPs), which encode the effects of different sources of systematic uncertainty affecting the measurement. The full likelihood of the measurement is now given as the product of all bins:

$$L(\vec{\mu}, \vec{\theta}) = \prod_i L_i(\vec{\mu}, \vec{\theta}) \cdot G(\vec{\theta}). \quad (5.2)$$

The function $G(\vec{\theta})$ represents the *constraint terms* of the NPs, encoding any possible prefit uncertainties on them. For example, an experimental source of uncertainty (e.g. an efficiency) f might be measured with a mean value of \hat{f} and standard deviation Δf . Then, the corresponding NP would be normalized as $\theta_f = (f - \hat{f})/\Delta f$, and the constraint terms $G(\vec{\theta})$ would include a factor $\mathcal{N}(\theta_f | 0, 1)$, i.e. the standard normal distribution for θ_f . This way, the range $\theta_f = \pm 1$ corresponds to one standard deviation of the corresponding systematic uncertainty source.

In practice, the functional form of the expectation n_i must be given by the physics model studied in the experiment. In this work, it is modeled as a sum of signal and background processes. An important case is a linear signal, where the only POI is the *signal strength* μ and the expectation for bin i is

$$n_i(\mu, \vec{\theta}) = \mu s_i(\vec{\theta}) + b_i(\vec{\theta}). \quad (5.3)$$

The functions s_i and b_i are the signal and background expectations, respectively, which both can be influenced by NPs.

To extract a best-fit value of the POI (or multiple POIs), one now maximizes the full likelihood simultaneously over both the POIs $\vec{\mu}$ and the NPs $\vec{\theta}$, giving the *maximum likelihood estimator* for $\vec{\mu}$. In practice, usually the function $-2 \ln L$ is minimized instead to have numerically tractable quantities.

5.2 Confidence intervals

In the Frequentist approach to statistics, an uncertainty can be assigned to the estimate in the form of *confidence intervals*. To do so, a *test statistic* has to be defined, which usually takes the form of a *profile likelihood ratio*, e.g. [148]

$$\lambda(\vec{\mu}) = -2 \ln \frac{\hat{L}(\vec{\mu})}{\max_{\vec{\mu}'} \hat{L}(\vec{\mu}') } \quad \text{with} \quad \hat{L}(\vec{\mu}) = \max_{\vec{\theta}} L(\vec{\mu}, \vec{\theta}). \quad (5.4)$$

$\hat{L}(\vec{\mu})$ is the profile likelihood, i.e. the likelihood maximized over the NPs, and the ratio is taken between the probed POI values $\vec{\mu}$ and the best-fit values $\vec{\mu}'$. Small values of $\lambda(\vec{\mu})$ now signalize good agreement with the data for the POI values $\vec{\mu}$. The value of the test statistic λ depends on the observed data N_i , and can thus be seen as a random variable with a probability density $f(\lambda|\vec{\mu})$, which again depends on the POIs as parameters. Then, given an observed value of the test statistic λ^{obs} , a set of POIs $\vec{\mu}$ is excluded at confidence level (CL) α if

$$\mathcal{P} (\lambda(\vec{\mu}) < \lambda^{\text{obs}}) = \int_0^{\lambda^{\text{obs}}} f(\lambda|\vec{\mu}) d\lambda > \alpha. \quad (5.5)$$

The probability density $f(\lambda|\vec{\mu})$ can be evaluated numerically using toy data sets.

Alternatively, for simple signal models like the linear signal given in Eq. (5.3), it can be analytically shown that λ is approximately χ^2 -distributed, with the degrees of freedom equaling the number of POIs [149, 150].

In particular, for the case of one POI μ with best-fit value $\hat{\mu}$, a two-sided confidence interval at $\sim 68\%$ CL (corresponding to one standard deviation of the normal distribution) is then simply given as [148]

$$\lambda(\hat{\mu} \pm \Delta\mu) = -2(\ln \hat{L}(\hat{\mu} \pm \Delta\mu) - \ln \hat{L}(\hat{\mu})) = 1. \quad (5.6)$$

That is, the uncertainty corresponds to a change in the negative profile log-likelihood $-2 \ln \hat{L}$ by 1 with respect to the best-fit point.

Significance The framework of confidence intervals can also be used to define the *significance* of an observed signal. To do so, a hypothesis test is performed, with the background-only case as the null hypothesis to be rejected. For an observed value of the test statistic λ^{obs} (defined again by Eq. (5.4)), the probability to make this observation under the background-only hypothesis (the *p-value*) is

$$p_0 = \int_0^{\lambda^{\text{obs}}} f(\lambda | \vec{\mu} = 0) d\lambda. \quad (5.7)$$

To translate this into a significance, the *p*-value is compared to the area under the curve of a standard normal distribution: a significance of 2 standard deviations, giving $\approx 95\%$ probability under the normal distribution, corresponds to a *p*-value of 0.05. Similar to the case described above, the *p*-value can be obtained from analytical approximate distributions in the case of a simple linear signal.

Exclusion limits A different application of confidence intervals are *exclusion limits*, used in experiments where no or little signal was observed. Here, for a POI that is bounded from below (usually by zero, e.g. a signal strength), an upper limit μ^{up} is sought such that all values $\mu > \mu^{\text{up}}$ are excluded at a certain CL. At the LHC, the CL_s method [151, 152] is commonly used for this purpose. The test statistic is modified from Eq. (5.4) to be

$$q(\mu) = \begin{cases} \lambda(\mu), & \hat{\mu} \leq \mu \\ 0, & \hat{\mu} > \mu \end{cases} \quad (5.8)$$

where $\hat{\mu}$ again refers to the best-fit value of μ . The point of this modification is that a certain value of μ should not be seen as excluded if the data is more compatible with a higher μ value; thus, the test statistic is set to zero in this case.

Following that, for an observed test statistic q^{obs} , the CL_s value is defined as

$$\text{CL}_s(\mu) = \frac{p_{s+b}(\mu)}{1 - p_b} \quad (5.9)$$

with

$$p_{s+b}(\mu) = \int_0^{q^{\text{obs}}} f(q|\mu) dq \quad \text{and} \quad p_b = \int_0^{q^{\text{obs}}} f(q|\mu=0) dq. \quad (5.10)$$

p_{s+b} and p_b are the probabilities to observe a test statistic of q^{obs} under the signal+background and background-only hypotheses, respectively, defined similarly as in Eq. (5.7). The ratio of the two probabilities is used instead of p_{s+b} directly to prevent exclusion of small signals in the case that the data is not well compatible with neither the background-only or the signal+background hypothesis (particularly if the experiment is not very sensitive to a certain kind of signal and p_{s+b} and p_b are thus similar). The exclusion limit at CL α is then simply given by $\text{CL}_s(\mu^{\text{up}}) = 1 - \alpha$. A common choice, used in this work, is $\alpha = 95\%$ (corresponding to a p -value of 0.05).

5.3 Nuisance parameter diagnostics

Real maximum likelihood fits used in analyses at the LHC are often very complex, with more NPs than there are bins. In such under-constrained fits, the behavior of the different NPs - encoding the different sources of uncertainty - is often not intuitively clear *a priori*, and it is thus important to investigate their postfit behavior to check whether the fit is healthy and numerically stable.

Pulls and constraints To do so, first, the *pull* of a given NP θ is defined as

$$P_\theta = \frac{\hat{\theta} - \theta_0}{\Delta\theta_0} \quad (5.11)$$

where $\hat{\theta}$ is the best-fit value of the NP, θ_0 is the prefit value, and $\Delta\theta_0$ is the prefit uncertainty. To have an NP pulled thus means that its best-fit value is different from the prefit expectation. Similarly, the *constraint* of the NP is defined as

$$C_\theta = \frac{\Delta\hat{\theta}}{\Delta\theta_0} \quad (5.12)$$

where $\Delta\hat{\theta}$ is the estimated postfit uncertainty of the NP, defined in the same fashion as for the POIs above.¹ To have an NP constrained means that its estimated postfit uncertainty is smaller than the assumed prefit value.

¹In case the NP is normalized to a standard normal distribution as defined above, one has simply $P_\theta = \hat{\theta}$ and $C_\theta = \Delta\hat{\theta}$.

Both of these effects are not necessarily a sign of an unhealthy fit: if the observables considered in the fit are sensitive to a particular physical or experimental parameter as encoded by the NP in question, a constraint, and possibly a pull, are expected, and simply show the power of the fit to measure that particular parameter.

If, on the other hand, a strong constraint or pull (beyond what is expected from statistical fluctuations) is seen in an NP to which no sensitivity is expected, it might be a sign of problems with the fit, such as spurious constraints from noisy inputs, missing degrees of freedom to describe the data, or too small prefit uncertainties. Whether this casts doubt on the result or not needs to be gauged on a case-by-case basis, and depends on the relevance of the NP in question.

The relevance of individual NPs to the result can be quantified using *impacts*. The impact of an NP θ with best-fit value $\hat{\theta}$ and postfit uncertainty $\Delta\hat{\theta}$ is defined by repeating the maximum likelihood fit at values of $\hat{\theta} \pm \Delta\hat{\theta}$, with θ then held fixed in the maximization of Eq. (5.4). The shift in the resulting POI values with respect to the best-fit POI is the impact on that particular POI. In a fit with a single POI, the impacts can be used to rank the NPs and the systematic uncertainties they encode in order of importance to the fit result. In particular, NPs with very small impact can be considered irrelevant for the fit result. However, it should be kept in mind that this procedure does not fully account for possible correlations between the NPs.

Uncertainty breakdown Related but not identical to the concept of impacts is an *uncertainty breakdown*, which can be used to quantify the contribution from different sources of uncertainty to the total postfit uncertainty on the POI. To do so, either a single NP or a group of NPs originating from the same source (e.g. all NPs corresponding to a certain correction) are frozen at their postfit values, and the fit is repeated with the POI and remaining parameters left untouched. The result will yield the same best-fit value for the POI, but with a possibly reduced uncertainty (as estimated from the likelihood). The uncertainty due to the frozen NP or NP group is then defined as the quadratic difference to the nominal uncertainty. This method does not account for correlations between different uncertainty sources (though it does consider correlations between the NPs in a certain group). As a result, the uncertainties obtained in this way will in general not sum up in quadrature to the original uncertainty.

A further use of this method is to define the statistical component of the uncertainty on a POI: it is simply the remaining uncertainty when all considered NPs are frozen to their postfit values simultaneously. Conversely, the quadratic difference between the total and the statistical uncertainty can be considered the systematic uncertainty.

5.4 Technical implementation

In this work, two different tools are used to implement the methods described above. In Chapters 6 and 8, where experimental data is analyzed, the CMS general-purpose statistics tool `combine` is used [153]. In Chapter 9, on the other hand, the Python-based tool `pyhf` [154] is employed for the purpose of calculating expected significances and limits.

6 Measurement of the inclusive $t\bar{t}$ cross section at $\sqrt{s} = 13.6$ TeV

6.1 Introduction

In July 2022, the LHC officially resumed collecting data after over three years of shutdown, thereby starting LHC Run 3. It did so at a new, unprecedented center-of-mass energy of $\sqrt{s} = 13.6$ TeV, inviting the experiments to measure physical observables at the new energy frontier.

One important such observable is the inclusive $t\bar{t}$ production cross section. It is, in essence, the total rate of top quark pair production at the LHC, integrated over the kinematic distributions of the particles produced. As mentioned in Chapter 2, the top quark has a special place in the standard model as the heaviest known elementary particle, as well as the only colored particle that decays before hadronizing. It is thus important for many potential BSM scenarios, such as models with additional Higgs bosons, which might couple strongly to the top quark. As such, measurements of top quark-related observables at the highest possible energies are attractive tests of the SM. The inclusive $t\bar{t}$ production cross section, as one of the simplest top quark observables, is well suited for a first measurement at the new center-of-mass energy.

Simultaneously, restarting such a large experiment as CMS after a three-year shutdown poses many experimental challenges. Due to the change in energy, as well as physical changes in the accelerator and detector, new calibrations as well as validations of some previous calibrations are required to ensure that the detector performance is understood. An early measurement of the inclusive $t\bar{t}$ cross section is well suited to serve as such a cross-check: Because of the decay chain of the top quark, a top quark measurement involves many of the different objects reconstructed at CMS, which allows for a check of a wide landscape of calibrations.

The measurement described in this chapter was designed specifically with these motivations in mind, and as such exhibits several novel features. Firstly, it combines events from both the dilepton and $\ell+\text{jets}$ decay channels of $t\bar{t}$, categorized by lepton flavor content, combining the higher statistics of the $\ell+\text{jets}$ channel with the high purity of the $e\mu$ channel and allowing to constrain uncertainties on the lepton identification efficiency directly from the data. This is done using a simultaneous maximum likelihood fit (cf. Chapter 5) to the event yields in the different categories, with experimental and theoretical uncertainties treated as nuisance parameters.

Secondly, the events are additionally categorized by their number of b-tagged jets

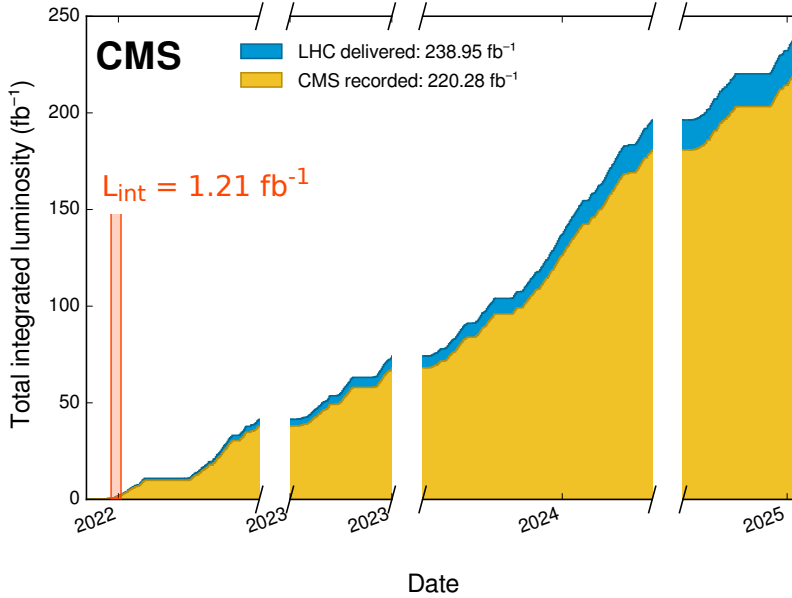


Figure 6.1: **Integrated luminosity in Run 3.** The cumulative integrated luminosity delivered to and recorded by CMS in Run 3 at the time of writing, corresponding to the period July 2022–August 2025. The data set used for the analysis in this chapter, corresponding to 1.21 fb^{-1} , is marked in orange. *Figure adapted from Ref. [155].*

(cf. Sec. 3.3), which similarly allows for an in-situ measurement of the b-tagging efficiencies. This averts needing to wait for external b-tagging calibrations, allowing for a measurement as early as possible.

The results of this work were first presented as a Physics Analysis Summary in September 2022 [156], only two months after the start of data taking, as the first public physics result of LHC Run 3. It was published later in *JHEP* as Ref. [5], again representing the first published Run 3 result. A similar result by ATLAS was published afterwards in Ref. [157].

This chapter is structured as follows: In Sec. 6.2, the used data sets, object definitions, and event selection criteria are described, followed by the derivation and application of needed corrections in Sec. 6.3, and the resulting data-MC agreement is shown in Sec. 6.4. The considered systematic uncertainties are listed in Sec. 6.5, and the fit results are presented in Sec. 6.6. The chapter is concluded by a short summary and outlook in Sec. 6.7.

Trigger	Lepton requirement
e+jets	$e(p_T > 32 \text{ GeV})$
$\mu+\text{jets}$	$\mu(p_T > 27 \text{ GeV})$
ee	$e(p_T > 23 \text{ GeV})$ and $e(p_T > 12 \text{ GeV})$
$\mu\mu$	$\mu(p_T > 17 \text{ GeV})$ and $\mu(p_T > 8 \text{ GeV})$
$e\mu$	$e(p_T > 23 \text{ GeV})$ and $\mu(p_T > 8 \text{ GeV})$ or $e(p_T > 12 \text{ GeV})$ and $\mu(p_T > 23 \text{ GeV})$

Table 6.1: **Trigger definitions** as used for the $t\bar{t}$ cross section measurement. The leptons are required to be isolated and in the pseudorapidity range $|\eta| < 2.5$.

6.2 Data sets and event selection

In this section, the choice of data sets for experimental data and for simulation, as well as the choice of triggers, is described. Following that, the object and event selection procedure is outlined and several event categories to be used in the likelihood fit are defined.

6.2.1 Data sets

Experimental data The measurement is performed on data recorded during the period between July 27th and August 02nd 2022, corresponding to an integrated luminosity of 1.21 fb^{-1} . This amount of data is chosen as a balance between sensitivity and speed for the early measurement: It roughly corresponds to the point where the measurement precision is no longer primarily limited by the quantity of the data, while at the same time restricting to a data set where beam and detector conditions were stable and comparable to the data-taking in Run 2.

Both single-lepton and dilepton triggers were used to select events used in this measurement during detector operation, identifying leptons in the pseudorapidity range of $|\eta| < 2.5$. The p_T requirements of the triggers are summarized in Tab. 6.1.

Simulation To compare the data with predictions, Monte Carlo (MC) simulation is used to simulate both the $t\bar{t}$ signal, as described in Sec. 4.1.2, as well as most important background processes, specifically single-top quark production in the t -channel, associated tW production, $Z+\text{jets}$ production, $W+\text{jets}$ production, and diboson (WW , WZ and ZZ) production. Example Feynman diagrams for these processes are shown in Fig. 6.2. The programs used for the different samples, as well as the respective orders in QCD, are collected in Tab. 6.2. For $Z/W+\text{jets}$ production, up to two four additional partons are included in the LO matrix element using the MLM merging scheme [134].

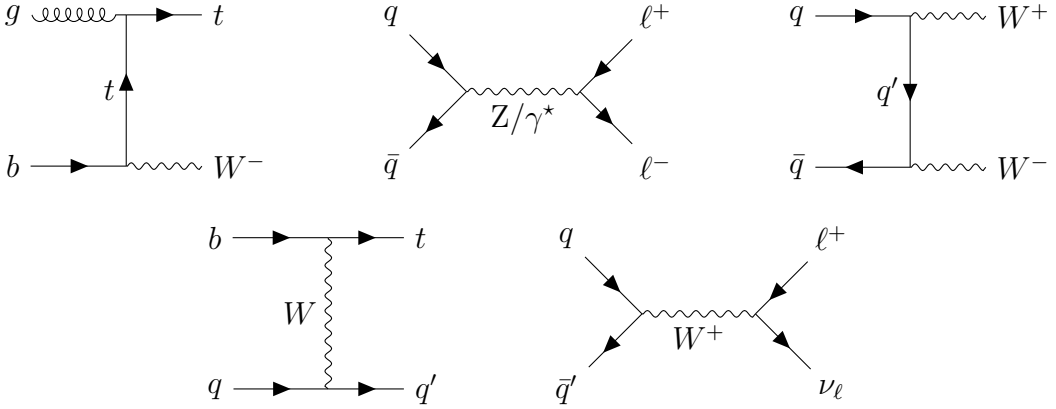


Figure 6.2: **Feynman diagrams for the background processes.** Examples of Feynman diagrams for (from top left to bottom right) tW production, $Z/\gamma^* \rightarrow \ell\ell$ production, WW production, t -channel single top production, and $W \rightarrow \ell\nu$ production, constituting the most important backgrounds.

All of the generated events are interfaced to PYTHIA 8 for parton showering and hadronization, and further processed in a full simulation of the CMS detector as described in Chapter 4. The proton structure in the matrix element calculation is described by the NNPDF3.1 parton distribution function (PDF) set at NNLO. Note that another background contribution, from QCD-produced multijet events with fake or non-prompt leptons, is not simulated, but estimated from data (see Sec. 6.3.2).

Theoretical predictions, as well as the measured integrated luminosity, are used to normalize the cross sections of the signal and background samples, which are collected in Tab. 6.3. In particular, the $t\bar{t}$ signal is normalized to a cross section of 921^{+29}_{-37}pb computed at NNLO+NNLL in QCD [158], which is also used as a prediction for comparison with the SM.

6.2.2 Object definition

Leptons Electrons or muons are considered for the analysis if they have $p_T > 10$ GeV and $|\eta| < 2.4$. For electrons, the range $1.44 < |\eta_{\text{SC}}| < 1.57$ is removed, where η_{SC} is the pseudorapidity of the ECAL supercluster from which the electron was reconstructed and the interval corresponds to the transition region between barrel and endcaps in the ECAL. Furthermore, additional identification criteria (ID) are applied to remove non-prompt or fake (i.e. wrongly reconstructed) leptons and enrich the selection with $t\bar{t}$ events.

For electrons, the “tight” working point of the cut-based ID described in Ref. [103] is applied, which includes information from both the details of the electromagnetic shower in the ECAL and the track, as well as the matching between the two. It also includes a requirement for the electron to be isolated from other particles such as

Process	QCD order	ME Generator
t <bar>t</bar>	NLO	POWHEG v2 (hvq [129])
tW	NLO	POWHEG v2 (ST_wtch [159])
t-channel single top	NLO	POWHEG v2 (ST_tch [160]) + MADSPIN [131]
Z/W+jets	LO	MG5_AMC@NLO (MLM merging [134])
WW, WZ & ZZ	LO	PYTHIA 8.2

Table 6.2: **Simulated signal and background samples.** An overview of the different simulated processes, as well as the theoretical order in QCD and the ME generator (and, if applicable, the subprocess) used to simulate them. For all samples, PYTHIA 8.2 is used for showering and hadronization.

hadrons, which is implemented in the form of the relative isolation variable I_{rel} . It is defined as the scalar p_{T} sum of all particles in a cone around the lepton in question, divided by the lepton p_{T} . Here, $\Delta R = \sqrt{(\Delta\eta)^2 + (\Delta\varphi)^2} < 0.3$ is used for the radius of the cone. Additional corrections accounting for pileup particles are applied.

Process	Cross section (pb)	Order	Program / reference
t <bar>t</bar>	921	NNLO+NNLL	Top++ [158]
tW	87.6	NNLO (approx.)	[161]
t-channel single top	232.2	NNLO	MCFM [162]
Z/ γ^* +jets $\rightarrow \ell\ell$ $m_{\ell\ell} > 10$ GeV	25.5×10^3	NNLO	DYTurbo [163]
W + jets $\rightarrow \ell\nu$, WW	63.2×10^3	NNLO	DYTurbo [163]
WZ	116.8	NNLO	MATRIX [164]
ZZ	54.3	NLO	MATRIX [164]
	16.7	NLO	MATRIX [164]

Table 6.3: **Cross sections for signal and background processes at $\sqrt{s} = 13.6$ TeV.** The cross sections used for the normalization of the signal and background processes, as well as the orders in QCD at which they were computed. Where applicable, cross sections are given as the sum of the process and its charge conjugate.

For muons, a similar cut-based ID is used as described in Ref. [165], also at the tight working point. Here, criteria on the compatibility of tracks in the inner tracker, the muon detectors and the reconstructed primary vertex are employed. Again, a cut on I_{rel} is used, defined equivalently but with a cone size of $\Delta R < 0.4$.

Jets The anti- k_T algorithm [115] is used to cluster reconstructed particles into jets with a distance parameter of 0.4. In order for a jet to be considered, it is required to have $p_T > 30$ GeV and $|\eta| < 2.4$, and jets overlapping with any considered leptons (i.e. fulfilling the above criteria) are removed.

Tagging of b jets A special role is played by jets originating from the showering and hadronization of b quarks. Naively, two such jets are expected per $t\bar{t}$ event from the two top decays, although in practice one or both jets may fall out of acceptance of the detector or otherwise not be identified. Furthermore, additional b quarks may be produced by radiation at higher orders in QCD. Correctly tagging these jets as such can greatly improve signal purity by cutting away backgrounds such as Z+jets, W+jets and QCD multijet events.

Here, the DEEPJET algorithm [116, 166], which is based on a deep neural network (DNN) classifier, is used to identify (“tag”) b jets. A working point with an identification efficiency of more than 75% is used, with misidentification rates of around 17% for charm jets and around 1% for other jets from light quarks or gluons.

6.2.3 Channel definition

Events are selected with either one or two leptons, corresponding respectively to the ℓ +jets and dilepton decay channels of $t\bar{t}$. They are categorized into separate channels by their lepton flavor content, and additional requirements are applied for the different channels.

Dilepton channels Events with exactly two leptons, required to have opposite electric charge, are sorted into three dilepton channels ($e\mu$, ee , and $\mu\mu$). The presence of at least one jet is required, and in the same-flavor channels (ee and $\mu\mu$), at least one jet is required to be b tagged in order to reject Z+jets and QCD multijet background. In the much purer $e\mu$ channel, on the other hand, events without b tags are retained to later help constrain the b tagging efficiency in the fit to data.

In order to reject even more Z+jets background, events in the same-flavor channels with an invariant dilepton mass of $|m_{\ell\ell} - m_Z| < 15$ GeV, where m_Z is the Z boson mass, are removed. Furthermore, background arising from $\gamma^* \rightarrow \ell\ell$, low-mass dilepton resonances (e.g. quarkonia), or fake leptons is rejected by requiring $m_{\ell\ell} > 20$ GeV regardless of lepton flavor.

ℓ +jets channels Events with exactly one lepton are sorted into the e+jets or μ +jets channels based on their flavor. At least three jets are required, of which at least one needs to be b tagged. Note that regardless of these selections, there is still non-negligible background from QCD multijet events where the lepton is non-prompt or fake, which is estimated from data (see Sec. 6.3.2).

p_T requirement In all channels, the considered leptons are required to have $p_T > 35$ GeV. This requirement is needed in the $\ell + \text{jets}$ channels in order to stay above the single-lepton trigger p_T thresholds (compare Tab. 6.1). In this measurement, the choice is made to apply the same p_T requirement also both leptons in the dilepton channels to ensure consistency between the lepton definitions. This is done to help constrain the lepton ID scale factors using the combination of lepton flavor channels, which otherwise might not be accurate since the scale factors for different lepton definitions might differ. In particular it opens up the possibility to extract a result on the cross section without any prior knowledge on the lepton ID efficiencies, which was done in the first published version of this analysis [156].

Cut	Data yield			$t\bar{t} \rightarrow \ell\ell$ MC	
	ee	e μ	$\mu\mu$	efficiency (%)	purity (%)
Triggers ($\ell\ell/\ell + \text{jets}$)	36803494			65.2	–
Two OS leptons	429200	15128	873626	17.5	1.5
Lepton p_T	245607	6712	474191	9.6	1.4
$m_{\ell\ell} > 20$ GeV	244805	6639	471448	9.5	1.4
Z window (ee/ $\mu\mu$)	15049	6639	26458	8.7	21.4
At least 1 jet	5225	5643	9004	8.0	51.2
At least 1 b tag (ee/ $\mu\mu$)	1550	5643	2773	7.4	82.3

Table 6.4: **Selection cuts and event yields in the dilepton channels.** The data yield after successively applying all selection cuts separately for the three dilepton channels. The second-to-last column shows the selection efficiency of $t\bar{t} \rightarrow \ell\ell$ events ($\ell = e, \mu, \tau$), and the last column shows the purity, defined as the fraction of $t\bar{t} \rightarrow \ell\ell$ events and total event yield. Both efficiency and purity are evaluated using simulation.

b tag and jet categorization In practice, the efficiency of the b tagging algorithm used might be different between simulation and data, necessitating a correction to prevent bias. In this analysis, this efficiency is measured simultaneously with the cross section directly in the data. To do so, the lepton flavor channels are additionally split into categories based on the number (exactly 0, 1, or 2) of b tagged jets. Since only the e μ channel allows events with 0 b tags, this results in 11 categories total. To gain further sensitivity to the b tagging efficiency and to increase possible separation between $t\bar{t}$ signal and background, the selected events are finally coarsely binned into the number of accepted jets for the eventual fit, giving a total number of 40 bins.

Cut	Data yield		$t\bar{t} \rightarrow \ell + \text{jets}$ MC	
	e+jets	$\mu + \text{jets}$	efficiency (%)	purity (%)
Triggers ($\ell\ell/\ell + \text{jets}$)	36803494		38.5	—
Exactly 1 lepton	6649607	12114488	32.7	0.8
Lepton p_T	5478022	6242142	27.6	1.1
At least 3 jets	160666	156698	19.2	30.6
At least 1 b tag	62261	71929	16.7	59.8

Table 6.5: **Selection cuts and event yields in the $\ell + \text{jets}$ channels.** The data yield after successively applying all selection cuts separately for the two $\ell + \text{jets}$ channels, as well as the selection efficiency and purity of $t\bar{t} \rightarrow \ell + \text{jets}$ events, defined analogously to Tab. 6.4. The data-driven QCD multijet estimation (Sec. 6.3.2) is used together with simulation to estimate the purity.

6.3 Corrections

While the simulation used in CMS tries to describe as many physics and detector effects as possible, in practice it should always be expected that not all observables agree with the experimental data perfectly. This is especially true for an early analysis such as this, as the detector conditions might have changed significantly during the long shutdown between LHC Runs 2 and 3, and the simulation had not been recalibrated at the time of the measurement.

Because of this, the analysis setup is designed to either directly measure or cross-check as many required experimental calibration and correction factors as possible. This includes pileup corrections, efficiency scale factors for triggers, electrons, muons and b tags, as well as jet energy corrections, all of which are briefly described in this section.

In addition to these experimental corrections, background processes might also be imperfectly described by the simulation because of theoretical shortcomings. In this case, ways have to be found to correct them directly from the experimental data. Here, two such cases are relevant and will be presented in the latter half of this section: The Z+jets background in the dilepton channels and in the presence of b tagged jets, for which the normalization is taken from data; and the QCD background in the $\ell + \text{jets}$ channels, which uses a fully data-driven estimation and foregoes simulation entirely.

6.3.1 Experimental corrections

Pileup reweighting The simulation samples used in this analysis were generated before the start of Run 3 data taking using a projected estimate of the average

pileup. As a result, the pileup distribution in the simulation does not match the one observed in data, which could influence mostly jet-related variables such as the number of jets and the jet p_T .

Since at the time of the measurement, no theory-based calculation for the correct pileup distribution were available, an experimental approach was taken. Three experimental observables that are strongly correlated with pileup were identified:

- The number of well-reconstructed primary vertices per event n_{PV} ;
- The median p_T density in the calorimeter, calculated from calorimeter-only jets as $\rho^{\text{calo}} = \text{med}(p_T/A)$, where A is the jet area defined in the φ - η plane and the median is taken over all jets in the event;
- The median p_T density in the tracker ρ^{trk} , defined equivalently as ρ^{calo} , but for jets calculated only from tracker information.

A binned reweighting from simulation to data is derived for each observable based on the full data sample, and the average of the three weights is applied to the simulation, so that approximate agreement is achieved in all three variables. The distributions before and after reweighting can be seen in Fig. 6.3. The agreement is greatly improved by the reweighting, and while it is not perfect for all three variables, it is similar to the level of agreement expected in the theory-based method [146] and thus deemed suitable.

Trigger scale factors The trigger efficiency, i.e. the probability for an event falling into the selection phase space to be triggered by the low- and high-level triggers, can differ between simulation and data. In principle, both dilepton and single-lepton triggers are used for this measurement and should be considered for the efficiency calculation. However, due to the high offline p_T requirements for the two leptons applied in all channels, the fraction of events that are triggered only by the dilepton triggers is negligibly small, and can be neglected for the purpose of determining the scale factor. Thus, only the single-lepton triggers are considered in this section for simplicity.

The efficiency measurement is performed by the so-called tag-and-probe method, using $Z \rightarrow e^+e^-$ and $Z \rightarrow \mu^+\mu^-$ events. They are selected using the same definitions presented above, including the lepton identification, except for requiring their invariant mass to fulfill $|m_{\ell\ell} - m_Z| < 20$ GeV. At least one of the leptons is required to pass the relevant single-lepton trigger and is then designated the tag, while the other lepton might or might not pass the trigger and is designated the probe. Assuming the probability for the two leptons to pass the trigger to be independent of each other, the trigger efficiency, given by probability of the probe to pass, can be written as

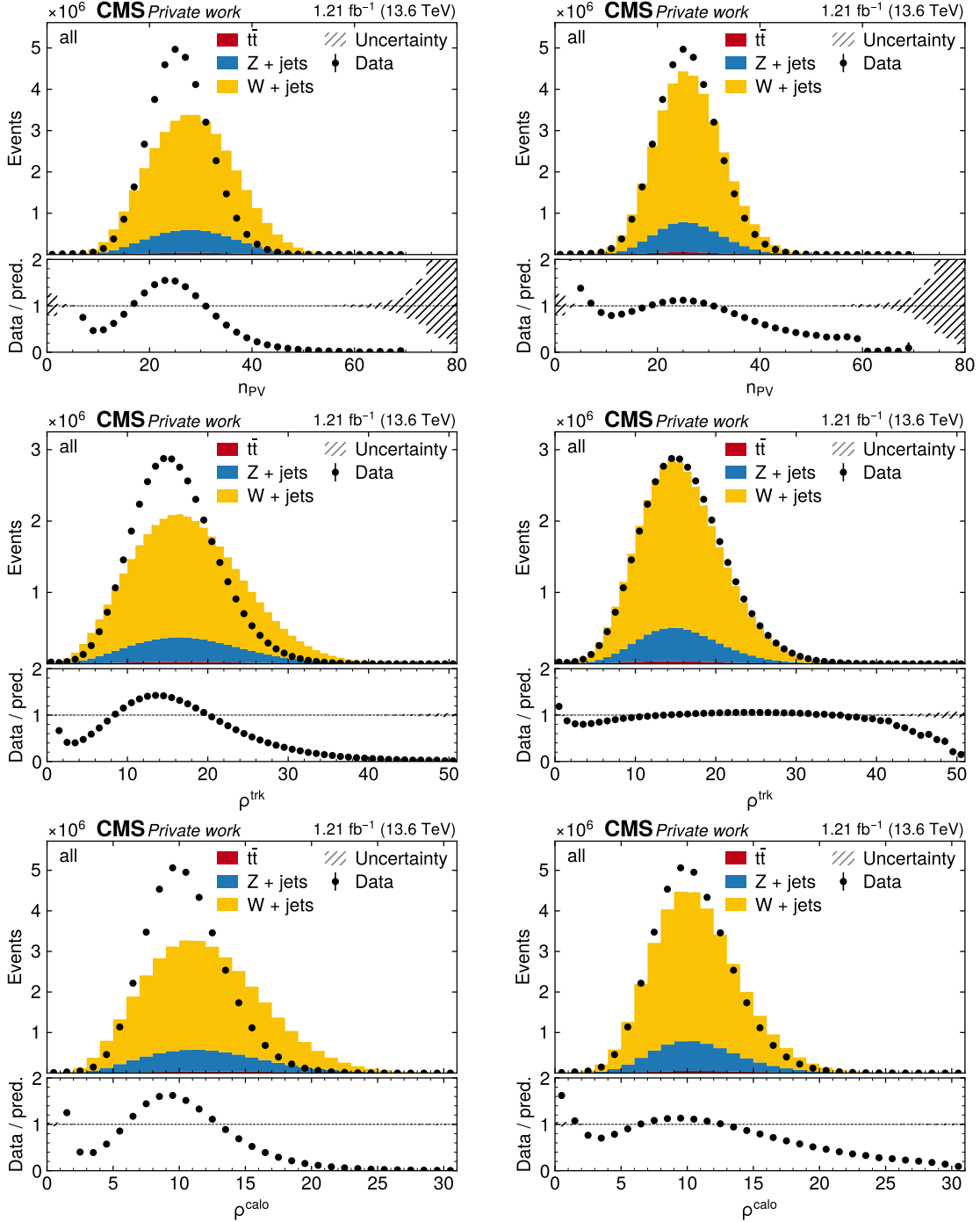


Figure 6.3: Pileup reweighting. Pileup-related distributions in MC and data in before (left) and after reweighting (right). From top to bottom: number of primary vertices as well as the mean energy densities ρ^{trk} (calculated using tracker input) and ρ^{calo} (calculated using calorimeter input).

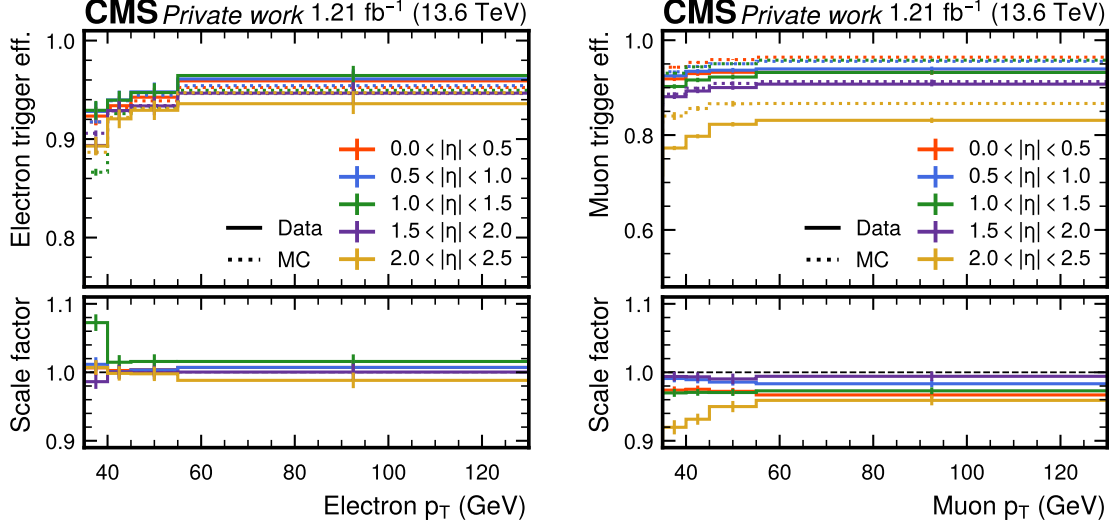


Figure 6.4: **Trigger scale factors.** Single-lepton trigger efficiencies in data and MC (top) and scale factors (bottom) for electrons (left) and muons (right) as a function of lepton p_T and $|\eta|$, calculated using a tag-and-probe-method. The error bars designate both statistical and systematic uncertainties.

$$\epsilon_{\text{tr}} = \frac{N(\text{Probe passes})}{N(\text{Probe passes}) + \frac{1}{2}N(\text{Probe fails})} \quad (6.1)$$

where N corresponds to the number of events in which the second lepton either passes or fails the trigger, and the combinatoric factor $\frac{1}{2}$ comes from the fact that either one or the other lepton can fail.

The efficiency is measured in this way in coarse bins of lepton p_T and $|\eta|$, separately for muons and electrons, in both simulation and experimental data. It is then applied to simulation in the following way: For $\ell+\text{jets}$ events, a simple ratio $\epsilon_{\text{tr,data}}/\epsilon_{\text{tr,sim}}$ is applied to each simulation event as a scale factor, which is displayed in Fig. 6.4. For dilepton events, on the other hand, the fact that only one lepton needs to pass the single-lepton trigger needs to be taken into account. This leads to a per-event efficiency given by

$$\epsilon_{\text{tr},\ell\ell} = \epsilon_{\text{tr},\ell 1} + \epsilon_{\text{tr},\ell 2} - \epsilon_{\text{tr},\ell 1}\epsilon_{\text{tr},\ell 2} \quad (6.2)$$

where $\epsilon_{\text{tr},\ell 1}$ and $\epsilon_{\text{tr},\ell 2}$ are the efficiencies evaluated at the p_T and $|\eta|$ of the two leptons, respectively. Again, the ratio of this event efficiency in data and simulation is applied to the simulation.

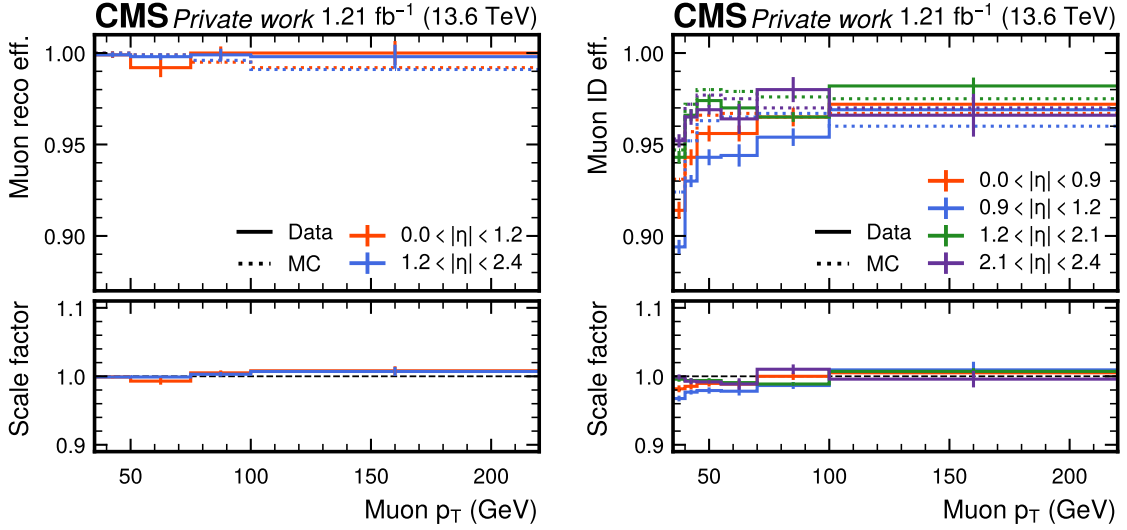


Figure 6.5: **Muon scale factors.** Muon efficiencies in data and MC (top) and scale factors (bottom), split into reconstruction (left) and identification (right) and shown as a function of lepton p_T and $|\eta|$, calculated using a tag-and-probe-method. The error bars designate both statistical and systematic uncertainties.

Lepton scale factors Similarly to the triggers, the reconstruction and identification of leptons can exhibit different efficiencies between simulation and data, and thus require scale factors. The efficiencies are measured with a similar tag-and-probe method as for the triggers, and the simulation is corrected to the data. This is the standard approach commonly taken in CMS, detailed in Refs. [103, 165] for electrons and muons, respectively. The efficiency measurement was not performed as part of this thesis, but is still shown in Figs. 6.5 and 6.6 for reference. The muon scale factors are split into a reconstruction and an identification part, while these are combined for the electron scale factors.

b tagging scale factors The performance of b tagging algorithms, such as the DEEPJET algorithm used in this analysis, is known to differ between simulation and data, necessitating corrections. This is particularly relevant here, as the multivariate classifier behind DEEPJET had not been re-trained on Run 3 data at the time of the measurement; instead, the Run 2 calibration was used.

Since no external calibration of b tagging efficiencies for Run 3 was available within the time frame of this study, the b tagging efficiency in data is extracted directly from the data itself. This is achieved by performing a simultaneous likelihood fit with the $t\bar{t}$ cross section, as described in Sec. 6.5. As a result, no b tagging scale factors are applied beforehand.

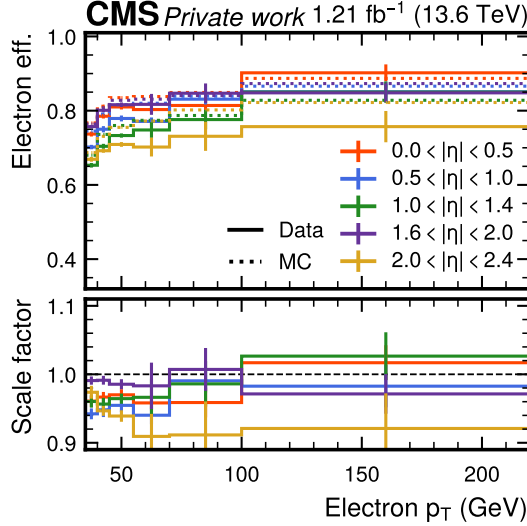


Figure 6.6: **Electron scale factors.** Combined electron efficiencies in data and MC (top) and scale factors (bottom) as a function of lepton p_T and $|\eta|$, calculated using a tag-and-probe-method. The error bars designate both statistical and systematic uncertainties.

Jet energy corrections Another observable that often differs significantly between observed data and simulation is the measured energy response of the jets. Both its mean value, the jet energy scale (JES), and the jet energy resolution (JER) require corrections, which are together referred as jet energy corrections (JECs). Both are centrally provided by CMS following the methods of Ref. [167]. The `Winter22Run3_V1` version of the JECs, which was the first available version for Run 3, were used here.

The derivation of the JES is performed in multiple steps: first, the expected fraction of jet energy due to pileup, determined from MC simulation, is removed from all jets in data and MC. Second, the difference in jet energy between detector- and particle-level jets in simulation is determined as a function of jet kinematics, and detector-level jets are corrected accordingly in both data and simulation. Third, residual disagreements of the simulation with the data are corrected using experimental jet measurements in dijet, γ +jets, Z+jets, and multijet events, again parameterized as a function of jet kinematics [167].

Similarly, JER scale factors are determined by correcting the resolution in simulation to the one seen in data, based on dijet, γ +jets and Z+jets events [168]. They are then applied to jets in simulation by scaling the difference between detector- and particle-level jet energy for jets where a matched particle-level jet is found, while a stochastic smearing is used otherwise.

6.3.2 Data-driven background estimation

QCD background A significant background contribution in the $\ell + \text{jets}$ channels, especially in the categories with only one b tag, is given by QCD multijet events with one reconstructed lepton. The lepton in question might be non-prompt, e.g. from radiated photons splitting into leptons or decays of heavy flavor hadrons, or it might be fake, i.e. a different particle (such as a photon or pion in the case of electrons) misidentified as a lepton.

It is often not practical to estimate this background using MC simulation as is done for the other backgrounds in this analysis. The reason is that, due to the large cross section of QCD multijet events at the LHC but low ratio of events with a fake or non-prompt lepton, very large MC data sets are needed to achieve significant statistics in the selected phase space, requiring excessive computing power. In addition to that, simulating how leptons can be faked in the detector is known to be difficult, and thus fake leptons are not well-described by the simulation.

Instead, a fully data-driven approach is taken to estimate the QCD background in the $\ell + \text{jets}$ channels. For this, multiple control regions (CRs) orthogonal to the signal region (SR) are defined. In the first CR, denoted “QCD CR”, the same cuts as in the SR are applied, except that the requirement for the single lepton to be isolated from other particles (I_{rel} , see Sec. 6.2.2) is inverted. It is expected that QCD events that fall in either the QCD CR or the SR show similar shapes in observable distributions, as long as said observables are uncorrelated with the lepton isolation. Thus, the shape of the QCD background can be extracted from the CR and applied in the SR. Figs. 6.7 and 6.8 show the distributions of several key distributions for the QCD background in the $\mu + \text{jets}$ and $e + \text{jets}$ channels, respectively, which is estimated by subtracting all simulated (MC) processes from the data.

The normalization of the QCD background is fixed through the so-called *ABCD method* [169, 170], for which an additional CR (the “1-jet CR”) is defined. It again contains events that pass the main selection, except for requiring exactly one jet (as opposed to at least three jets in the SR or QCD CR). These events are enriched with QCD events and contain negligible amounts of $t\bar{t}$ signal. They are used to measure the ratio f_{fake} of QCD events that pass or fail the lepton isolation requirement, given by

$$f_{\text{fake}} = \frac{N_{1 \text{ jet}, \text{ pass}}^{\text{data}} - N_{1 \text{ jet}, \text{ pass}}^{\text{MC}}}{N_{1 \text{ jet}, \text{ fail}}^{\text{data}} - N_{1 \text{ jet}, \text{ fail}}^{\text{MC}}} \quad (6.3)$$

where $N_{1 \text{ jet}, \text{ pass}}$ and $N_{1 \text{ jet}, \text{ fail}}$ denote 1-jet-events that pass and fail the lepton isolation requirement, respectively; “data” refers to the experimental data, and “MC” refers to the sum of all non-QCD processes, which are estimated by MC simulation. Here, this ratio is measured in four coarse bins of lepton p_T and $|\eta|$ to accurately model lepton-related distributions; it can be seen in Fig. 6.9.

Naively, the full distribution of the QCD background in the SR for any observable

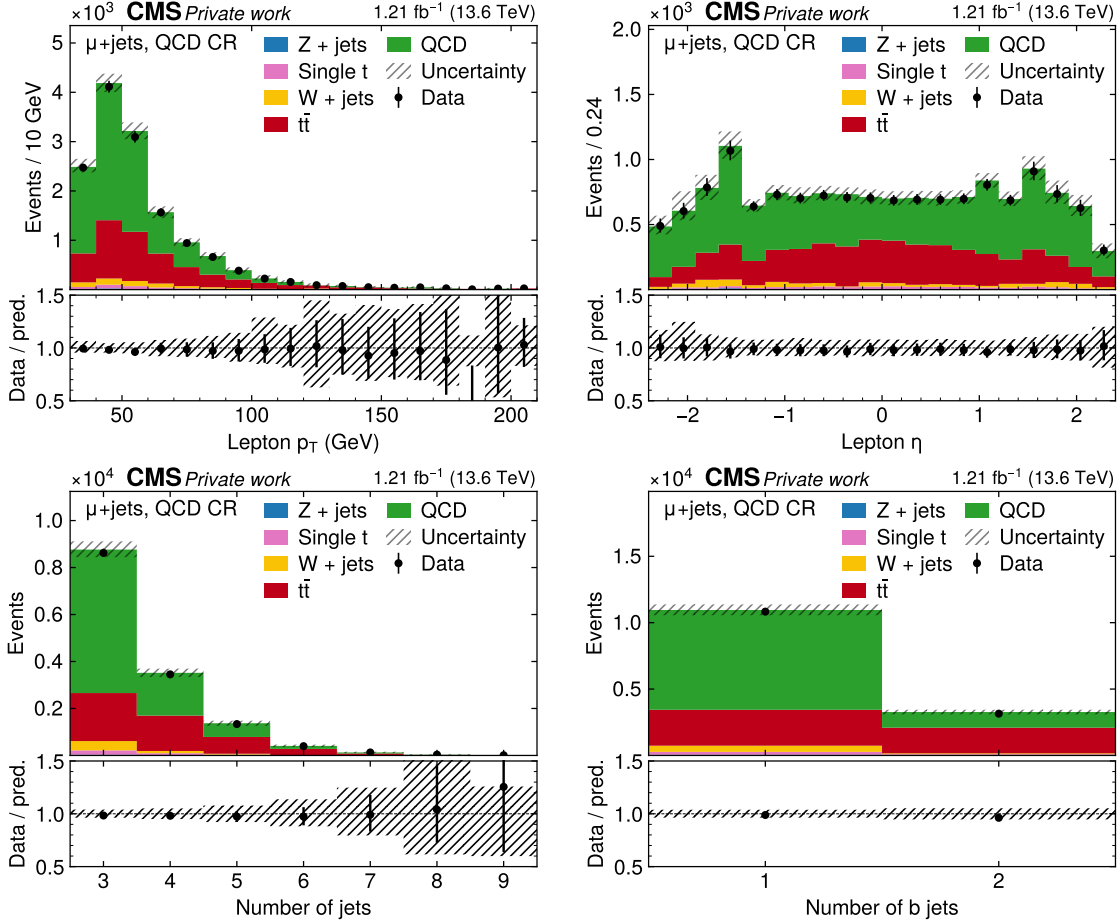


Figure 6.7: **QCD control region for $\mu + \text{jets}$.** Distributions in the QCD CR for the $\mu + \text{jets}$ channel. From top left to bottom right: p_T of the lepton, η of the lepton, the number of jets, and the number of b-tagged jets. The uncertainty bands include MC statistical and systematic uncertainties. The difference between data and MC prediction is considered QCD background and shown in green.

can then be written as

$$N_{\text{SR}}^{\text{QCD}} = (N_{\text{CR}}^{\text{data}} - N_{\text{CR}}^{\text{MC}}) \times f_{\text{fake}} \quad (6.4)$$

where $N_{\text{CR}}^{\text{data}}$ and $N_{\text{CR}}^{\text{MC}}$ refer to the total data and non-QCD MC yields in the QCD CR.

In practice, this is complicated by the fact that a non-negligible amount of $t\bar{t}$ signal is present in the QCD CR, whose cross section, as the parameter of interest in the measurement, is not known *a priori*. To circumvent this problem, a modified method is introduced, which is agnostic about the prediction for the $t\bar{t}$ cross section.

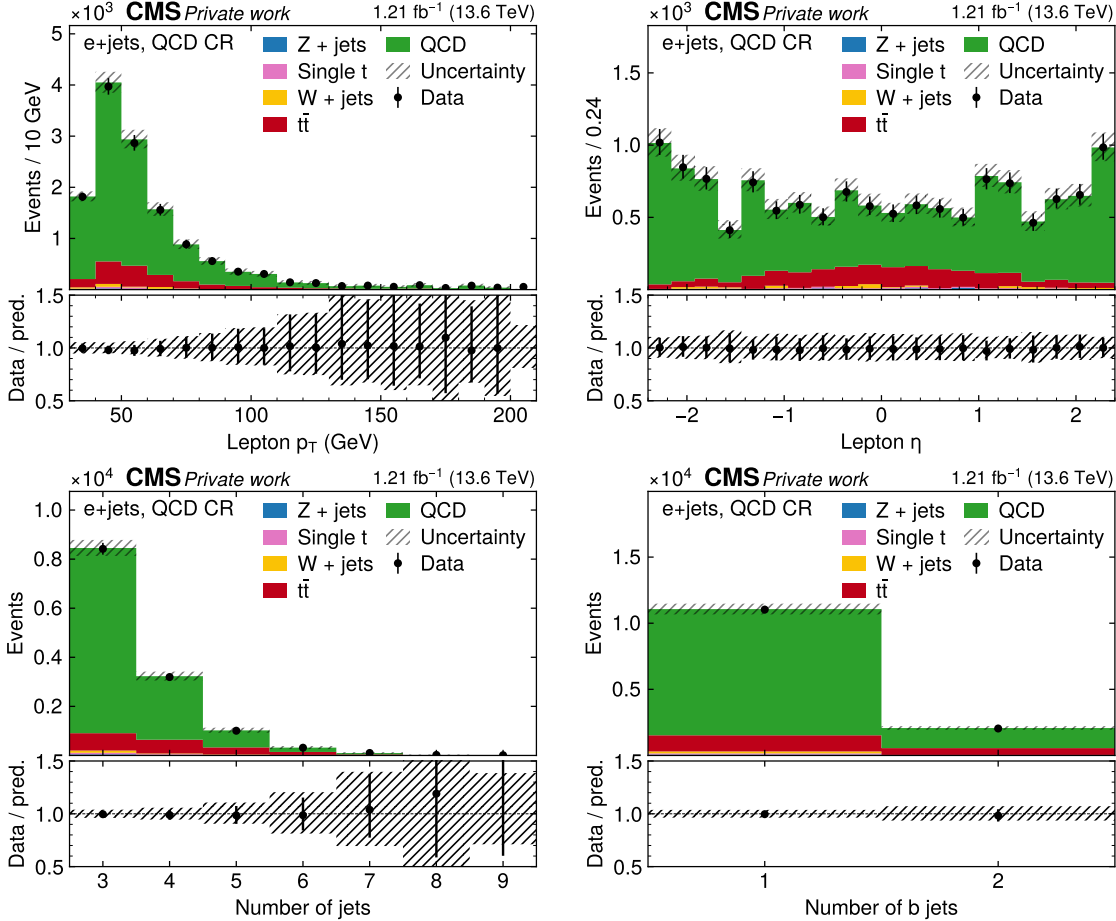


Figure 6.8: **QCD control region for e+jets.** Distributions in the QCD CR for the e+jets channel, same as in Fig. 6.7. The difference between data and MC prediction is considered QCD background and shown in green.

One sets for the SR

$$N_{\text{SR}}^{\text{data}} = N_{\text{SR}}^{t\bar{t}} + N_{\text{SR}}^{\text{MC,BG}} + N_{\text{SR}}^{\text{QCD}} \quad (6.5)$$

and similarly for the QCD CR

$$N_{\text{CR}}^{\text{data}} = N_{\text{CR}}^{t\bar{t}} + N_{\text{CR}}^{\text{MC,BG}} + N_{\text{CR}}^{\text{QCD}}, \quad (6.6)$$

where N^{data} is the total data yield, $N^{t\bar{t}}$ is the $t\bar{t}$ signal contribution, $N^{\text{MC,BG}}$ is the contribution of non-QCD backgrounds as predicted by MC, and N^{QCD} is the QCD contribution. It is assumed that the ratio f_{sig} of signal events in the QCD CR and SR (but not necessarily the normalization) is correctly predicted by MC:

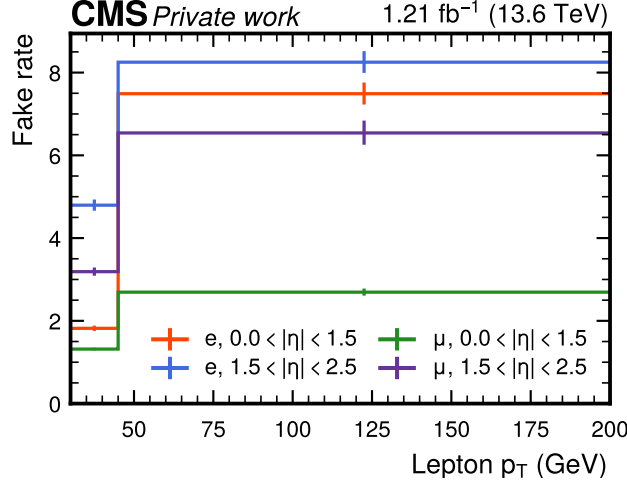


Figure 6.9: **QCD fake rate.** The fake rate for the QCD background estimated in the 1 jet bin, separately for electrons and muons as, a function of lepton p_T and $|\eta|$. The error bars designate statistical uncertainties only.

$$f_{\text{sig}} := \frac{N_{\text{CR}}^{\text{t}\bar{t}}}{N_{\text{SR}}^{\text{t}\bar{t}}} = \frac{N_{\text{CR}}^{\text{t}\bar{t}, \text{MC}}}{N_{\text{SR}}^{\text{t}\bar{t}, \text{MC}}} \quad (6.7)$$

This is equivalent to assuming that the relative isolation I_{rel} used to separate the QCD CR and SR is well-described in $t\bar{t}$ simulation. Furthermore, one sets similar to Eq. (6.4)

$$N_{\text{SR}}^{\text{QCD}} = N_{\text{CR}}^{\text{QCD}} \times f_{\text{fake}} \quad (6.8)$$

where f_{fake} is still given by Eq. (6.3), which is unaffected since the $t\bar{t}$ signal contamination in the 1-jet CR is negligible.

Combining all these equations, one can first replace $N_{\text{CR}}^{\text{t}\bar{t}}$ in Eq. (6.6) by $f_{\text{sig}} N_{\text{SR}}^{\text{t}\bar{t}}$ according to Eq. (6.7); further replace $N_{\text{CR}}^{\text{QCD}}$ by $N_{\text{SR}}^{\text{QCD}} / f_{\text{fake}}$ according to Eq. (6.8); and then combine Eq. (6.5) and Eq. (6.6) to eliminate $N_{\text{SR}}^{\text{t}\bar{t}}$ in favor of $N_{\text{SR}}^{\text{data}}$, i.e. the total data yield in the SR. This gives

$$N_{\text{SR}}^{\text{QCD}} = f_{\text{fake}} \left(N_{\text{CR}}^{\text{data}} - N_{\text{CR}}^{\text{MC,BG}} - f_{\text{sig}} \left(N_{\text{SR}}^{\text{data}} - N_{\text{SR}}^{\text{MC,BG}} - N_{\text{SR}}^{\text{QCD}} \right) \right). \quad (6.9)$$

Solving this equation for $N_{\text{SR}}^{\text{QCD}}$ finally yields the corrected QCD contribution in the SR:

$$N_{\text{SR}}^{\text{QCD}} = \left(N_{\text{CR}}^{\text{data}} - N_{\text{CR}}^{\text{MC,BG}} - f_{\text{sig}}(N_{\text{SR}}^{\text{data}} - N_{\text{SR}}^{\text{MC,BG}}) \right) \times \frac{f_{\text{fake}}}{1 - f_{\text{sig}}f_{\text{fake}}} \quad (6.10)$$

The resulting QCD distributions from this method are further treated in the same way as the MC backgrounds, and can be seen together with them in Figs. 6.10 to 6.12.

Z+jets background In contrast to the QCD background, the Z+jets background is generally well-described by MC simulation. However, in the considered phase space, the requirement of at least one reconstructed b jet can introduce modeling challenges, as b quarks are treated as massless at the matrix-element level. This approximation may lead to inaccuracies in the predicted kinematic properties of b quarks compared to those observed in data.

Here, a data-driven normalization is derived for Z+jets events with one or two b tags in the dilepton channels, following the method of Ref. [71]. This is important especially in the same-flavor channels, where Z+jets is a dominant background.

The normalization is derived using a CR in which the cut on $m_{\ell\ell}$ is inverted, i.e. in events with $|m_{\ell\ell} - m_Z| < 15$ GeV (“inside the Z window”), which are strongly enriched in Z+jets contributions. It is assumed that the Z+jets contribution in the eμ channel (which stems mostly from $Z \rightarrow \tau\tau$ events) is negligible compared to the ee and μμ channels, and that all other backgrounds (including $t\bar{t}$) are approximately equal in the three dilepton channels up to combinatorics, in the sense that their differences are small compared to the Z+jets event yield. Then, said Z+jets yield in the Z window in the same-flavor channels can be estimated directly from data by subtracting the eμ channel – and with it, the other backgrounds – from the ee and μμ channels. This results in

$$N_{\text{ee}/\mu\mu}^{\text{Z+jets}} = N_{\text{ee}/\mu\mu, \text{in}}^{\text{data}} - \frac{1}{2} N_{\text{e}\mu, \text{in}}^{\text{data}} k_{\text{ee}/\mu\mu, \text{in}} \quad (6.11)$$

where $N_{\ell\ell, \text{in}}^{\text{data}}$ refers to the number of observed events inside the Z window for the respective channel, the factor $\frac{1}{2}$ comes from the fact that the branching ratio of $t\bar{t}$ to eμ is twice that to ee or μμ, and $k_{\text{ee}} = k_{\mu\mu}^{-1} = \sqrt{N_{\text{ee, in}}^{\text{data}}/N_{\mu\mu, \text{in}}^{\text{data}}}$ is an efficiency factor to correct for the different acceptance of electrons and muons.

To estimate the Z+jets background in the SR, the ratio $R_{\text{in/out}} = N_{\text{in}}^{\text{Z+jets}}/N_{\text{out}}^{\text{Z+jets}}$, defined as the number of Z+jets events inside and outside the Z mass window, needs to be determined. While this ratio could be taken directly from simulation (as done in Refs. [22, 171]), it may be inaccurately modeled in MC. To reduce potential bias, a more conservative strategy is adopted. A second CR with zero b-tagged jets, which is not used in the main measurement for the same-flavor channels, is introduced to estimate the ratio under looser assumptions:

channel	ee	e μ	$\mu\mu$
scale factor	1.36 ± 0.04	1.32 ± 0.03	1.28 ± 0.03

Table 6.6: **Z+jets scale factors.** Ratio of the Z+jets event yields estimated in data using the method described in Sec. 6.3.2 to the prediction by the MC simulation. Uncertainties are statistical only.

$$\frac{R_{\text{in/out}}^{\text{data}}(\geq 1 \text{ b tag})}{R_{\text{in/out}}^{\text{MC}}(\geq 1 \text{ b tag})} = \frac{R_{\text{in/out}}^{\text{data}}(0 \text{ b tags})}{R_{\text{in/out}}^{\text{MC}}(0 \text{ b tags})} \quad (6.12)$$

This equation means that the *ratio of ratios* $R_{\text{in/out}}(\geq 1 \text{ b tag})/R_{\text{in/out}}(0 \text{ b tags})$ is assumed to be well described by MC. It can be solved for the Z+jets yield outside of the Z window in the same-flavor channels, yielding

$$\begin{aligned} N_{\text{out}}^{\text{Z+jets}} &= \frac{N_{\text{in}}^{\text{Z+jets}}}{R_{\text{in/out}}^{\text{data}}(\geq 1 \text{ b tag})} \\ &= \frac{R_{\text{in/out}}^{\text{MC}}(0 \text{ b tags})}{R_{\text{in/out}}^{\text{data}}(0 \text{ b tags})} \frac{N_{\text{in}}^{\text{Z+jets}}}{R_{\text{in/out}}^{\text{MC}}(\geq 1 \text{ b tag})} \end{aligned} \quad (6.13)$$

where $N_{\text{in}}^{\text{Z+jets}}$ is given by Eq. (6.11). In practice, this yield is quoted as a scale factor compared to the nominal MC prediction. For the e μ channel (in which Z+jets is much less important), the scale factor is simply assumed to be the geometric mean of the ee and $\mu\mu$ scale factors.

The final scale factors can be seen in Tab. 6.6.

6.4 Control distributions

The agreement between simulation and data in several control distributions is presented in Figs. 6.10 to 6.12. All corrections described in the previous section are applied in these figures. In addition, they are scaled by the b tagging efficiency scale factors obtained in the final likelihood fit (Sec. 6.6) to better reflect the estimates for essential calibrations.

Good agreement between data and simulation within the full uncertainties is seen in all distributions.

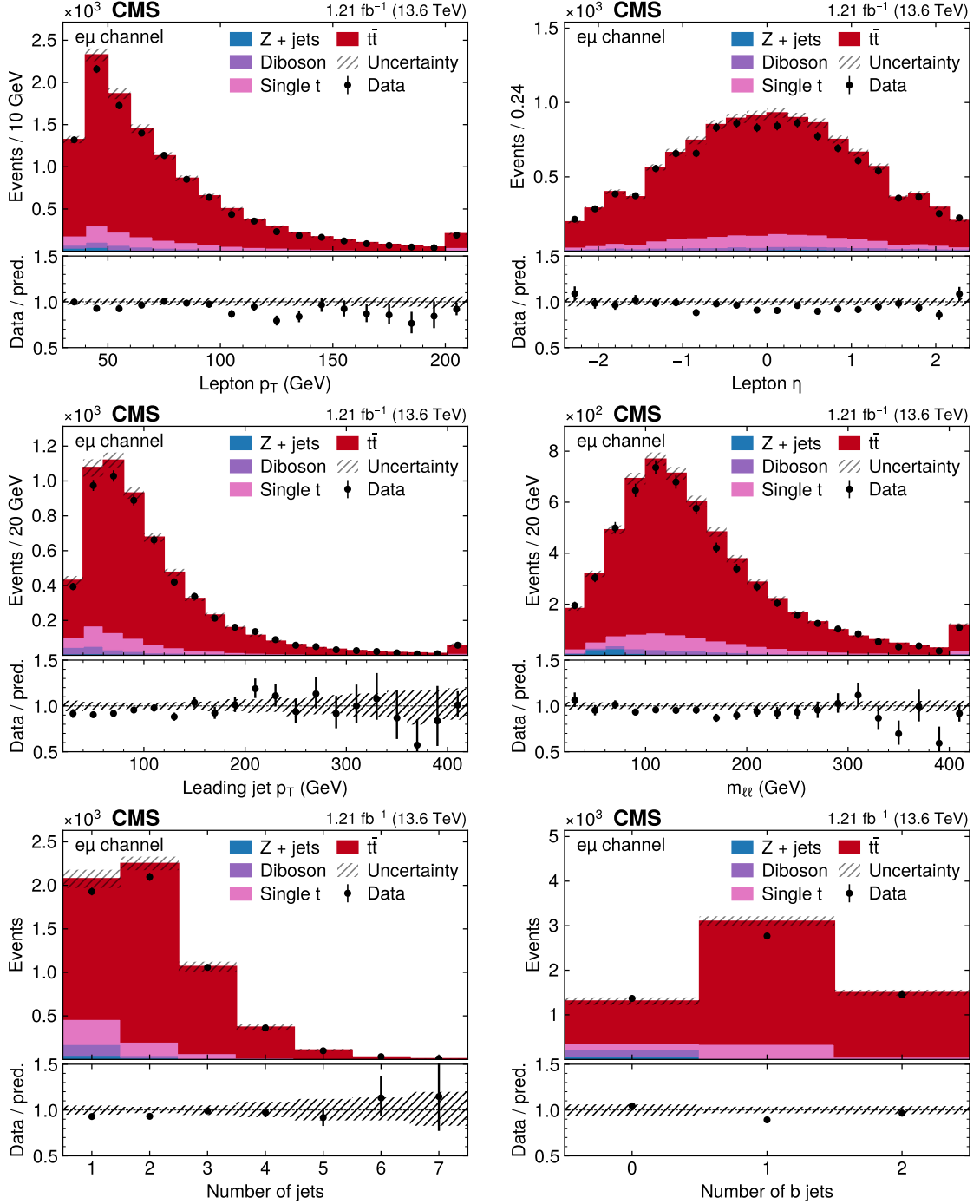


Figure 6.10: **Control distributions in the $e\mu$ channel.** Shown are (from top left to bottom right) the distributions of p_T of both leptons, $|\eta|$ of both leptons, p_T of the leading jet, the invariant lepton mass $m_{\ell\ell}$, the number of jets and the number of b jets. All figures show both data (black dots) and different simulated background processes (colored bars). For the latter, all corrections described in Sec. 6.3 as well as post-fit b tagging scale factors (Sec. 6.6) are applied, and the shaded area covers both statistical and systematic uncertainties [5].

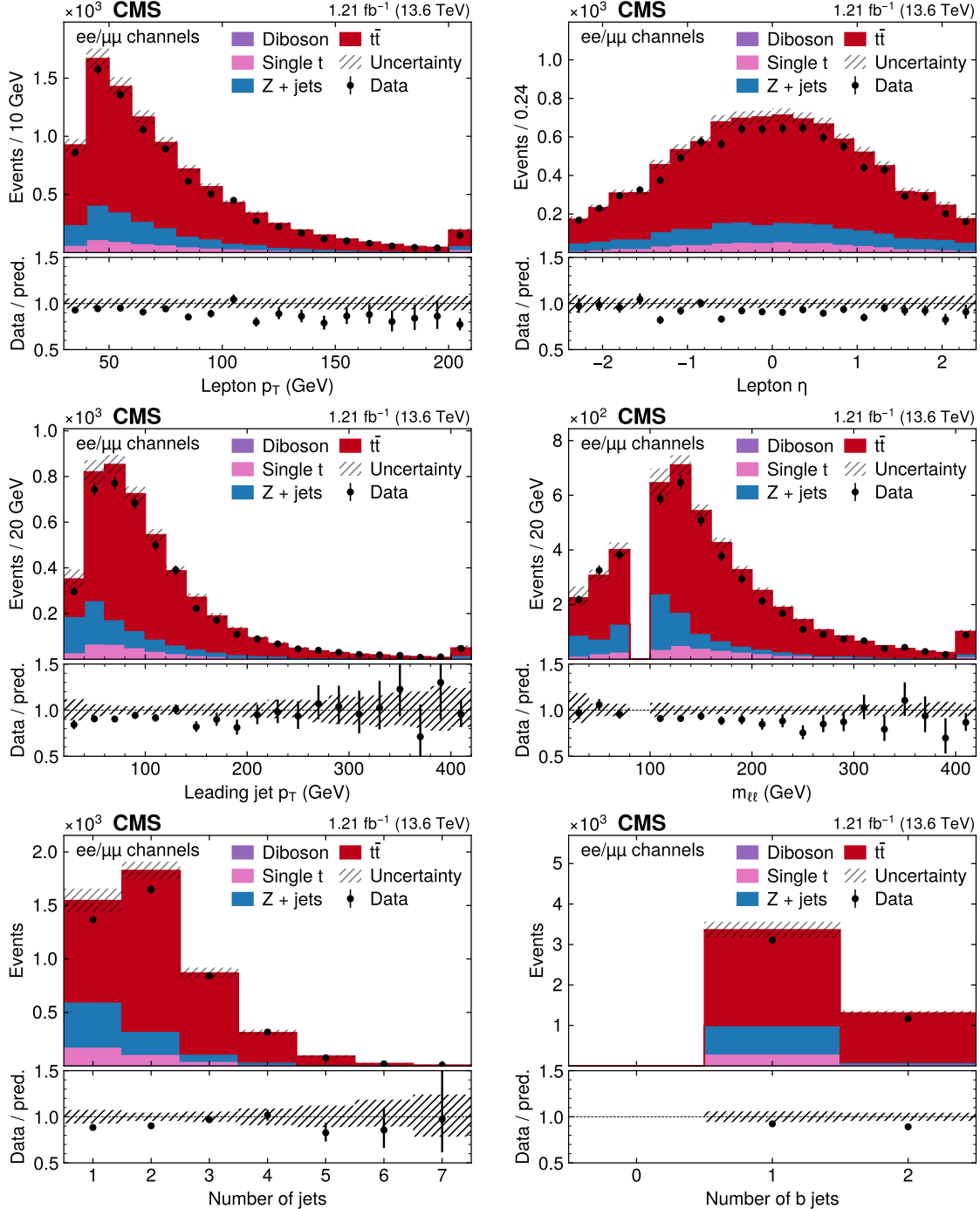


Figure 6.11: **Control distributions in the ee and $\mu\mu$ channels.** The distributions are shown in the same manner as in Fig. 6.10 [5].

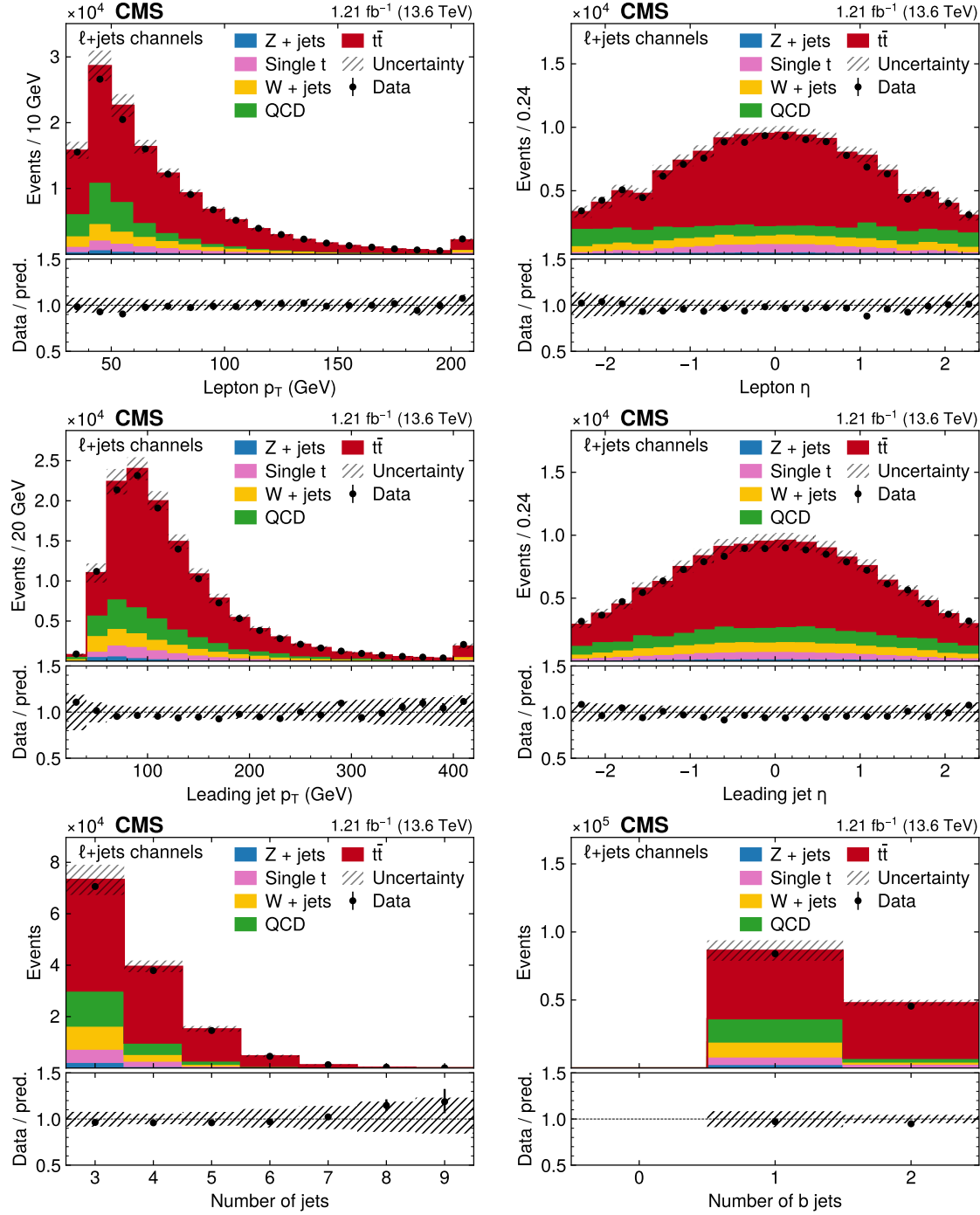


Figure 6.12: **Control distributions in the $\ell+\text{jets}$ channels.** The distributions are shown in the same manner as in Fig. 6.10, except for the center-right figure, which here shows $|\eta|$ of the leading jet [5].

6.5 Systematic uncertainties

In order to translate the distribution of observed and expected events into a result for the inclusive $t\bar{t}$ cross section while taking into account all relevant sources of systematic uncertainties, a binned profile maximum likelihood fit as described in Chapter 5 is performed using the tool `combine` [153]. The parameter of interest (POI) used for this fit is the signal strength $r = \sigma_{t\bar{t}}/\sigma_{t\bar{t}}^{\text{pred}}$, i.e. the inclusive $t\bar{t}$ cross section normalized to its theoretical prediction. A linear signal model is used as defined in Eq. (5.3), and the $t\bar{t}$ cross section is extracted using its maximum likelihood estimate and uncertainty.

This section describes the considered systematic uncertainties, which can be divided into experimental uncertainties, arising from incomplete knowledge of the details of the detector and resulting differences between data and simulation, and theoretical uncertainties, which concern imperfect modeling of the underlying physical processes in the different event generators.

All systematic uncertainties are included in the fit as nuisance parameters (NPs) as discussed in Chapter 5. In practice, NPs which encode shape effects on the considered observables are implemented using *template morphing*, i.e. a smooth polynomial interpolation between the nominal shape and the shapes encoding the variations by ± 1 standard deviations. NPs that encode only normalization effects are instead implemented as simple log-normal uncertainties. Both definitions can be found in detail in Ref. [153].

Special attention is given in this section to some experimental uncertainties which are important to this measurement. This includes the luminosity, which is the dominating uncertainty, as well as the b tagging uncertainties due to the special way they are treated in the fit.

Luminosity uncertainty In order to translate event yields into a result on any cross section, the total integrated luminosity is required as a calibration constant. Any experimental error on the luminosity will be directly transferred to the total error on the measurement, and thus minimizing the luminosity uncertainty is crucial for any cross section measurement.

For the data set used in this analysis, the total integrated luminosity was measured by the CMS Collaboration with an estimated uncertainty of 2.3%. Of this number, 2.1% is due to the calibration of the integrated luminosity, using the methods presented in Ref. [146].

The agreement in the absolute scale is checked by comparing different independently calibrated luminosity measurements. The integrated luminosity measured with the hadronic forward calorimeter and the silicon pixel detector is found to agree at a level of better than 0.8% [5]. Accounting for residual differences in time stability and linearity between the luminosity detectors results in a total uncertainty of 2.3%. This preliminary estimate of the integrated luminosity at the time of publication

was further validated using the yield of reconstructed Z bosons decaying into muon pairs [172]. After correcting for efficiencies and normalizing to the fiducial cross section predicted at NNLO with next-to-NNLL corrections, good agreement was observed.¹

In contrast to all other uncertainties described below, the uncertainty in the integrated luminosity is not directly included in the likelihood fit, but rather treated as an external uncertainty and added in quadrature afterwards, since it is expected to factorize completely from all other uncertainties. The impact of varying the normalization of the backgrounds estimated from simulation by the integrated luminosity uncertainty was found to be negligible.

b tagging uncertainty As mentioned in Sec. 6.3.1, the efficiency for correctly identifying a jet originating from a b quark (b tagging) is expected to be different in data and simulation. At the time of this measurement, directly after the start of Run 3, no general-purpose b tagging studies had been available. Thus, the approach adopted here is to consider the b tagging efficiency in data to be completely unknown and measure it concurrently with the cross section in the likelihood fit.

For this purpose, the probability for an event with n_{jet} selected jets to have n_{btag} correctly identified b jets, depending on the assumed b tagging efficiency ϵ_b , is assumed to be a multinomial of the form

$$P(n_{\text{btag}}|n_{\text{jet}}) \propto \epsilon_b^{n_{\text{btag}}} (1 - \epsilon_b)^{n_{\text{no tag}}} \quad (6.14)$$

Here, $n_{\text{no tag}}$ is the number of true b jets in the event which fall into the acceptance of the selection, but fail to be tagged by DEEPJET. It is estimated from MC simulation.

By taking the ratio of eq. 6.14 in data and simulation, one can derive a per-event weight which corrects the number of b tags in MC:

$$w_b = \frac{(\epsilon_b^{\text{data}})^{n_{\text{btag}}} (1 - \epsilon_b^{\text{data}})^{n_{\text{no tag}}}}{(\epsilon_b^{\text{MC}})^{n_{\text{btag}}} (1 - \epsilon_b^{\text{MC}})^{n_{\text{no tag}}}} = (f_b)^{n_{\text{btag}}} \left(\frac{1 - f_b \epsilon_b^{\text{MC}}}{1 - \epsilon_b^{\text{MC}}} \right)^{n_{\text{no tag}}} \quad (6.15)$$

Here, $f_b = \epsilon_b^{\text{data}} / \epsilon_b^{\text{MC}}$ is the unknown b tagging scale factor. It is left freely floating in the likelihood fit. This is technically implemented by producing shape templates from MC with f_b varied up and down by a fixed value and interpolating in between. This shape template can be seen in Fig. 6.13, where it is evident that the categorization in the number of b tags gives significant constraining power for f_b . In the 1b categories, the shape with respect to the number of jets deviates significantly from a flat variation proportional to f_b . This is because of out-of-acceptance jets, corresponding to the second factor in Eq. (6.15).

¹Since publication of this result, a more precise luminosity measurement for 2022 data has become available in Ref. [173].

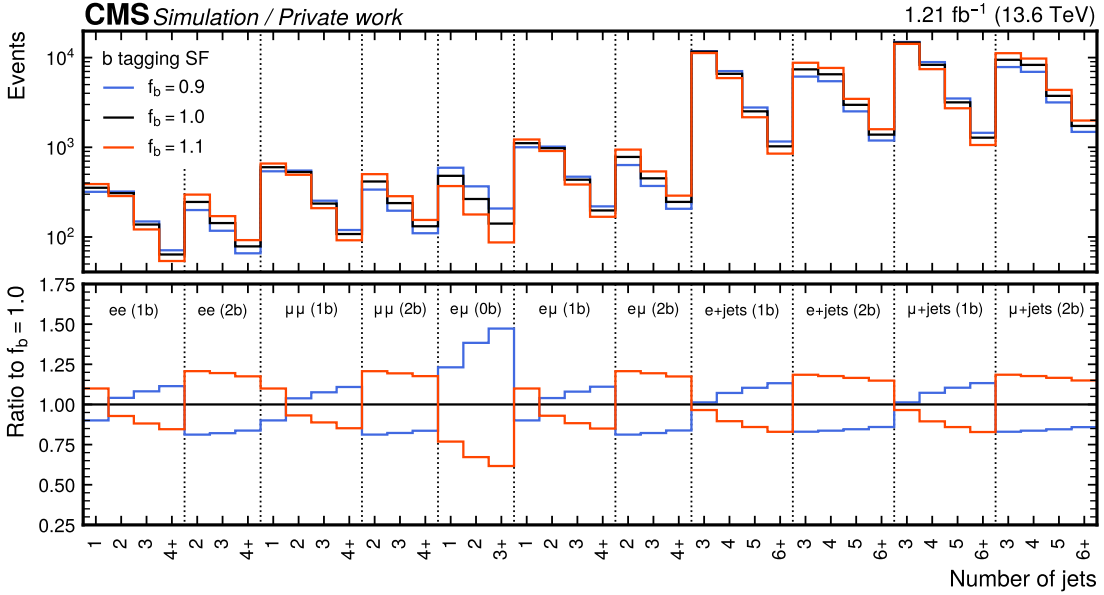


Figure 6.13: **b tagging scale factor variation.** The effect of varying the b tagging scale factor f_b in $t\bar{t}$ MC by an arbitrary value of ± 0.1 , shown for the number of jets in the 11 fit categories.

Note that, since f_b is taken to be a single number, this method only corrects the overall b jet efficiency and does not consider any dependence of ϵ_b on jet kinematics. Because this measurement uses the same jet quality requirements (particularly the same p_T cuts) in all channels, and assuming that the b jet p_T and η spectra in the different channels are roughly similar, any kinematic dependence is effectively integrated out in the overall efficiency scale factor f_b . The lack of corrections to the spectrum is not considered as problematic in this context since the likelihood fit does not rely directly on kinematic information.

Lepton identification uncertainty The uncertainty assumed on the lepton identification scale factors comes from two different sources: First, an inherent uncertainty originating in the tag-and-probe method (as described in Sec. 6.3.1) is considered. It consists of statistical uncertainties from both data and simulation, a systematic uncertainty derived from a comparison with a different Z+jets simulation sample produced at NLO in QCD, and another systematic uncertainty due to the choice of fitting function. Together, they make up for an uncertainty of $\sim 0.8\%$ (0.5%) on the electron (muon) scale factors in the bulk of the phase space, and can rise up towards $\sim 5\%$ for high lepton p_T .

Secondly, it is taken into account that the scale factor between data and simulation might be slightly different in the Z+jets selection used for the tag-and-probe method

and the $t\bar{t}$ selection used for the measurement of the cross section. The most important reason for this is the requirement of (b tagged) jets in almost all considered categories, as well as the requirement for at least three jets in the lepton+jets channels. This effect has been studied at CMS in the past and the difference found to be less than 0.5% for muons and 1.0% for electrons. Taking a conservative approach, these values are used as an additional component in the respective uncertainties.

In the first, preliminary version of this measurement [156], the dedicated lepton efficiency scale factors as measured with the tag-and-probe method were not yet available, and a different approach was taken. Similar to the b tagging efficiency, the lepton efficiency scale factors were kept freely floating the likelihood fit. Due to the different dependency on the lepton efficiencies in the different lepton flavor channels, the fit was able to constrain the efficiencies to a precision of 2% [5]. The resulting scale factors were later found to be in good agreement with those obtained from the tag-and-probe method, serving as a valuable cross-check and showing the power of the channel combination to constrain the lepton efficiencies. However, this method ultimately led to less precision and was thus not used in the final result.

Pileup uncertainty As described in Sec. 6.3.1, three different pileup-related variables are employed to reweight the simulation to the observed data, and the average of the three weights is used as the nominal value. This method is repeated using only one of the variables - the number of good reconstructed vertices n_{PV} - and the difference in expected yields is treated as an uncertainty. This procedure was compared to the usual estimation of pileup-related uncertainties in CMS since the latter was not yet available in Run 3. There, the theoretical expectation for the number of interactions is taken as the product of the instantaneous luminosity and the total inelastic cross proton-proton cross section of $69.2(32)$ mb at $\sqrt{s} = 13$ TeV [146]. It was found that the heuristic method used here leads to larger uncertainties than the one from the inelastic cross section, and can thus be considered more conservative.

Jet energy uncertainties Uncertainties in the jet energy calibration are split into 26 different sources concerning different experimental and theoretical effects, following the standard CMS procedure outlined in Ref. [167]. 17 of these sources are found to be non-negligible and included in the fit, while the others are indistinguishable from fluctuations due to limited MC statistics. The non-negligible sources include, among others, uncertainties due to jet p_T resolution and jet flavor composition, statistical uncertainties in the derivations of the energy corrections, and residual differences between data and simulation.

Trigger uncertainties Since the trigger scale factors are derived using the tag-and-probe method in the same way as the lepton scale factors, similar uncertainties are applied, including the uncertainties of 0.5% for muons and 1.0% for electrons due

to extrapolation between $Z + \text{jets}$ and $t\bar{t}$ topologies. The only difference is that in the dilepton channels the uncertainties need to be propagated according to Eq. (6.2). This has the effect of greatly reducing the impact of the trigger uncertainties in those channels compared to the lepton ID uncertainties, since the nominal per-event trigger efficiency is already very close to one.

Matrix element scale uncertainties The theoretical predictions of both signal and background are calculated using matrix elements at either LO or NLO in perturbative QCD, matched to a parton shower. Since this effectively means truncating the perturbative expansion of the scattering amplitude at a given power in the strong coupling constant, the effect of higher-order terms is neglected in the calculation.

At the same time, the necessity of renormalization of divergent diagrams and factorization of non-perturbative contributions introduces non-physical parameters into the prediction in the form of the renormalization and factorization scales μ_R and μ_F , respectively (cf. Sec. 4.1). These parameters are usually set to typical energy scales of the considered process, and might also depend on the event kinematics (dynamic scales).

To estimate possible uncertainties due to these missing terms as well as due to the choice of scales, the scales μ_R and μ_F are varied separately by a factor of 2 up and down, and the resulting change in simulation is taken as an uncertainty in the form of shape templates [174]. To avoid double-counting uncertainties in the background cross section predictions (see below) while still accounting for possible rate variations due to acceptance effects, the templates are normalized to the nominal cross section values before applying any selection cuts.

PDF uncertainties The PDFs used to evaluate the non-perturbative contribution of the proton-proton collision have systematic uncertainties attached. They are estimated by independently reweighting the simulation to 100 different replicas of the used NNPDF 3.1 PDF set and taking the envelope of the resulting changes, following the recommendations of the PDF4LHC working group [175]. Additionally, the effect of the choice of the strong coupling constant in the PDF is assessed using a similar reweighting, and attached as a separate nuisance parameter. Analogously to the matrix element uncertainties, the resulting variations are normalized before any selection cuts to keep acceptance and shape effects while not double-counting cross section changes.

Parton shower uncertainties The parton shower model used for the predictions is only accurate (at most) at LL and leading color in QCD (cf. Sec. 4.2) and thus requires appropriate uncertainties. For this purpose, the scales at which the strong coupling constant is evaluated are varied up and down by a factor 2 separately for

initial and final state radiation and for different processes, and the resulting changes are propagated to the fit as shape templates.

ME/PS matching uncertainty For the simulation of the $t\bar{t}$ signal, an additional uncertainty concerning the matching between matrix element simulation in POWHEG and parton showering in PYTHIA is considered. This is done by varying the h_{damp} parameter in POWHEG controlling the amount of radiation generated at matrix element level, following Ref. [176].

Top quark p_T uncertainty It has been shown in previous measurements of $t\bar{t}$ differential cross sections that the p_T spectrum of the top quark is significantly softer in data than in the standard POWHEG MC simulation [177–179]. This effect is propagated to the p_T spectra of the top decay products and can thus lead to misestimation of the acceptance due to lepton and b jet p_T requirements. Fixed-order predictions at NNLO in QCD and NLO in EW are known to largely alleviate the discrepancy [180]. Thus, a common strategy is to reweight the top quark p_T spectrum in MC simulation to the one extracted from such fixed-order predictions.

At the time of the measurement, fixed-order predictions at NNLO in QCD and NLO EW were available only for $\sqrt{s} = 13$ TeV and could not be directly applied to the MC simulation at $\sqrt{s} = 13.6$ TeV. Instead, the simulation is left uncorrected for the nominal prediction, and a variation is constructed by calculating the ratio of the fixed-order prediction from Ref. [180] and the POWHEG MC simulation at $\sqrt{s} = 13$ TeV, and applying it to the POWHEG MC simulation at $\sqrt{s} = 13.6$ TeV. The difference between uncorrected prediction and the variation is assigned as an additional uncertainty, which is one-sided by construction.

Background cross section uncertainties For the cross sections of the different processes, log-normal rate uncertainties are assigned based on the process and order at which it was calculated. Separate 15% uncertainties are used for the t -channel single-top and tW backgrounds since they are generated at NLO with a NNLO prediction for the cross section, while for W+jets and Diboson, 30% is used since these samples are only generated at LO. For Z+jets, this is reduced to 20% due to the data-driven estimation of the normalization as described in Sec. 6.3.2. Additionally, for the fully data-driven QCD background, two separate nuisance parameters for the e+jets and μ +jets channels are defined, covering a conservative uncertainty of 30% each.

Background statistical uncertainties Finally, since the background in this measurement is estimated either using MC simulation or data-driven methods, an independent statistical uncertainty needs to be attached to each bin, reflecting the finite number of events it contains. This is done using the so-called *Barlow–Beeston*

light method [181]. For MC backgrounds, these uncertainties are minuscule. However, for the data-driven QCD background, they also contain the propagated statistical uncertainty due to the limited number of data events in the CRs, which is in general non-negligible.

6.6 Fit results

Performing the fit yields a $t\bar{t}$ signal strength of $r = 0.953 \pm 0.025$, where the uncertainty includes statistical and all systematic contributions, except for the 2.1% uncertainty on the luminosity. This corresponds to an inclusive $t\bar{t}$ cross section of

$$\sigma_{t\bar{t}} = 881 \pm 23 (\text{stat+syst}) \pm 20 (\text{lumi}) \text{ pb}.$$

The result is in good agreement with the standard model prediction of $\sigma_{t\bar{t}}^{\text{pred}} = 924^{+32}_{-40} \text{ pb}$.

Fig. 6.14 shows the agreement between data and simulation before and after the fit. It can be immediately seen that the fit greatly reduces the uncertainty on the prediction by constraining systematic uncertainties and simultaneously improves the agreement compared to the data.

Of particular note here is the free-floating b tagging efficiency (compare sec. 6.5), whose effect can be directly read off from the categorization in the number of b jets: Before the fit (Fig. 6.14 top), the event yield for two or more b jets is overestimated in the simulation, while the yield for zero b jets is underestimated. This suggests that the b tagging efficiency is slightly lower in the data than assumed in the simulation. Indeed, the fit confirms this: the b tagging scale factor between data and simulation in the phase space of this measurement is measured to be $f_b = 0.980 \pm 0.009$. As a result, after the fit (Fig. 6.14 bottom), the event yields agree in all b jet categories.

6.6.1 Statistical checks

To better understand the sources of systematic uncertainty, as well as the contributions of the different measurement channels, the fit is repeated twice, restricted to either the dilepton or the $\ell+\text{jets}$ channels. For both cases as well as the combination, the contribution of different groups of nuisance parameters is calculated by freezing the groups to their postfit values and repeating the fit, as explained in Chapter 5. It should be noted that this procedure does not take into account correlations between the groups, and thus the sum in quadrature of the separate components will in general not add up to the total uncertainty.

The results can be found in Tab. 6.7, where it can be seen how the combination of channels helps to reduce the total uncertainty: in the dilepton channels, the dominating uncertainties are the lepton identification uncertainty, which enters twice compared to the $\ell+\text{jets}$ channels, as well as the statistical uncertainty of the data

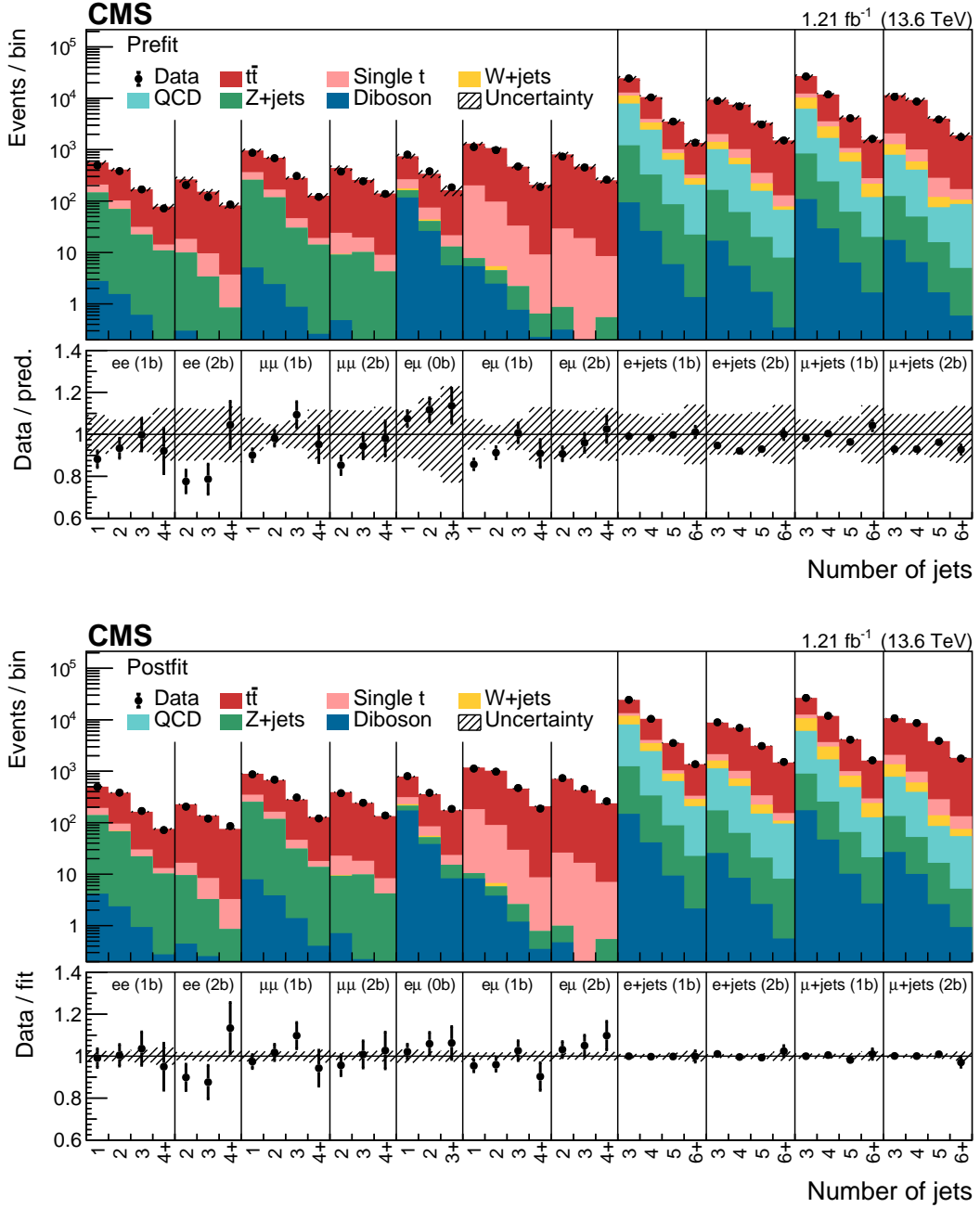


Figure 6.14: Comparison of data and simulation before and after the fit.
 The distribution of the number of jets in the different fit categories is shown for data and simulation before (top) and after the likelihood fit (bottom). The fit greatly improves the agreement and strongly constrains the background uncertainties [5].

Source	Full measurement	dilepton only	$\ell+$ jets only
Lepton ID efficiencies	1.6	2.2	1.0
Trigger efficiency	0.3	<0.1	0.5
JES	0.6	0.7	1.1
b tagging efficiency	1.1	0.8	2.1
Pileup reweighting	0.5	0.2	1.1
ME scale, $t\bar{t}$	0.5	0.4	0.5
ME scale, backgrounds	0.2	0.1	0.3
ME/PS matching	0.1	0.4	0.7
PS scales	0.3	0.5	0.4
PDF and α_S	0.3	0.4	0.4
Top quark p_T	0.5	0.3	0.5
tW background	0.7	1.0	0.4
t -channel single-t background	0.4	<0.1	0.5
Z+jets background	0.3	0.2	<0.1
W+jets background	<0.1	<0.1	0.2
Diboson background	0.6	0.6	<0.1
QCD multijet background	0.3	—	0.5
Statistical uncertainty	0.5	1.2	0.5
Combined uncertainty	2.6	3.4	3.3
Integrated luminosity	2.3	2.3	2.3

Table 6.7: **Sources of systematic uncertainty.** The relative per-cent contribution of different groups of sources of systematic uncertainty for the full measurement as well as for restrictions to the dilepton and $\ell+$ jets channels only. They are calculated according to Chapter 5 and do not take correlations between the different groups into account.

due to the relatively low branching ratio. In the $\ell+$ jets channels, b tagging, JES, and pileup uncertainties dominate, reflecting the less clean selection and increased importance of jets. When the channels are combined, the uncertainty contribution of these groups lies in between the two separate numbers, showing how the channel combination represents a trade-off between the advantages and disadvantages of either channel.

Furthermore, the nuisance parameter pulls, constraints and impacts, as defined in Chapter 5, are shown in Fig. 6.15 for the channel combination. One can see how the electron identification scale factors, which are the leading impact, are constrained by the combination of channels, while the same is not true of the muon identification scale factors due to their lower prefit uncertainty.

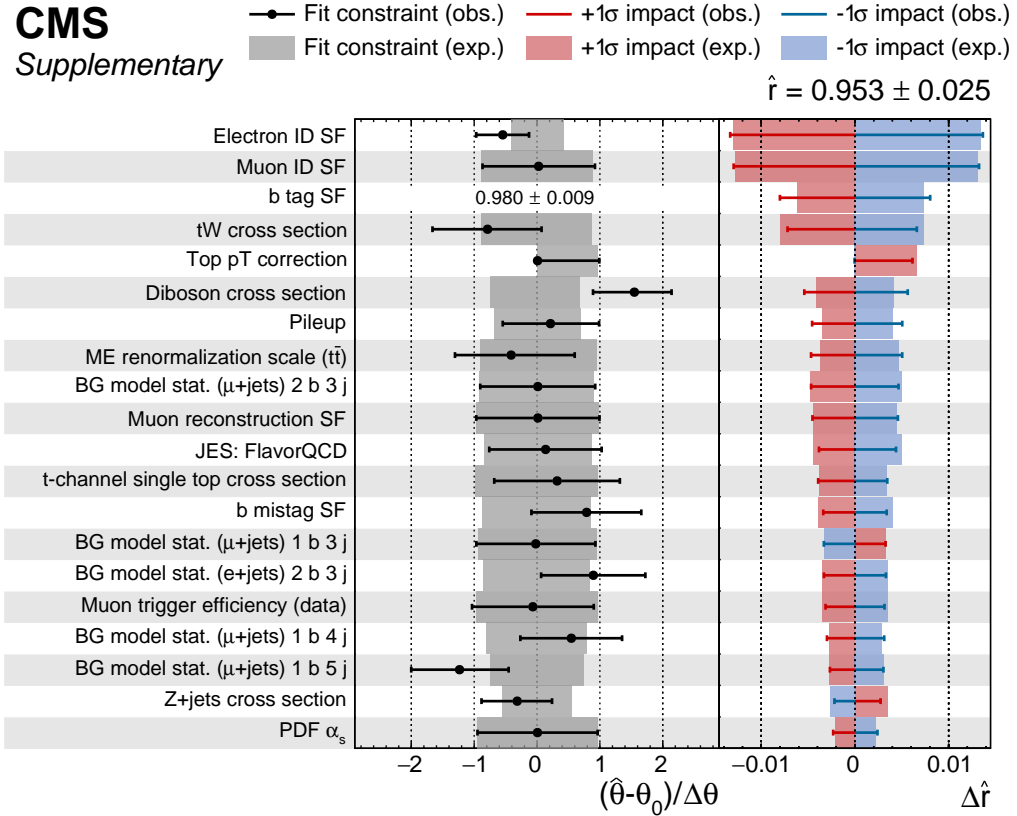


Figure 6.15: **Nuisance parameter pulls, constraints and impacts.** The expected and observed values are shown as shaded bands and error bars, respectively. Nuisance parameters are sorted by their observed impact on the signal strength r . For the b tagging scale factor, for which no prefit uncertainty is defined, the post-fit uncertainty is shown instead of the pull [5].

6.6.2 Top quark mass dependence

An additional source of uncertainty that has not been considered so far is the choice of top quark mass in the $t\bar{t}$ MC simulation. It affects the selection efficiency indirectly via the p_T cuts on leptons and jets, with higher top quark mass values leading to harder spectra and thus to larger efficiencies.

Contrary to other uncertainty sources, the top quark mass is not profiled in the likelihood fit. Instead, the dependence of the extracted $t\bar{t}$ cross section is explicitly quantified as a function of the top quark mass by shifting its value in simulation by ± 3 GeV from its default of $m_t = 172.5$ GeV. The extraction of $\sigma_{t\bar{t}}$ is then repeated and the dependence on m_t extracted through a simple linear fit. This strategy has been taken in previous CMS and ATLAS $t\bar{t}$ cross section measurements [182, 183],

and thus facilitates comparison with previous results.

For an upwards shift of $\Delta m_t = 1 \text{ GeV}$, the $t\bar{t}$ cross section is found to shift downwards by 8.5 pb, and vice versa. If one takes the current experimental uncertainty of 0.3 GeV [13] as an allowed range for m_t , this would lead to an additional uncertainty on $\sigma_{t\bar{t}}$ of 0.3%.

6.7 Summary and Outlook

In this chapter, the inclusive $t\bar{t}$ cross section is measured for the first time at a center-of-mass energy of $\sqrt{s} = 13.6 \text{ TeV}$. Data corresponding to an integrated luminosity of 1.21 fb^{-1} from the beginning of LHC Run 3 are analyzed. Despite this comparatively small amount of data, a total precision of ca. 3% with respect to the inclusive cross section is achieved.

Fig. 6.16 compares the result of this chapter to other inclusive $t\bar{t}$ cross section measurements performed by CMS at other center-of-mass energies [182, 184–190], as well as to the SM prediction [191]. The precision is comparable to other measurements at $\sqrt{s} = 7, 8$, and 13 TeV , some of them with significantly higher integrated luminosities. All results are in agreement with the SM.

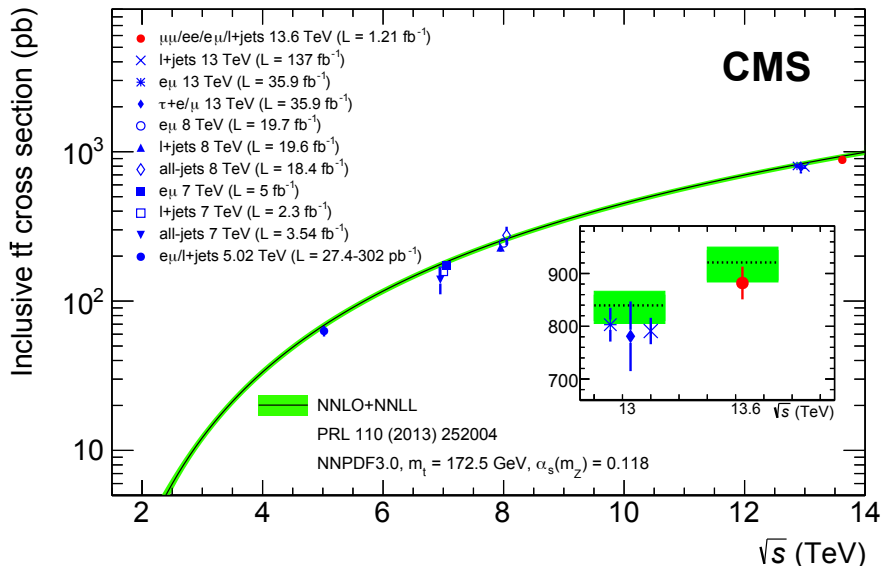


Figure 6.16: **Summary of $\sigma_{t\bar{t}}$ measurements.** An overview of inclusive $t\bar{t}$ cross section measurements at CMS at different center-of-mass energies [182, 184–190] as well as comparison to the SM prediction [191]. This measurement is displayed as the red dot [5].

This measurement was designed specifically for the earliest data of Run 3, in

order to achieve high precision without relying on a full suite of calibrations being available. In particular, b tagging and lepton efficiencies can be constrained *in situ* using the combination of dilepton and $\ell + \text{jets}$ channels as well as the categorization by number of b-tagged jets. No large inconsistencies for any of the considered physics objects were found. The measurement was made public in September of 2022 just two months after the start of Run 3 and constituted the first public physics result of LHC Run 3. At the time, it provided a valuable first proof that CMS data taken in Run 3 were of high quality and ready for physics.

The next step for this result would be to transfer the technique developed in this work to well-understood data and high integrated luminosities in order to achieve the highest precision possible for $\sigma_{t\bar{t}}$. Such a measurement will certainly be dominated by systematic uncertainties, most importantly due to integrated luminosity and the lepton identification efficiencies (as already partly the case here). The channel combination method developed here could potentially help reduce the latter uncertainty through an *in situ* constraint, while the former is independent of the analysis strategy and requires more precise luminosity measurements for improvement. In addition, a more detailed study of the individual sources of uncertainty will likely be necessary to assess whether some can be reduced through improved calibrations.

Additionally, one could try to use such a high-precision $t\bar{t}$ cross section measurement to indirectly measure the top quark mass, one of the fundamental parameters of the Standard Model, by comparing the measured value of $\sigma_{t\bar{t}}$ to SM predictions for different top quark masses. With this method, one could directly extract the pole mass of the top quark, which is a well-defined QFT parameter as opposed to the mass parameter in the default MC generators [192]. For this purpose, it would be important to reduce the dependence on the top quark mass in simulation (c.f. Sec. 6.6.2), for example by reducing the p_T requirements on leptons and jets as much as experimentally feasible. All of this leaves multiple parts for future studies to tread, which will be exciting to follow in the coming years as larger parts of the Run 3 data set are analyzed at CMS.

7 Simulation of on- and off-shell $t\bar{t}$ production with the Monte Carlo generator **bb41**

7.1 Introduction

The accurate modeling of top quark production processes at the LHC is of crucial importance for precision measurements of top quark properties. In particular, the fact the top quark is an unstable colored resonance with a short lifetime presents challenges for correctly modeling its mass line shape as used for top mass and width measurements [192–194].

Typically, the modeling is done with full NLO MC simulations matched to a parton shower (NLO+PS), and multiple such generators are available with different features and degrees of accuracy. As discussed in Sec. 4.1.2, this usually invokes the narrow-width approximation (NWA), where the top quarks are treated as stable in the computation of the matrix element, and their decays handled approximately afterwards. This has the disadvantage that the top quark mass used as an input to these generators can not be easily matched to a well-defined mass parameter in QFT such as e.g. the top quark pole mass [192]. As a result, direct top mass measurements using these generators can be difficult to interpret.

An alternative is presented by the MC generator **bb41** [6] as implemented in the Powheg Box framework (cf. Sec. 4.1), which calculates the full amplitude $pp \rightarrow b\bar{b}\ell^+\ell^-\nu_\ell\bar{\nu}_\ell$ and thus inherently treats the production and decay of $t\bar{t}$ on the same footing. As a result, it employs a well-defined top quark mass and width, and could be used to extract these in future measurements. At the same time, it is important for the modeling of the $t\bar{t}$ production threshold, at which off-shell top quarks appear naturally. **bb41** is used for this purpose in Chapter 8 of this thesis in the context of a search for $t\bar{t}$ bound state effects.

In this chapter, the predictions of **bb41** are compared to several other generators from the Powheg framework [126, 127] of lower accuracy, as well as to unfolded data measured in Ref. [195], for different variables relevant to top mass and/or width measurements. In the course of this, **bb41** is implemented and validated for the first time in the CMS simulation setup. The comparison is done at the generator level, i.e. including parton showering and hadronization but not detector simulation and experimental reconstruction.

The results of this work have been published in a CMS public note as Ref. [7]. Since

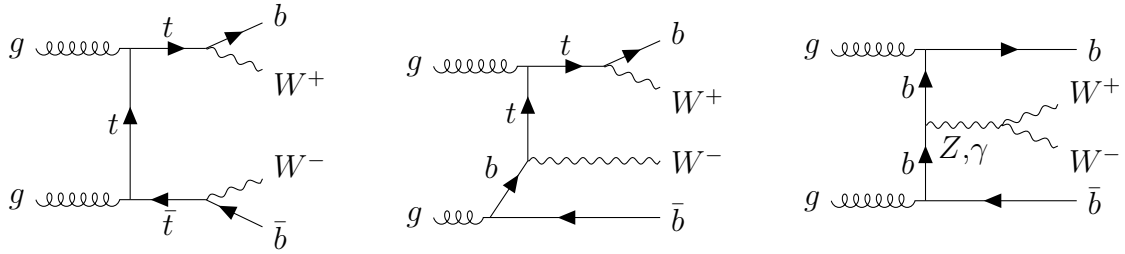


Figure 7.1: **Feynman diagrams for bb41.** Examples of Feynman diagrams for the $pp \rightarrow b\bar{b}W^+W^-$ process as described by bb41, including $t\bar{t}$ (left), tW (center) and non-top contributions (right). The decay of the W bosons into leptons is not shown for brevity.

the publication of this note, a new version of bb41 has been made available [196]. In this thesis, updated results including both versions will be shown.

7.2 The Monte Carlo generator bb41

bb41 [6, 196] is a full NLO+PS MC generator for the process $pp \rightarrow b\bar{b}\ell^+\ell^-\nu_\ell\bar{\nu}_\ell$, including all off-shell contributions. This includes the dilepton decay channel of both $t\bar{t}$ and tW production, as well as non-top contributions involving Z or Higgs bosons, as shown in Fig. 7.1. Since these processes all lead to the same final state at NLO in QCD, they interfere which each other and in principle cannot be separated. bb41 includes this interference by construction since it computes the full amplitude including all diagrams at once.

In addition, by considering the full amplitude instead of splitting it into production and decay, bb41 treats the top quark as an unstable resonance without approximations. The top quark is implemented as a Breit-Wigner propagator with the well-defined pole mass and width as input parameters. This is in contrast to MC generators for $t\bar{t}$ based on the NWA, such as the POWHEG Box subprocess `hvj` discussed in Sec. 4.1.2 and used in Chapter 6 for the measurement of the inclusive $t\bar{t}$ cross section. As such, bb41 is expected to improve the modeling of the top quark line shape compared to previously available generators.

A further difference between bb41 and NWA-based $t\bar{t}$ generators in the POWHEG Box framework is the treatment of real QCD emissions. As discussed in Sec. 4.1, in the POWHEG method of matching ME and parton shower, the hardest real QCD emission is already included almost always in the matrix element, while the second-hardest and further emissions are handled by the parton shower. For NWA-based $t\bar{t}$, where the top quarks are stable during event generation, this can mean initial state radiation (ISR) emitted off the gluons or quarks in the initial state or final state radiation (FSR) emitted off the top quarks, as shown in Fig. 7.2. The FSR

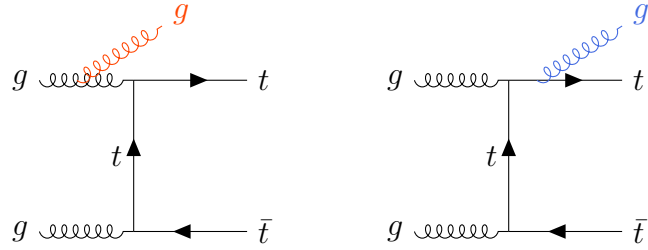


Figure 7.2: **Real emissions for $t\bar{t}$ in the NWA.** Examples of real emission diagrams in NWA-based ME generators for $t\bar{t}$. The left diagram shows an ISR emission (orange), and the right shows in FSR emission (blue).

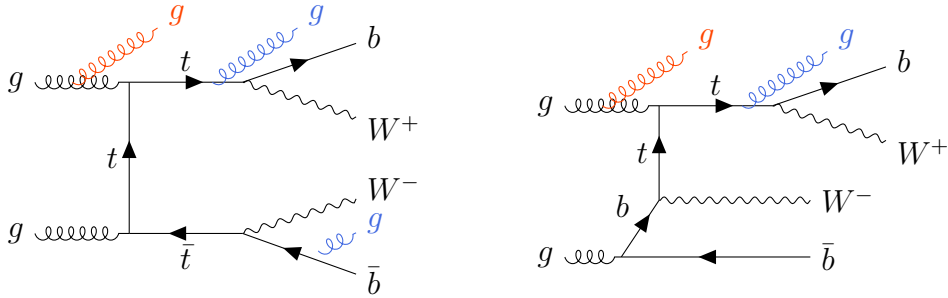


Figure 7.3: **Real emissions in **bb41**.** Examples of real emission diagrams in **bb41**, for a $t\bar{t}$ topology (left) and a tW topology (right). Up to one emission from the production process (orange) and one emission from each top decay (blue) can be present at the same time. The decay of the W bosons into leptons is not shown for brevity.

contribution, and its interplay with the emissions from the parton shower, is often relevant for the top quark line shape and p_T spectra since it causes energy to be lost.

This simple picture of one hard emission per event can not be translated directly to **bb41**: when the top quark is treated as an unstable resonance, a real emission off one of the top quarks can still become singular when it is collinear to the (virtual) top quark. Since the top quark is not in the final state, this singularity is not canceled by the default POWHEG subtraction method [197].

To alleviate this, a “resonance-aware” extension of the POWHEG method is used for **bb41**, implemented in the POWHEG Box vRES [197]. Here, real emissions and their required counterterms are generated separately for the production process (including ISR) and each unstable resonance. For **bb41**, this means that in each event, up to three real emissions are already present at the matrix element level: one from the production, one from the top decay, and one from the antitop decay. This is illustrated in Fig. 7.3. All of them are generated using real matrix elements and are thus LO-accurate, same as in the usual POWHEG method (cf. Sec. 4.1). This implies

a more accurate description especially of FSR in the top and antitop decay, which is relevant e.g. for observables related to the mass of the top quark. However, it does make the matching to the parton shower more complicated, which is discussed in detail in Sec. 7.4.1.

7.2.1 Version differences

This work investigates two different versions of **bb41**. The first version is the one originally published in Ref. [6] and publicly available on the POWHEG website [198]. In the following, it will be referred to as **bb41 v1**.

The second version of **bb41** was recently published in Ref. [196]. Its most prominent feature compared to the previous version is the addition of the lepton+jets decay channel of $t\bar{t}$, i.e. the $b\bar{b}\ell\nu_\ell q\bar{q}'$ final state. Moreover, it includes several improvements to the dilepton final state, such as avoidance of spurious finite width effects and improved resonance history projectors (see Ref. [196] for details). At the time of writing this thesis, the new code is not publicly available. A preview version was made available to the CMS Collaboration by the authors, and the dilepton final state of this version - referred to as **bb41 v2** - is shown in this work. The lepton+jets final state, on the other hand, was not ready for validation in the preview version, and so could not be included.

7.3 Other $t\bar{t}$ Monte Carlo generators

The distributions predicted by **bb41** are compared to three other MC generators for the $t\bar{t}/tW$ final state, which are briefly presented in this section. All of these are implemented in POWHEG v2, and as such do not contain explicit treatment of radiation in unstable resonances.

7.3.1 $t\bar{t} + tW$

As the main point of comparison, $t\bar{t}$ events in the NWA using Breit-Wigner smearing are generated with the POWHEG Box subprocess **hvq**, as discussed in Sec. 4.1.2. Since this generates only the $t\bar{t}$ amplitude, a second generator has to be used alongside it for the tW and $t\bar{t}/tW$ interference contributions in order to provide a fair comparison to **bb41**.

Here, another POWHEG Box subprocess called **ST_wtch** [159] is used for this purpose. It similarly works in the NWA, treating both the top quark and the W boson as stable while calculating the matrix element, and then smearing both with their respective Breit-Wigner distributions for the decay.

However, in order to at least approximately recover the full $b\bar{b}W^+W^-$ amplitude, it is necessary to select a scheme for the treatment of the $t\bar{t}/tW$ interference to

prevent double-counting. Since the separation between $t\bar{t}$ and tW is not well defined at NLO, such schemes will to some degree always be ad-hoc and ambiguous. Two such schemes are implemented in `ST_wtch`, and both are compared in this work: in the first, called diagram removal (DR), all terms involving the square of $t\bar{t}$ diagrams are simply removed from the squared amplitude. This is the most intuitive choice, but has the disadvantage of not being gauge invariant [199]. The second method, diagram subtraction (DS), keeps $t\bar{t}$ diagrams in the squared amplitude, and subtracts a gauge invariant counter-term to remove the double counting [159, 199, 200]. For both schemes, the tW prediction is added to the one of `hvq`, together called $t\bar{t} + tW$ in the following, to produce distributions that can be compared to `bb41`.

7.3.2 `ttb_NLO_dec`

The generator `ttb_NLO_dec` [201] (another POWHEG Box subprocess) also works in the NWA and thus generates stable $t\bar{t}$ pairs with ad-hoc Breit-Wigner smearing. However, unlike `hvq`, it is fully NLO-accurate not only in the production, but also in the decay of the top quarks. This means that, like `bb41`, it generates up to one hard emission at matrix element level per decaying top quark, leading to up to three hard emissions in the final state (cf. Fig. 7.3). The exact mechanism on how this is achieved in the POWHEG method differs between `ttb_NLO_dec` and `bb41`, details can be found in Refs. [6].

It also provides an LO-accurate treatment of the $t\bar{t}/tW$ interference by reweighting the generated $t\bar{t}$ events to the full off-shell LO amplitude. Thus, like `bb41`, it can be used on its own and does not need to be added together a tW contribution, but is expected to work at a lower accuracy since it includes more approximations.

7.4 Technical setup

For all generators, hard-scattering events were generated and then showered and hadronized with the multi-purpose generator PYTHIA. Wherever possible, the same settings were used for the different generators, an overview of which can be found in Tab. 7.1. They are mostly identical to the default settings used by CMS for MC generation, as discussed in Ref. [139].

7.4.1 Parton shower matching

Special care has to be taken regarding the matching of the POWHEG ME generators to the parton shower as provided by PYTHIA. For the NWA-based generators, this is accomplished here using a shower veto as described in Sec. 4.2, and technically implemented using the `PowhegHooks` module of PYTHIA. By default, this module can only handle one emission at matrix element level, and thus needs to be extended

Parameter	Value
POWHEG settings	
Top quark mass	172.5 GeV
Top quark width	1.33 GeV
h_{damp}	$1.38 m_t$ [176]
PDF set	NNPDF 3.1 [120]
PYTHIA settings	
PYTHIA version	8.307
PYTHIA tune	CP5 [139]
PowhegHooks settings [118]	
POWHEG:veto	on
POWHEG:pThard	0
POWHEG:pTdef	1

Table 7.1: **Generator settings.** An overview of the settings for POWHEG and PYTHIA, as well as the matching between them, for all considered processes.

for **bb41** and **ttb_NLO_dec**, which contain additional hard emissions in the top decay. This was implemented by the **bb41** authors in the **PowhegHooksBB4L** module as described in detail in Ref. [202]. An updated form of this module compatible with **bb41** v2 is used here. Similarly to the standard $t\bar{t}$ case, it is possible to directly start the shower at the energy scale of the POWHEG emission, or alternatively employ a veto for emissions above this scale. The latter is used as the default option, and compared to the former in Sec. 7.5.2.

7.4.2 Same-flavor leptons

By default, both versions of **bb41** generate only dilepton final states with opposite-flavor leptons (electrons, muons or τ leptons). This is because, in principle, there are additional diagrams contributing to the $b\bar{b}\ell^+\ell^-\nu_\ell\bar{\nu}_\ell$ amplitude for same-flavor leptons, such as $b\bar{b}ZZ$ with $ZZ \rightarrow \ell^+\ell^-\nu_\ell\bar{\nu}_\ell$, that are not included in **bb41**.

In practice, the effect of these diagrams will be small, especially in experimental analyses where a cut is applied to reject resonant same-flavor lepton pairs close to the Z boson mass (compare Sec. 6.2.3). To make sure that **bb41** can be used in CMS for experimental analyses involving all lepton flavors, a relabeling procedure already included in **bb41** is extended to also produce same-flavor lepton final states, neglecting the aforementioned diagrams. This procedure is used for all **bb41** distributions shown in this chapter.

7.5 Results

7.5.1 Comparison between generators

In this section, the two `bb41` versions are compared against each other, as well as to the alternative generators introduced in Sec. 7.3, for different observables. All of these comparisons are done after parton showering and hadronization (i.e. considering all physical scales as shown in Fig. 4.1), but without any detector simulation.

The package RIVET [203] was used to analyze the events. For some observables, publicly available analysis packages were employed, which is stated in the captions of the figures where applicable. Furthermore, some observables include distributions at the jet level, which are obtained by running an anti- k_T algorithm with distance parameter $\Delta R = 0.4$ (AK4) [115].

Lepton observables To begin the comparison, events with at least two leptons of opposite sign satisfying $p_T > 20 \text{ GeV}$ and $|\eta| < 2.4$ are selected. Photons surrounding the leptons in a small cone of $\Delta R < 0.1$, originating from photon radiation, are clustered together with the leptons (“dressed leptons”). The p_T distributions of the leading and subleading of these two leptons are shown in Fig. 7.4. They show good agreement between the generators within the renormalization and factorization scale uncertainties. $t\bar{t} + tW$ using the DR scheme predicts a slightly harder lepton spectrum than the others, while the DS scheme agrees with `bb41` and `ttb_NLO_dec`.

The same trend can be seen in Fig. 7.5 for the invariant lepton mass $m_{\ell\ell}$, both inclusively and split by lepton flavor channels. The per-channel distributions are all comparable within statistical uncertainties. This validates that the extension to same-flavor leptons for `bb41` presented in Sec. 7.4.2 is working as intended, i.e. up to neglecting $b\bar{b}ZZ$ diagrams which would cause differences between opposite-flavor and same-flavor leptons.

Jet observables Next, some selected AK4 jet observables are compared. Jets containing a B hadron are identified as b jets using a ghost association technique intended for truth-level objects [204, 205].

Fig. 7.6 shows the inclusive jet multiplicity and the transverse momentum of the leading b jet for the different generator setups. Several differences can be observed, both between the two versions of `bb41` and between `bb41` and the other generators. For the jet multiplicity `ttb_NLO_dec` predicts significantly less events with low jet multiplicities compared to all other generators. A possible cause for this could be the methods used to generate hard emissions from the top decay in the POWHEG method, which are less sophisticated for `ttb_NLO_dec` than for `bb41` (cf. Sec. 7.3.2); it is possible that this leads to an overestimation of FSR and thus less events with a low number of jets.

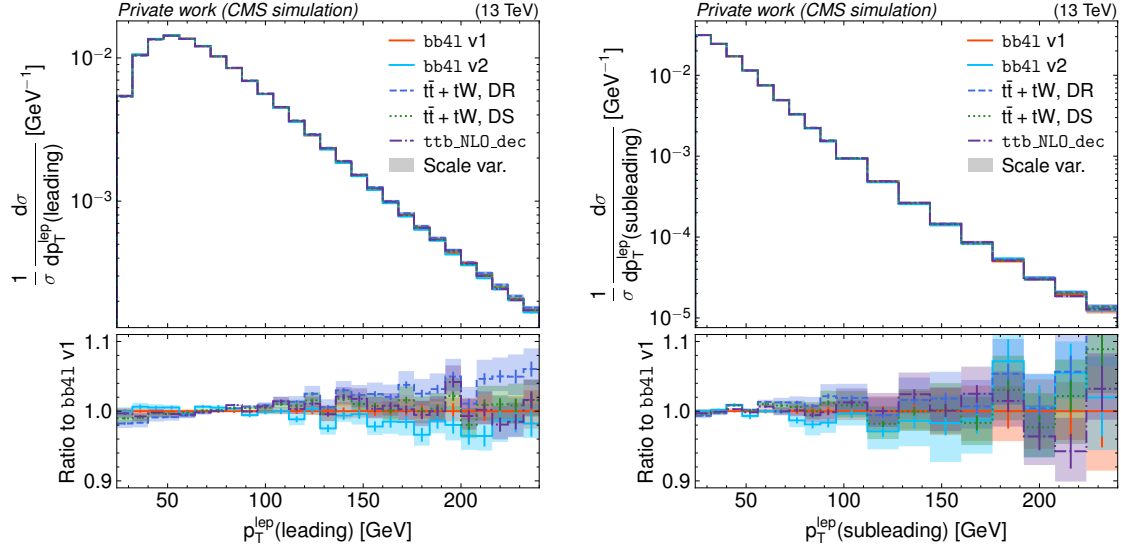


Figure 7.4: **Distributions of lepton p_T** of the leading (left) and subleading (right) lepton for **bb41** v1 (red), v2 (aqua), $t\bar{t} + tW$ with the DR (blue) and DS scheme (green), as well as **ttb_NLO_dec** (magenta). The shaded bands show the uncertainty due to scale variations, while the error bars show the statistical uncertainty [7].

It is further interesting that the number of jets agrees well between $t\bar{t} + tW$ and **bb41** v2, while **bb41** v1 disagrees and predicts a larger number of jets (though the disagreement is within the scale uncertainties). The origin of this discrepancy, especially between the **bb41** versions, is not yet understood and subject of discussion with the authors of the program.

For the b jet p_T , there is a large uncovered discrepancy between the different generators at very low p_T . This phase space region is naturally sensitive to the details of FSR emissions, and so it is not surprising that the generators disagree here due to their different treatment. In particular, **ttb_NLO_dec** predicts a harder b jet p_T spectrum compared to **bb41** and $t\bar{t}/tW$, while $t\bar{t}/tW$ predicts more low p_T b jets than **bb41** but shows agreement in the bulk of the p_T spectrum. There is further a small difference between the two **bb41** versions at very low p_T ($p_T \lesssim 20$ GeV), which again is not yet understood.

Next, Fig. 7.7 shows the b quark fragmentation, defined as the fraction of energy of the central B hadron in a jet compared to the total jet energy, as well as the average differential b jet shape $\langle \rho(R) \rangle$, defined as

$$\rho(R) = \frac{1}{p_{T,\text{tot}}} \frac{d}{dR} \left(\sum_i p_{T,i} \Theta(\Delta R_i \leq R) \right) \quad (7.1)$$

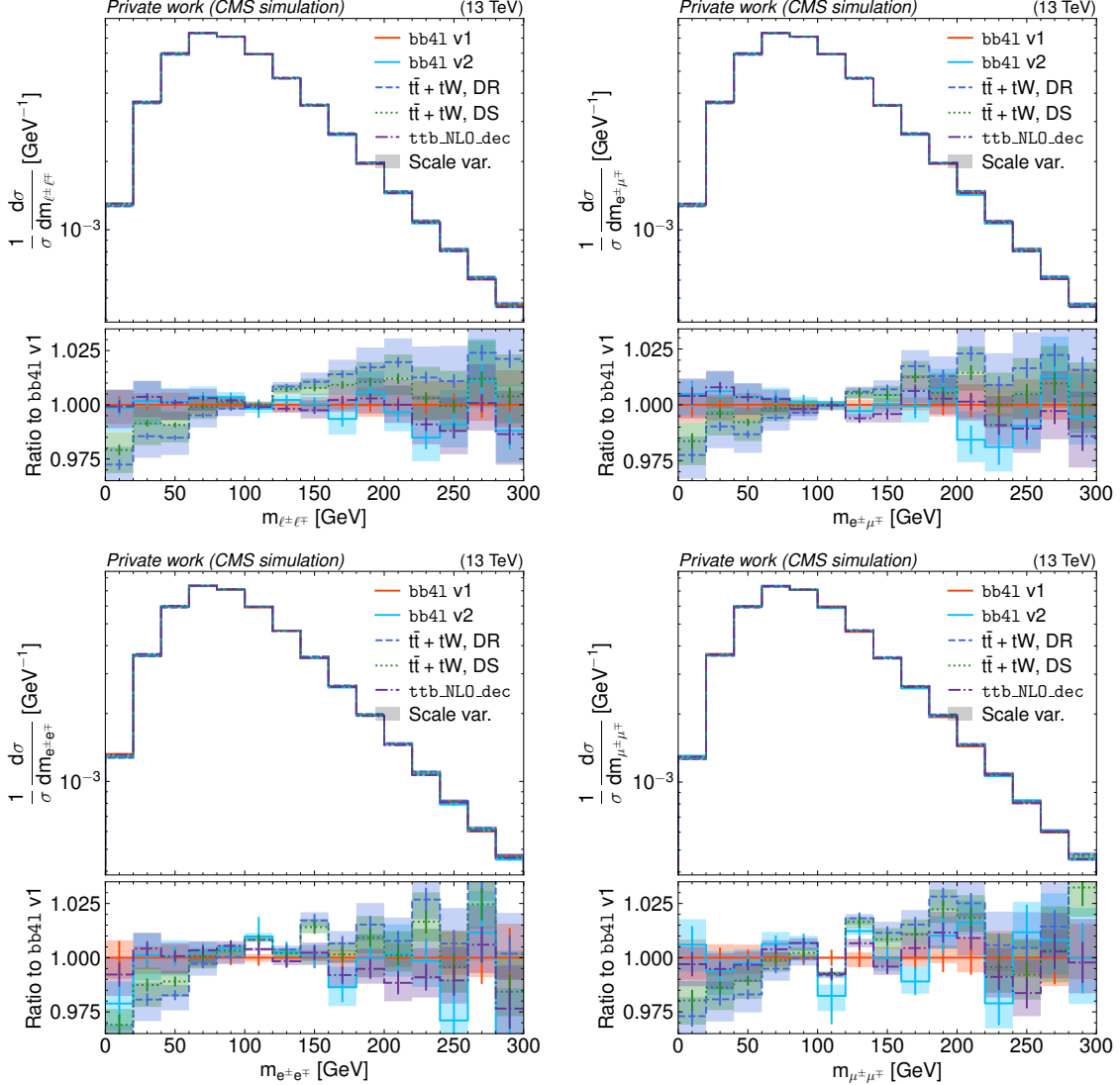


Figure 7.5: **Distributions of $m_{\ell\ell}$** for all lepton flavors combined (upper left) as well as in the $e\mu$ (upper right), ee (lower left) and $\mu\mu$ channels (lower right), shown in the same manner as in Fig. 7.4 [7].

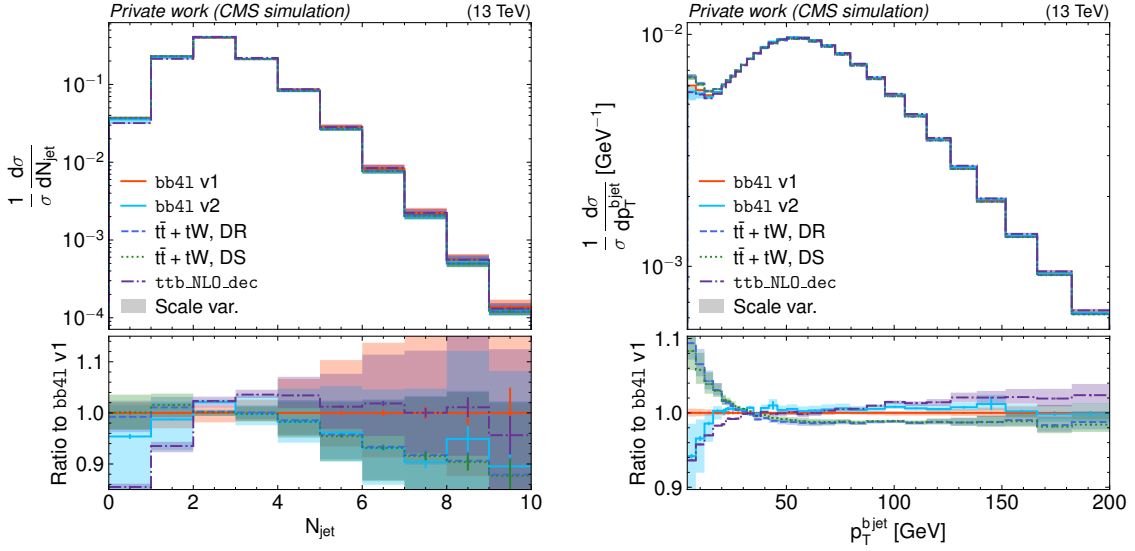


Figure 7.6: **Number of jets and b jet p_T .** Distributions of the inclusive number of AK4 jets (left) and the p_T of the leading b jet (right, RIVET analysis MC_HFJETS [203]), shown in the same manner as in Fig. 7.4 [7].

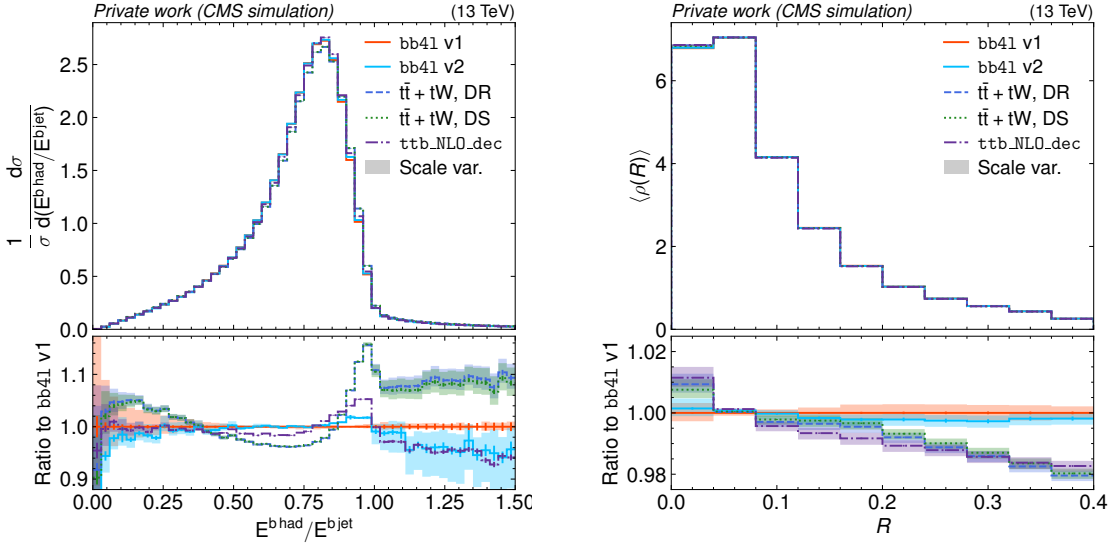


Figure 7.7: **b fragmentation and jet shape.** Distributions of the b quark fragmentation (left, RIVET analysis MC_HFJETS [203]) and the average differential b jet shape (right, RIVET analysis MC_HFDECAYS [203]), shown in the same manner as in Fig. 7.4 [7].

where the sum runs over all particles i in the considered jet, $p_{\mathrm{T},i}$ is the p_{T} of particle i , ΔR_i is its distance to the jet center in the $\varphi-\eta$ plane, and $p_{\mathrm{T},\mathrm{tot}}$ is the total jet p_{T} . This variable encodes the transverse momentum fraction of the particles making up the b jet as a function of its radius R . Both of these variables are sensitive to final-state radiation from the top decay, and are thus expected to be affected by the full NLO calculation performed by `bb41`.

It can be seen that both versions of `bb41` predict softer b jet spectra and wider jets than both $t\bar{t} + tW$ and `ttb_NLO_dec`, which can be interpreted as more FSR emissions being generated. Notably, this effect cannot be solely due to the inclusion of hard FSR emissions in `bb41` since these are also present in `ttb_NLO_dec` (though the method to include them is not identical as discussed in Sec. 7.3.2).

In general, all of these trends for `bb41` (softer lepton and b jet spectra as well as wider jets) agree with what was observed by the authors of the code in Ref. [202] and the ATLAS Collaboration in Ref. [206], though they differ from the results initially reported in Ref. [6]. The exact origin of the trends is still under investigation.

Invariant $b\ell$ mass A common proxy observable to use for measurements of the top quark mass in dilepton events is the invariant mass of a b jet and a lepton, $m_{b\ell}$. To do so, a procedure is needed to unambiguously assign the leptons and b jets (of which there might be varying numbers per event depending on the event selection) to each other. Here, exactly two b jets per event are required, and the so-called “minimax” mass is used, defined as

$$m_{b\ell}^{\mathrm{minimax}} = \min [\max(m_{b_1\ell_1}, m_{b_2\ell_2}), \max(m_{b_1\ell_2}, m_{b_2\ell_1})]. \quad (7.2)$$

This prescription amounts to maximizing the invariant mass over the two $b\ell$ pairs in the event, and then minimizing it over the two possible assignments of b jets and leptons. It is notable in that, for on-shell $t\bar{t}$ events, it shows a kinematic cutoff at a value of $\sqrt{m_t^2 - m_W^2} \approx 150 \text{ GeV}$. As a result, the tail above this cutoff is sensitive to tW events as well as $t\bar{t}/tW$ interference. The amplitude of the interference contribution here always involves an off-shell top quark decaying to Wb in the $t\bar{t}$ diagram (which is then contracted with the W boson not from a top decay and the spectator b quark in the tW diagram, cf. Fig. 7.1). The Breit-Wigner propagator of this top quark causes the interference amplitude to be sensitive to the top quark width.

Fig. 7.8 shows the distribution of $m_{b\ell}^{\mathrm{minimax}}$, again for all considered cases. It can be seen that both versions of `bb41` are in good agreement with each other, and are also in agreement with `ttb_NLO_dec` except for a small deviation in the lowest bin. Unfolded ATLAS data taken from Ref. [195] is overlaid on top of the predictions, and shows agreement for both `bb41` and `ttb_NLO_dec`. In the tail, the DR and DS interference handling schemes for $t\bar{t} + tW$ show significant differences as expected, with `bb41` and `ttb_NLO_dec` lying between them. Since `bb41` is expected to provide

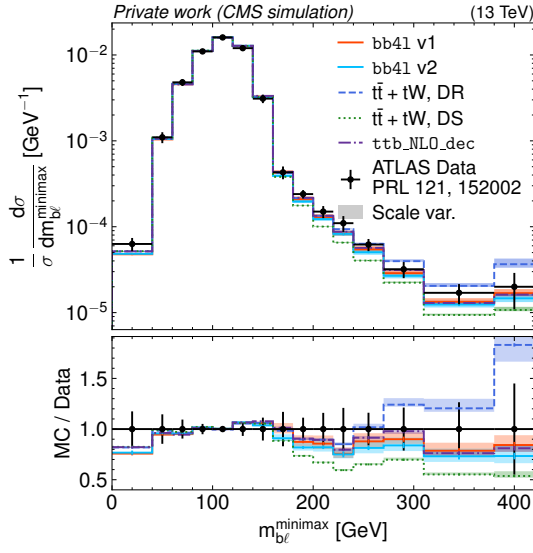


Figure 7.8: **Distribution of $m_{b\ell}^{\text{minimax}}$** , shown in the same manner as in Fig. 7.4. ATLAS data from Ref. [195] is overlaid as black dots, and the RIVET routine from said reference was used to obtain the distributions [7].

a more accurate prediction of the interference than either scheme, this validates that using the difference of the DR and DS schemes as an uncertainty covers the true values, as is done in many CMS and ATLAS measurements. Going forward, such uncertainties could be dropped from future measurements by using `bb41` predictions directly.

Top quark reconstruction Finally, in order to directly study the effects on top quark observables, a simple generator-level top quark reconstruction is performed. To do so, two dressed leptons and two b jets are selected as before, while the two neutrinos in the dileptonic top decay are taken from truth-level information. The W bosons are reconstructed from the neutrinos and charged leptons according to the lepton charge, and then combined with the b jets by choosing the pairs for which the difference Δm_t between the invariant masses is minimal.

This reconstruction procedure is not equivalent to a full experimental reconstruction, in which neutrinos are measured only as missing transverse momentum and thus cannot be directly assigned to the leptons. It also does not include any detector resolution effects. However, it does take into account the effects of FSR off the top quarks by considering the full b jets instead of parton-level b quarks, which is why it was chosen for the comparison.

Fig. 7.9 shows the resulting distributions for the top quark mass and p_T . It can be seen that the different generators show different line shapes for the top quark mass: Around the peak at 172.5 GeV, `bb41` predicts a small shift towards lower values

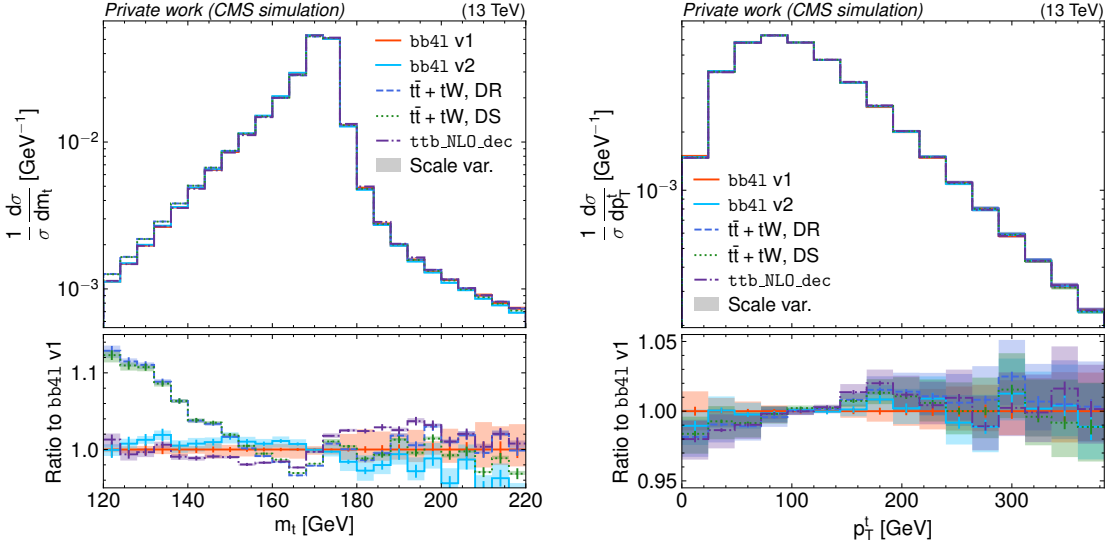


Figure 7.9: **Top quark line shape and p_T .** Distributions of the reconstructed top quark mass (left) and p_T (right), summed for both top and antitop quark, shown in the same manner as in Fig. 7.4 [7].

compared to $t\bar{t} + tW$ for both interference handling schemes as well as ttb_NLO_dec . It at the same time predicts significantly lower amounts of far off-shell tops with masses below ≈ 150 GeV compared to $t\bar{t} + tW$.

Both of these effects are important for precision top mass measurements, in which such shifts can influence the final fit results. The presence of the shift around the mass peak is expected: due to the use of the NWA for both $t\bar{t} + tW$ and ttb_NLO_dec , the top line shape can only be modeled approximately in these generators, while $bb41$ provides a true NLO-accurate description. It can furthermore be seen that the two $bb41$ versions are not in perfect agreement with each other, though the difference is within the scale uncertainties.

The suppression for low masses could indicate that both the DR and DS scheme similarly overestimate the amount of off-shell $t\bar{t}$ production when masses of the top quarks are below their pole mass. Alternatively, it could mean that the NLO effects included in $bb41$ suppress the cross section in this phase space compared to the naive Breit-Wigner smearing used in the NWA-based generators.

For the top quark p_T , on the other hand, any trend in the comparison between the generators is covered by the scale uncertainties. $bb41$ seems to again predict slightly softer p_T spectra than the other generators, consistent with increased FSR emissions as also seen in the trends for the lepton p_T and m_{ee} .

Lastly, the invariant mass and p_T distributions of the $t\bar{t}$ system as a whole are shown in Fig. 7.10. For $m_{t\bar{t}}$, no clear trend can be seen for any of the considered generators. The p_T of the $t\bar{t}$ system, on the other hand, shows significant differences

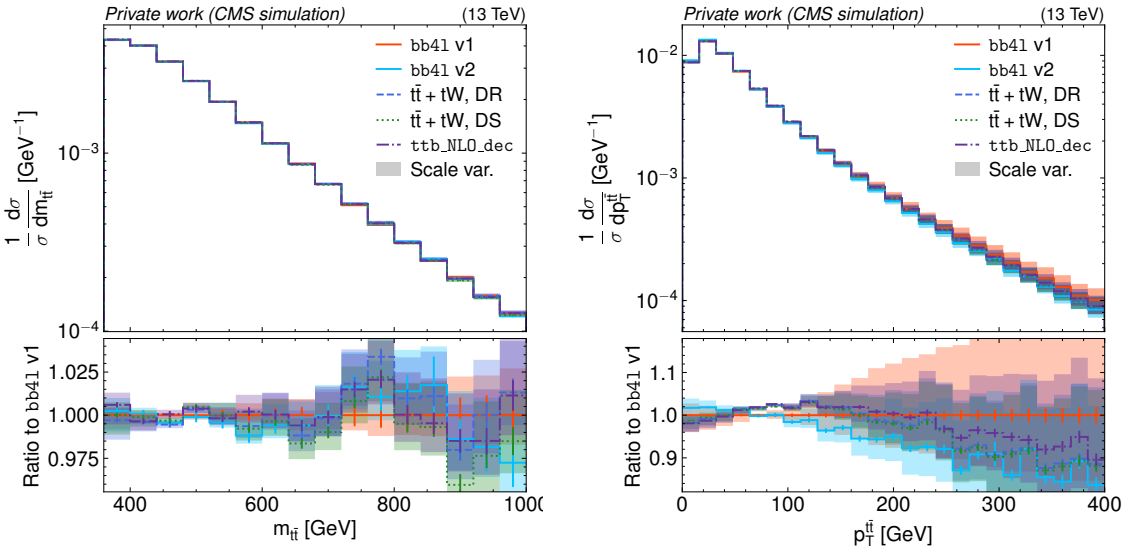


Figure 7.10: **Kinematics of the $t\bar{t}$ system.** Distributions of the reconstructed invariant mass (left) and p_T (right) of the $t\bar{t}$ system, shown in the same manner as in Fig. 7.4 [7].

both between the two `bb41` versions and between `bb41` and the other generators (which agree with each other). It should be noted that, since the initial state partons in the $pp \rightarrow t\bar{t}$ process have no p_T ¹, this variable is exactly zero at LO in QCD, and consequently determined only by emissions at NLO and beyond. As a result, it is expected to be sensitive to the NLO calculation and matching between matrix element and parton shower.

7.5.2 Comparison of FSR matching settings

Complementary to the previous generator comparisons, this section investigates the effect of the matching between matrix element and parton shower for FSR in `bb41`. As explained in Sec. 7.4.1, two principal options are available to match `bb41` to PYTHIA in the used module PowhegHooksBB4L: In the first and nominal approach (denoted “FSR veto”), the initial value of the ordering variable used in the evolution of the parton shower (cf. Sec. 4.2) is set to the kinematically allowed maximum, and FSR emissions that lie above the POWHEG energy scale of the relevant emission from the top decay as generated by POWHEG are vetoed.

In the second approach (“Res. scale”), the initial value of the ordering variable for FSR emissions in the shower is set directly to the p_T of the POWHEG FSR emission. This neglects the fact that the p_T definitions used in POWHEG and PYTHIA as

¹Non-zero p_T of the incoming partons can be modeled with transverse momentum distributions for the partons inside the proton [207], but this is not considered here.

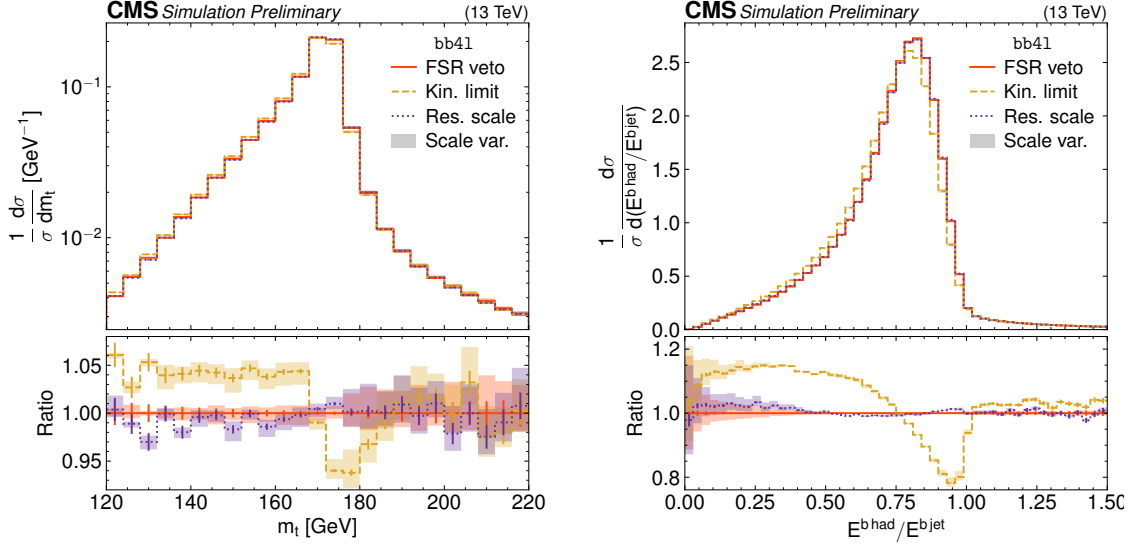


Figure 7.11: **Comparison of FSR matching settings.** Distributions of the reconstructed top quark mass (left, same as in Fig. 7.9) and the b quark fragmentation (right, same as in Fig. 7.7), for bb41 with different FSR matching settings as explained in the text (Sec. 7.5.2). The shaded bands show scale uncertainties [7].

ordering variables are similar but do not match exactly. When the PYTHIA emission is only slightly softer (by the PYTHIA definition) than the POWHEG emission, it is thus possible that it is in fact harder than the POWHEG emission by the POWHEG definition, leading to double-counting. Similarly, an emission that is only slightly harder by the PYTHIA definition and is thus not generated might in fact be softer by the POWHEG definition, leading to under-counting.

In order to demonstrate the importance of correct parton shower matching, a third case (“Kin. limit”) is considered. Here, the ordering variable used for FSR emissions in the shower is set naively to the kinematic limit without any veto procedure specifically directed at bb41. This approach is thus expected to double-count FSR emissions.

The comparison in this section has been performed with bb41 v1. The matching for ISR emissions, done by PowhegHooks, is left identical between the three cases, as given in Tab. 7.1.

Fig. 7.11 shows the distributions of the top quark mass, reconstructed the same as before, and the b fragmentation for the different matching choices. Both of these observables were chosen for their sensitivity to FSR effects. It can be seen that the options “FSR veto” and “Res. scale” agree reasonably well with each other, with the top mass line shape showing a small shift between them within the scale uncertainties. This implies that the mismatch between the ordering variable definitions in POWHEG

and PYTHIA has a subleading effect in practice. On the other hand, the naive “Kin. limit” approach shows a large discrepancy due to its double-counting of FSR emissions, highlighting the importance of correct FSR matching procedures for NLO generators.

7.6 Summary and Outlook

In this chapter, several generator-level studies of the MC generator **bb41**, which generates the full $b\bar{b}\ell^+\ell^-\nu_\ell\bar{\nu}_\ell$ final state including $t\bar{t}/tW$ interference and off-shell top effects at NLO in QCD, have been presented. **bb41** has been compared to different generators for $t\bar{t} + tW$ working in the narrow-width approximation (NWA), including different schemes for handling $t\bar{t}/tW$ interference, for different lepton, b jet and reconstructed top quark observables. For $m_{b\ell}^{\text{minimax}}$, **bb41** agrees well with ATLAS data from Ref. [195], improving greatly upon the two interference handling schemes DR and DS for $t\bar{t} + tW$. For the reconstructed top quark mass, **bb41** shows a significant shift compared to $t\bar{t} + tW$. In addition, two different **bb41** versions have been compared, finding slight differences within scale uncertainties, and the matching of ME and parton shower in **bb41** has been studied further.

These studies represent valuable information for the choice of $t\bar{t}$ MC generator in upcoming CMS measurements. For analyses in which $t\bar{t}$ and tW are major backgrounds, **bb41** can help reduce uncertainties originating in the $t\bar{t}/tW$ interference treatment. Furthermore, **bb41** will be crucial for a simultaneous top mass and width measurement using MC templates, as originally proposed in Ref. [202], in CMS. Alternatively, one might perform an differential $t\bar{t} + tW$ cross section measurement, where **bb41** could be used to unfold the data to generator level.

In addition, correct modeling of off-shell effects is of particular importance close to the $t\bar{t}$ production threshold, where $t\bar{t}$ bound state effects are expected in the SM (cf. Sec. 2.3). In this region of phase space, **bb41** could provide a more accurate description compared to NWA-based generators. This is outlined in the next chapter and discussed in detail in Sec. 8.5.4.

8 Search for heavy scalar or pseudoscalar bosons in $t\bar{t}$ final states

8.1 Introduction

Having studied $t\bar{t}$ production at the energy frontier of $\sqrt{s} = 13.6$ TeV in Chapter 6 as well as the modeling of off-shell top quarks in Chapter 7, this chapter is dedicated to a precision analysis of $t\bar{t}$ using the large, well-studied Run 2 data set at $\sqrt{s} = 13$ TeV, in the context of a search for new scalar or pseudoscalar bosons.

Additional spin-0 particles are predicted in many attractive extensions of the Standard Model, and can be searched for in $t\bar{t}$ final states at the LHC if the new states are heavy (i.e. have a mass larger than $2m_t$), electrically neutral, and exhibit Yukawa-like couplings to fermions (see Sec. 2.4.1). A generic model for such states with either pseudoscalar (A) or scalar (H) couplings to top quarks was given in Eq. (2.29).

In addition, $t\bar{t}$ bound state effects are expected in the SM in several calculations, with a pseudoscalar component dominating at the LHC as discussed in Sec. 2.3. Since additional BSM particles and bound state effects are expected to lead to similar experimental signatures, it makes sense to search for them for using the same methods.

This chapter presents such a search for new spin-0 states with either scalar or pseudoscalar interactions with the top quark, using the full Run 2 data set with an integrated luminosity of 138 fb^{-1} at the CMS experiment. It follows up on a similar search done using only 35.9 fb^{-1} of data taken in 2016 [22]. Similar searches have also been published by ATLAS, one with 20.3 fb^{-1} of data taken at $\sqrt{s} = 8$ TeV [208] and one with 140 fb^{-1} of data taken at $\sqrt{s} = 13$ TeV [209].

The work done as part of this thesis focused on the dilepton decay channel of $t\bar{t}$, which is thus described in detail in Secs. 8.2 to 8.6. A significant excess of events is observed at invariant masses close to the $t\bar{t}$ threshold, which is interpreted either as a pseudoscalar $t\bar{t}$ bound state (Secs. 8.7.1 to 8.7.3) or as an additional scalar or pseudoscalar boson (Sec. 8.7.4). For the latter interpretation, exclusion limits for a large mass range are also presented in Sec. 8.8. Following this, the dilepton channel is combined with a similar analysis of the $\ell + \text{jets}$ decay channel, which is discussed in Sec. 8.9, and exclusion regions are provided for the presence of either one or two additional bosons. The results of this work are briefly compared in Sec. 8.10 to preliminary ATLAS results in Ref. [210] which confirmed this measurement, to

earlier ATLAS results in Ref. [209] in which no excess was observed, and to other $t\bar{t}$ measurements. Finally, a summary and outlook are given in Sec. 8.11.

The results presented here were first made public as a Physics Analysis Summary [211], and later submitted to *Reports on Progress in Physics* in an updated form in two parts: first in Ref. [8] focusing solely on the interpretation of a $t\bar{t}$ bound state, and second in Ref. [9] focusing on the interpretation in terms of additional bosons. They build upon the framework developed in Refs. [33, 212], with this work consisting of the implementation of matrix element reweighting for the signal simulation (Sec. 8.4), the simulation and scrutinization of the $t\bar{t}$ bound state signal (Sec. 2.3), the comparison with other MC generators for the $t\bar{t}$ continuum (Sec. 8.5.4), the interpretation of the observed excess in terms of $t\bar{t}$ bound states or additional bosons including all corresponding cross-checks (Sec. 8.7), the combination with the $\ell+jets$ channel (Sec. 8.9), the comparison to other results (Sec. 8.10), and the preparation of the results for publication in Refs. [9] and [8].

8.2 Analysis setup

This section describes the analysis strategy in the dilepton channels, consisting of the considered data sets, object definitions, event selection criteria, corrections and reconstruction algorithms.

8.2.1 Data sets

Experimental data The analysis is performed using the full CMS Run 2 ultra-legacy (UL) data set, which is the final, re-reconstructed and recalibrated data set recommended by CMS for physics analyses. It is split into the three data taking years of Run 2: 2016, 2017 and 2018, where 2016 is further split into two parts, denoted “2016pre” and “2016post”, because of a modification of the silicon strip tracker readout chip settings that affects the efficiency of the track hit reconstruction during the 2016 data-taking period [213].

A similar combination of dilepton and single-lepton triggers as in Sec. 6.2.1 is used for all years, with the p_T thresholds varying slightly between data taking eras, as shown in Tab. 8.1.

Background simulation Since the final state of the signals considered in this analysis are the same as in the SM $t\bar{t}$ background, it is clear that a large irreducible background is expected. As a result, it is essential that the SM Monte Carlo simulation is as both theoretically precise and has sufficient statistics, and that any remaining imprecisions are covered by the systematic uncertainty model.

The SM $t\bar{t}$ background is again simulated at NLO in QCD, employing the narrow-width approximation (NWA) with a Breit-Wigner smearing for the top decay, using

Trigger	Year	Lepton p_T requirement
single-e	2016	e ($p_T > 27 \text{ GeV}$)
	2017	e ($p_T > 35 \text{ GeV}$)
	2018	e ($p_T > 32 \text{ GeV}$)
single- μ	2016	μ ($p_T > 24 \text{ GeV}$)
	2017	μ ($p_T > 27 \text{ GeV}$)
	2018	μ ($p_T > 24 \text{ GeV}$)
e μ	all	e ($p_T > 12 \text{ GeV}$) and μ ($p_T > 23 \text{ GeV}$) or e ($p_T > 23 \text{ GeV}$) and μ ($p_T > 8 \text{ GeV}$)
ee	all	e ₁ ($p_T > 23 \text{ GeV}$) and e ₂ ($p_T > 12 \text{ GeV}$)
$\mu\mu$	all	μ_1 ($p_T > 17 \text{ GeV}$) and μ_2 ($p_T > 8 \text{ GeV}$)

Table 8.1: **Trigger p_T thresholds.** Overview of the used triggers in the three data taking years, as well as their lepton p_T thresholds.

the MC generator package POWHEG v2 and interfaced to PYTHIA 8 for showering, as discussed in detail in Sec. 4.1.2. Equivalent settings as in Sec. 6.2.1 and Sec. 7.4, corresponding to the CMS defaults, have been used. To achieve the necessary precision, the NLO simulation is reweighted to higher orders in both QCD and electroweak (EW) processes, which is described in Sec. 8.3.

In addition, several minor backgrounds are included, a summary of which can be found in Tab. 8.2. Of note here is the Z+jets background, which is simulated at NNLO in QCD using the MiNNLO method in Powheg v2 [214, 215]. It was found here that the higher-order corrections are relevant to the analysis especially for low values of the invariant dilepton mass $m_{\ell\ell}$. Most processes are normalized to cross sections predicted at higher orders of QCD where available, which can be found in Tab. 8.3.

Signal simulation The signal for the general A/H model described in Sec. 8.1 is generated at LO in QCD using MG5_AMC@NLO with a custom Universal FeynRules Output (UFO) model. The $pp \rightarrow A/H \rightarrow t\bar{t}$ resonance and the A/H-SM interference are simulated separately, and both are again showered with PYTHIA 8. In order to cover the phase space of the A/H model, the signals are generated for all combinations of the following values of the A/H masses and widths:

$$\begin{aligned} m_{A/H} &\in \{365, 400, 500, 600, 800, 1000\} \text{ GeV} \\ \Gamma_{A/H}/m_{A/H} &\in \{2.5, (5), 10, 25\} \% \end{aligned} \tag{8.1}$$

Samples with a width of 5%, indicated by the bracket, were generated only for a mass of 400 GeV, which leads to 38 signal points total. In addition, samples for the

Process	QCD order	ME Generator
$t\bar{t}$	NLO	POWHEG v2 (<code>hvq</code> [129])
tW	NLO	POWHEG v2 (<code>ST_wtch</code> [159])
$Z/\gamma^* + \text{jets}$	NNLO	POWHEG v2 (<code>Zj MiNNLO</code> [214, 215])
t -channel single top	NLO	POWHEG v2 (<code>ST_tch</code> [160]) + MADSPIN [131]
s -channel single top	NLO	MG5_AMC@NLO
$t\bar{t}W$	NLO	MG5_AMC@NLO
$t\bar{t}Z$	NLO	MG5_AMC@NLO
$WW, WZ \& ZZ$	LO	PYTHIA 8.2
A/H signal	LO	MG5_AMC@NLO
η_t signal	LO	MG5_AMC@NLO

Table 8.2: **Simulated background and signal samples.** An overview of the different background and signal processes considered, as well as the theoretical order in QCD and the ME generator used to simulate them. For all samples, PYTHIA 8.2 is used for showering and hadronization.

Process	Cross section (pb)	Order	Program / reference
$t\bar{t}$	833.9	NNLO+NNLL	Top++ [158]
tW	71.7	NNLO (approx.)	[161]
t -channel single top	217.0	NLO	HATHOR [216, 217]
s -channel single top	10.3	NLO	HATHOR [216, 217]
$t\bar{t}W$	0.64	NLO	MG5_AMC@NLO
$t\bar{t}Z$	0.75	NLO	MG5_AMC@NLO
$Z/\gamma^* + \text{jets} \rightarrow \ell\ell, m_{\ell\ell} > 10 \text{ GeV}$	24.7×10^3	NNLO	FEWZ [218, 219]
WW	118.7	NNLO	[220]
WZ	47.1	NLO	MCFM [221]
ZZ	16.5	NLO	MCFM [221]

Table 8.3: **Cross sections for background processes at $\sqrt{s} = 13 \text{ TeV}$.** The cross sections used for the normalization of background processes, as well as the orders in QCD at which they were computed. Where applicable, cross sections are given as the sum of the process and its charge conjugate.

pseudoscalar case only were generated with

$$m_A \in \{450, 550, 700, 900\} \text{ GeV}, \quad \Gamma_A/m_A = 9\%. \quad (8.2)$$

All of these samples were combined and reweighted at matrix element level to obtain phase space points between these mass and width values, as described further in Sec. 8.4.

Furthermore, signal samples for possible $t\bar{t}$ bound state effects are generated using the color-singlet η_t and χ_t models as defined in Sec. 2.3, using custom UFO models implemented in MG5_AMC@NLO and again showered with PYTHIA. The branching ratio of $W \rightarrow \ell\nu$ is taken to be 11.1%, corresponding to the default value used by MG5_AMC@NLO.

For all signal and background samples, the detector response is simulated with GEANT 4 and the full CMS simulation and reconstruction chain as described in Sec. 4.6 is performed.

8.2.2 Object definition

Leptons All electrons and muons are required to have $|\eta| < 2.4$ and $p_T > 20 \text{ GeV}$, corresponding to a less stringent cut than in Chapter 6. Similar to Sec. 6.2.2, electrons in the transition region between barrel and endcaps in the ECAL, corresponding to $1.44 < |\eta_{SC}| < 1.57$, are removed, and additional ID criteria are applied for both types of leptons.

For electrons, instead of a cut-based ID as in Sec. 6.2.2, the multivariate classifier (MVA)-based ID described in Ref. [103] is used at a working point giving 90 % background rejection. This ID already includes an isolation requirement as part of the MVA training, and no further requirement is applied.

For muons, on the other hand, the same cut-based ID from Ref. [165] as in Sec. 6.2.2, also at the tight working point, is used, and the same I_{rel} requirement using a cone size of $\Delta R < 0.4$ is applied in addition.

Jets Like in Sec. 6.2.2, jets are reconstructed using the anti- k_T algorithm [115] with a distance parameter of 0.4. They are required to fulfill $p_T > 20 \text{ GeV}$, $|\eta| < 2.4$, and have a minimum distance of $\Delta R > 0.4$ from all leptons passing the above criteria in the event. The Charged Hadron Subtraction (CHS) method [112] is used to remove hadrons that originate from pileup from the jet clustering.

Additional ID criteria are applied to reject jets originating in detector noise and reconstruction failures [114]. They consist of requirements on the multiplicities of the different jet constituents (charged hadrons, neutral hadrons, and electrons or photons) as well as their energy fractions relative to the total jet energy. The required values are centrally provided depend on the jet $|\eta|$ as well as on the analysis era. In

total, a genuine jet efficiency of about 99 % is achieved, while about 99.9 % of noise jets are rejected in the relevant $|\eta|$ range [114].

The DEEPJET algorithm [116], same as in Sec. 6.2.2, is used to identify jets originating from the showering and hadronization of b quarks. The medium working point of DEEPJET in CMS is chosen, which has a b jet identification efficiency of 77 %, as well as a misidentification rate of 15 % for c quark jets and of 2 % for light quark and gluon jets [166].

Missing transverse momentum In the dileptonic decay of $t\bar{t}$, the two neutrinos leave the detector unseen, leading to a loss of information. However, their combined transverse momentum can be inferred through the missing transverse momentum \vec{p}_T^{miss} , defined as the negative vectorial sum of all reconstructed objects (jets, leptons and photons) [117]. As with the jets, hadrons likely to originate from pileup are removed from the calculation of \vec{p}_T^{miss} using the CHS method [112]. Along with the leptons and jets, \vec{p}_T^{miss} will be used to reconstruct the $t\bar{t}$ system.

8.2.3 Event selection

Events are selected with exactly two leptons of opposite electric charge and sorted into three channels (ee , $e\mu$ and $\mu\mu$) by lepton flavor, similar to Sec. 6.2.3. The two leptons need to fulfill $p_T > 25 \text{ GeV}$ and $p_T > 20 \text{ GeV}$ for the leading and subleading lepton, respectively, and their invariant mass is required to be $m_{\ell\ell} > 20 \text{ GeV}$ in order to reject background from $\gamma^* + \text{jets}$ production and low-mass resonances.

In all channels, at least two jets with $p_T > 30 \text{ GeV}$ are required, of which at least one needs to be b tagged. Furthermore, in the same-flavor lepton channels (ee and $\mu\mu$), additional cuts are applied to reject $Z + \text{jets}$ background: Events with $|m_{\ell\ell} - m_Z| < 15 \text{ GeV}$, i.e. close to the Z boson mass peak, are discarded (again just as in Sec. 6.2.3), and the magnitude of the missing transverse momentum is required to be $p_T^{\text{miss}} > 40 \text{ GeV}$.

The effect of all selection cuts is summarized in Tab. 8.4.

8.2.4 Experimental corrections

Similar as in Sec. 6.3, several corrections are applied to the MC simulation in order to achieve good agreement with the data. In contrast to the $t\bar{t}$ cross section measurement, where most of these corrections were derived as part of this work, many of the experimental corrections used in this chapter were provided centrally by the CMS collaboration. These will only be described very briefly; more details can be found in the associated references.

Trigger scale factors The selection efficiency of the triggers from Tab. 8.1 needs to be corrected in simulation to the one measured in data. This is done via scale

Cut	Data yield/ 10^3			$t\bar{t} \rightarrow \ell\ell$ MC	
	ee	e μ	$\mu\mu$	efficiency (%)	purity (%)
Triggers	3504932			64.4	–
Two OC leptons	65589	2240	108363	20.6	1.4
Lepton p_T	65189	2169	106112	20.3	1.4
$m_{\ell\ell} > 20$ GeV	64746	2081	103276	19.8	1.4
Z window (ee/ $\mu\mu$)	5795	2081	9367	17.6	12.7
At least 2 jets	1235	1287	1947	15.4	43.2
Jet p_T	644	999	985	12.9	59.2
At least one b tag	319	853	489	11.7	84.6
p_T^{miss} (ee/ $\mu\mu$)	234	853	354	10.7	88.9

Table 8.4: **Selection cuts and event yields.** The data yield in all analysis eras after successively applying all selection cuts, separately for the three lepton flavor channels. The second-to-last column shows the selection efficiency of $t\bar{t} \rightarrow \ell\ell$ events ($\ell = e, \mu, \tau$), and the last column shows the purity, defined as the fraction of $t\bar{t} \rightarrow \ell\ell$ events and total event yield. Both efficiency and purity are evaluated using simulation.

factors, which were centrally derived by CMS as a function of the p_T of the two leptons using the so-called cross-trigger method: Events are selected using a different set of triggers - here, a combination of jet and p_T^{miss} triggers - which is assumed to be fully orthogonal to the lepton triggers used for the main selection. Thus, the event sample is unbiased with respect to the lepton triggers, and the lepton trigger efficiency can be measured as the fraction of the events who pass the lepton triggers in addition to the jet/ p_T^{miss} triggers. This is done independently for all data taking years. The resulting scale factor can differ from unity by up to 5 % for leptons with $p_T \approx 20$ GeV and less than 1 % for higher p_T values.

Lepton scale factors Differences in the efficiency for a lepton to pass the identification and isolation criteria as defined in Sec. 8.2.2 are measured using the tag-and-probe method, as in Sec. 6.3, and applied to simulation using scale factors binned in p_T and $|\eta|$ of the lepton. The scale factor typically differs from unity by about 1-5 %, with the magnitude increasing for high $|\eta|$. For more details on this method see Refs. [103, 165].

Pileup reweighting In contrast to the data-driven reweighting method used for the inclusive $t\bar{t}$ cross section measurement (Sec. 6.3), the mean number of pileup interactions per bunch crossing in simulation is reweighted to year-dependent distributions provided centrally by CMS. These have been derived from measurements of the instantaneous luminosity combined with a total inelastic proton-proton cross

section of $69.2(32)$ mb at $\sqrt{s} = 13$ TeV [146].

Jet energy and p_T^{miss} corrections The difference in the jet energy response of the detector (JES) as well as the jet energy resolution (JER) in data and simulation was corrected in the same way as described in Sec. 6.3, using centrally derived jet energy corrections (JECs) as described in Ref. [167]. These corrections are further propagated to the calculation of \vec{p}_T^{miss} [117]. Possible additional corrections to the x and y components of \vec{p}_T^{miss} were investigated, but found to not be required for good description of the observables considered in this analysis.

b tagging scale factors The identification efficiency of the DEEPJET b tagging algorithm was calibrated using events with jets containing a muon, likely originating from the semileptonic decay of a B hadron, following the methodology described in Ref. [166]. Note that the calibration done on dileptonic $t\bar{t}$ events presented in the same reference is not used as an input here, since it was derived in part on the same data set and would thus lead to double-counting. However, similar to the discussion in Sec. 6.6, it is expected that the b tagging efficiency will be constrained from the data during the likelihood fit.

ECAL L1 pre-firing In the 2016 and 2017 data-taking years, the L1 trigger of the electromagnetic calorimeter was affected by a gradual shift in the timing of the inputs in the forward region ($|\eta| > 2.0$) [109]. This effect, called L1 pre-firing, is corrected for using simulation scale factors computed from data.

Z+jets background normalization In the same-flavor lepton channels (ee and $\mu\mu$), Z+jets events constitute a minor but important background. Since this analysis is sensitive to small shape effects, it is necessary to precisely model this background both in shape and normalization. An NNLO Monte Carlo simulation (see Tab. 8.2) is used for this purpose, which generates up to two additional partons (including b quarks) in the final state, as required by the event selection of at least two jets and at least one b tag. Still, in order to be certain of the Z+jets rate, the same data-driven estimation as presented in Sec. 6.3.2, using a control region with $|m_{\ell\ell} - m_Z| < 15$ GeV and a sideband with zero b tagged jets, is performed. The resulting ratios of Z+jets yields compared to the prediction of the original simulation can be found in Tab. 8.5.

8.2.5 Reconstruction of the $t\bar{t}$ system

Having identified the relevant objects - leptons, jets and \vec{p}_T^{miss} - in an event, the next step consists of reconstructing the $t\bar{t}$ system, i.e. the four-momenta of the top and antitop quark. The presence of two neutrinos in dileptonic $t\bar{t}$ decays, which escape detection except through missing transverse momentum, leads to a significant loss

	2016pre	2016post	2017	2018
ee	0.96 ± 0.010	0.97 ± 0.008	0.87 ± 0.006	0.88 ± 0.005
e μ	0.96 ± 0.007	0.97 ± 0.005	0.88 ± 0.004	0.89 ± 0.003
$\mu\mu$	0.96 ± 0.009	0.97 ± 0.006	0.90 ± 0.005	0.90 ± 0.004

Table 8.5: **Z+jets scale factors.** Ratio of the Z+jets event yields estimated in data using the method described in Sec. 6.3.2 to the prediction by the MC simulation for the four data-taking periods. The results in the e μ channel are the geometric means of those in the ee and $\mu\mu$ channels. Uncertainties are statistical only.

of information. As a result, reconstructing the full event kinematics is non-trivial and requires several assumptions. In this work, a variation of the algorithm first presented in Ref. [222] is used, which is briefly outlined in this section.

The algorithm works in two steps, starting with the assignment of jets to the b and \bar{b} quarks originating from the $t\bar{t}$ decay. To do so, pairs of jets are selected from all jets in the event (passing the requirements outlined in Sec. 8.2.2) depending on the number n_b of b tagged jets: For events with $n_b \geq 2$, all permutations of two b tagged jets each are considered as candidate pairs, while for events with $n_b = 1$, the candidate pairs are formed by pairing the single b tagged jet with all other jets in the event.

From these candidates, the best pair is now chosen based on the invariant masses $m_{\ell+b}$ and $m_{\ell-\bar{b}}$ of the b/ \bar{b} candidate and the corresponding (anti)lepton. First, the expected truth-level distribution of $m_{\ell b}$ is determined from MC simulation, which can be seen in Fig. 8.1. Then, in each event, the likelihoods to observe the respective values of $m_{\ell+b}$ and $m_{\ell-\bar{b}}$ for each candidate pair are computed from the expected distribution. The candidate pair that maximizes the product of the two likelihoods for $m_{\ell+b}$ and $m_{\ell-\bar{b}}$ is chosen for the remainder of the reconstruction.

Next, the four-momenta of the top and antitop quark are reconstructed using the momentum conservation equations. That is, one demands

$$\begin{aligned} p_t &= p_{W^+} + p_b = p_{\ell^+} + p_{\nu_\ell} + p_b \\ p_{\bar{t}} &= p_{W^-} + p_{\bar{b}} = p_{\ell^-} + p_{\bar{\nu}_\ell} + p_{\bar{b}} \end{aligned} \tag{8.3}$$

where all variables are understood as four-momenta. The lepton and b quark momenta are experimentally measured, while the neutrino momenta are unknowns. Demanding them to be massless, i.e. $p_{\nu_\ell}^2 = p_{\bar{\nu}_\ell}^2 = 0$, yields the six components of the two neutrino three-momenta as free parameters.

To resolve the ambiguities, several assumptions need to be made. First, it is assumed that all of the missing transverse momentum in the event stems from the neutrinos, i.e.

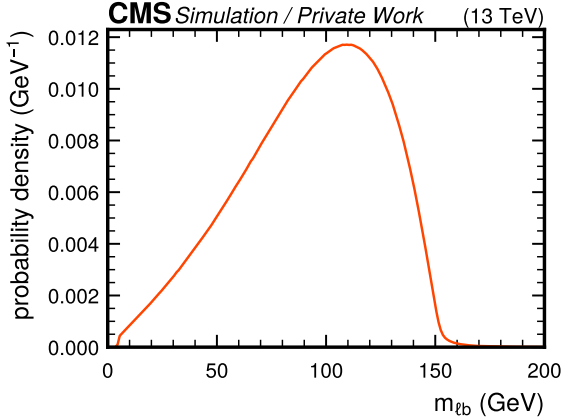


Figure 8.1: **Probability distribution of m_{tb} .** The truth-level probability distribution of m_{tb} , as calculated from $t\bar{t}$ MC simulation and used for assigning the b/\bar{b} candidates as well as for the weighted average over the smeared solutions. *Figure reproduced from Ref. [212].*

$$p_{\nu_\ell,x} + p_{\bar{\nu}_\ell,x} = p_x^{\text{miss}}, \quad p_{\nu_\ell,y} + p_{\bar{\nu}_\ell,y} = p_y^{\text{miss}}. \quad (8.4)$$

Additionally, it is assumed that both the top quarks and W bosons are exactly on-shell, that is

$$p_{W^+}^2 = m_W^2, \quad p_{W^-}^2 = m_W^2 \quad (8.5)$$

and

$$p_t^2 = m_t^2, \quad p_{\bar{t}}^2 = m_t^2 \quad (8.6)$$

where m_t and m_W are the pole masses of the top quark and W boson, respectively. Applying these six constraints leads to a system of quartic equations for the neutrino three-momenta \vec{p}_{ν_ℓ} and $\vec{p}_{\bar{\nu}_\ell}$, which was solved in Ref. [223]. From these, the top and antitop quark four-momenta can then be calculated. Since the quartic equation can in general have up to four solutions, the solution with the lowest value of the invariant $t\bar{t}$ mass $m_{t\bar{t}}$ is chosen. This was found in Ref. [224] to minimize the bias in $m_{t\bar{t}}$ especially for low- $m_{t\bar{t}}$ events.

In practice, however, this method will often not give a solution even for those b jets which are correctly assigned to the truth-level b quarks. This is because the experimental inputs to the method - the jet and lepton four-momenta as well as \vec{p}_T^{miss} - will deviate from their truth-level values within the experimental resolution of the detectors and object reconstruction. In addition, the constraints will not be fulfilled exactly: There might be additional p_T^{miss} in the event because of e.g. neutrinos

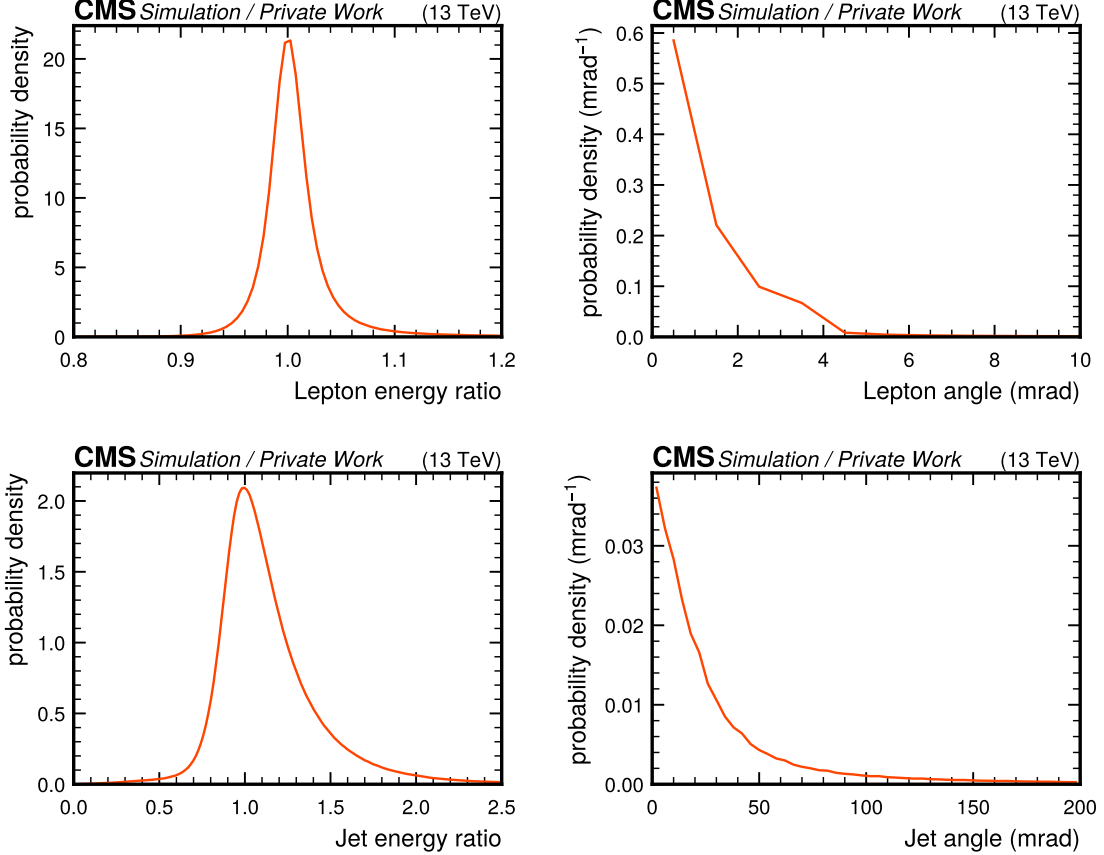


Figure 8.2: **Probability distributions used in the smearing of jets and leptons.**

The probability distributions for the ratio of measured and truth-level energies (left) as well as the angular difference between measured and truth-level three-momenta (right) for leptons (top) and jets (bottom). All distributions were calculated using $t\bar{t}$ MC simulation. *Figure reproduced from Ref. [212].*

produced in τ lepton or B hadron decays, and the W bosons and top quarks might be off-shell with respect to their pole masses within their respective widths.

To alleviate this, several of the input variables are randomly smeared to model the experimental resolution. For both the b jets and leptons, the energies are varied while keeping their masses constant, and the directions of their three-momenta are varied in a uniformly random direction. For both of these cases, the variations are randomly sampled from distributions obtained by comparing the measured and truth-level four-momentum in the nominal $t\bar{t}$ MC simulation, as shown in Fig. 8.2. The smearing of the jets is also propagated to the calculation of \vec{p}_T^{miss} . Additionally, the values of m_W used for the constraints on p_{W+} and p_{W-} are randomly sampled

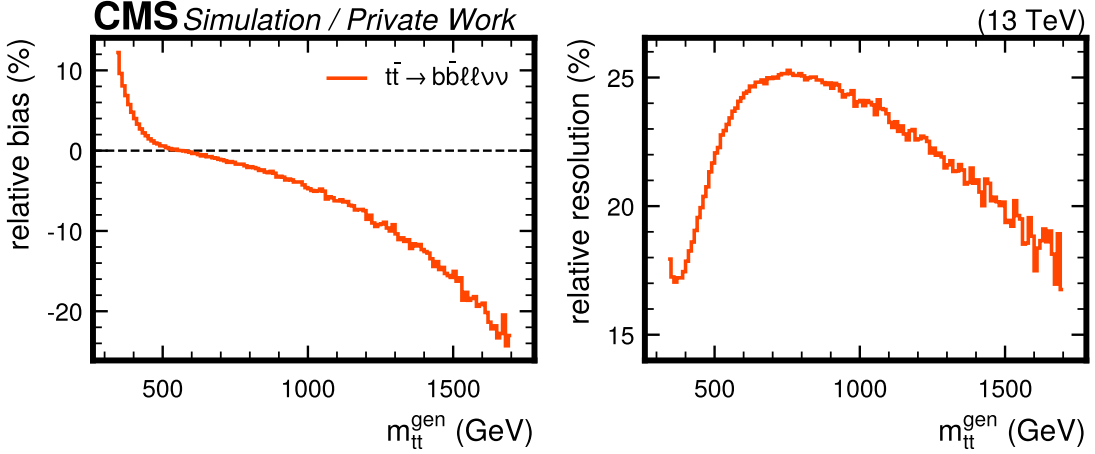


Figure 8.3: **Bias and resolution of $m_{t\bar{t}}$.** Relative bias and resolution of the $t\bar{t}$ reconstruction algorithm, defined in Eq. (8.8), as a function of parton-level $m_{t\bar{t}}$ after parton showering and evaluated in MC simulation of dileptonic $t\bar{t}$.

from a relativistic Breit-Wigner distribution corresponding to the W boson width Γ_W . This smearing procedure is repeated 100 times per event with different random values, resulting in up to 100 reconstructed $t\bar{t}$ systems per event, depending on the number of cases where there is no real solution.

Finally, one unambiguous solution per event is constructed by again using the invariant lepton-b quark masses and their truth-level likelihoods. For each iteration of the smearing procedure that yielded a real solution, a weight is defined as the product of the likelihoods for obtaining the smeared values of $m_{\ell+b}$ and $m_{\ell-\bar{b}}$, i.e.

$$w = \mathcal{P}(m_{\ell+b}) \cdot \mathcal{P}(m_{\ell-\bar{b}}) \quad (8.7)$$

The final solution for the reconstructed top and antitop four-momenta is defined as the weighted average over all real solutions, using the weight as given in Eq. (8.7).

For $t\bar{t} \rightarrow bb\ell\ell\nu\bar{\nu}$ events passing all previous selection steps, the efficiency of the full reconstruction algorithm to give any solution is ca. 90%, as evaluated in MC simulation. To assess the accuracy of the reconstruction relative to the parton-level top quarks, defined after parton showering, a per-event relative deviation is defined as

$$\Delta m_{t\bar{t}} = \frac{m_{t\bar{t}}^{\text{reco}} - m_{t\bar{t}}^{\text{gen}}}{m_{t\bar{t}}^{\text{gen}}}, \quad (8.8)$$

where $m_{t\bar{t}}^{\text{reco}}$ and $m_{t\bar{t}}^{\text{gen}}$ stand for the reconstructed and truth-level $m_{t\bar{t}}$, respectively. The mean and standard deviation of $\Delta m_{t\bar{t}}$ are then the relative bias and resolution of

the reconstruction algorithm. They are evaluated in simulation of dileptonic $t\bar{t}$ and shown in Fig. 8.3 as a function of truth-level $m_{t\bar{t}}$. The method shows a bias towards high $m_{t\bar{t}}$ for events with $m_{t\bar{t}}^{\text{gen}} \lesssim 500$ GeV and towards low $m_{t\bar{t}}$ for $m_{t\bar{t}}^{\text{gen}} \gtrsim 600$ GeV, with resolutions in the range of 17 – 25%. It should be noted here that this bias relative to the truth level is by itself not problematic as long as the MC describes the data well, since it is expected to be the same in both simulation and data and e.g. no unfolding of the reconstructed distributions to the truth level is attempted. This is explicitly checked in Sec. 8.7.3.

8.2.6 Sensitive observables

To distinguish the A/H and η_t signals from the background, three sensitive observables are considered. The first is the invariant $t\bar{t}$ mass $m_{t\bar{t}}$, defined with the reconstruction procedure as explained in the last section. As shown in Fig. 2.8, an A/H signal is expected to result in a peak-dip structure in $m_{t\bar{t}}$, where the zero crossing between peak and dip should be in the vicinity of the A/H mass. The magnitude as well as ratio of the peak and the dip depend non-linearly on the coupling modifier. The η_t signal, on the other hand, is expected to peak slightly below the $t\bar{t}$ production threshold at $m_{t\bar{t}} \simeq 2m_t - 2$ GeV as discussed in Sec. 2.3 and shown in Fig. 2.6. In practice, due to the limited detector resolution, the exact position of this peak will not be observable, and the signal will result in a generic enhancement of the yield for very low values of $m_{t\bar{t}}$.

In addition, the two spin correlation observables c_{hel} and c_{han} , as defined in Eq. (2.4) and Eq. (2.10), are used to gain further sensitivity. Both variables are again defined using the $t\bar{t}$ system reconstruction as described in the previous section. As discussed in Sec. 2.2.2, they are ideal for separating spin-singlet and spin-triplet states, respectively. Thus, A and η_t signals, producing singlet states, will have enhanced contributions at high values of c_{hel} , while H signals, producing 3P_0 triplet states, will be enhanced at low values of c_{han} . This allows not only for better discrimination between signal and background, but also to probe the \mathcal{CP} structure of a possible observed signal.

To combine all three variables, three-dimensional templates are created with $20 \times 3 \times 3$ bins in the three observables $m_{t\bar{t}}$, c_{hel} and c_{han} . For $m_{t\bar{t}}$, a non-equidistant binning is chosen to account for the decrease in production cross section at high values. An example can be seen in Fig. 8.4 for SM $t\bar{t}$ and three different signals (A, H and η_t).

8.3 Higher-order corrections in $t\bar{t}$

In this analysis, the SM $t\bar{t}$ background is irreducible - after all, it leads to the exact same final state as the signal. As a result, it is crucial to model it as precisely as

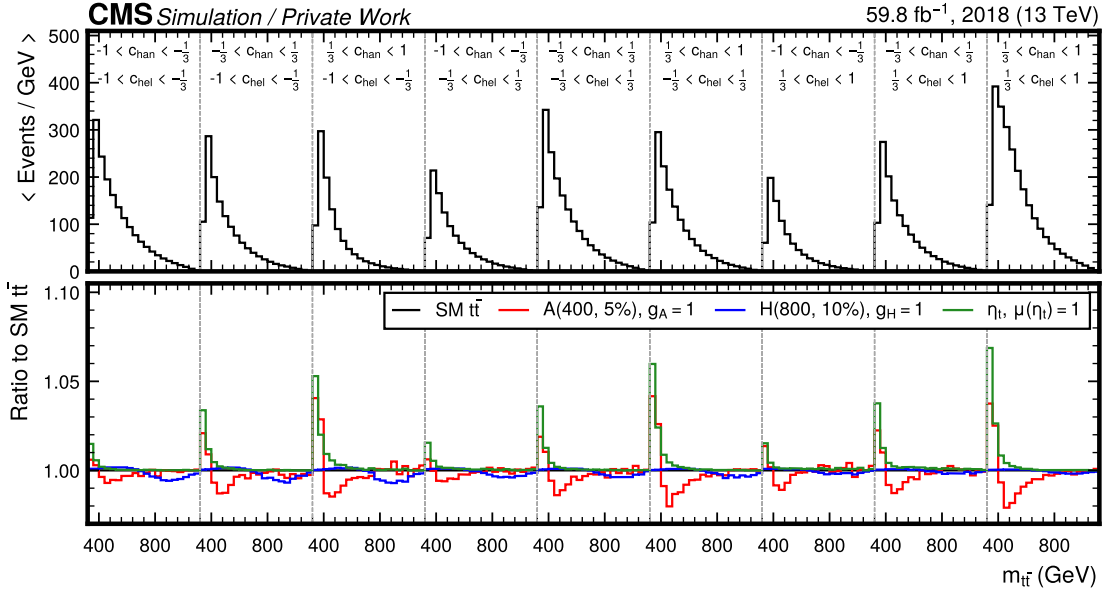


Figure 8.4: **3D template for** $m_{t\bar{t}} \times c_{\text{hel}} \times c_{\text{chan}}$ **for SM** $t\bar{t}$ (top) as well as three different example signals (bottom, shown as the ratio to SM $t\bar{t}$), corresponding to the luminosity taken in 2018 only.

possible: a mismodeling of the $t\bar{t}$ kinematic distribution, especially in $m_{t\bar{t}}$, might otherwise be confused for a signal and lead to bias.

As discussed in Sec. 4.1.2, the MC simulation used for the SM $t\bar{t}$ background is performed at NLO in QCD, employing the NWA for the top quarks. On top of this, two different sets of corrections are applied to include missing higher orders, namely NNLO QCD and NLO electroweak (EW) corrections. Both of these are estimated by comparing the MC simulation, which is matched to a parton shower, to fixed-order predictions. The simulation is then reweighted using scale factors binned two-dimensionally in $m_{t\bar{t}}$ and $\cos\theta_t^*$, where the latter is the cosine of the scattering angle of the top quark to the beam axis in the $t\bar{t}$ rest frame. These two variables fully define the kinematics of the top quarks in the $t\bar{t}$ rest frame, save for FSR emissions.

8.3.1 NNLO QCD corrections

The NNLO QCD predictions are obtained with the program MATRIX [164]. They are computed at the level of stable top quarks with a dynamic scale choice of

$$\mu_R = \mu_F = \frac{1}{2} \left(\sqrt{m t^2 + p_{T,t}^2} + \sqrt{m_{\bar{t}}^2 + p_{T,\bar{t}}^2} \right), \quad (8.9)$$

where $p_{T,t}$ and $p_{T,\bar{t}}$ are the transverse momenta of the top and antitop. Fig. 8.5

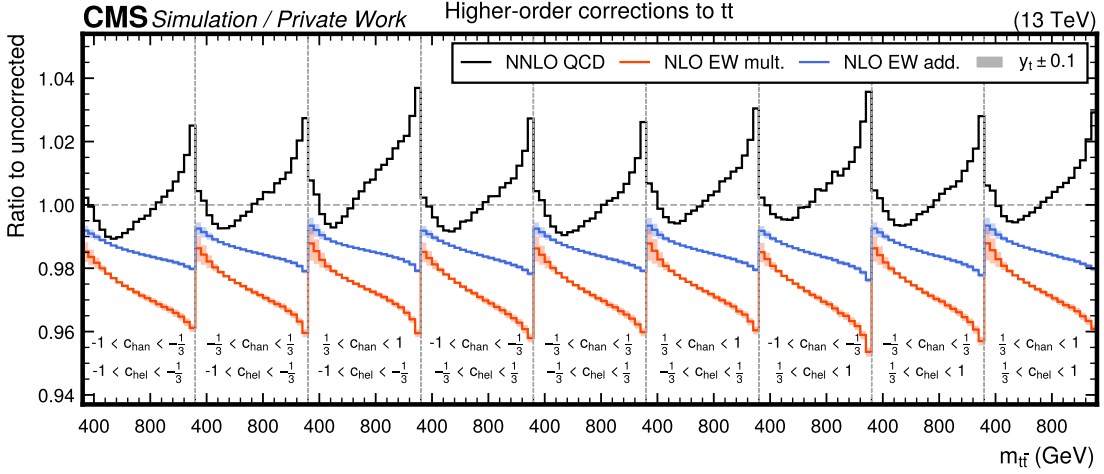


Figure 8.5: **Effect of NNLO QCD and NLO EW corrections** on the 3D $m_{t\bar{t}} \times c_{\text{hel}} \times c_{\text{han}}$ distribution after reconstruction in the form of ratios to the uncorrected distributions. The NNLO QCD corrections are shown as the solid black line, while the NLO EW corrections are shown in orange for the multiplicative scheme and in blue for the additive scheme. The effect of varying y_t by ± 0.1 in the NLO EW corrections is shown as the shaded bands.

shows the resulting effect on the 3D $m_{t\bar{t}} \times c_{\text{hel}} \times c_{\text{han}}$ distribution at the detector level as the black line. They are on the order of 1 – 2%.

8.3.2 NLO EW corrections

The NLO corrections in the electroweak coupling α_{EW} are computed with the HATHOR code [216, 225–227] using a dynamic scale choice of $\mu_R = \mu_F = \frac{1}{2}m_{t\bar{t}}$. Of particular interest here is a class of diagrams which contain an exchange of a virtual SM Higgs boson, an example of which is seen in Fig. 8.6. The matrix element for this diagram is proportional to the square of the SM Higgs-top Yukawa coupling y_t , giving a y_t^2 -dependent correction to $t\bar{t}$ distributions from the interference with LO diagrams. This correction is sizable mostly for low $m_{t\bar{t}}$ values, and is important for this analysis because the SM Higgs exchange might change the $t\bar{t}$ spin state and thus c_{hel} and c_{han} . To accurately account for this, the correction is derived separately for the different initial states (gg , $q\bar{q}$ and gq) of $t\bar{t}$ production.

The results obtained with HATHOR are accurate only to LO in α_S , i.e. $\mathcal{O}(\alpha_S^2)$, and as of the time of writing no full calculation including both NLO QCD and EW effects exists. Thus, there is an ambiguity on how the NLO-accurate (in QCD) MC simulation and the NNLO-accurate corrections presented in the previous section

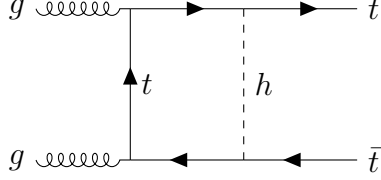


Figure 8.6: **EW correction involving a SM Higgs boson.** An example Feynman diagram for NLO EW corrections to $t\bar{t}$ production involving the exchange of a virtual SM Higgs boson h .

should be combined with the EW corrections.

Formally, the differential cross section as predicted by POWHEG can be decomposed as

$$\sigma_{\text{POWHEG}} = \alpha_S^2 \sigma_{\text{LO}} + \alpha_S^3 \sigma_{\text{NLO}} \quad (8.10)$$

where additional terms beyond $\mathcal{O}(\alpha_S^3)$ due to additional radiation in POWHEG and PYTHIA are not written for simplicity. On the other hand, HATHOR predicts

$$\sigma_{\text{HATHOR}} = \alpha_S^2 \sigma_{\text{LO}} + \alpha_S^2 \alpha_{\text{EW}} \sigma_{\text{EW}}. \quad (8.11)$$

One possible way to combine the calculations is the additive scheme, given by

$$\begin{aligned} \sigma_{\text{add.}} &= \sigma_{\text{POWHEG}} + \sigma_{\text{HATHOR}} - \alpha_S^2 \sigma_{\text{LO}} \\ &= \alpha_S^2 \sigma_{\text{LO}} + \alpha_S^3 \sigma_{\text{NLO}} + \alpha_S^2 \alpha_{\text{EW}} \sigma_{\text{EW}} \end{aligned} \quad (8.12)$$

which is formally accurate to $\mathcal{O}(\alpha_S^3)$ and $\mathcal{O}(\alpha_S^2 \alpha_{\text{EW}})$. This approach does not include any cross terms of order $\mathcal{O}(\alpha_S^3 \alpha_{\text{EW}})$, which are not fully calculated by either POWHEG or HATHOR. However, it is reasonable to assume that these cross terms factorize approximately, leading to the alternative multiplicative scheme [227]

$$\begin{aligned} \sigma_{\text{mult.}} &= \sigma_{\text{POWHEG}} \times \frac{\sigma_{\text{HATHOR}}}{\alpha_S^2 \sigma_{\text{LO}}} \\ &= \alpha_S^2 \sigma_{\text{LO}} + \alpha_S^3 \sigma_{\text{NLO}} + \alpha_S^2 \alpha_{\text{EW}} \sigma_{\text{EW}} + \alpha_S^3 \alpha_{\text{EW}} \frac{\sigma_{\text{NLO}} \sigma_{\text{EW}}}{\sigma_{\text{LO}}} \end{aligned} \quad (8.13)$$

The difference between the two schemes is in the last term of order $\mathcal{O}(\alpha_S^3 \alpha_{\text{EW}})$, which is an approximation to the QCD-EW cross terms. In this work, the multiplicative approach is used for all nominal results, while the difference to the additive approach is included as a systematic uncertainty. In both cases, the needed term $\alpha_S^2 \sigma_{\text{LO}}$ is computed with MG5_AMC@NLO.

The effect of both approaches on the 3D $m_{t\bar{t}} \times c_{\text{hel}} \times c_{\text{han}}$ distribution at the

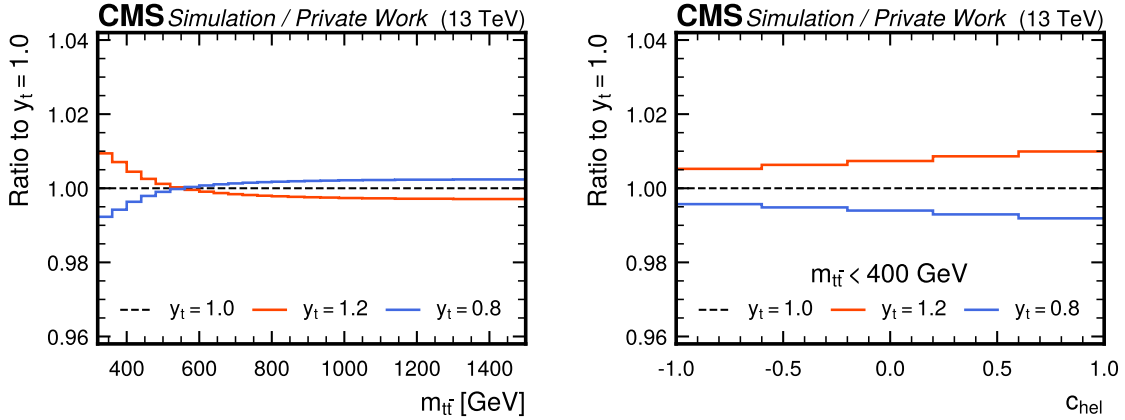


Figure 8.7: **Effect of y_t variations** in the NLO EW corrections for inclusive $m_{t\bar{t}}$ (left) and c_{hel} for $m_{t\bar{t}} < 400 \text{ GeV}$ (right), shown as the ratio to the nominal distributions ($y_t = 1.0$) for detector-level reconstructed observables.

detector level after parton showering can be seen in Fig. 8.5. The multiplicative scheme leads to a larger correction of roughly 2 – 4%, while the additive scheme only gives 1 – 2%.

Furthermore, the effect of varying y_t modifies not only the $m_{t\bar{t}}$ distribution close to the $t\bar{t}$ threshold, but also the distribution of c_{hel} . This is shown again more explicitly in Fig. 8.7 for the one-dimensional $m_{t\bar{t}}$ and c_{hel} distributions. As a result, such a variation in data could potentially be confused for a pseudoscalar signal. It is thus important to include it as a systematic uncertainty, as described in Sec. 8.5.

8.4 Matrix element reweighting for A/H signals

In order to probe the full phase space of the generic A/H model as described in Sec. 8.1, predictions at different A/H masses and widths with a sufficiently small spacing are required so that interpolation between the points is possible. However, generating a separate MC sample for each mass and width point is computationally very expensive.

8.4.1 Principle of the method

As an alternative, it is possible to re-use existing samples for different mass and width points via matrix element reweighting. This method works by noting that a given MC sample can be seen as a random sample, drawn from a probability distribution of the form

$$\mathcal{P}(x_i^{\text{ME}}, x_j^{\text{reco}}) = \mathcal{P}^{\text{ME}}(x_i^{\text{ME}}) \cdot \mathcal{P}^{\text{rem}}(x_j^{\text{reco}} | x_i^{\text{ME}}) \quad (8.14)$$

Here, x_i^{ME} are all variables defining the event at the matrix element (ME) level, i.e. at the level of the hard interaction, and x_j^{reco} are all variables after detector simulation and object reconstruction. For the case of the A/H signals, which are generated at LO in QCD, x_i^{ME} is given by the four-momenta and helicities of the final-state particles (leptons, neutrinos and b quarks) in the hard process. The x_j^{reco} consist of all possible reconstruction-level variables that are relevant to the analysis, such as e.g. jet and lepton four-momenta, lepton identification criteria or \vec{p}_T^{miss} .

$\mathcal{P}^{\text{ME}}(x_i^{\text{ME}})$ refers to the probability density of the ME-level variables as predicted by the ME generator, which will be proportional to the absolute square of the matrix element. This function will depend on the chosen scenario of the A/H model, i.e. $m_{\text{A}/\text{H}}$ and $\Gamma_{\text{A}/\text{H}}$. Meanwhile, the conditional probability density $\mathcal{P}^{\text{rem}}(x_j^{\text{reco}}|x_i^{\text{ME}})$ encodes the effects of all other components of the simulation chain, such as the parton shower, hadronization, detector simulation and reconstruction. It gives the probability to observe reconstruction-level variables x_j^{reco} for an event with ME-level variables x_i^{ME} .

The principal assumption of the method is now that \mathcal{P}^{rem} , and thus the whole simulation chain except for the matrix element, is independent of the underlying A/H signal scenario ($m_{\text{A}/\text{H}}$ and $\Gamma_{\text{A}/\text{H}}$). This assumption is certainly true for the detector simulation and reconstruction, while care must be taken for the parton shower, which in general needs to be matched to the matrix element and can this way have a residual dependence. The validity of the assumption will be discussed in more detail below.

If the assumption is fulfilled, a given A/H MC sample generated with parameters $m_{\text{A}/\text{H}}^0$ and $\Gamma_{\text{A}/\text{H}}^0$ can now be reweighted to a different A/H scenario with parameters $\hat{m}_{\text{A}/\text{H}}$ and $\hat{\Gamma}_{\text{A}/\text{H}}$ by applying to each event i a weight

$$w_i = \frac{\mathcal{P}^{\text{ME}}(x_i^{\text{ME}}|\hat{m}_{\text{A}/\text{H}}, \hat{\Gamma}_{\text{A}/\text{H}})}{\mathcal{P}^{\text{ME}}(x_i^{\text{ME}}|m_{\text{A}/\text{H}}^0, \Gamma_{\text{A}/\text{H}}^0)} \quad (8.15)$$

The quantities in the denominator and nominator are the ME-level probability densities for each event, evaluated at the original and target A/H parameters, respectively. When this weight is inserted into Eq. (8.14), the original probability cancels, giving the correct probability density for the target scenario $\hat{m}_{\text{A}/\text{H}}$ and $\hat{\Gamma}_{\text{A}/\text{H}}$.

In practice, this method will only work if the MC sample used for the reweighting has sufficient phase space overlap with the target A/H scenario, i.e. if the two probabilities in Eq. (8.15) are not too different from each other for the majority of the events. Otherwise, the weights will become very small in some regions of the phase space and very large in others, resulting in poor statistics for the reweighted sample.

The method was implemented by directly evaluating the squared matrix elements for the different A/H hypotheses, using the standalone reweighting interface provided by MG5_AMC@NLO and the same UFO model as for the signal generation.

8.4.2 Combination of multiple origin samples

At the time of this analysis, a set of signal samples for different A/H scenarios (as given in Sec. 8.2.1) was already available. These samples were used as origin samples for the reweighting. To maximize the statistical power of the method and to mitigate problems from poor phase space overlap, subsets of the available samples were combined during reweighting and ranked with an average event weight.

In detail, this procedure works as follows: First, a set of several samples j (the origin samples) with different parameters $m_{A/H}$ and $\Gamma_{A/H}$ are all reweighted separately to the same target parameters $\hat{m}_{A/H}$ and $\hat{\Gamma}_{A/H}$ with per-event weights $w_{i,j}$ as given in Eq. (8.15). These need to be multiplied with a possible generator weight of the origin sample $u_{i,j}$, giving the total per-event weight $\hat{w}_{i,j} = w_{i,j}u_{i,j}$. For fully unweighted origin samples, $u_{i,j} = 1$.

Then, the different samples are weighted with a per-sample weight v_j proportional to

$$v_j \propto \langle \hat{w}_{i,j} \rangle^{-1} = \frac{\sum_i \hat{w}_{i,j}}{\sum_i \hat{w}_{i,j}^2} \quad (8.16)$$

where the sums run over all the events i in the considered sample j . This expression is the inverse of the average ME weight for sample j . It is chosen such that samples with large phase space overlap with the target A/H scenario - and thus small ME weights $w_{i,j}$ - are assigned a large weight v_j in the combination of samples. Similarly, samples with poor phase space overlap, and thus large average ME weights, get assigned small weights and contribute less strongly to the combined sample. Finally, the total combined sample is normalized to the expected cross section for the target scenario, which is calculated independently. It is shown in App. C.1 that this procedure minimizes the total statistical error of the combined sample.

In practice, all available masses and parities (A and H) are combined for each target A/H mass. Resonance and interference contributions are treated separately from each other. Furthermore, it was found that, for the resonance contribution only, it is necessary to split the combination of different A/H widths into two halves: those with $\Gamma_{A/H}/m_{A/H}$ less or greater than 10%. This is due to an interplay of MG5_AMC@NLO and the PYTHIA shower leading to a dependency on the A/H width in the matrix element, which is not taken into account in the reweighting. For $\Gamma_{A/H}/m_{A/H} < 10\%$ (narrow resonance), MG5_AMC@NLO includes the intermediate A/H particle in the event record, which is then treated by PYTHIA as a unstable resonance and its virtuality as predicted by the matrix element is preserved. For $\Gamma_{A/H}/m_{A/H} \geq 10\%$ (broad resonance), the A/H particle is not included in the event record, and its virtuality is thus not preserved. This leads to slight differences in distributions affected by the parton showering. The choice of 10% for the transition between the two modes is an arbitrary parameter, and thus not necessarily physical. Nonetheless, it was decided in this analysis to not mix the two width ranges in the

reweighting in order to obtain full closure with a standalone generation.

8.4.3 Validation

The combined reweighting is validated for two masses of $m_{A/H} = 400$ and 800 GeV as well as widths of 2.5 and 10% . For each of these points, the reweighting is performed as stated above, but leaving out A/H scenarios with the same mass from the combination of origin samples since otherwise the weights would be trivially one. The reweighted $m_{t\bar{t}}$ distributions at generator level are then compared to the standalone samples at the same $m_{A/H}$ and $\Gamma_{A/H}$.

The resulting comparisons and residuals can be seen in Fig. 8.8 for A and H, separated into the resonance and interference contributions. It can be seen that the closure between reweighting and standalone generation is excellent within the statistical uncertainties.

8.5 Systematic uncertainties

Similar to Sec. 6.5, systematic uncertainties affect the distributions of both SM background and signal processes. They are listed in this section, split into theory (Sec. 8.5.1) and experimental uncertainties (Sec. 8.5.2).

8.5.1 Theory uncertainties

Scale uncertainties Uncertainties due to missing higher orders in the matrix element as well as the parton shower are included separately for the SM $t\bar{t}$, tW, and Z+jets backgrounds as well as all considered signals by varying the associated scales by a factor 2 up and down independently, same as in Sec. 6.5. Only the shape components of the ME scales are taken from the respective ME generators, while the normalization uncertainty is treated externally, as described below. For A and H, the uncertainties are considered uncorrelated between the resonance and interference components, which is found to be conservative. For η_t , the renormalization scale uncertainty is not included since the considered model does not encode any dependence on either μ_R or α_S .

PDF uncertainties For the SM $t\bar{t}$ background, the uncertainty due to the PDF is again included based on the 100 provided eigenvalues of the NNPDF 3.1 PDF set. However, it is not sufficient to simply take the envelope of these variations since this would capture only the change in $t\bar{t}$ normalization, while this analysis is mostly sensitive to shape variations.

Instead, a principal component analysis (PCA) is performed on the final 3D $m_{t\bar{t}} \times c_{\text{hel}} \times c_{\text{han}}$ templates obtained from the different eigenvalues, thus finding those

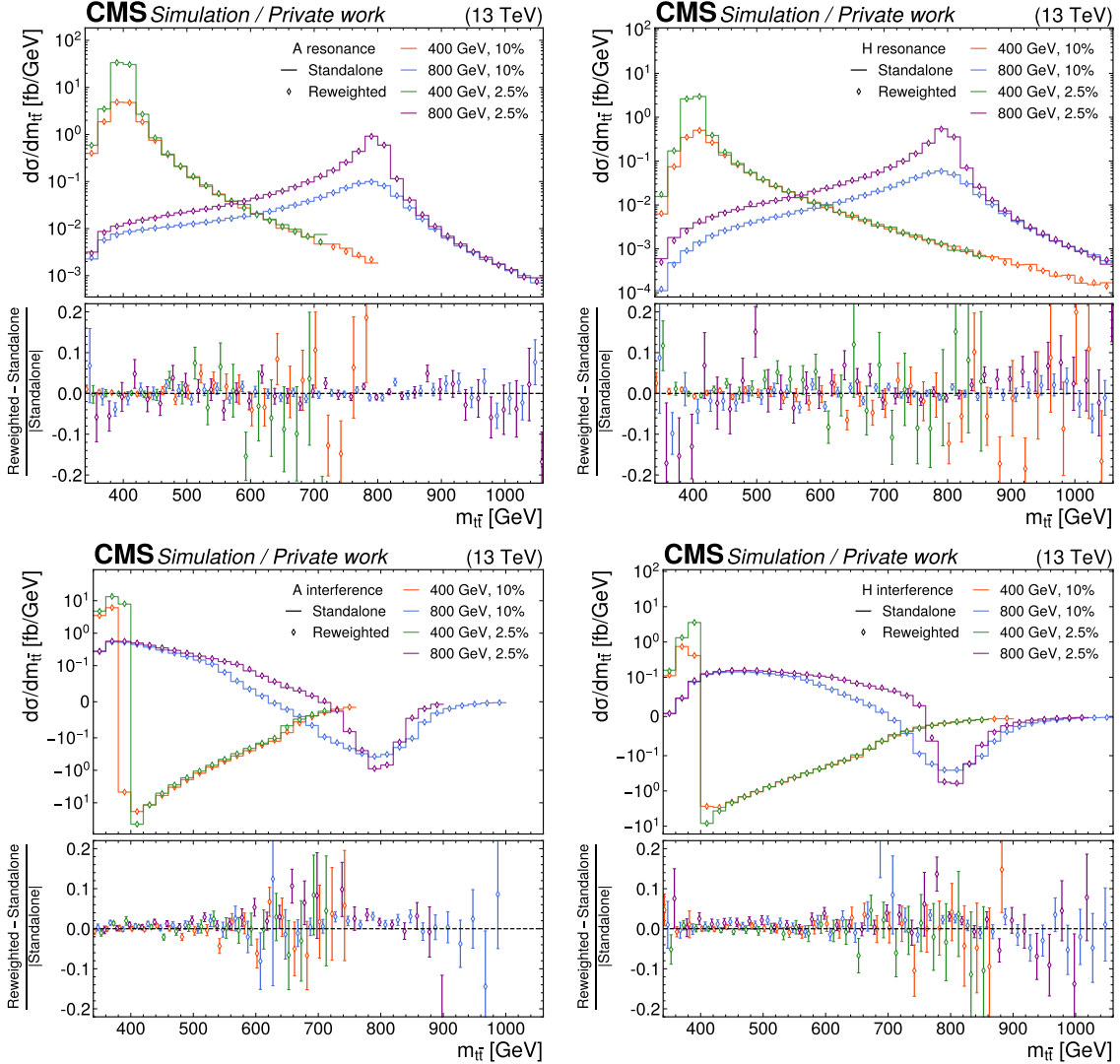


Figure 8.8: **Validation of the ME reweighting.** Comparison of standalone generated (lines) and reweighted (diamond markers) $m_{t\bar{t}}$ distributions for different values of $m_{A/H}$ and $\Gamma_{A/H}$. From top left to bottom right: A resonance, H resonance, A interference, H interference. The lower panel shows the difference of reweighted and standalone distributions, normalized to the standalone distributions. The error bars give the combined statistical uncertainty of the reweighted and standalone sample.

linear combinations that have a noticeable shape effect. Only the first eigenvector (corresponding to the largest eigenvalue) is non-negligible, and this variation is considered as the PDF uncertainty. For more details on this procedure, see Ref. [212]. Independently of this, another uncertainty based on the value of α_S in the PDF is considered similarly to Sec. 6.5.

EW correction uncertainties As described in Sec. 8.3.2, two independent uncertainties are attached to the NLO electroweak correction of SM $t\bar{t}$: First, the value of the SM top-Higgs Yukawa coupling is allowed to vary in the range $y_t = 1.00^{+0.11}_{-0.11}$, with the range given by the uncertainty of the experimental measurement in Ref. [228]. Second, the difference between the additive and multiplicative application scheme (Eqs. (8.12) and (8.13)) is considered as a separate uncertainty, as recommended in Ref. [227], and symmetrized around the nominal.

Top quark mass uncertainty The top quark mass uncertainty in SM $t\bar{t}$ is estimated by varying it from its nominal value of $m_t = 172.5 \text{ GeV}$ by $\pm 3 \text{ GeV}$ in the POWHEG simulation, and then scaling down the resulting relative deviation by a factor $1/3$, leading to a $\pm 1 \text{ GeV}$ uncertainty. This is done since the variation, obtained from an independent MC sample, is otherwise plagued by large statistical uncertainties. Furthermore, the top mass is also varied in all considered signal samples directly by $\pm 1 \text{ GeV}$ through an ME reweighting method similar to Sec. 8.4. The chosen range of $\pm 1 \text{ GeV}$ is conservative with respect to the most precise top mass measurements at the time of writing, which have uncertainties on the order of 0.4 GeV [20, 144]. The top mass uncertainties between background and signals are considered as fully correlated.

Further uncertainties in SM $t\bar{t}$ Additionally, separate SM $t\bar{t}$ samples are used to evaluate uncertainties due to ME/PS matching (same as in Sec. 6.5), the underlying event tune [139], and the color reconnection model in PYTHIA [143, 229]. All of these effects are found to be small.

Background cross section uncertainties For the SM $t\bar{t}$ background, the shift in the predicted NNLO+NNLL $t\bar{t}$ cross section due to the ME scale variations as well as the top quark mass is calculated with Top++ [158] in the same manner as the nominal cross section. The resulting shifts in the cross section are $^{+20.5}_{-17.9} \text{ pb}$ for a variation of μ_F by a factor two up and down, $^{+30.1}_{-9.6} \text{ pb}$ for a similar variation of μ_R , and $^{+22.5}_{-23.5} \text{ pb}$ for a top mass variation in the range $\pm 1 \text{ GeV}$. These three variations are treated as fully correlated with the respective shape uncertainties obtained at NLO from the POWHEG simulation as described above, so that no additional nuisance parameter for the $t\bar{t}$ normalization is introduced.

For minor backgrounds, explicit uncertainties of 15% for tW and t-channel single top [230–232], 30% for diboson and $t\bar{t} + X$ [233, 234], and 5% for the data-driven Z/γ^* +jets normalization [235] are considered, which are all based on the precision of relevant cross section measurements.

Background statistical uncertainties Again similar to Sec. 6.5, per-bin background statistical uncertainties for all simulated processes are included following Ref. [181].

8.5.2 Experimental uncertainties

Jet and p_T^{miss} uncertainties The uncertainty on the calibration of the jet p_T detector response is assessed through the “reduced” set of subsources provided by the CMS Collaboration, which encompasses seven different subsources. Of these, five subsources are found to be relevant for this analysis, while two subsources affecting mainly the endcaps and hadronic forward calorimeter are negligible. The five relevant subsources are:

- The absolute scale uncertainty, referring to the constant term in the jet p_T response (“**Absolute- The relative scale uncertainty in the barrel and first part of the endcaps ($|\eta| < 2.5$), encoding the p_T dependence of the jet p_T response (“**BBEC1- An uncertainty due to residual differences in the η dependence between JECs derived in dijet, Z+jets, and γ +jets selections (“**RelativeSample- An uncertainty due to residual differences between different methods of deriving the JECs (“**RelativeBal- An uncertainty due to the difference in jet flavor response in PYTHIA and HERWIG, considered separately for b quark jets (“**FlavorPureBottomFlavorQCD**********

Furthermore, the uncertainty in the jet p_T resolution is considered separately, again uncorrelated between years. All jet uncertainties are fully propagated to the calculation of p_T^{miss} , and an additional p_T^{miss} uncertainty based on soft, unclustered hadronic activity is also considered.

b tagging uncertainties Similarly, the uncertainty on the b tagging efficiency is split into 17 subsources, corresponding e.g. to different parton shower modeling, the treatment of leptons in the jet, or the propagation of the jet p_T scale uncertainties [166]. One component represents the statistical uncertainty and is thus considered uncorrelated, while all others are correlated among years. Moreover, an uncertainty on mistagging of light-flavor jets is included, also split into a statistical and a systematic component.

Lepton and trigger uncertainties Uncertainties on the lepton reconstruction, identification, and isolation efficiencies, as measured centrally in CMS using the tag-and-probe method, are considered separately for muons and electrons [103, 165]. For the muons, the uncertainty is split into a statistical component (uncorrelated between the analysis years) and a systematic component (correlated), which is based on e.g. the requirements applied to the tag muon or the choice of function used for the tag-and-probe fit. Similarly, the dilepton trigger efficiency uncertainties are considered uncorrelated between years and lepton flavor channels. Finally, in data taken in 2016 or 2017, an additional uncertainty is assigned due to an inefficiency in the ECAL L1 trigger [109], as described in Sec. 8.2.4.

Luminosity uncertainty The uncertainty on the total integrated luminosity is included following Refs. [146, 236, 237], leading to a total luminosity uncertainty of 1.6%, split into a total of seven components that encode the correlations between the years. Similar as in Sec. 6.5, the largest single contributions to the uncertainty come from factorization between the x and y axes during scans used for the luminosity calibration as well as due to residual differences between different luminosity detectors [146].

Pileup uncertainty To estimate the uncertainty on the amount of pileup per pp bunch crossing, the effective inelastic proton-proton cross section used for pileup reweighting in the simulation is varied by 4.6% from its nominal value [238].

8.5.3 Uncertainty smoothing

Several of the considered uncertainty sources, e.g. the top quark mass in SM $t\bar{t}$, are estimated by comparing to separate MC samples, which causes the relative deviation due to the source to be affected by large statistical noise. A similar problem appears for uncertainties which effectively vary the cuts applied on MC events, such as e.g. the jet p_T scale uncertainties by way of jet acceptances. If left untreated, fitting these noisy shape templates to the data could lead to erroneous constraints in the likelihood fit.

To prevent this, a smoothing procedure based on the algorithm LOWESS (short for *locally weighted scatterplot smoothing*) [239, 240] is applied to these sources. The procedure follows Ref. [33] and is described briefly in the following. First, the relative deviation of the respective source is defined as $r^\pm = (N^\pm - N^0)/N^0$, where N^0 , N^+ , and N^- are the event yields for the nominal template, the up variation, and the down variation. They are considered three-dimensionally (3D) as a function of the sensitive observables $\vec{x} = (m_{t\bar{t}}, c_{\text{hel}}, c_{\text{han}})$. To avoid artifacts from the choice of binning in the analysis, the number of bins along each direction of \vec{x} is doubled for the purpose of the smoothing.

Second, for each bin in \vec{x} , a 3D hyperplane is fitted to r^\pm using a least-squares fit. The fit is performed in a 3D *sliding window* with a fixed size of $2h_i$ in each direction, where h_i with $i = 1, 2, 3$ is the *bandwidth* along each axis. This means that only bins close to the bin that is being evaluated enter in the fit. Furthermore, the bins enter the fit with a weight depending on their distance to the bin being evaluated. If \vec{x} denotes the bin being evaluated, the weight of bin \vec{y} is given by [33]

$$w(\vec{x}, \vec{y}) = (1 - d(\vec{x}, \vec{y})^3)^3, \quad d(\vec{x}, \vec{y}) = \sqrt{\sum_i \left(\frac{x_i - y_i}{2h_i} \right)^2}. \quad (8.17)$$

The function $w(\vec{x}, \vec{y})$ equals 1 for $\vec{x} = \vec{y}$, i.e. each bin enters with maximal weight 1 in its own fit, and falls off to 0 when \vec{y} tends towards the edge of the sliding window as given by h_i . This local weighting thus favors points close to the bin being evaluated.

The bandwidths h_i are free parameters of the method and are chosen using *leave-one-out cross validation* for each uncertainty source separately. In this method, the events making up the templates are randomly split into 10 batches, and nine of these batches are combined into the *training set* while the last is considered the *testing set*. The smoothing is applied to the relative deviation as computed from the training set, where the three bandwidths are scanned in fixed grids given by $h_i \in (0.1, 0.2, 0.5, 0.7, 1.0)$ for $m_{t\bar{t}}$ and $h_i \in (0.33, 0.50, 0.83, 1.0)$ for c_{hel} and c_{han} , all understood as relative to the total bin range in the respective axis. The resulting smoothed template is compared to the unsmoothed template in the testing set, and a χ^2 is computed taking into account the statistical uncertainty of the testing set. This procedure is repeated with each of the ten batches as the testing set, and it is further repeated 50 times with different random partitions. For each choice of bandwidths, the average χ^2 from all repetitions is computed, and the set of bandwidths which minimizes the average χ^2 is chosen for the smoothing.

To further prevent the algorithm from erroneously interpreting statistical noise as shape information, each relative deviation is also fitted using a constant line. The χ^2 is again calculated, and if it is found to be smaller than the χ^2 obtained from the smoothing, the uncertainty source in question is replaced by a pure normalization

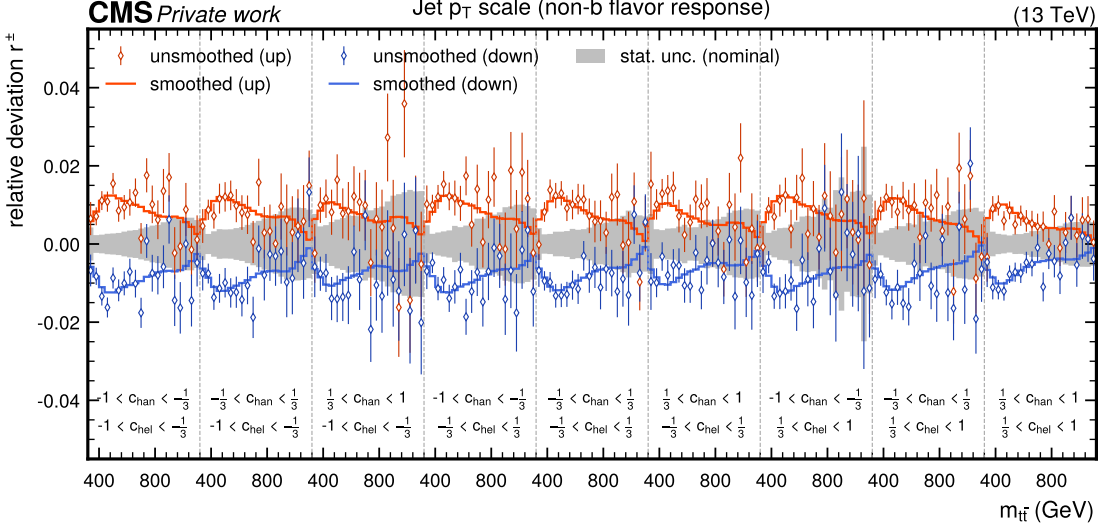


Figure 8.9: **Uncertainty smoothing.** The smoothed (solid lines) and unsmoothed (diamond markers) relative deviations in $m_{t\bar{t}} \times c_{\text{hel}} \times c_{\text{han}}$, shown for the example of the JEC subsource encoding the flavor response of non-b quark jets. The MC statistical uncertainty of the nominal sample is shown in gray.

uncertainty as given by the constant line fit. In practice, this is relevant for some of the minor backgrounds as well as the signals due to the small statistics of their samples, but never occurs for the SM $t\bar{t}$ background.

The results of the smoothing for the optimal bandwidth are shown for the example of the JEC subsource encoding the flavor response of non-b quark jets (the largest of the JEC subsources) in Fig. 8.9. The noise visible in the unsmoothed distributions is fully mitigated by the smoothing procedure.

8.5.4 Differences between MC generators

It has been observed that the theoretical uncertainties collected in Sec. 8.5.1 do not necessarily cover the differences in the predictions of different MC generators for $t\bar{t}$ [31, 32, 195, 241]. To assess the size of these effects, the standard $t\bar{t}$ prediction, as computed using POWHEG in the NWA matched to PYTHIA (cf. Sec. 4.1.2), is compared to alternate generator setups.

The first of these is the same POWHEG matrix element in the NWA (using the hvq subprocess in POWHEG) matched to the multi-purpose event generator HERWIG instead of PYTHIA. The angular-ordered parton shower in HERWIG is used (as opposed to the p_T -ordered dipole shower in PYTHIA) together with the CMS CH3 tune [242]. Furthermore, HERWIG uses a cluster hadronization model [243] instead

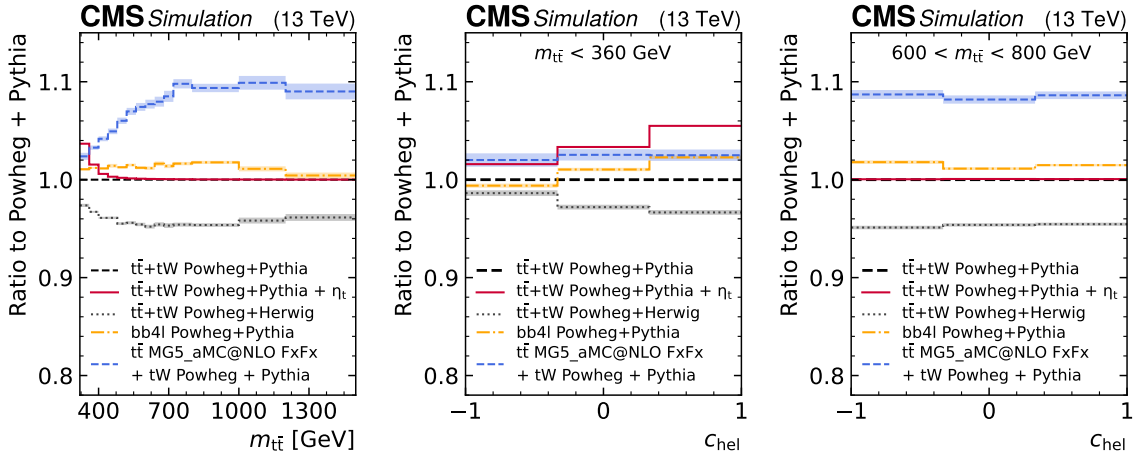


Figure 8.10: **Comparison between MC generators for $t\bar{t} + tW$.** The predictions of different MC setups, namely POWHEG $t\bar{t} + tW$ matched to HERWIG (gray), bb4l matched to PYTHIA (orange), and MG5_AMC@NLO matched to PYTHIA (blue), all shown as the ratio to the prediction of POWHEG $t\bar{t} + tW$ matched to PYTHIA, for the inclusive reconstructed $m_{t\bar{t}}$ distribution (left) as well as the reconstructed c_{hel} distribution, restricted to $m_{t\bar{t}} < 360 \text{ GeV}$ (center) and to $600 < m_{t\bar{t}} < 800 \text{ GeV}$ (right). The effect of the η_t signal is also shown in red for comparison [8].

of the string hadronization model of PYTHIA as described in Sec. 4.4.

Figure 8.10 shows the ratios of the predictions from HERWIG and PYTHIA for the reconstructed $m_{t\bar{t}}$ distribution, as well as for the c_{hel} distribution close to the $t\bar{t}$ threshold (i.e. where the η_t signal is located) and in the $t\bar{t}$ continuum. Besides a significantly lower $t\bar{t}$ acceptance, HERWIG predicts an increase of events at the $t\bar{t}$ threshold similar to η_t . This appears concerning at first glance since, should the data follow the prediction from HERWIG instead of PYTHIA, this enhancement could be confused with an η_t signal if PYTHIA is used as the baseline prediction. However, as seen in Fig. 8.10 in the center, HERWIG at the same predicts a flatter slope in c_{hel} than PYTHIA at the $t\bar{t}$ threshold, equivalent to a reduction of $t\bar{t}$ spin correlations¹. This is in contrast to the η_t signal, in which the $t\bar{t}$ spins are maximally anti-correlated. The inclusion of the spin correlation variable c_{hel} in the analysis thus ensures that a possible signal cannot be faked if the data follow the HERWIG instead of the PYTHIA prediction.

The second alternative generator is bb4l matched to PYTHIA, as studied extensively in Chapter 7. Here, particularly the off-shell effects included in bb4l might be of interest for the extraction of η_t since the latter is located below the $t\bar{t}$ threshold.

¹This effect was also seen in the context of Ref. [32].

The setup denoted as “**bb41 v2**” in Sec. 7.2, corresponding to Ref. [196], is used, and compared to the sum of the NWA-based POWHEG $t\bar{t}$ and tW predictions for consistency exactly like in Sec. 7.3.1.

A caveat here is presented by the corrections to NNLO QCD and NLO EW as described in Sec. 8.3. These are derived from fixed-order corrections assuming stable top quarks, and are not available for the full $b\bar{b}\ell\ell\nu\bar{\nu}$ final state. To still be able to apply them to **bb41** predictions, the **bb41** sample is split into a $t\bar{t}$ and a tW part in an ad-hoc way by using the matrix element history projectors implemented in **bb41 v2** [196]. The corrections are then applied to the $t\bar{t}$ part only, in the same manner as to the NWA-based POWHEG $t\bar{t}$ sample.

The ratios of the predictions are also shown in Fig. 8.10. It can be seen that **bb41** does not predict major differences in the reconstructed $m_{t\bar{t}}$ spectrum (left) even at its lower edge. However, it results in a significantly steeper slope in reconstructed c_{hel} close to the threshold (center). This increase in slope is of similar magnitude as the effect expected due to η_t .

The source of this difference is not yet fully understood. **bb41** contains NLO QCD corrections to the top decay which are not present in the NWA-based $t\bar{t}$ sample (though they are approximated through the matrix element corrections in PYTHIA). However, NLO corrections to spin correlations are expected to be only on the percent level and to reduce the spin correlation instead of enhancing it [23].

It is possible that the effect instead originates in the $t\bar{t}/tW$ interference: For the tW contribution, where one of the leptons is not actually the decay product of a top quark, c_{hel} does not analyze spin correlation, since there is only one (anti-)top involved in the process. Therefore, the slope of the reconstructed c_{hel} distribution under the SM prediction for tW is not related to $t\bar{t}$ spin correlation and thus in general different to the slope in SM $t\bar{t}$. The same holds for the $t\bar{t}/tW$ interference. Since **bb41** now gives a true prediction of the $t\bar{t}/tW$ interference instead of the ad-hoc treatment of the DR and DS schemes (cf. Sec. 7.3), it is expected that the magnitude of the interference contribution in **bb41** will be different. Thus, it is possible that the total c_{hel} slope, arising from the combination of $t\bar{t}$, tW, and $t\bar{t}/tW$ interference, will be different as well.

A third alternative prediction is provided by $t\bar{t} + \text{jets}$ production simulated with MG5_AMC@NLO, matched to PYTHIA with the FxFx scheme [135]. While this prediction is formally also NLO-accurate in QCD in the NWA, and thus comparable to the NWA-based POWHEG prediction, it has been observed in past measurements that MG5_AMC@NLO does not agree as well with data as POWHEG for $t\bar{t}$ production. Indeed it shows a large slope in the $m_{t\bar{t}}$ distribution, as also seen in Fig. 8.10. As a result, MG5_AMC@NLO is given less focus compared to the other two predictions here.

At high values of $m_{t\bar{t}}$, the slope of c_{hel} is consistent between all considered generators, as shown in Fig. 8.10 (right). Only normalization differences due to acceptance as well as the shape differences in $m_{t\bar{t}}$ remain. This shows that the modeling of spin

correlations in the bulk of the $m_{t\bar{t}}$ distribution is reliable and should be considered uncontroversial.

In this work, NWA-based $t\bar{t}$ using POWHEG + PYTHIA is considered for the nominal background prediction in all cases. A comparison to POWHEG + HERWIG, MG5_AMC@NLO + PYTHIA, and bb4l + PYTHIA is shown in Sec. 8.7.3 in the context of measuring the η_t cross section. Furthermore, the effect of including the differences to POWHEG + HERWIG and bb4l + PYTHIA as two additional shape-based nuisance parameters in the fit is similarly given in Sec. 8.7.3. Note that in Ref. [8], these nuisance parameters were considered as part of the main result in order to be conservative with respect to the total uncertainty.

8.6 Pre-fit distributions

The agreement between the total MC prediction, including all corrections described in Secs. 8.2.4 and 8.3, and the observed data are presented in this section. Shown observables are lepton p_T , η , and $\Delta\phi_{\ell\ell}$ (Fig. 8.11); jet p_T , η , and number of jets (Fig. 8.12); as well as p_T^{miss} , the invariant mass of the two leptons $m_{\ell\ell}$, and the invariant mass of the two leptons and two b tagged jets $m_{b\bar{b}\ell\ell}$ (Fig. 8.13). All of them are shown after all lepton, jet, b tag and p_T^{miss} requirements, but before the $t\bar{t}$ reconstruction, summed over all analysis years, and separately for the same-flavor (ee and $\mu\mu$) and opposite-flavor ($e\mu$) channels, since the latter have different backgrounds and cuts.

Furthermore, different distributions resulting from the $t\bar{t}$ reconstruction are shown in Fig. 8.14 for all three channels combined. They consist of top quark p_T , η , and scattering angle $\cos\theta^*$, as well as the three observables used for the fit $m_{t\bar{t}}$, c_{hel} , and c_{chan} .

It can be seen that there is a slight but consistent over-prediction of the background normalization compared to the data in almost all distributions, which could be due to a small misestimation of the acceptance. Alternatively, it could originate from the NNLO+NNLL $t\bar{t}$ cross section used to normalize the sample; inclusive cross section measurements have consistently shown a slightly lower cross section in data compared to this prediction (cf. Fig. 6.16). Since this analysis is mostly sensitive to shape effects, and the normalization difference is covered by the uncertainties, this is unproblematic in this context.

Furthermore, there is a slight slope in the ratio of data and simulation yields in the p_T of leptons, jets or the reconstructed top quarks. This is likely a result of the well-known top quark p_T mismodeling at the LHC, which is not fully removed by NNLO QCD corrections as used here [177, 179]. It is fully covered by the matrix element scale uncertainties, which are evaluated at NLO as discussed in Sec. 8.5.1. A related discrepancy is seen for high values of $|\eta|$ and is similarly covered. Moreover, there is a small discrepancy for large number of jets, which is fully covered by matrix

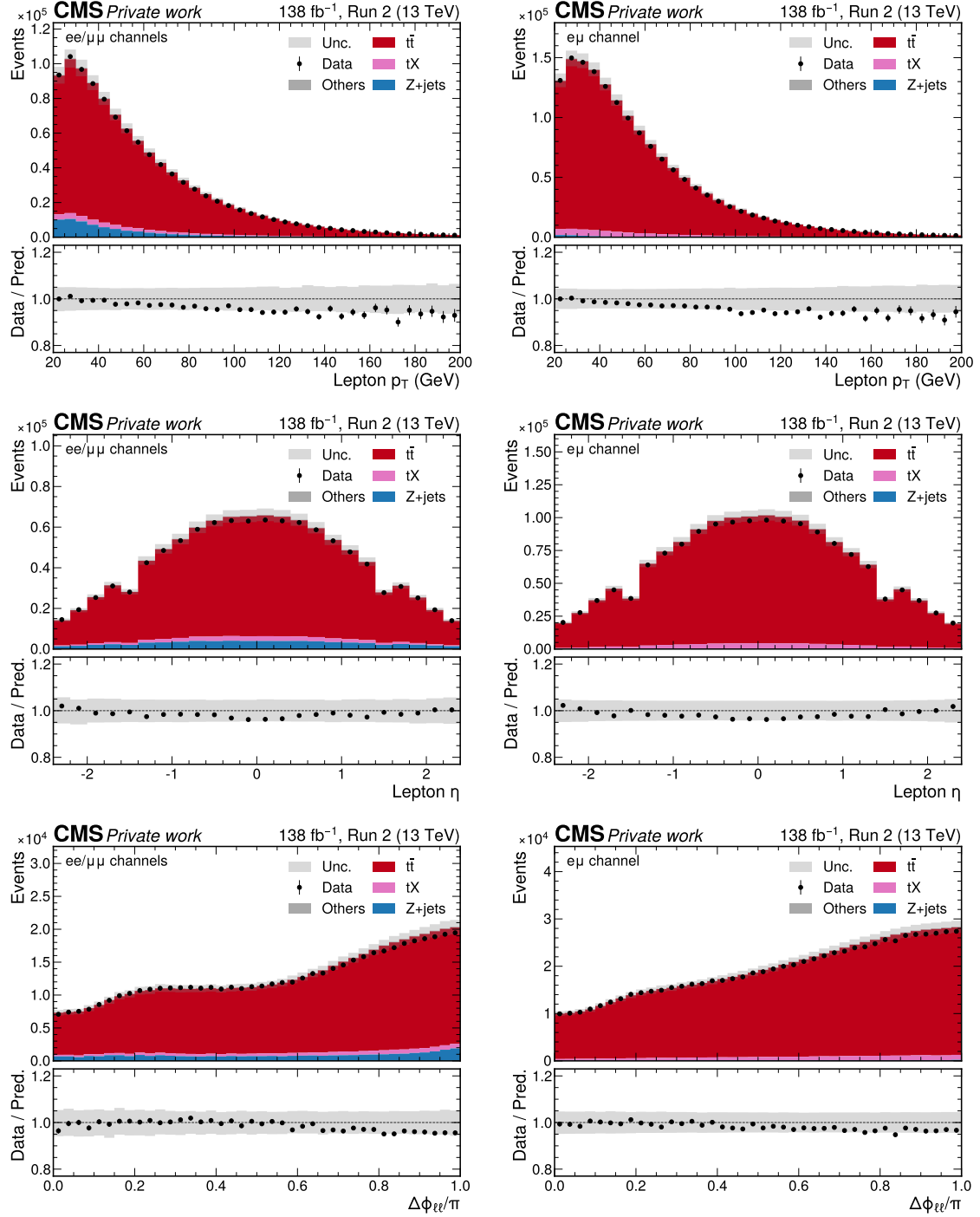


Figure 8.11: **Control distributions.** Shown are the distributions of p_T of both leptons (top), η of both leptons (center), and the azimuthal angle $\Delta\phi_{\ell\ell}/\pi$ between the leptons (bottom) in the combined $ee/\mu\mu$ channels (left) and the $e\mu$ channel (right). All figures show both data (black dots) and different simulated background processes (colored bars), as well as the total systematic uncertainty (gray band).

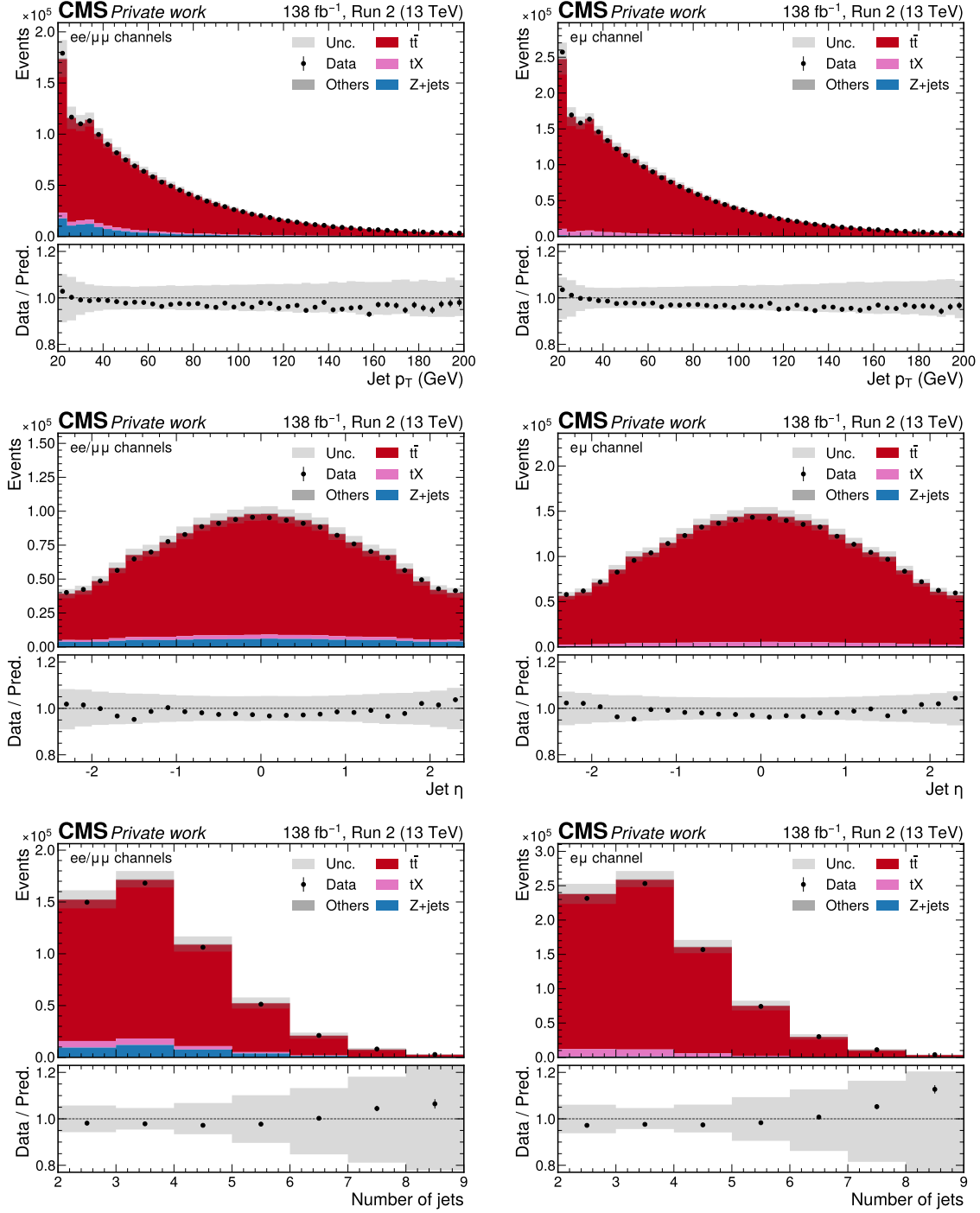


Figure 8.12: **Control distributions.** Shown are the distributions of p_T of all jets (top), η of all jets (center), and the number of jets (bottom) in the combined ee/μμ channels (left) and the eμ channel (right). All figures show both data (black dots) and different simulated background processes (colored bars), as well as the total systematic uncertainty (gray band).

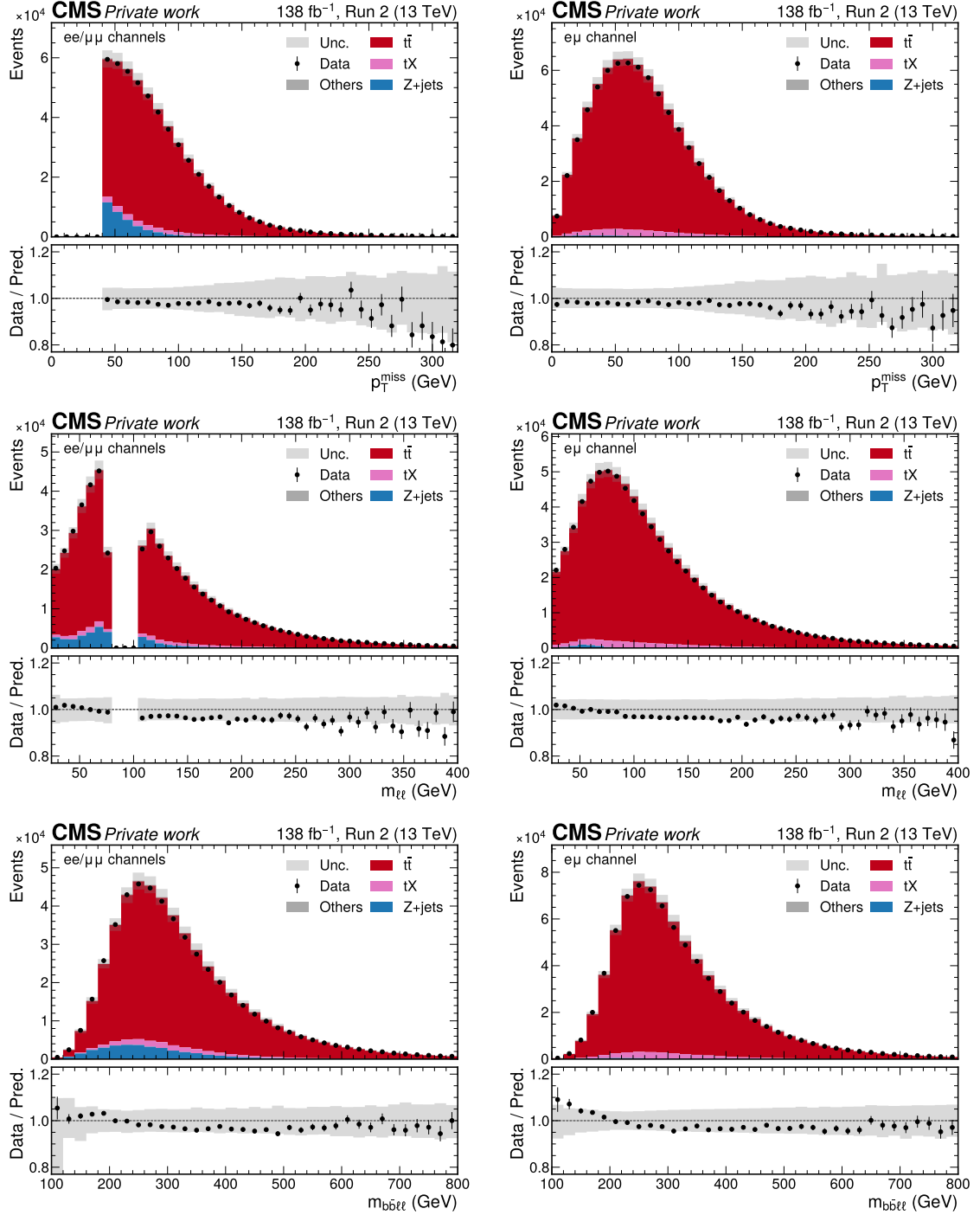


Figure 8.13: Control distributions. Shown are the distributions of p_T^{miss} (top), $m_{\ell\ell}$ (center), and the invariant mass $m_{bb\ell\ell}$ of both b candidates and both leptons (bottom) in the combined ee/ $\mu\mu$ channels (left) and the e μ channel (right). All figures show both data (black dots) and different simulated background processes (colored bars), as well as the total systematic uncertainty (gray band).

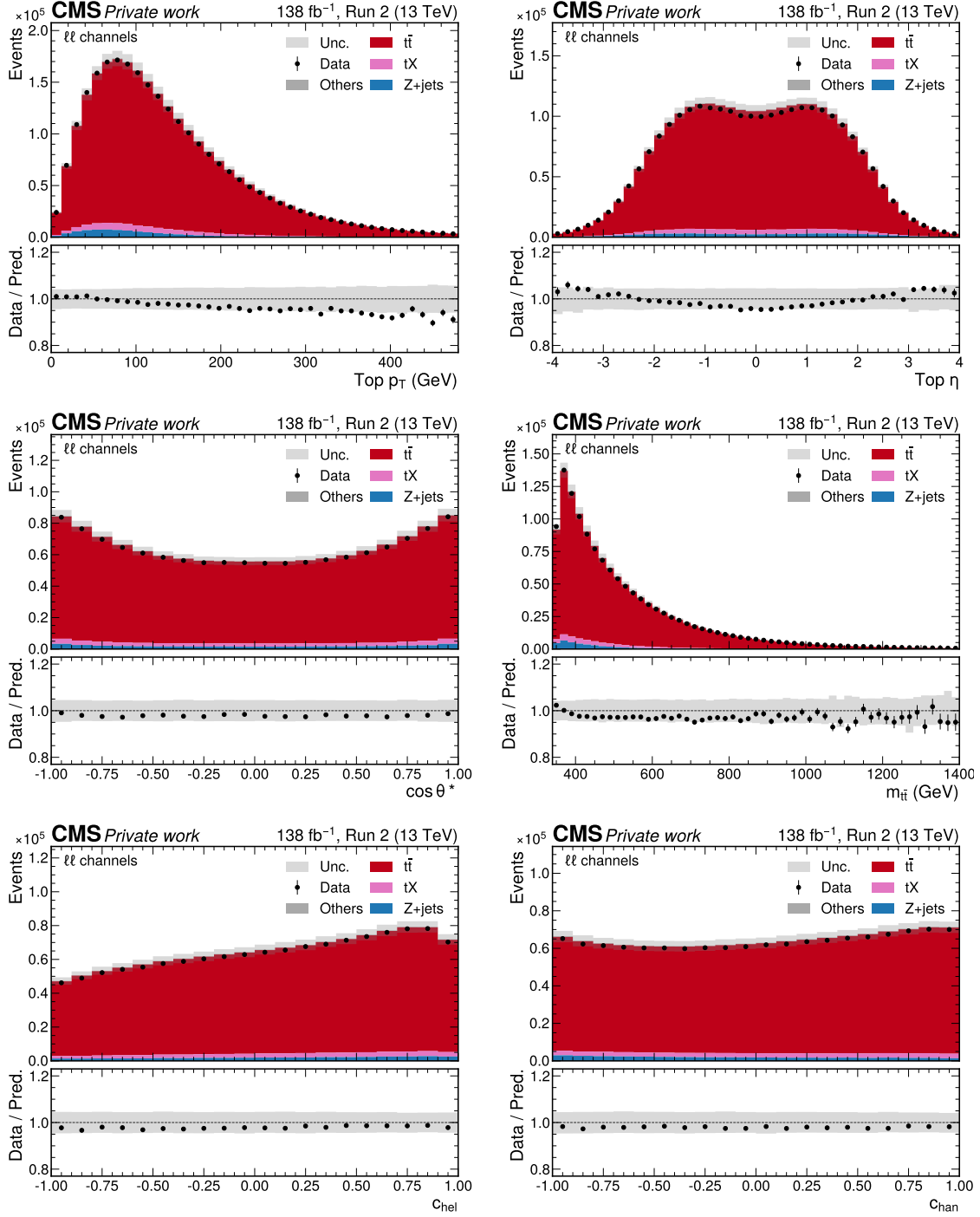


Figure 8.14: **Control distributions after $t\bar{t}$ reconstruction.** Shown are (from top left to bottom right) the distributions of the top quark p_T , top quark η , $m_{t\bar{t}}$, $\cos \theta^*$, c_{hel} and c_{han} for the combined dilepton channels. All figures show both data (black dots) and different simulated background processes (colored bars), as well as the total systematic uncertainty (gray band).

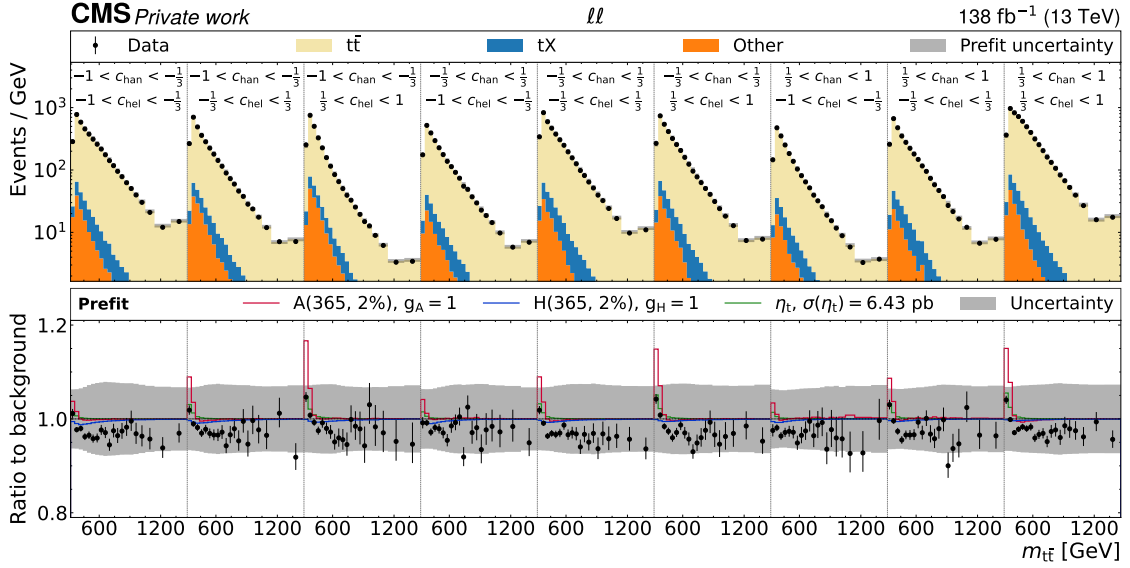


Figure 8.15: **Prefit distributions of $m_{t\bar{t}} \times c_{\text{hel}} \times c_{\text{han}}$.** The unrolled three-dimensional distribution in $m_{t\bar{t}}$, c_{hel} and c_{han} as used for statistical analysis before the fit to the data, summed over all years and lepton flavors. The upper panel shows the sum of the background simulation (colored bars) and the observed data (black dots), while the lower panel shows the ratio of the data to the prediction, with different signals overlaid: A (red) and H (blue), both for $m_{A/H} = 365$ GeV and $\Gamma_{A/H}/m_{A/H} = 2\%$, and η_t (green) [9].

element and parton shower scale systematics (cf. Sec. 8.5.1). In total, all distributions show agreement within the statistical and systematic uncertainties.

Finally, the three-dimensional $m_{t\bar{t}} \times c_{\text{hel}} \times c_{\text{han}}$ distribution used for the statistical analysis is shown before the fit, including all systematic uncertainties, in Fig. 8.15. A notable excess of the data compared to the prediction is observed for low values of $m_{t\bar{t}}$, consistent with the excess seen in the one-dimensional $m_{t\bar{t}}$ distribution (Fig. 8.14) and in the related observables $m_{\ell\ell}$ and $m_{b\bar{b}\ell\ell}$ (Fig. 8.13). The excess is stronger for large values of c_{hel} as seen from the multi-dimensional binning, while no trend can be seen by eye regarding c_{han} .

8.7 Interpretation of the excess

8.7.1 Extraction of $t\bar{t}$ bound state effects

The prefit excess visible in Fig. 8.15 is interpreted in terms of a pseudoscalar $t\bar{t}$ bound state by performing a signal+background fit with η_t as the signal, as defined

in Sec. 2.3. The POI in the fit is $\sigma(\eta_t)$, the cross section of the η_t model, which can be understood as the difference between the data and the fixed-order perturbative QCD (FO pQCD) background prediction. It is measured to be

$$\sigma(\eta_t) = 8.7 \pm 0.5(\text{stat}) \pm 1.0(\text{syst}) \text{ pb} = 8.7 \pm 1.1 \text{ pb}. \quad (8.18)$$

The statistical and systematic component of the uncertainty are estimated as described in Chapter 5. The significance of the result compared to a background-only hypothesis, i.e. without a bound state, is more than five standard deviations.

The result is in agreement with the estimate of 6.4 pb given in Ref. [47], obtained by fitting the results of an NRQCD calculation from Ref. [43]. No uncertainty for this number is given in Ref. [47], and it is furthermore not one-to-one comparable since it considers only the range of $m_{t\bar{t}} \in [338, 350]$ GeV. It should be noted that the results of Ref. [43] (as well as the newer ones in Ref. [44]) were obtained by using NLO hard functions for the NRQCD calculations, and moving to NNLO might give a significant increase in cross section, by analogy to the difference in NNLO and NLO cross sections for the $t\bar{t}$ continuum. Furthermore, the NRQCD approach employed in these calculations considers only the ground state wavefunction of the bound $t\bar{t}$ system, and independent calculations have shown that including contributions from excited states could increase the cross section by orders of 15–20% [244, 245].

The postfit $m_{t\bar{t}} \times c_{\text{hel}} \times c_{\text{han}}$ distribution can be seen in Fig. 8.16 for the combined dilepton channels. The data, including the excess at low $m_{t\bar{t}}$, is described well by the η_t model combined with the FO pQCD background. To illustrate this further, one-dimensional projections of the $m_{t\bar{t}} \times c_{\text{hel}} \times c_{\text{han}}$ template into inclusive $m_{t\bar{t}}$, as well as into c_{hel} for both low and high $m_{t\bar{t}}$, are shown in Fig. 8.17. One can clearly see that the data at the $t\bar{t}$ threshold shows a stronger slope in data than in the FO pQCD prediction, consistent with the η_t signal. At the same time, no such slope is seen above the threshold, i.e. in the $t\bar{t}$ continuum where no $t\bar{t}$ bound state effects are expected (Fig. 8.17 right).

8.7.2 Parity of the excess

To investigate whether the observed excess is \mathcal{CP} -odd (pseudoscalar) or \mathcal{CP} -even (scalar) in nature, a simultaneous fit is performed with both η_t and χ_t , as defined in Sec. 2.3, as freely floating signals. These correspond to pure 1S_0 and 3P_0 $t\bar{t}$ states, respectively, both localized at the $t\bar{t}$ threshold.

The result is shown in Fig. 8.18 in the form of compatibility contours. Consistent with the result of the η_t -only fit, a non-zero η_t contribution is preferred by the fit by more than 5 standard deviations. By contrast, the measured χ_t cross section, which can be seen as the 3P_0 component of the excess, is compatible with zero within one standard deviation. Based on this, it can be said that the observed excess is dominated by a pseudoscalar or 1S_0 spin state.

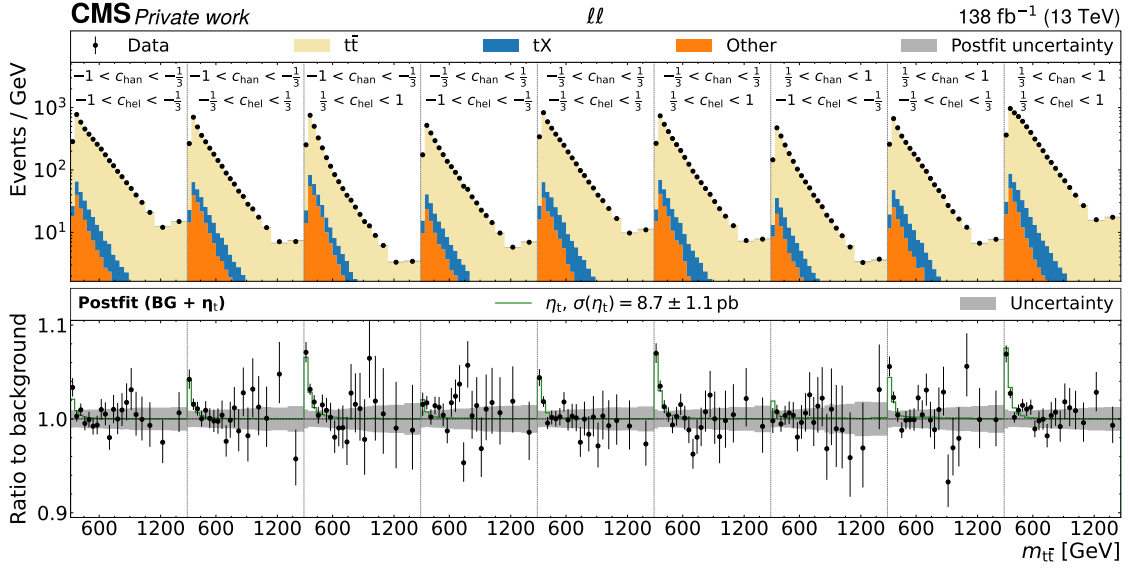


Figure 8.16: **Postfit distributions of $m_{t\bar{t}} \times c_{\text{hel}} \times c_{\text{han}}$ for the η_t fit.** The unrolled three-dimensional distribution in $m_{t\bar{t}}$, c_{hel} and c_{han} as after the fit to data with η_t as the signal, summed over all years and lepton flavors. The upper panel shows the sum of the background simulation (colored bars) and the observed data (black dots), while the lower panel shows the ratio of the data to the prediction with the postfit η_t signal overlaid [8].

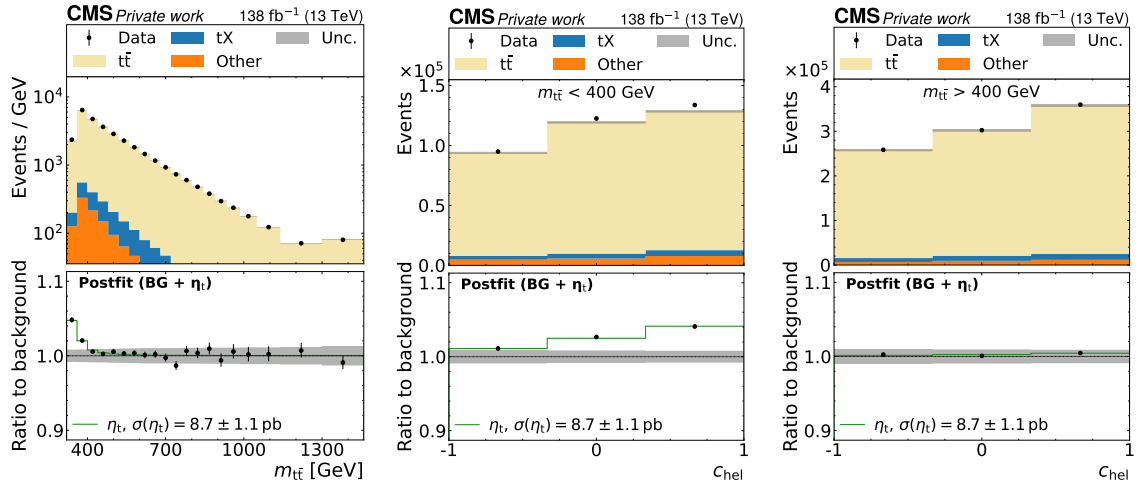


Figure 8.17: **Postfit distributions of $m_{t\bar{t}}$ and c_{hel} for the η_t fit.** One-dimensional distributions of inclusive $m_{t\bar{t}}$ (left), c_{hel} for $m_{t\bar{t}} < 400$ GeV (center), and c_{hel} for $m_{t\bar{t}} > 400$ GeV (right), projected from the $m_{t\bar{t}} \times c_{\text{hel}} \times c_{\text{han}}$ template in Fig. 8.16 with the same notations [8].

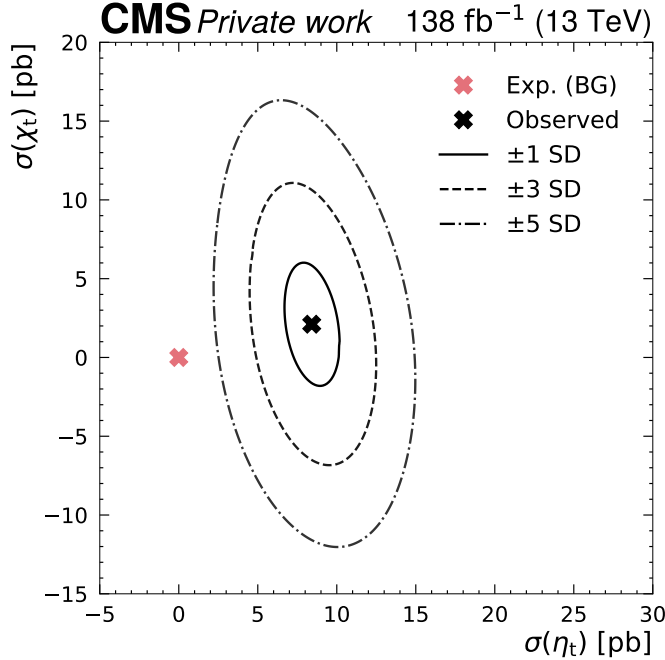


Figure 8.18: **Parity of the excess.** Observed compatibility contours in a simultaneous fit of η_t (corresponding to ${}^1\text{S}_0$) and χ_t (corresponding to ${}^3\text{P}_0$). The best-fit point is shown as the black cross, while the BG-only expectation (i.e. $\sigma(\eta_t) = \sigma(\chi_t) = 0$) is marked in pink [8].

8.7.3 Checks of the result

Nuisance parameter pulls and impacts In Fig. 8.19, nuisance parameter pulls, constraints and impacts for the η_t extraction fit are presented, following the definitions in Chapter 5. The most impactful nuisances are all related to the modeling of the $t\bar{t}$ background. In particular, the value of the top Yukawa coupling y_t in the EW corrections is the leading uncertainty. This is notably one of the few uncertainties which can lead to a steeper c_{hel} slope in the $t\bar{t}$ prediction and could thus to some degree be confused for η_t , as discussed in Sec. 8.3.2.

Further important modeling uncertainties for both η_t and FO pQCD $t\bar{t}$ production are the FSR scales in the parton shower as well as the top quark mass. The latter is constrained to a postfit uncertainty of ± 0.4 GeV, and fully compatible with the nominal value of 172.5 GeV. This strong constraint is similar in size to the current most precise direct top quark mass measurements [20, 144]. While it is expected that the $m_{t\bar{t}}$ distribution is strongly sensitive to the top quark mass, it is still surprising that the constraint competes with dedicated top quark mass measurements.

To verify that the constraint does not lead to an underestimation of the uncertainty on $\sigma(\eta_t)$, the top quark mass nuisance parameter is decorrelated in two different

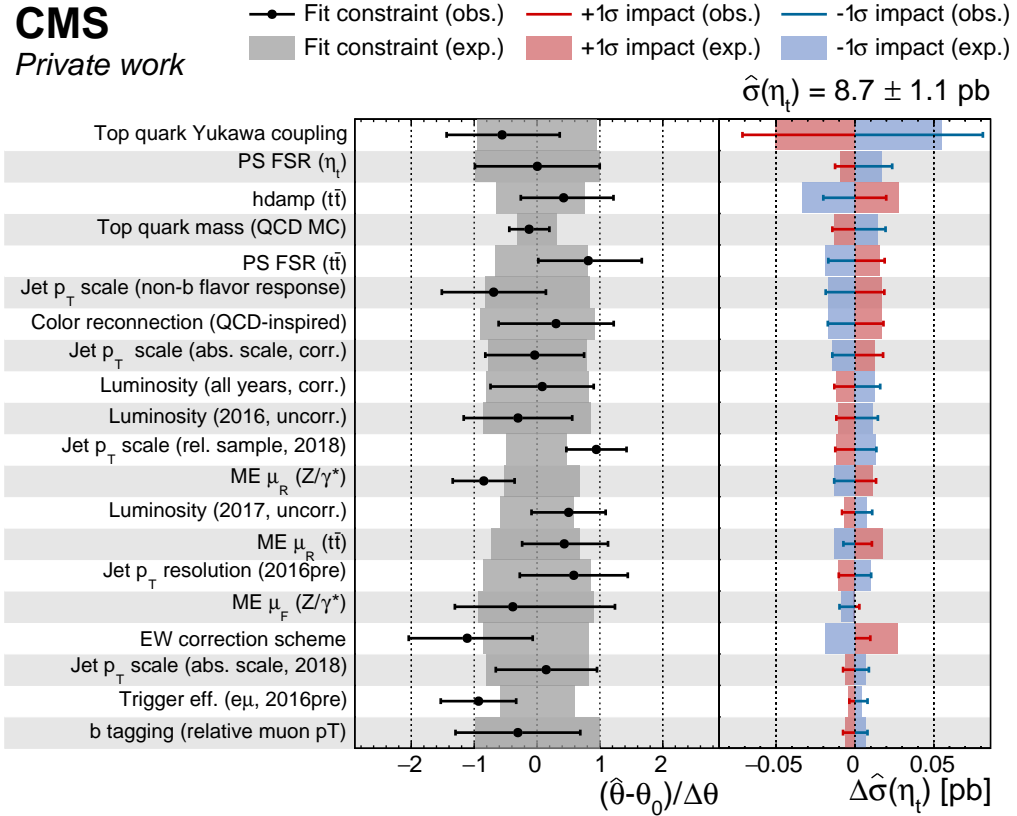


Figure 8.19: **Nuisance parameter pulls and impacts.** Expected and observed pulls, constraints, and impacts on the η_t cross section for the most impactful nuisance parameters in the η_t -only fit [8].

ways: either by splitting it into three regions defined by $m_{t\bar{t}} < 400 \text{ GeV}$, $400 < m_{t\bar{t}} < 600 \text{ GeV}$, and $m_{t\bar{t}} > 600 \text{ GeV}$, or by decorrelating it between the nine c_{hel} and c_{han} bins used for the measurements. In both cases, similar constraints are found on those nuisance parameters corresponding to the sensitive regions of phase space, i.e. for the threshold region when splitting in $m_{t\bar{t}}$ and for the high- c_{hel} bins when splitting in c_{hel} and c_{han} , and the extracted η_t cross section is compatible with the nominal result.

A strong pull of around -1 is further observed in the EW correction scheme uncertainty. This uncertainty effectively encodes missing knowledge from NLO QCD-NLO EW cross terms in the higher-order corrections to $t\bar{t}$ as discussed in Sec. 8.3.2, with a nuisance parameter value of $+1$ corresponding to no cross terms (the additive scheme) and 0 corresponding to approximated cross terms (the multiplicative scheme). A pull of -1 could thus imply that the cross terms are underestimated by this approximation, though this is speculation as no full computation of the cross terms has been performed at the time of writing.

Experimental nuisances like the jet energy scales, on the other hand, influence mostly $m_{t\bar{t}}$ and thus do not have a large impact on the POI. Of note here are the pulls and constraints in nuisance parameters which influence only one of the four analysis eras, namely a subsource of the jet p_T scale in 2018, the uncorrelated component of the integrated luminosity in 2017, and the $e\mu$ trigger efficiency in 2016pre. The pulls imply that there are small inconsistencies (within one standard deviation) between the eras that are not accounted for in the MC simulation. Since this measurement is performed in a high-statistics region of phase space and with a large luminosity, it is expected to constrain ratios between normalization effects in different years, while of course the overall normalization (i.e. the total integrated luminosity) should be not pulled or significantly constrained. The exact source of the per-year differences is not clear; however, due to the small impact on the POI, this is not considered a problem.

In total, no pulls much larger than one prefit standard deviation are observed, indicating that the uncertainty model accommodates the data well.

Fit using $m_{b\bar{b}\ell\ell}$ instead of $m_{t\bar{t}}$ The three observables $m_{t\bar{t}}$, c_{hel} and c_{han} are all obtained from the kinematic reconstruction as described in Sec. 8.2.5. This procedure assumes, among others, that the top quarks are exactly on-shell with a fixed mass of 172.5 GeV. For η_t , which is located below the $t\bar{t}$ threshold, this assumption is clearly violated. Since the same kinematic reconstruction procedure is applied to simulation and data, this is in principle not a problem as long as the virtuality of the top quarks is well described by simulation and residual differences are covered by systematic uncertainties. However, since the modeling of η_t in particular is rather uncertain, it is still important to check whether this assumption in the kinematic reconstruction introduces any bias.

This is done by repeating the fit with the observable $m_{t\bar{t}}$ replaced by $m_{b\bar{b}\ell\ell}$ (as shown also in Fig. 8.13), thus removing kinematic information obtained via the reconstruction from the fit. The kinematic reconstruction is still performed, however, to obtain c_{hel} and c_{han} ².

The resulting $m_{b\bar{b}\ell\ell} \times c_{\text{hel}} \times c_{\text{han}}$ postfit distribution can be found in Figs. 8.20 and 8.21. It can be seen that the excess is still clearly present, though with a wider spread due to the coarser resolution of $m_{b\bar{b}\ell\ell}$ compared to $m_{t\bar{t}}$. An η_t cross section of $\sigma(\eta_t) = 7.5 \pm 1.8$ pb is extracted, which is in agreement with the nominal result within one standard deviation. For high $m_{b\bar{b}\ell\ell}$ values, corresponding to events far above the $t\bar{t}$ threshold, the data agrees well with the FO pQCD prediction.

Alternate generator setups The influence of the choice of generator setup for the $t\bar{t}$ prediction is further quantified by repeating the η_t extraction fit with alternate setups. Besides the nominal setup using NWA-based $t\bar{t}$ calculated in POWHEG

²It has separately been checked that the requirement for events to pass the kinematic reconstruction does not bias the result, either.

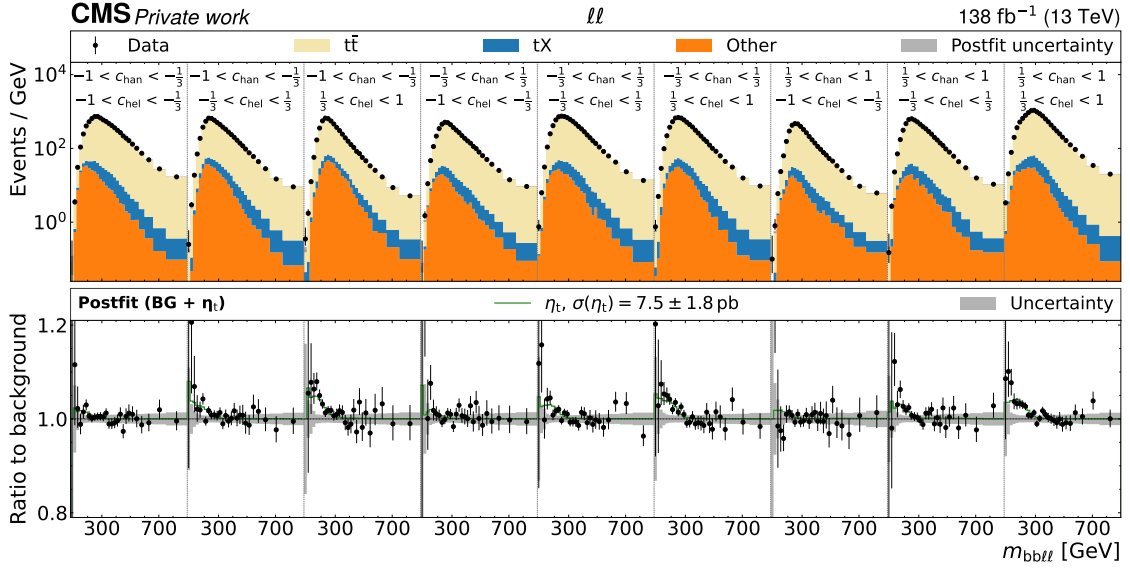


Figure 8.20: **Postfit distributions of $m_{b\bar{b}\ell\ell} \times c_{\text{hel}} \times c_{\text{han}}$ for the η_t fit.** The unrolled three-dimensional distribution in $m_{b\bar{b}\ell\ell}$, c_{hel} and c_{han} after the fit to data with η_t as the signal using $m_{b\bar{b}\ell\ell}$ instead of $m_{t\bar{t}}$, summed over all years and lepton flavors. The first $m_{b\bar{b}\ell\ell}$ bin in each $c_{\text{hel}} \times c_{\text{han}}$ slice is an underflow bin containing events with $m_{b\bar{b}\ell\ell} < 80$ GeV. Otherwise, notations are as in Fig. 8.16.

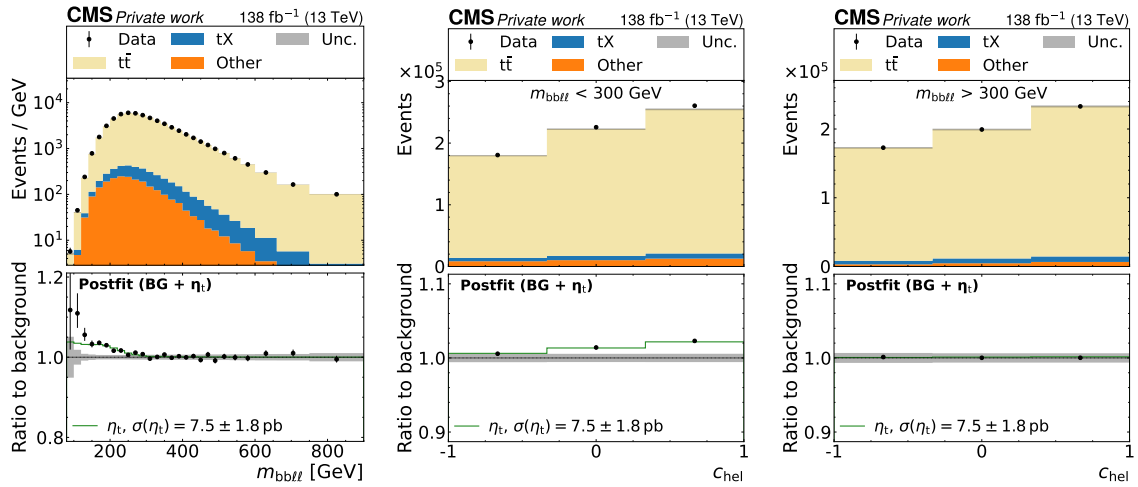


Figure 8.21: **Postfit distributions of $m_{b\bar{b}\ell\ell}$ and c_{hel} for the η_t fit.** One-dimensional distributions of inclusive $m_{b\bar{b}\ell\ell}$ (left), c_{hel} for $m_{b\bar{b}\ell\ell} < 300$ GeV (center), and c_{hel} for $m_{b\bar{b}\ell\ell} > 300$ GeV (right), projected from a 3D template of $m_{b\bar{b}\ell\ell} \times c_{\text{hel}} \times c_{\text{han}}$. The first $m_{b\bar{b}\ell\ell}$ bin in the left figure is an underflow bin containing events with $m_{b\bar{b}\ell\ell} < 80$ GeV. Otherwise, notations are as in Fig. 8.16 [8].

matched to PYTHIA (cf. Sec. 4.1.2), the three setups introduced in Sec. 8.5.4 are considered: POWHEG matched to HERWIG, MG5_AMC@NLO matched to PYTHIA with the FxFx scheme, and bb4l matched to PYTHIA.

Generator setup	$\sigma(\eta_t)$ [pb]
POWHEG (NWA) + PYTHIA (nominal)	8.7 ± 1.1
POWHEG (NWA) + HERWIG	8.6 ± 1.1
MG5_AMC@NLO FxFx (NWA) + PYTHIA	9.8 ± 1.3
POWHEG bb4l + PYTHIA	6.6 ± 1.4

Table 8.6: **Results for alternate generators.** Results for $\sigma(\eta_t)$ obtained with different simulated event samples for the FO pQCD $t\bar{t}+tW$ prediction.

The results can be found in Tab. 8.6. The results from PYTHIA and HERWIG are fully in agreement with each other, while MG5_AMC@NLO results in a higher η_t cross section by about one standard deviation, and bb4l results in a lower η_t cross section by about ~ 1.5 standard deviations. This is fully consistent with the distributions in Fig. 8.10 and the surrounding discussion in Sec. 8.5.4: the difference between PYTHIA and HERWIG can be distinguished from the effect of η_t due to the opposite slope in c_{hel} , and the extracted η_t cross section is thus not strongly sensitive to the choice of parton shower. By contrast, bb4l leads to an increased slope in c_{hel} compared to the NWA-based $t\bar{t}+tW$ prediction, and thus leaves room only for a reduced η_t contribution.

As an additional check, the differences between the predictions from POWHEG + HERWIG and POWHEG + PYTHIA as well as between bb4l and $t\bar{t}+tW$ in the NWA are included in the fit as additional nuisance parameters. In both cases, the NWA-based POWHEG + PYTHIA prediction is considered the nominal, and the alternate prediction is considered the $+1\sigma$ template. The -1σ template is constructed by symmetrizing the relative difference around the nominal, and intermediate values are obtained by interpolation.

The resulting η_t cross section with these nuisance parameters included is $\sigma(\eta_t) = 8.8^{+1.2}_{-1.4}$ pb³. This number is fully compatible with the nominal result without these additional nuisance parameters (Eq. (8.18)) with an asymmetrically increased uncertainty. The reason for the increase in uncertainty can be seen in Fig. 8.22, showing the nuisance parameter pulls and impacts: The nuisance parameter encoding the difference between bb4l and $t\bar{t}+tW$ represents the leading impact on the η_t cross section and is asymmetric. This is again understandable from the steeper slope in c_{hel} for bb4l as seen in Fig. 8.10, which is similar to the η_t signal, and is also in agreement with the reduced η_t cross section for a bb4l background prediction shown in Tab. 8.6. It is furthermore significantly constrained towards zero, i.e. towards the default

³In Ref. [8], this number is considered the nominal result.

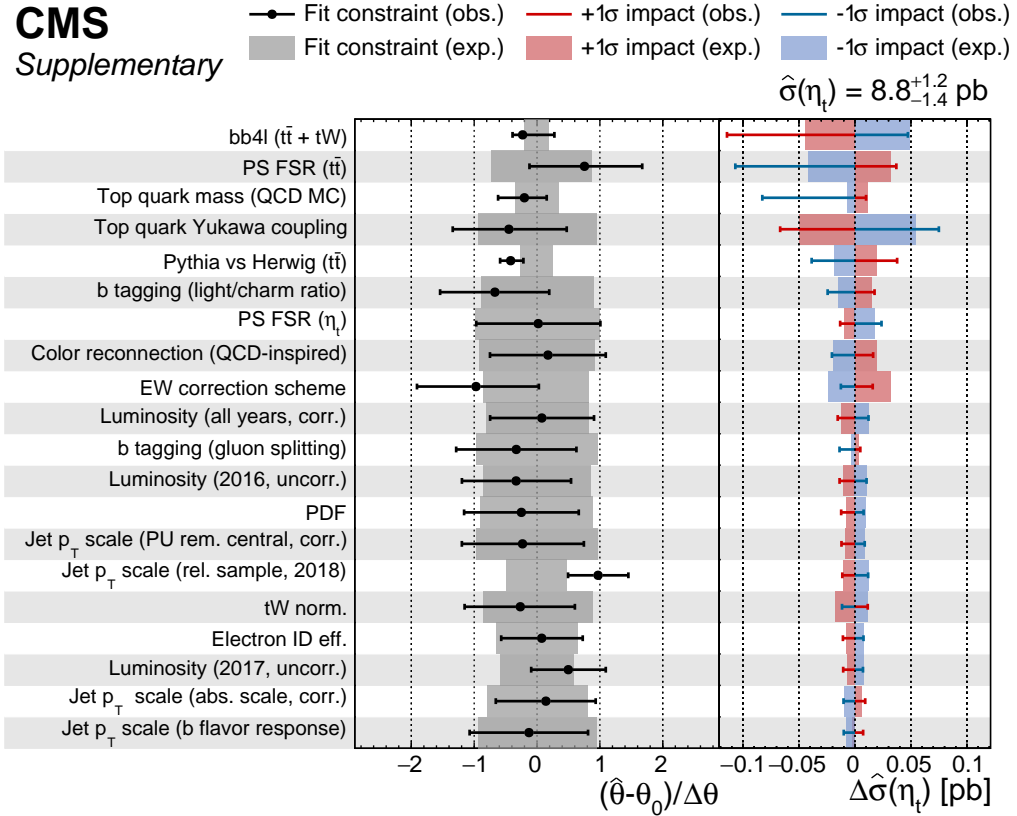


Figure 8.22: **Nuisance parameter pulls and impacts including alternate generators.** Expected and observed pulls, constraints, and impacts on the η_t cross section for the most impactful nuisance parameters in the η_t -only fit where the differences between the predictions from POWHEG hvq + HERWIG and bb4l + PYTHIA compared to POWHEG hvq + PYTHIA are included as additional nuisance parameters [8].

$t\bar{t} + tW$ prediction, implying that the data prefers the NWA approach over the *a priori* superior bb4l prediction. The reason for this is not readily apparent. One possible cause could be the fact that the NLO EW and NNLO QCD corrections are applied to bb4l in a necessarily ad-hoc manner, and might thus spoil the agreement with the data (cf. Sec. 8.5.4). However, in the scope of this work, this remains speculation.

On the other hand, the nuisance parameter encoding the difference of PYTHIA and HERWIG is less impactful, consistent with the results for HERWIG in Tab. 8.6, and similarly strongly constrained. Again, this is likely because the difference between PYTHIA and HERWIG can be distinguished from η_t based on the combination of $m_{t\bar{t}}$ and c_{hel} information, as expanded upon in Sec. 8.5.4.

8.7.4 Interpretation in terms of A and H

While a $t\bar{t}$ bound state is the conceptually simplest explanation of the enhancement at the $t\bar{t}$ threshold in the sense that it is predicted in the SM and does not invoke any further (BSM) degrees of freedom, it is also possible to perform an interpretation in terms of the generic spin-0 bosons A and H as introduced in Sec. 2.4.1. For this purpose, fits allowing the presence of both A and H at the same time are performed. The two independent POIs are the A/H-top coupling modifiers $g_{A\bar{t}\bar{t}}$ and $g_{H\bar{t}\bar{t}}$, and the interference with the SM is fully taken into account through a parameterization in terms of $g_{A\bar{t}\bar{t}/H\bar{t}\bar{t}}^2$ and $g_{A\bar{t}\bar{t}/H\bar{t}\bar{t}}^4$ (cf. Eq. (2.30)), thus allowing negative A/H contributions with respect to the SM.

A scan is performed over all pairs of considered A/H masses and widths (see Sec. 8.2.1), and the pair with the largest difference in logarithmic likelihood $\Delta \ln L$ is identified as the best-fit point. This results in $m_A = 365 \text{ GeV}$, $\Gamma_A/m_A = 2\%$ for A and $m_H = 925 \text{ GeV}$, $\Gamma_H/m_H = 3\%$ for H. It should be noted here that 365 GeV is the lowest mass point considered in the available signals for A and H, while η_t and χ_t are located at a lower value of 343 GeV. It is possible that considering a lower value of m_A would lead to an even better fit; however, close to the $t\bar{t}$ threshold, modeling the interference with the SM is difficult due to large corrections at higher orders in QCD, and current models are not reliable enough [246, 247]. In particular, the LO-to-NNLO K -factor for the A/H resonance cross section can become very large for masses close to the threshold, suggesting large higher-order QCD effects for both the resonance and interference with the SM.

Figure 8.23 shows the postfit $m_{t\bar{t}} \times c_{\text{hel}} \times c_{\text{han}}$ distribution, and Fig. 8.24 shows the allowed region for the two couplings $g_{A\bar{t}\bar{t}}$ and $g_{H\bar{t}\bar{t}}$ as obtained from a likelihood scan. From the latter, the best-fit values and uncertainties at 68 % confidence level for the coupling modifiers are found to be

$$g_{A\bar{t}\bar{t}} = 0.79^{+0.04}_{-0.05} \quad \text{and} \quad g_{H\bar{t}\bar{t}} = 1.47^{+0.17}_{-0.30}. \quad (8.19)$$

The same excess close to the $t\bar{t}$ threshold already seen in Sec. 8.7.1 manifests as a non-zero value of $g_{A\bar{t}\bar{t}}$, which Fig. 8.24 shows is preferred by more than five standard deviations, similar as for the interpretation in terms of η_t . It is important to stress that this result does not constitute any observation of a new BSM particle, since a low-mass A and η_t cannot be conclusively distinguished, as discussed in the following section.

In addition, there is also a preference for a non-zero value of $g_{H\bar{t}\bar{t}}$, though this is significant only at about 2 standard deviations and could thus be a simple statistical fluctuation⁴. It should be noted that both of these values are local significances, i.e.

⁴The uncertainty ranges on $g_{A\bar{t}\bar{t}}$ and $g_{H\bar{t}\bar{t}}$ given in Eq. (8.19) are non-linear with respect to the confidence level due to the quadratic and quartic dependence of the event yield on $g_{A\bar{t}\bar{t}/H\bar{t}\bar{t}}$, as also seen in Fig. 8.24. At 95 % confidence level, the uncertainty ranges are $^{+0.07}_{-0.08}$ for $g_{A\bar{t}\bar{t}}$ and

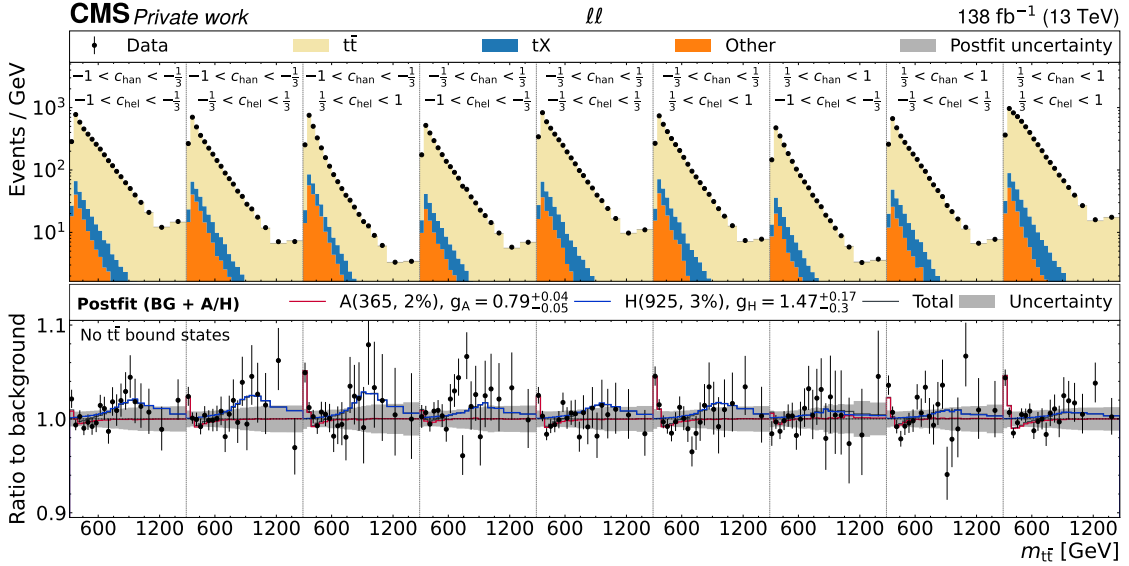


Figure 8.23: **Postfit distributions of $m_{t\bar{t}} \times c_{\text{hel}} \times c_{\text{han}}$ for the A+H fit.** The unrolled three-dimensional distribution in $m_{t\bar{t}}$, c_{hel} and c_{han} as after the fit to data with A and H as signals, summed over all years and lepton flavors. The A/H signals correspond to the best-fit masses and widths of $m_A = 365 \text{ GeV}$, $\Gamma_A/m_A = 2\%$ for A and $m_H = 925 \text{ GeV}$, $\Gamma_H/m_H = 3\%$ for H. The upper panel shows the sum of the background simulation (colored bars) and the observed data (black dots), while the lower panel shows the ratio of the data to the prediction with the postfit A and H signals, as well as their sum, overlaid.

they do not account for the look-elsewhere effect. The source of this preference is again evident from Fig. 8.23: it is due to a mild, broad excess in events compared to the prediction around $m_{t\bar{t}} \approx 900 \text{ GeV}$, which is more pronounced in the low c_{han} bins compared to the others as would be expected for a scalar particle H.

8.7.5 Comparison of η_t and A interpretations

To compare the interpretations of the excess close to the $t\bar{t}$ threshold in terms of either η_t or a low-mass A, the prefit templates as a function of $m_{t\bar{t}}$ are shown in Fig. 8.25 left for the best-fit points of the two interpretations: $m_A = 365 \text{ GeV}$, 2 % width, and $g_{A t\bar{t}} = 0.79$ for A, as well as $\sigma(\eta_t) = 8.7 \text{ pb}$ for η_t . The shapes of the two templates look different: the effect of η_t is a simple enhancement in expected events close to the threshold, while A shows the characteristic peak-dip structure. The difference between the two templates is comparable in size to the normalized

$^{+0.26}_{-1.47}$ for $g_{H t\bar{t}}$, i.e. the data are compatible with $g_{H t\bar{t}} = 0$ within two standard deviations.

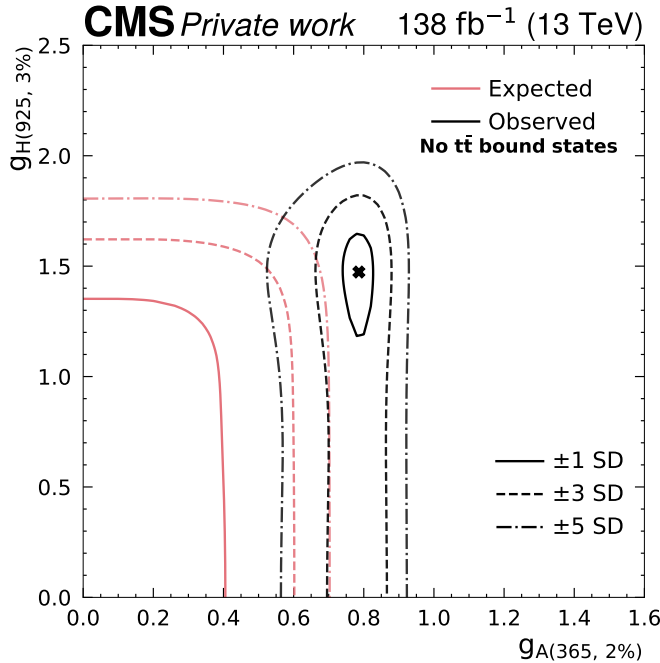


Figure 8.24: **Allowed coupling region in the A+H fit.** The two-dimensional allowed region for the coupling modifiers $g_{A\bar{t}\bar{t}}$ and $g_{H\bar{t}\bar{t}}$ in the A+H fit, for the best-fit A/H masses and widths of $m_A = 365$ GeV, $\Gamma_A/m_A = 2\%$ for A and $m_H = 925$ GeV, $\Gamma_H/m_H = 3\%$ for H, obtained through a scan of the profiled likelihood. The observed region is shown in black, while the SM expectation is shown in pink.

prefit systematic uncertainty for one standard deviation, shown in gray.

In Fig. 8.25 right, a scan of the profiled logarithmic likelihood with $g_{A\bar{t}\bar{t}}$ and $\sigma(\eta_t)$ as simultaneous POIs is performed. No H production is considered for this scan. From the observed allowed region, η_t is preferred over A at the level of one standard deviation. However, at two or more standard deviations, possible combinations of A and η_t including only A are allowed as well. The presence of neither A or η_t , on the other hand, is excluded. The expected allowed region, assuming $\sigma(\eta_t) = 8.7$ pb in the pseudodata, is also shown and is similar to the observed one.

It is important to stress that η_t represents a simplified model of a $t\bar{t}$ bound state, and its exact shape in $m_{t\bar{t}}$ is thus not precisely known. Furthermore, the $m_{t\bar{t}}$ shape of A might change when considering masses below the lower bound of $m_A = 365$ GeV considered in this analysis. Together with the only mild preference of η_t over A in the fit at the level of one standard deviation, it is clear that at the current level of precision the $t\bar{t}$ bound state η_t and a BSM pseudoscalar A cannot be conclusively distinguished. It is furthermore possible that a possible BSM contribution close to the $t\bar{t}$ threshold might itself influence bound state effects, leading to mixing between

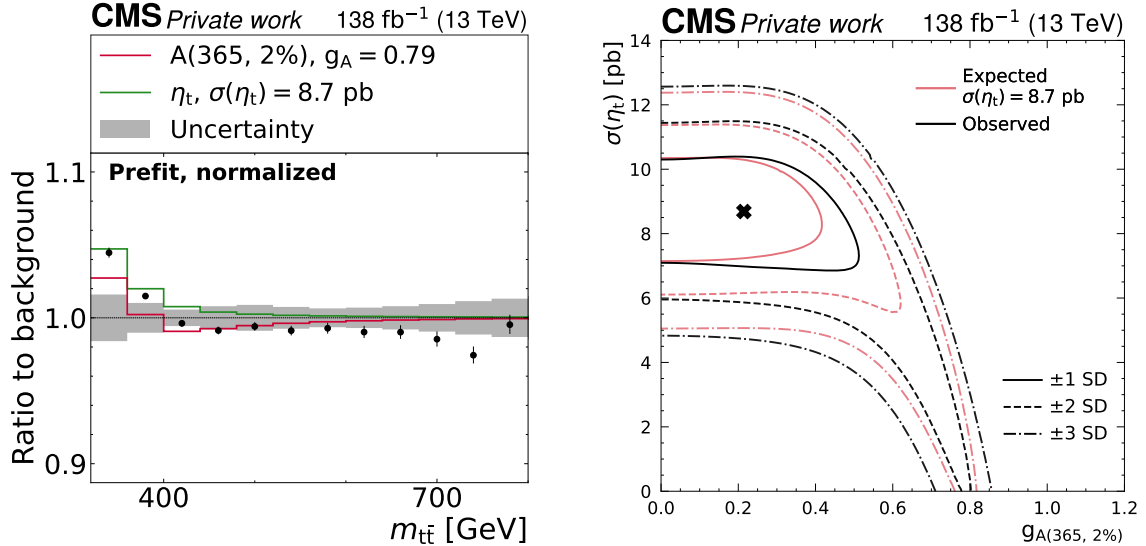


Figure 8.25: **Comparison of low-mass A and η_t .** Left: the normalized prefit $m_{t\bar{t}}$ distributions for A at $m_A = 365$ GeV, 2 % width, and the best-fit coupling of $g_{A\bar{t}} = 0.79$ (red) as well as η_t at the best-fit cross section of $\sigma(\eta_t) = 8.7$ pb (green), with the data overlaid (black markers). The normalized prefit uncertainty is shown as the gray band. Right: the two-dimensional allowed region as a function of $g_{A\bar{t}}$ and $\sigma(\eta_t)$, obtained through a scan of the profiled likelihood. The observed region is shown in black, while the expected region assuming $\sigma(\eta_t) = 8.7$ pb is shown in pink.

A and η_t , though no calculations of this are available at the time of writing.

8.8 Limits on A/H bosons

Having discussed the excess seen at the $t\bar{t}$ threshold and its possible interpretations, in this section exclusion limits on A/H bosons in the full considered mass range are presented. This is done for two different scenarios: In the first scenario, denoted “ A/H only”, the SM $t\bar{t}$ background is described by the FO pQCD prediction from POWHEG + PYTHIA reweighted to NLO EW and NNLO QCD, same as for the η_t extraction in Sec. 8.7.1 and for the $A+H$ fit in Sec. 8.7.4. The observed excess is thus expected to manifest in the limits in the form of a weaker observed than expected limit for low A/H masses.

In the second scenario, denoted “ $A/H + \eta_t$ ”, it is assumed that $t\bar{t}$ bound states exist in the SM and are well described by the η_t model. Under this assumption, η_t is added as an additional background, where the normalization of η_t is an additional

free-floating nuisance parameter. A and/or H contributions are then considered as signals on top of this background. The fit thus has the freedom to decide between possible η_t , A, and H contributions based on the data, similar to the previous section (Sec. 8.7.5).

In both scenarios, the limits are calculated with the CL_s prescription as introduced in Chapter 5. However, a complication arises from the non-linearity of the A/H signal as a function of $g_{A\bar{t}\bar{t}/H\bar{t}\bar{t}}$, which means that the distribution of the test statistic is not necessarily χ^2 -distributed. As a result, the p -values p_{s+b} and p_b cannot be easily computed. To avoid having to perform computationally expensive toy experiments, a *raster scan* method is used in the same way as in Ref. [22]. For a given A/H mass and width point, the coupling modifier $g_{A\bar{t}\bar{t}/H\bar{t}\bar{t}}$ is scanned in the range 0–5. For each value of $g_{A\bar{t}\bar{t}/H\bar{t}\bar{t}}$, the total signal contribution is computed as the sum of the resonant signal, scaling with $g_{A\bar{t}\bar{t}/H\bar{t}\bar{t}}^4$, and the SM-signal interference, scaling with $g_{A\bar{t}\bar{t}/H\bar{t}\bar{t}}^2$. An auxiliary linear signal strength μ is then introduced, so that the total signal contribution becomes

$$s(\mu) = \mu \left(g_{A\bar{t}\bar{t}/H\bar{t}\bar{t}}^4 s_{\text{res}} + g_{A\bar{t}\bar{t}/H\bar{t}\bar{t}}^2 s_{\text{int}} \right) \quad (8.20)$$

where s_{res} and s_{int} are the resonance and interference contributions, respectively, and $g_{A\bar{t}\bar{t}/H\bar{t}\bar{t}}$ is held fixed. $\mu = 1$ corresponds to the probed A/H signal, while $\mu = 0$ corresponds to the SM. Intermediate values of μ are in principle unphysical since they do not correspond to any value of $g_{A\bar{t}\bar{t}/H\bar{t}\bar{t}}$.

Since the A/H signal now scales linearly with μ , the usual asymptotic approximation can be used to obtain the CL_s value for $\mu = 1$. It has been shown as a part of Ref. [22] that the distribution of the test statistic obtained in this way approximates well the true test statistic for $g_{A\bar{t}\bar{t}/H\bar{t}\bar{t}}$ as evaluated using toy experiments. This procedure is repeated for all values of $g_{A\bar{t}\bar{t}/H\bar{t}\bar{t}}$, and a value of $g_{A\bar{t}\bar{t}/H\bar{t}\bar{t}}$ is, as usual, excluded at 95% confidence level when the CL_s value drops below 0.05.

The resulting observed and expected limits for all considered A and H masses and six representative width choices are shown in Figs. 8.26 and 8.27 for the “A/H only” scenario and in Figs. 8.28 and 8.29 for the “A/H + η_t ” scenario. The expected limits are mostly stronger for low masses since the signal cross sections fall off with rising A/H masses. An exception are H bosons with masses close to the threshold, for which the decay to $t\bar{t}$ is suppressed because the 3P_0 spin state requires one unit of orbital angular momentum, which in turn requires top quarks with non-zero velocity. This leads to lower cross sections for $pp \rightarrow H \rightarrow t\bar{t}$ than for $pp \rightarrow A \rightarrow t\bar{t}$ production, corresponding to less sensitivity and larger expected limits in the $t\bar{t}$ threshold region. It is most prominently seen in Fig. 8.27 top for low-width H bosons.

For low A/H widths, the rise of the expected limit with the mass is roughly linear. For higher widths, however, there is a jump in the limit in the mass range $m_{A/H} = 650\text{--}750\text{ GeV}$, coinciding with inflated uncertainty bands. The reason for this is a cancellation between the A/H resonance and A/H-SM interference components:

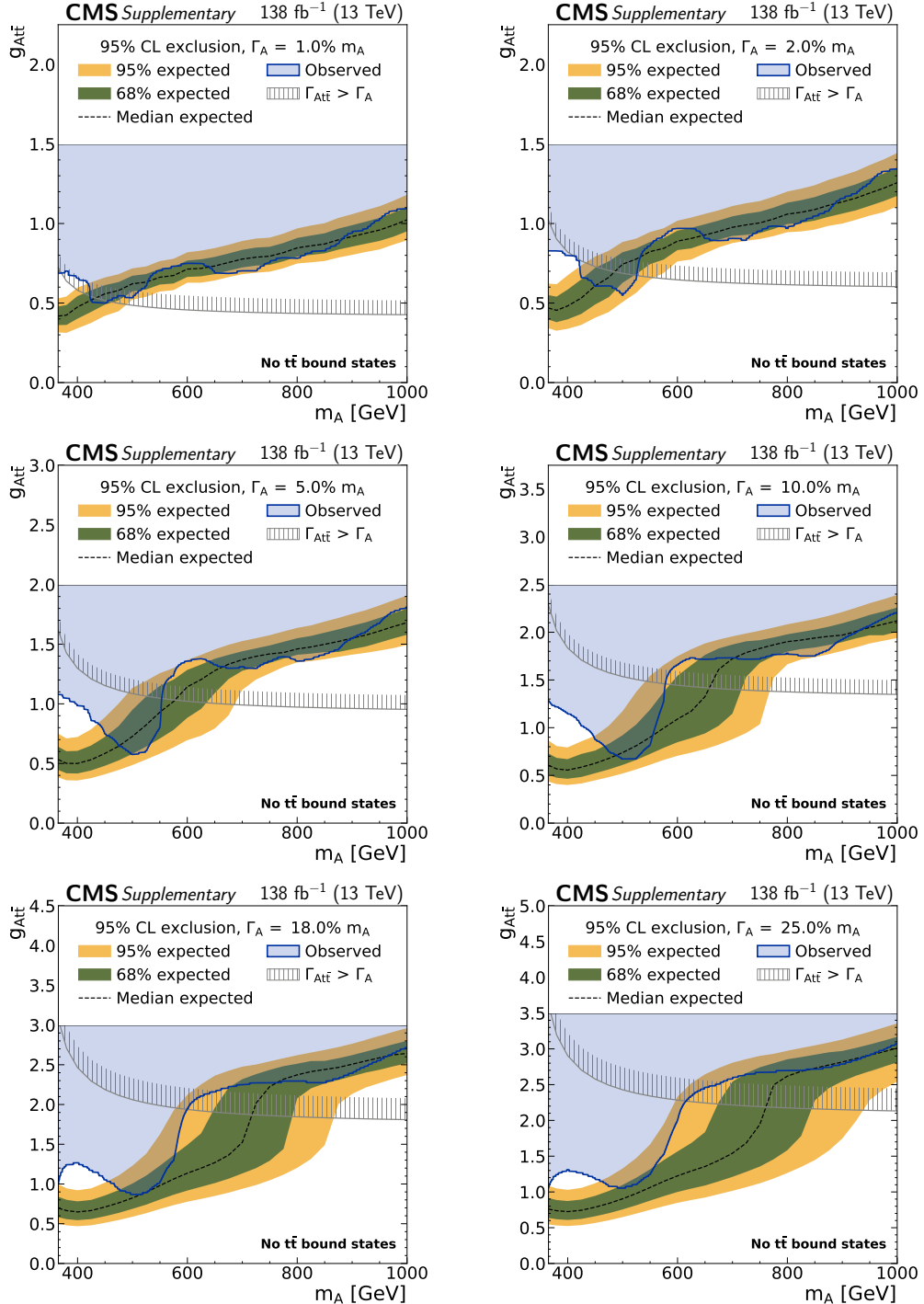


Figure 8.26: **Exclusion limits on $g_{A\bar{t}\bar{t}}$ in the “A only” scenario** in the dilepton channels as a function of the mass of the A boson for several relative widths. The observed limits are indicated by the blue shaded area, and the green and yellow bands indicate the regions containing 68 and 95% of limits expected under the SM hypothesis. The unphysical region of phase space in which the partial width $\Gamma_{A\rightarrow t\bar{t}}$ becomes larger than the total width of A is indicated by the hatched line [9].

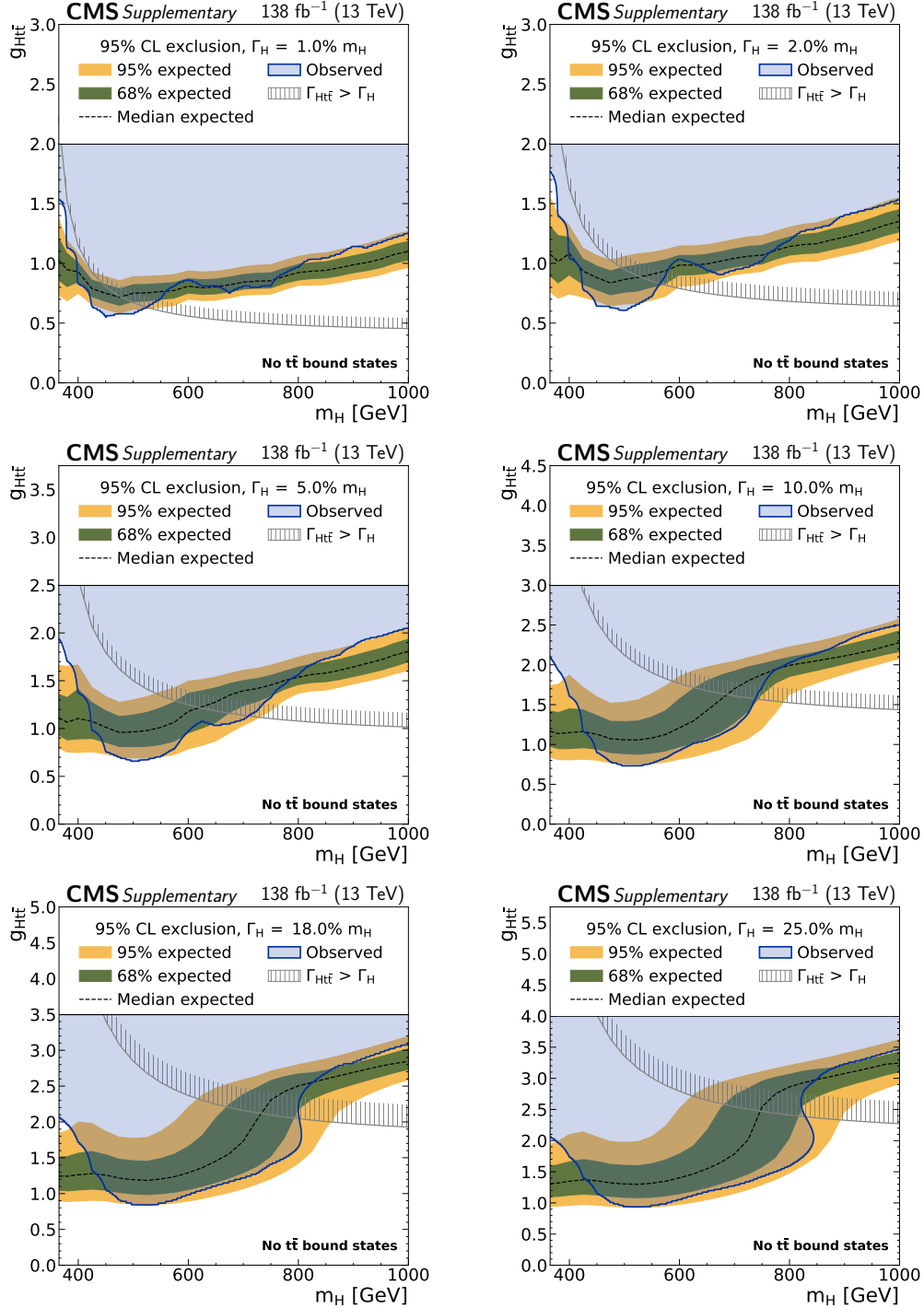


Figure 8.27: **Exclusion limits on g_{Ht} in the “H only” scenario** in the dilepton channels as a function of the mass of the H boson [9]. Notations are equivalent to Fig. 8.26.

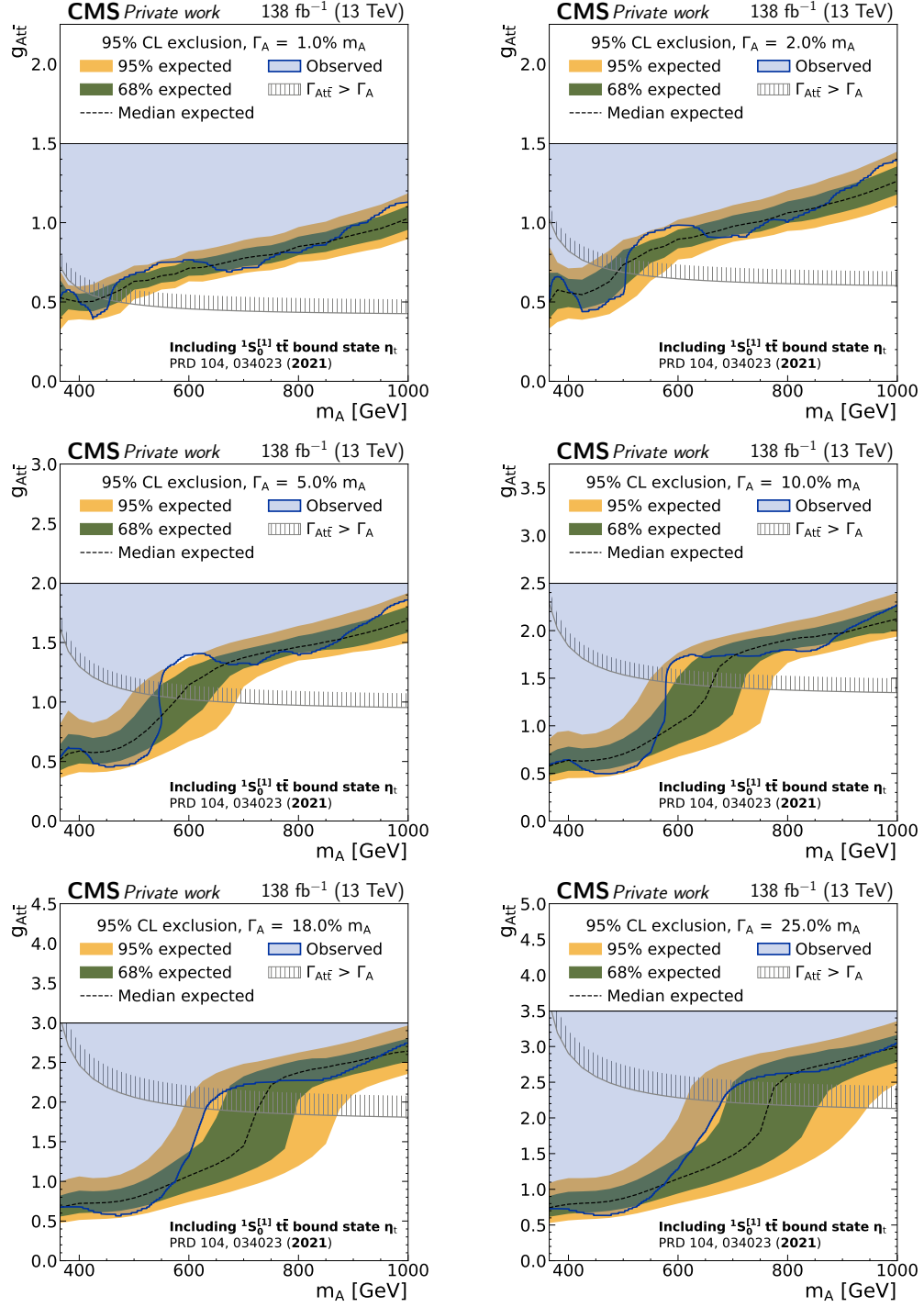


Figure 8.28: **Exclusion limits on $g_{A t\bar{t}}$ in the “A + η_t ” scenario** in the dilepton channels as a function of the mass of the A boson [9]. Notations are equivalent to Fig. 8.26.

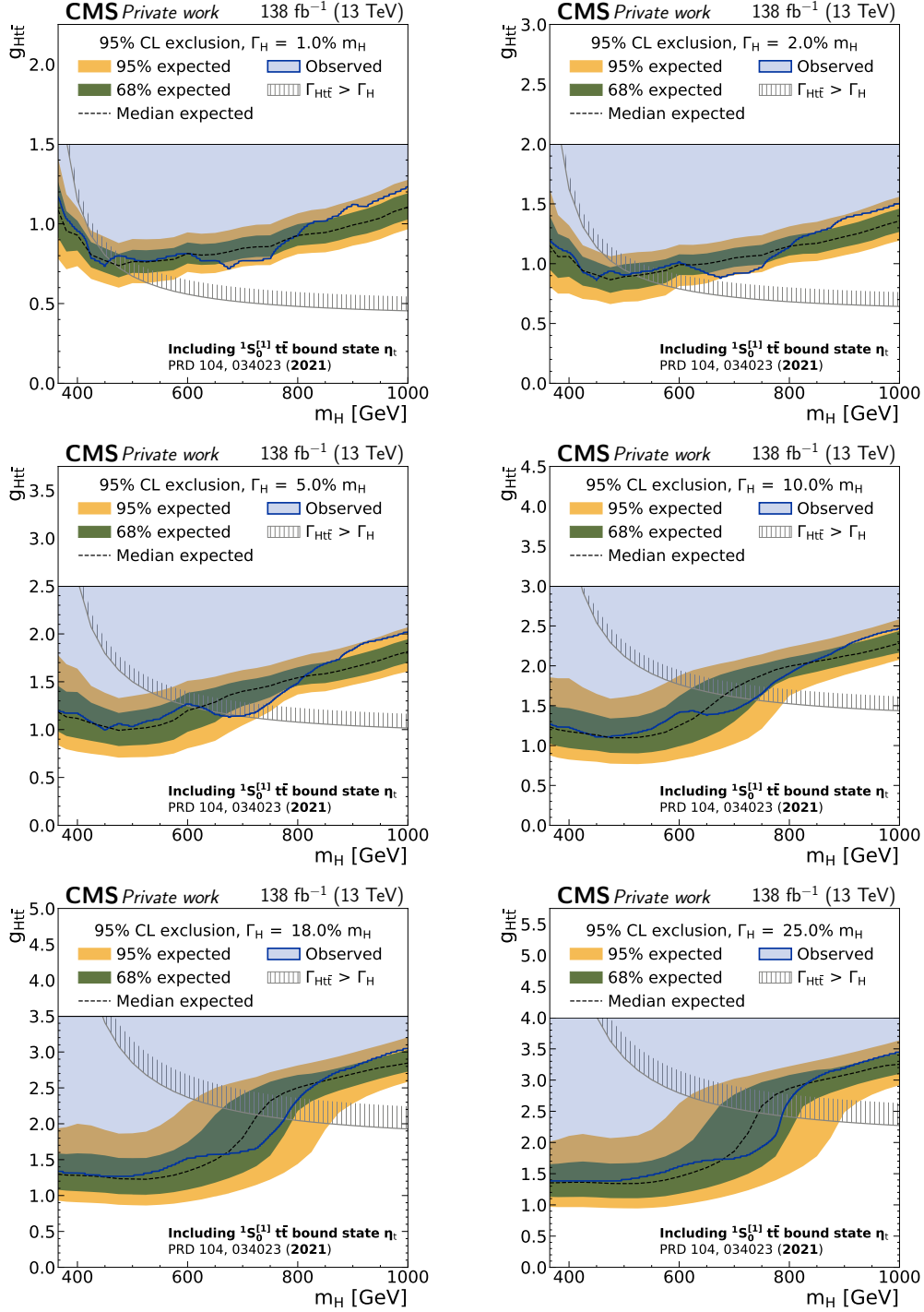


Figure 8.29: **Exclusion limits on $g_{H\bar{t}\bar{t}}$ in the “ $H + \eta_t$ ” scenario** in the dilepton channels as a function of the mass of the H boson [9]. Notations are equivalent to Fig. 8.26.

At the $g_{A\bar{t}\bar{t}/H\bar{t}\bar{t}}$ values relevant for the expected limits, the cross sections of resonance and interference approximately cancel, and because of the large width the peak-dip structure is not resolvable. Thus, the overall deviation from the SM and thus the sensitivity decrease.

In the observed limits, the excess at the $t\bar{t}$ threshold is visible in the “A/H only” scenario at low A/H masses as expected. It is stronger for the pseudoscalar A than for the scalar H, consistent with the preference of the data for a pseudoscalar over a scalar $t\bar{t}$ state as presented in Sec. 8.7.2. In the “A/H + η_t ” scenario, the excess is fully absorbed by the η_t contribution, and the observed and expected limits at low A/H masses agree. This is consistent with the slight preference of η_t over a low-mass A in the fit, as discussed in Sec. 8.7.5. By contrast, since the expected limits are calculated using pseudodata without η_t contribution, they change little between the scenarios.

Furthermore, the mild excess for H at high masses as seen in Fig. 8.24 is reproduced in the limits on $g_{H\bar{t}\bar{t}}$ in both scenarios in the approximate range of $900 < m_H < 1000$ GeV.

8.9 Combination with the $\ell+$ jets channels

So far, all results in this chapter have covered only the dilepton decay channel of $t\bar{t}$, which was analyzed as part of this thesis. In Ref. [9], the results on A/H bosons are combined with a separate analysis of the $\ell+$ jets decay channel. The combination (but not the $\ell+$ jets analysis) was also performed as part of this thesis, and is presented in this section. The $\ell+$ jets analysis strategy is roughly outlined in the following, for a more complete description, see Ref. [9].

8.9.1 Analysis strategy in the $\ell+$ jets channels

The selection performed in the $\ell+$ jets channels proceeds similarly to the $\ell+$ jets channels used for the inclusive $t\bar{t}$ cross section measurement in Sec. 6.2.3. Events with exactly one lepton and at least three jets are selected, of which at least two need to be b tagged. In addition to the criteria outlined in Sec. 8.2.2, both the lepton and the jets are required to fulfill $p_T > 30$ GeV to account for the higher single-lepton trigger thresholds. Furthermore, the cut-based identification criteria for electrons, as described in Ref. [103], are applied instead of MVA-based criteria. Similar as in the dilepton channel, as well as in Sec. 6.2.3, the events are categorized by the flavor of the lepton into the e+jets and $\mu+$ jets channels.

The algorithm described in Ref. [248] is used to reconstruct the neutrino from the leptonic top decay. It enforces mass constraints on the W boson and leptonically decaying top quark and then minimizes the distance $D_\nu = |p_T^\nu - p_T^{\text{miss}}|$ between the neutrino p_T and the missing transverse momentum. In events with four or more jets,

the same distance D_ν is then also used to assign the jets to the b and \bar{b} candidates as well as to the decay products of the hadronically decaying W boson. From this, the $t\bar{t}$ system can then be reconstructed. In events with exactly three jets, where information has been lost due to either an out-of-acceptance jet or the merger of two jets into one, additional steps have to be taken. The procedure described in Ref. [249] is applied to these events, which involves applying an energy correction factor to the four-momentum of the hadronically decaying top quark, depending on its reconstructed mass. Since the resolution of this procedure is necessarily worse than for events where all jets are available, events with three jets and four or more jets are treated as separate categories in the fit.

A two-dimensional template is constructed from the reconstructed value of $m_{t\bar{t}}$ as well as $|\cos \theta_\ell^*|$, where θ_ℓ^* is the scattering angle of the leptonically decaying top quark with respect to the direction of flight of the $t\bar{t}$ system in the laboratory frame. This variable probes the total angular momentum J of the $t\bar{t}$ system, and is thus sensitive to the spin of a possible mediator in $t\bar{t}$ production: For spin-0 mediators like A/H ($J = 0$), the top quarks are emitted isotropically in the $t\bar{t}$ rest frame, leading to a flat distribution of $|\cos \theta_\ell^*|$. By contrast, SM $t\bar{t}$ production consists of a mixture of different J states. At the $t\bar{t}$ threshold, gg initial states with $J = 0$ dominate, leading to only small deviations from a flat $|\cos \theta_\ell^*|$ distribution and low discriminating power. However, for high $m_{t\bar{t}}$, q \bar{q} initial states with $J = 1$ are more important, leading to a peak for high $|\cos \theta_\ell^*|$.⁵ Furthermore, $|\cos \theta_\ell^*|$ is not sensitive to the \mathcal{CP} structure of the mediator, in contrast to c_{hel} and c_{han} .

The $t\bar{t}$ and tW background predictions as well as the A/H signals are estimated using the same MC simulation as in the dilepton channels. Additionally, there is a significant background contribution from QCD multijet production with a fake or non-prompt lepton as well as EW processes such as W+jets production. These are difficult to model using MC, and are instead estimated together by a data-driven approach, similar to Sec. 6.3.2. A sideband in which the b tagging requirement on the jets is inverted is used for this purpose; details can be found in Ref. [9].

The dilepton and ℓ +jets channels are directly combined by performing a simultaneous likelihood fit to all categories. All systematic uncertainties described in Sec. 8.5 are applied in both channels as long as they are applicable, and the channels are always treated as fully correlated whenever an uncertainty is applicable in both. Furthermore, in the ℓ +jets channel, additional uncertainties related to the single-lepton trigger efficiencies and to the data-driven EW+QCD background estimation are applied [9]. An overview over all systematic uncertainties is given in Tab. 8.7.

Again, both the “A/H only” and “A/H + η_t ” scenarios are considered. For the latter, the ℓ +jets analysis uses a slightly different η_t model, in which the width of the bound state is set to $\Gamma(\eta_t) = 7$ GeV and a cut on the invariant mass $m_{WWb\bar{b}}$ is

⁵q \bar{q} initial states with $J = 0$ are forbidden at LO in QCD since the production proceeds through a spin-1 gluon in the s channel.

Uncertainty	Processes	Channels
Jet energy scale	all	all
Jet energy resolution	all	all
Unclustered p_T^{miss}	all	all
b tagging efficiency	all	all
b tagging misidentification	all	all
Single-electron trigger	all	e+jets
Single-muon trigger	all	μ +jets
Dilepton triggers	all	dilepton
Electron ID	all	e+jets, ee, e μ
Muon ID	all	μ +jets, e μ , $\mu\mu$
ECAL L1 trigger inefficiency	all	all
Pileup	all	all
Integrated luminosity	all	all
Top quark Yukawa coupling	$t\bar{t}$	all
EW correction scheme	$t\bar{t}$	all
Top quark mass	$t\bar{t}$, A/H, η_t	all
Matrix element scales	$t\bar{t}$, A/H, η_t , single t, Z+jets	all
Parton shower scales	$t\bar{t}$, A/H, η_t , single t, Z+jets	all
Color reconnection	$t\bar{t}$	all
ME-PS matching (h_{damp})	$t\bar{t}$	all
Underlying event tune	$t\bar{t}$	all
PDF	$t\bar{t}$	all
Single top normalization	single t	all
EW+QCD normalization	EW+QCD	ℓ +jets
EW+QCD shape	EW+QCD	ℓ +jets
$t\bar{t} + X$ normalization	$t\bar{t} + X$	dilepton
Z+jets normalization	Z+jets	dilepton
Diboson normalization	Diboson	dilepton

Table 8.7: **Systematic uncertainties in the channel combination.** An overview of the systematic uncertainties in the channel combination, including the processes and channels considered. All uncertainties that are applicable to both dilepton and ℓ +jets channels, as given in the rightmost column, are considered correlated between them.

applied, as described in Sec. 2.3. For the sake of consistency, the same model is also used in the dilepton channels when performing the combination only. The resulting impact on the limits from the choice of η_t model was found to be small.

8.9.2 A/H limits

The resulting observed and expected limits for the combination of both channels are found in Figs. 8.30 to 8.33 for both scenarios. It can be seen that the large excess for low A/H masses is still present in the channel combination in the “A/H only” scenario, and is again stronger for the pseudoscalar A. The mild excess for the scalar H at $m_H \approx 925$ GeV, on the other hand, is not confirmed in the channel combination.

In the “A/H + η_t ” scenario, there is no excess visible, similar to the dilepton-only result (Sec. 8.8), showing that the data again prefers an η_t contribution over the existence of a low-mass A. At the time of writing, these results are the most stringent limits for $pp \rightarrow H \rightarrow t\bar{t}$ for the considered mass range, while the limits on $pp \rightarrow A \rightarrow t\bar{t}$ are similar to the limits presented by ATLAS in Ref. [209] (see also Sec. 8.10.2).

To assess the impact of the different channels, the expected limits for the dilepton and ℓ +jets channels alone are also shown in red and orange, respectively. For most of the phase space, the ℓ +jets channel leads to stronger limits than the dilepton channel, which is mostly due to the higher branching ratio and thus higher available statistics as well as the better $m_{t\bar{t}}$ resolution in the ℓ +jets channel especially at high $m_{t\bar{t}}$. The difference is large at high A and H masses, where the contribution from the dilepton channels is rather small, while the dilepton channel becomes much more important for low masses, i.e. close to the $t\bar{t}$ threshold. This is because of the lack of sensitivity of $|\cos \theta_\ell^*|$ close to the $t\bar{t}$ threshold, while c_{hel} and c_{han} do not suffer from such a problem, as discussed in Sec. 8.9.1. For H at low masses in particular, the dilepton channel in fact gives stronger expected limits than ℓ +jets due to the sensitivity of c_{han} to scalar mediators.

8.9.3 Simultaneous A+H exclusion contours

In many possible BSM scenarios, multiple additional spin-0 states are expected at the same time, such as A and H in e.g. the 2HDM (cf. Sec. 2.4.2). Often, the masses of these scalars are close together since they originate from new physics at the same energy scale, in which case their signatures would not easily factorize. It is thus useful for future interpretations of the results to show exclusion contours not only for either A or H, but for the simultaneous presence of both.

To do so, simultaneous fits are performed with both A and H as freely floating signals as in Sec. 8.7.4. Since \mathcal{CP} conservation is assumed for the signal model, there is no interference between A and H (cf. Sec. 2.4.1). Frequentist exclusion contours are set with the Feldman–Cousins prescription [250, 251], in which the test statistic is numerically evaluated using toy experiments at each point in the $g_{At\bar{t}}-g_{Ht\bar{t}}$ plane. This procedure is fully correct in the Frequentist sense and does not rely on approximations of the test statistic, which are not guaranteed to hold for two non-linear signals, but is computationally expensive.

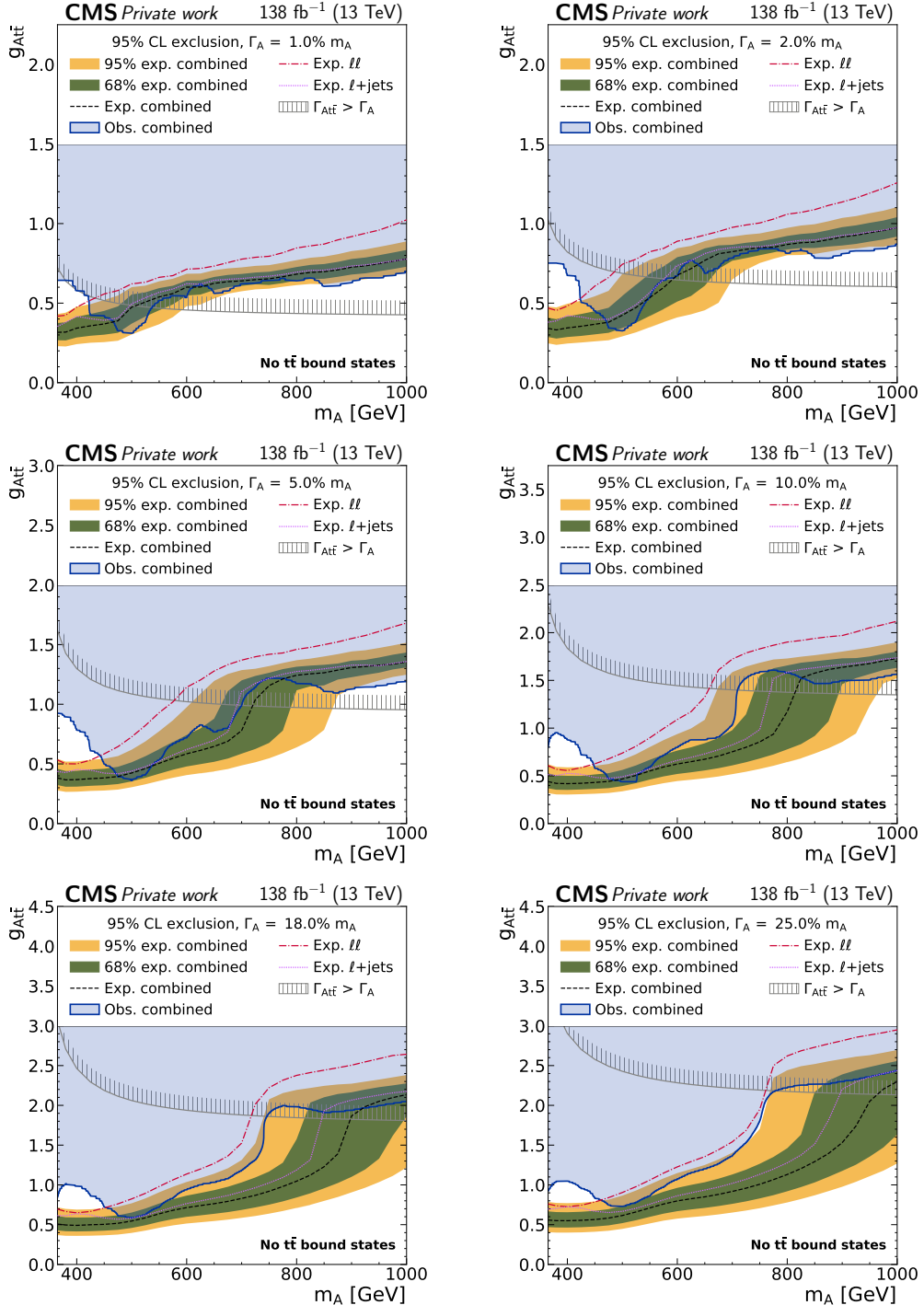


Figure 8.30: **Combined exclusion limits on $g_{At\bar{t}}$ in the “A only” scenario** in the dilepton and $\ell+\text{jets}$ channels as a function of the mass of the A boson. The expected limits in the dilepton and $\ell+\text{jets}$ channels alone are shown as the red and purple lines, respectively. Otherwise, notations are equivalent to Fig. 8.26 [9].

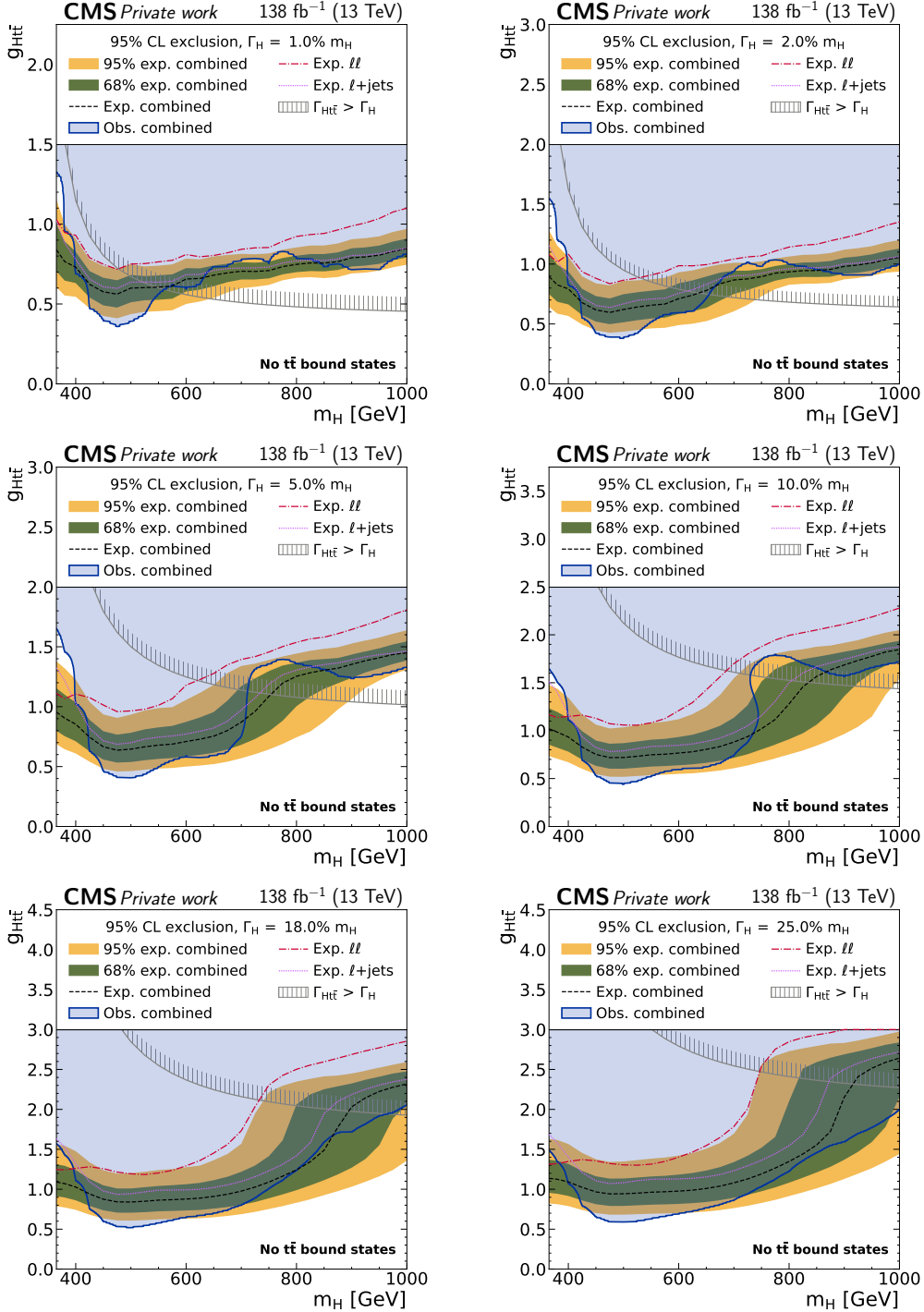


Figure 8.31: **Combined exclusion limits on $g_{H\bar{t}\bar{t}}$ in the “H only” scenario** in the dilepton and ℓ +jets channels as a function of the mass of the H boson. Notations are equivalent to Fig. 8.30 [9].

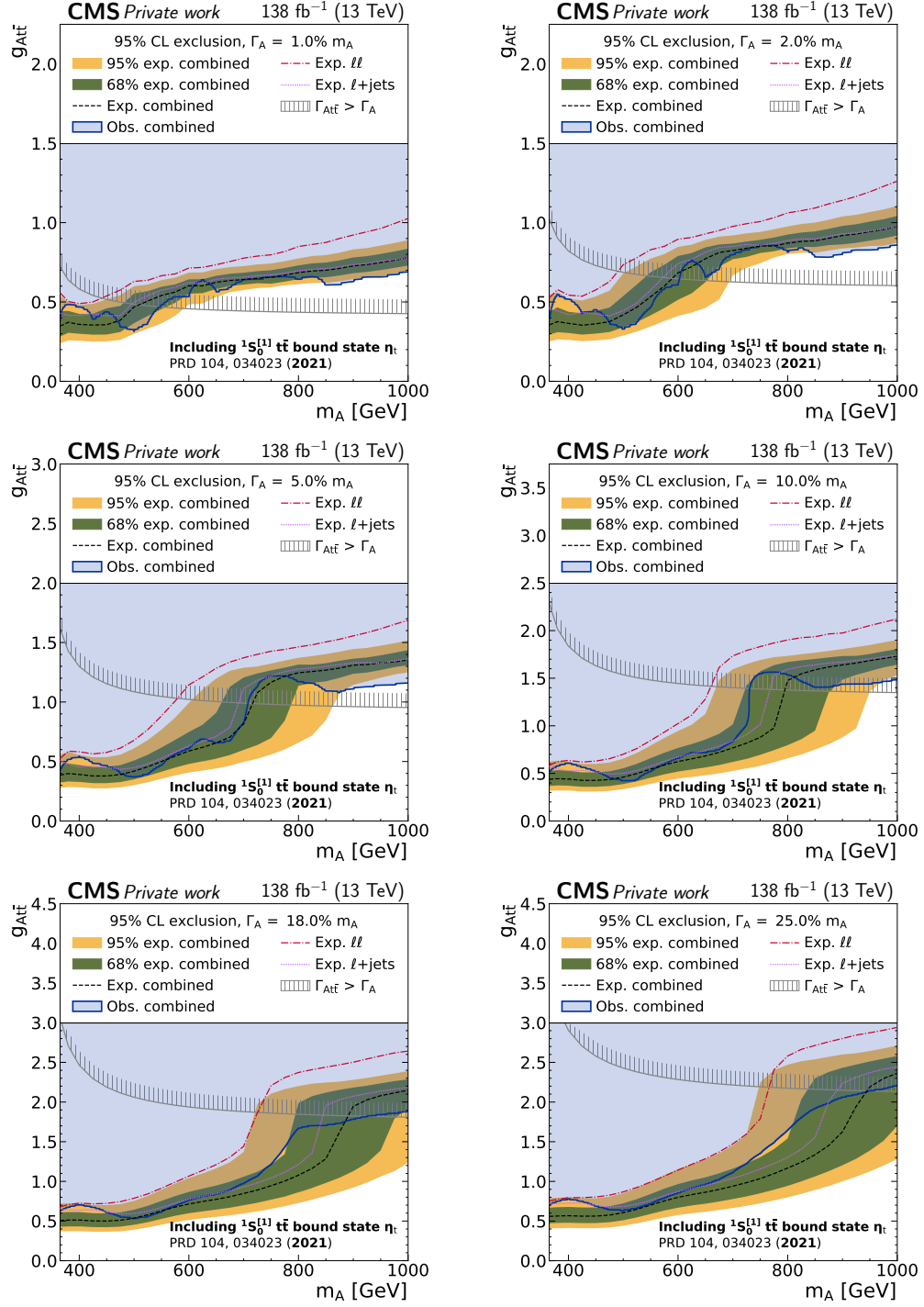


Figure 8.32: **Combined exclusion limits on $g_{A t\bar{t}}$ in the “A + η_t ” scenario** in the dilepton and $\ell+\text{jets}$ channels as a function of the mass of the A boson. Notations are equivalent to Fig. 8.30 [9].

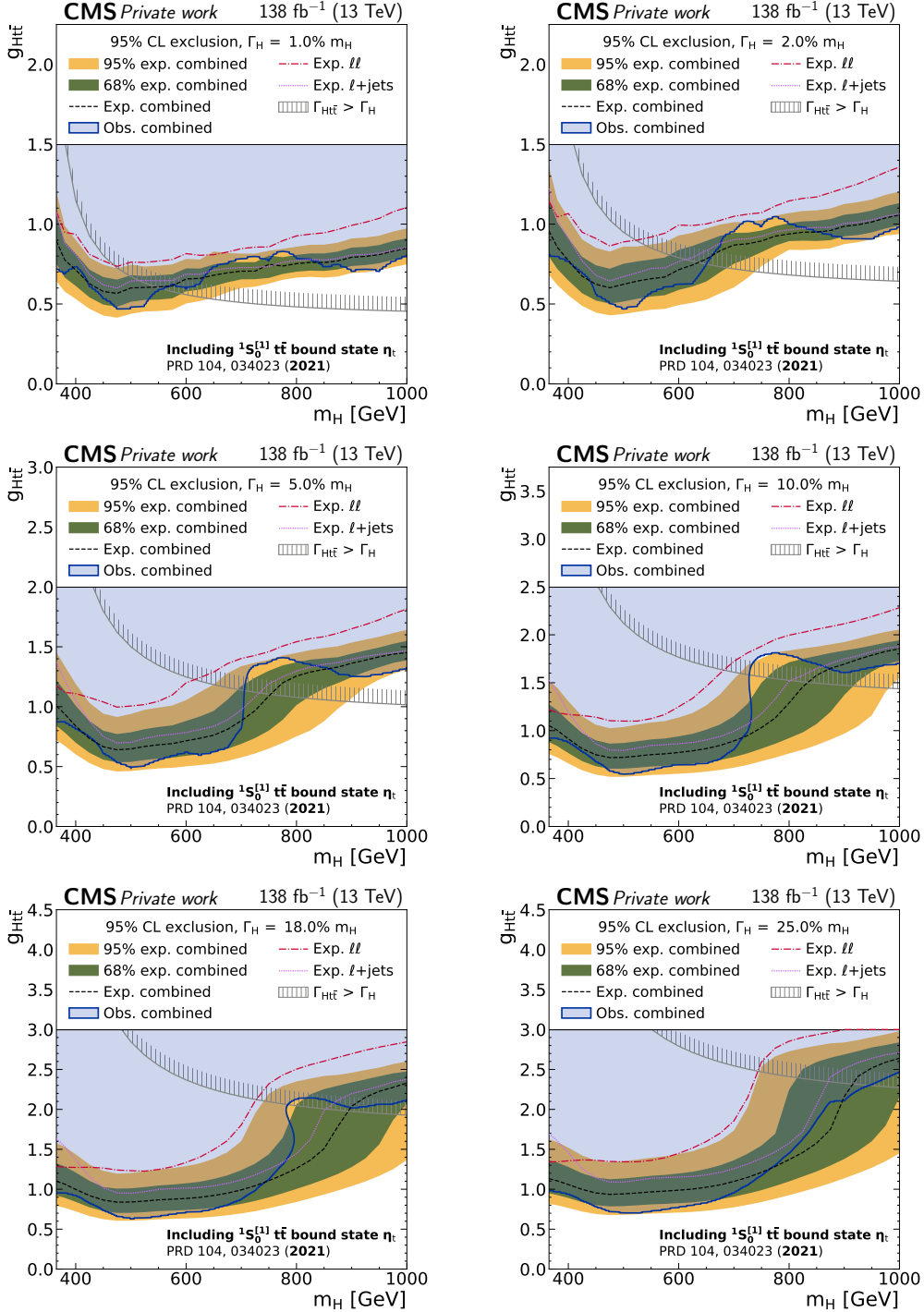


Figure 8.33: **Combined exclusion limits on $g_{H\bar{t}\bar{t}}$ in the “H + η_t ” scenario** in the dilepton and ℓ +jets channels as a function of the mass of the H boson. Notations are equivalent to Fig. 8.30 [9].

Due to this, combined with the large four-dimensional phase space of possible signals, only a few example mass and width points are shown in this work, and only for the dilepton and ℓ +jets combination in the “A/H + η_t ” scenario. They can be found in Fig. 8.34 for the case of identical A and H masses as well as in Fig. 8.35 for differing A and H masses. Alternatively, a coarse scan of the negative log-likelihood of the full span is available online as part of the HepData record [252].

Of particular note here is Fig. 8.34 (bottom left), in which a small local tension with the SM expectation at the level of ~ 1.4 standard deviations is observed for a scalar boson with $m_H = 750$ GeV, a width of 2%, and a coupling strength of $g_{Ht\bar{t}} \approx 0.88$. This tension is also visible at a similar level in the one-dimensional limits for the channel combination, Fig. 8.33 (top right), while it is not present for the dilepton channel alone (Fig. 8.29 top right). It can thus be inferred that it is driven by the ℓ +jets channels. Due to the smallness of local tension, it is fully consistent with a statistical fluctuation in the data.

In total, Figs. 8.34 and 8.35 constitute the first time that stringent limits have been set on the simultaneous production of A and H bosons decaying to $t\bar{t}$ in a model-agnostic way. Together with the supplemental material in the HepData record [252], they will be crucial inputs for interpretations in various specific BSM models.

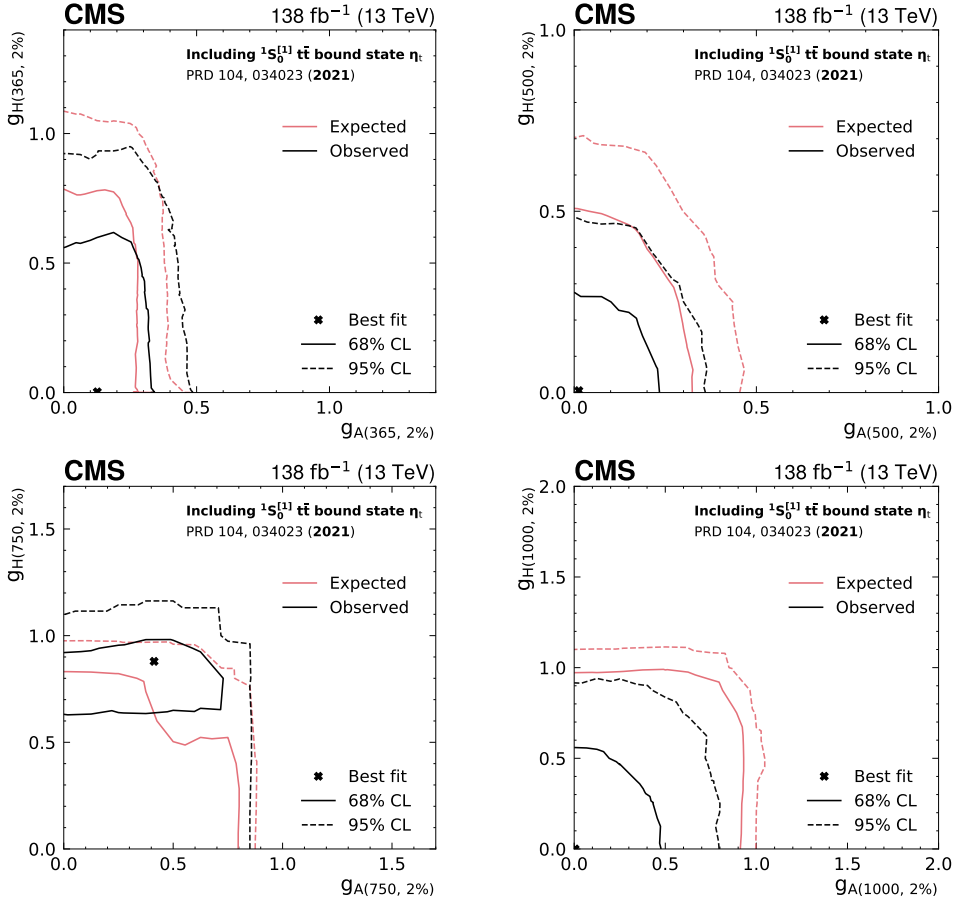


Figure 8.34: **Frequentist 2D exclusion contours for $g_{A t\bar{t}}$ and $g_{H t\bar{t}}$** for four different signal hypotheses with identical A and H masses of 365 GeV (upper left), 500 GeV (upper right), 750 GeV (lower left) and 1000 GeV (lower right), all assuming a width of 2%. In all cases, η_t production is added as a floating background [9].

8.10 Comparison to other results

8.10.1 ATLAS $t\bar{t}$ threshold measurement

After this work was made public, the ATLAS Collaboration presented preliminary results for a similar measurement at the $t\bar{t}$ threshold in Ref. [210], which confirmed the presence of a pseudoscalar excess over the $t\bar{t}$ continuum prediction.

The ATLAS result uses a very similar setup as presented in this work. It likewise considers only the dilepton decay channel of $t\bar{t}$, uses the full Run 2 data set (corresponding to 140 fb^{-1} for ATLAS), reconstructs the $t\bar{t}$ system using a similar algorithm, and finally bins in $m_{t\bar{t}}$, c_{hel} and c_{han} to extract the $t\bar{t}$ bound state compo-

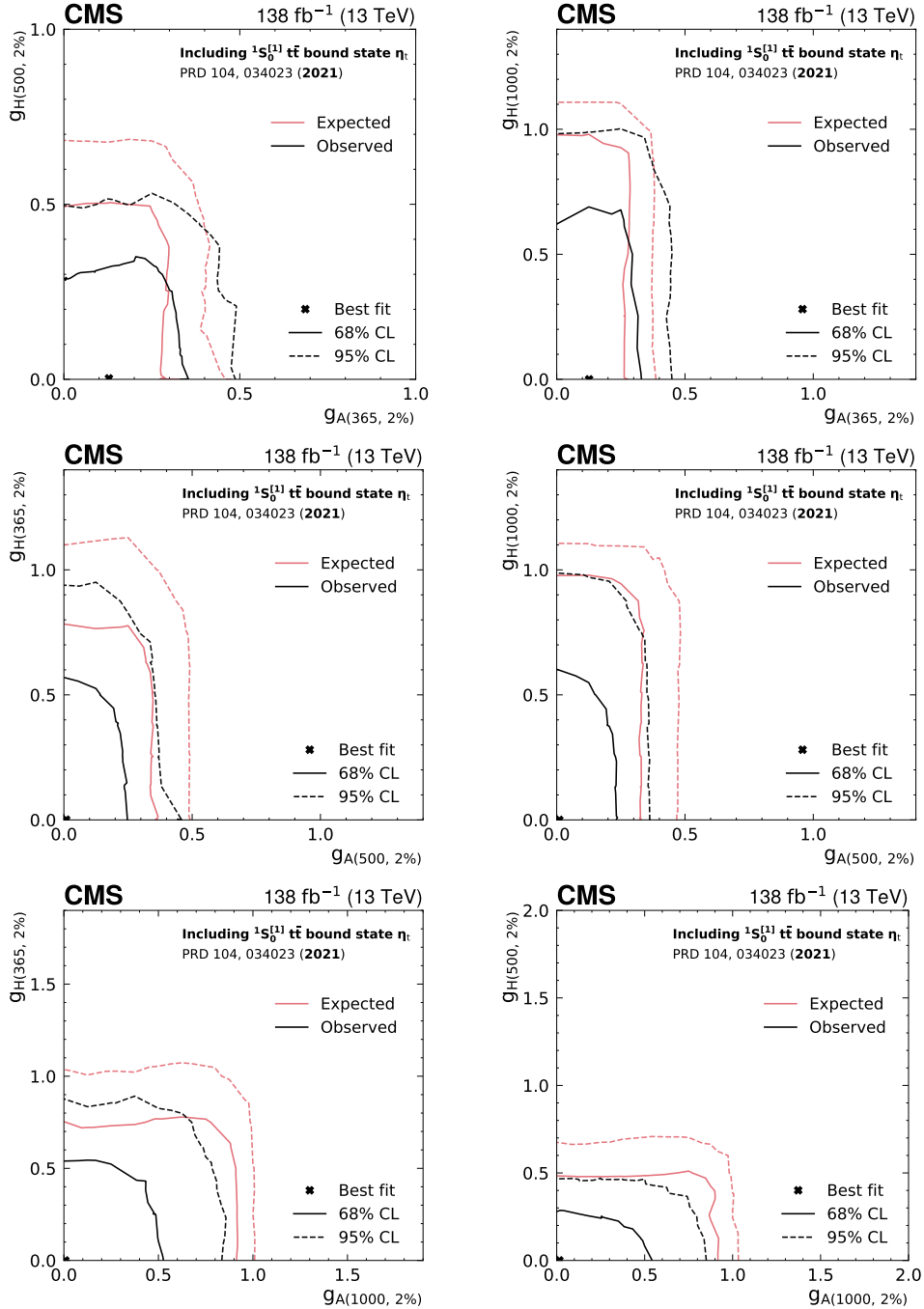


Figure 8.35: **Frequentist 2D exclusion contours for $g_{At\bar{t}}$ and $g_{Ht\bar{t}}$** for six different signal hypotheses with differing A and H masses, corresponding to combinations of 365 GeV, 500 GeV and 1000 GeV, all assuming a width of 2%. In all cases, η_t production is added as a floating background [9].

ment using a simplified model. The binning in c_{hel} and c_{han} is identical to this work, while in $m_{t\bar{t}}$ only four bins of 50 GeV width around the $t\bar{t}$ threshold are considered. Events with high values of $m_{t\bar{t}}$ are rejected. In the following, some further significant differences between the CMS and ATLAS results are briefly described.

First, ATLAS considers two additional sets of control regions (CRs) which are directly included in the likelihood fit. One is defined by requiring $m_{\ell\ell}$ to be within the vicinity of the Z boson mass, similar to the Z+jets scale factor estimation described in Secs. 6.3.2 and 8.2.4, and serves the same purpose of correcting the yield of the Z+jets simulation after the b tagging requirement. The other set of CRs targets fake or non-prompt leptons and is defined by requiring the two selected leptons to have the same charge. The dominant contribution here comes from $t\bar{t} \rightarrow \ell + \text{jets}$ events with an additional fake or non-prompt lepton. Such a CR is not included in the CMS result; it has however been internally checked using a similar selection that the data is well-described by the $t\bar{t} \rightarrow \ell + \text{jets}$ MC simulation.

Second, ATLAS employs a different systematics model, in particular for uncertainties related to the modeling of the $t\bar{t}$ continuum. Notable differences are:

- the ME scale uncertainties are estimated at NNLO by varying the scales in the reweighting to NNLO QCD and NLO EW (performed using the same tools as used here), while in this work the ME scales uncertainties are estimated at NLO directly in the POWHEG MC simulation;
- no uncertainty due to a variation of the top-SM Higgs Yukawa coupling is considered;
- two-point uncertainties comparing the POWHEG + PYTHIA prediction to POWHEG + HERWIG as well as to bb4l + PYTHIA are included in the nominal result, similar as in Ref. [8] and in Sec. 8.7.3; however, these uncertainties are treated as partially (50%) decorrelated between the nine bins of c_{hel} and c_{han} ;
- an additional ME-PS matching uncertainty is defined by varying the parameter p_T^{hard} in PYTHIA [118];
- an additional uncertainty due to the top recoil scheme in PYTHIA is considered [253].

In total, this results in significantly more degrees of freedom in the fit used by ATLAS than the one used by CMS.

Third, the nominal model used by ATLAS to probe $t\bar{t}$ bound state effects is based on Ref. [49], which includes a matrix-element level reweighting to an NRQCD calculation. As discussed in Sec. 2.3, this model could not be sufficiently scrutinized for inclusion in the results of this work, and particularly the modeling of spin correlations and the matching to the $t\bar{t}$ continuum is under question. Using this model, ATLAS extracts a cross section of $9.0 \pm 1.3 \text{ pb}$ [210].

However, ATLAS also provides results using the same η_t model considered in this work, using the same values for the η_t mass and width, which gives $\sigma(\eta_t) = 13.4 \pm 1.9$ pb [210]. This figure is more appropriate to compare to the result of this work, $\sigma(\eta_t) = 8.7 \pm 1.1$ pb. The results are thus in tension with each other at the level of ca. 2 standard deviations. Since the ATLAS results are preliminary and very recent at the time of writing, the source of this tension is not yet known. It will be the task of future studies and comparisons between the experiments to shed further light on this topic.

8.10.2 ATLAS A/H $\rightarrow t\bar{t}$ search

Before the appearance of this result and Ref. [210], the ATLAS collaboration presented a similar search for heavy pseudoscalar or scalar bosons in $t\bar{t}$ events using the full LHC Run 2 data set in Ref. [209], and observed no excess at the $t\bar{t}$ threshold. To decide whether that result contradicts the one presented here as well as the preliminary ATLAS result of Ref. [210], it is necessary to understand the differences between the analyses.

Ref. [209] combines the dilepton and $\ell+jets$ decay channels of $t\bar{t}$, similar to the combination presented in Sec. 8.9 for A and H, though the definitions of the channels are different: In the $\ell+jets$ channel, ATLAS does not consider events with only three jets as described in Sec. 8.9.1, but instead includes events with only one b tag in addition to events with two or more b tags. Furthermore, ATLAS defines an additional category with $\ell+jets$ events in which the decay products of the hadronically decaying top quark are merged, though this is expected to contribute mostly at high $m_{t\bar{t}}$.

In the dilepton channels, Ref. [209] uses a fundamentally different strategy than the one presented in this work. Instead of performing an explicit $t\bar{t}$ reconstruction, thus giving access to $m_{t\bar{t}}$ and the spin correlation observables c_{hel} and c_{han} , Ref. [209] uses the invariant mass $m_{b\bar{b}\ell\ell}$ of the visible decay products as well as $\Delta\phi_{\ell\ell}$, the azimuthal distance between the two leptons in the laboratory frame. The former can be considered a proxy for $m_{t\bar{t}}$, though with significant smearing due to the loss of information from the two neutrinos, as also studied in Sec. 8.7.3. The latter has indirect sensitivity to the $t\bar{t}$ spin correlation, but this sensitivity is intermixed with kinematic information due to the boosts of the leptons from their top quark parents. As a result, it is known to be hard to model accurately and it is thus affected by theoretical uncertainties [29, 254].

Combining all these differences, it is expected that the dilepton channels in Ref. [209] give only subdominant sensitivity compared to the $\ell+jets$ channels. In this work, while the situation is similar for high $m_{t\bar{t}}$, the dilepton channels contribute significantly close to the $t\bar{t}$ threshold. Furthermore, the direct use of spin correlation information means that the effect of many systematic uncertainties which only affect the kinematics is lessened greatly, as elaborated on in Sec. 8.7.3. It has been checked

internally that adopting the strategy employed in Ref. [209] for the dilepton channels in this work would lead to a greatly lessened sensitivity at the $t\bar{t}$ threshold, and likely no claims of a significant excess.

A further cause of differences could be the different treatment of systematic uncertainties, similar as in Ref. [210]. Ref. [209] considers additional nuisance parameters for the modeling of the $t\bar{t}$ continuum regarding the choice of parton shower (PYTHIA vs. HERWIG), the choice of calculation for the top quark decay (POWHEG vs. MADSPIN), and the choice of PDF in the calculation of the NNLO QCD and NLO EW corrections. The first of these has been studied here in Sec. 8.5.4, and found to not influence the results strongly in the dilepton channels due to the effect of c_{hel} . However, the important uncertainties due to the top quark Yukawa coupling and the EW correction scheme are not included in Ref. [209], since the EW corrections are calculated in a different manner. Moreover, several significant uncertainties are treated as decorrelated between different bins of the angular variables $\cos\theta^*$ and $\Delta\phi_{\ell\ell}$, which would lose the shape information provided by these variable and could thus reduce the sensitivity gained from them.

Since no explicit signal model for a $t\bar{t}$ bound state is considered in Ref. [209], the expected sensitivities to η_t cannot be directly compared. Instead, the closest considered signal is the generic pseudoscalar A at a mass of 400 GeV, higher than the minimum of 365 GeV considered here. Since a non-negligible excess is still present at that value both in the dilepton channels alone (Fig. 8.26) and in the combination with $\ell+\text{jets}$ (Fig. 8.30), while no such excess is visible in Fig. 15 of Ref. [209], the choice of signals is not the cause of the differences on its own. However, the shape difference between A at 400 GeV including the SM interference and η_t is not negligible. It is conceivable that, if the excess truly originates from a $t\bar{t}$ bound state manifesting as a narrow peak at the $t\bar{t}$ threshold, fitting the non-matching A signal to the data will worsen the issues due to modeling and systematic uncertainties as described in the previous paragraphs.

Even with all this information, it is not fully clear whether the result of this work and the preliminary ATLAS result in Ref. [210] on the one hand, which both claim the presence of an excess, and the ATLAS result in Ref. [209] on the other hand should be considered in conflict with each other or not. At the time of writing, there has also been no statement from the ATLAS Collaboration on the consistency between their two results in Ref. [209] and Ref. [210]. Together with the cross-checks performed in Sec. 8.7.3, it seems likely that the $t\bar{t}$ kinematic reconstruction in the dilepton channels, in particular the access to spin correlation, is the most important difference.

8.10.3 Other $t\bar{t}$ measurements

While this work constitutes the first time that an excess consistent with a $t\bar{t}$ bound state has been observed with a large significance by combining kinematic information

from $m_{t\bar{t}}$ with $t\bar{t}$ spin correlation observables, there have been slight hints of tensions between data and MC predictions in measurements of such observables before. First, several measurements of unfolded $t\bar{t}$ differential cross sections have observed excesses in data compared to MC predictions of the $t\bar{t}$ continuum at low invariant masses, such as $m_{t\bar{t}}$ in dilepton events [255], $m_{\ell\ell}$ in e μ events [256], and $m_{t\bar{t}}$ in $\ell+$ jets events [241]. For the $m_{t\bar{t}}$ measurements, the tension is only present in the lowest- $m_{t\bar{t}}$ bin of the unfolded distributions due to the coarse $m_{t\bar{t}}$ resolution. The significances of these excesses vary depending on the MC generator the data is compared to, and are also strongly influenced by systematic uncertainties for the two $m_{t\bar{t}}$ measurements.

Secondly, the measurements of quantum entanglement in $t\bar{t}$ pairs in the dilepton channel presented in Refs. [31, 32] measure as a sensitive observable the expectation value of c_{hel} , called D (cf. Sec. 2.2.1), for low $m_{t\bar{t}}$ events. This is conceptually similar to the observables $m_{t\bar{t}}$ and c_{hel} used in the dilepton channel of this work, though the measurement is only performed one-dimensionally in c_{hel} , employing a simple cut on $m_{t\bar{t}}$, instead of the full 3D $m_{t\bar{t}} \times c_{\text{hel}} \times c_{\text{han}}$ template used here. In both Refs. [31, 32], a smaller (i.e. more negative) value of D is observed in data compared to MC $t\bar{t}$ continuum predictions for low $m_{t\bar{t}}$ ($m_{t\bar{t}} < 380$ GeV in Ref. [32] and $m_{t\bar{t}} < 400$ GeV in Ref. [31]), though the significance is only at the level of one standard deviation. The contribution of a pseudoscalar $t\bar{t}$ bound state as observed in this work is fully consistent with this tension.

8.11 Summary and Outlook

In this chapter, a generic search for spin-0 states in $t\bar{t}$ events with the full data of LHC Run 2 was presented, targeting the dilepton decay channel of $t\bar{t}$. In addition to the invariant mass $m_{t\bar{t}}$, it uses the spin correlation variables c_{hel} and c_{han} to probe the spin and \mathcal{CP} structure of $t\bar{t}$ and possible new particles.

A statistically significant excess was observed in data for low $m_{t\bar{t}}$ events, close to the $t\bar{t}$ production threshold, showing spin correlations consistent with a pseudoscalar state. This excess is interpreted as a pseudoscalar $t\bar{t}$ quasi-bound state η_t , which is expected to be present in the SM according to NRQCD calculations. A simplified model for the production of η_t is used to measure its cross section, yielding $\sigma(\eta_t) = 8.7 \pm 1.1$ pb. Several cross-checks of this result, relaxing assumptions on the $t\bar{t}$ kinematic reconstruction as well as considering alternative MC generator setups, validate the observed excess. This result represents the first observation of η_t .

Alternatively, the excess could be interpreted as an additional pseudoscalar boson A, with mass close to the $t\bar{t}$ threshold, or as any possible mixture of A and a $t\bar{t}$ bound state. While the explanation as a $t\bar{t}$ bound state might be favored *a priori* as it is part of the SM and does not invoke any new physics, experimentally the two interpretations cannot be distinguished with the current resolution.

In addition to the interpretation of the excess, exclusion limits are set on new

pseudoscalar or scalar bosons A/H through their coupling strengths to the top quark, allowing for either one or both of these bosons simultaneously. They are presented for two scenarios, where the observed excess is either assumed to be described fully by the new boson A or by any combination of A and the bound state η_t . These limits are further combined with a separate analysis targeting the $\ell+\text{jets}$ decay channel of $t\bar{t}$. These combined limits represent the most stringent limits to date for the production of scalar bosons H decaying to $t\bar{t}$, while the limits for A are similar to those presented in Ref. [209] by ATLAS using the same integrated luminosity.

It is clear that much remains to be studied about the excess observed in this work. Firstly, the interpretation in terms of η_t presented here is performed only in the dilepton channels. In the preliminary results of Ref. [211], the combination with the $\ell+\text{jets}$ channels was also performed for the measurement of the η_t cross section; however, since the $\ell+\text{jets}$ analysis used was not optimized for signals at the $t\bar{t}$ threshold, little sensitivity could be gained compared to the dilepton channels alone. Instead, a separate $\ell+\text{jets}$ analysis optimized for a $t\bar{t}$ bound state should be performed in the future. In particular, spin correlation variables analogous to c_{hel} and c_{han} could be defined also in the $\ell+\text{jets}$ channel, as has already been done in Ref. [30] through ML-based identification of the decay products of the hadronically decaying top quark. Further sensitivity in both channels could possibly be gained from leveraging color flow observables [257, 258] to distinguish the color-singlet η_t and A/H from the dominant color-octet $t\bar{t}$ contribution.

By contrast, in the dilepton channel, the most pressing targets of improvement are the kinematic reconstruction and the $t\bar{t}$ modeling uncertainties. For the former, it would again be useful to investigate ML-based reconstruction techniques, for which several proof-of-concept studies have already been performed [212, 259], in a realistic setup. For the latter, the differences between different generator setups, as briefly studied in Sec. 8.5.4, needs to be understood more deeply. It would be ideal to cover the difference between predictions by a set of well-motivated nuisance parameters with clear physical meaning, as has been recently used by CMS in the measurement of the W boson mass [122, 260]. Extending this approach to the $t\bar{t}$ process however requires many theoretical advancements, and is likely to lie far in the future for now.

The modeling of the $t\bar{t}$ threshold region in particular is complicated, and further theory progress is urgently needed to both improve the $t\bar{t}$ continuum predictions close to the $t\bar{t}$ threshold and the prediction for the $t\bar{t}$ bound state itself. Ideally, these two parts should be unified into one prediction, as already done for the NRQCD predictions in e.g. Ref. [44], since the bound state effects and the continuum are not truly physically separable. A possible approach to do so for fully differential MC predictions, involving the reweighting of $t\bar{t}$ events by the ratio of Green's functions, is presented in Ref. [49], though this remains to be validated. Both the implementation of such a new η_t model in an experimental analysis and the precise understanding of its limitations and uncertainties will be crucial for future advancements.

To further sidestep the issue of imperfect modeling of both η_t and the $t\bar{t}$ continuum, one could attempt to observe the $t\bar{t}$ bound state in other decay channels, the most promising being the decay to two photons, $\eta_t \rightarrow \gamma\gamma$. This final state is experimentally extremely clean and does not require MC modeling of the $\gamma\gamma$ background. Instead, a possible signal could be extracted using a parametric fit of a peak over a falling background, similar to the measurement of the SM Higgs boson in the $h \rightarrow \gamma\gamma$ channel. The most important obstacle in such a project would be the small branching ratio of η_t to $\gamma\gamma$. Extrapolations of the partial width to $\gamma\gamma$ from $b\bar{b}$ and $c\bar{c}$ bound states give $\Gamma(\eta_t \rightarrow \gamma\gamma) \approx 57 \text{ keV}$ [50]. Combined with an expected total width of $\Gamma(\eta_t) \approx 2\Gamma_t$, this results in a branching ratio of $\approx 2 \times 10^{-5}$, though this is a rough estimate that could be wrong by as much as an order of magnitude. If this prediction holds, it might be possible to probe this decay channel with the full statistics collected in Runs 2 and 3 of the LHC.

Moreover, one should investigate the possibility to distinguish the effects of a $t\bar{t}$ bound state from a BSM pseudoscalar particle. A preliminary such study was already presented in Ref. [247]. Since an explicit measurement of the line shape close to the $t\bar{t}$ threshold seems to lie in the future for now due to the coarse $m_{t\bar{t}}$ resolution, alternative channels will have to be found. Possible avenues are e.g. measurements of the ratio of branching fractions to $t\bar{t}$ and $\gamma\gamma$ (see above) or $t\bar{t}$ and Zh ; investigations of four-top final states [261, 262]; or investigations of other observables in $t\bar{t}$, though this would require precise predictions of both the bound state effects and the BSM model in question.

In the more distant future, the problem of distinguishing a $t\bar{t}$ bound state and BSM pseudoscalar could be solved at a possible e^+e^- collider as long as its center-of-mass energy is large enough to reach the $t\bar{t}$ threshold. Proposals for such machines are e.g. linear colliders such as CLIC [263] and the high-energy stage of the ILC [264] or circular colliders like FCC-ee [265] and a possible high-energy stage of the CEPC [266]. Since the initial state of the collision is known at a lepton collider, a precision measurement of the $m_{t\bar{t}}$ line shape close to the $t\bar{t}$ threshold would be possible at such machines by way of an energy scan. In addition, the clean environment of an e^+e^- collision greatly reduces theory uncertainties from QCD modeling.

It is expected that, analogously to the proton-proton case, a peak originating from $t\bar{t}$ bound state effects will be visible below the $t\bar{t}$ threshold in such an energy scan. Since the initial state of e^+e^- collisions is a colorless vector state, this peak will correspond to the 3S_1 spin state (“vector toponium”), analogously to J/ψ and Υ , in contrast to the 1S_0 state considered in this work. Predictions of the line shape have been carried out at N^3LO in QCD with NNLL resummation [267, 268], and the theory uncertainties are thus greatly reduced compared to the proton-proton case. By comparing the results of a threshold scan to these predictions, one could thus directly test possible additional contributions from BSM effects [247]. Moreover, as extensively discussed in e.g. Refs. [269–271], a fit of the bound state peak could yield

a precise measurement of the top quark mass in a well-defined mass scheme, with a projected uncertainty of around 50 MeV [265, 272], as well as precise determinations of the top quark width, the top quark Yukawa coupling, and α_S [270, 273].

Returning to the more immediate future, it is of course necessary to repeat the analysis presented here with the data of LHC Run 3, ideally combining the results. While the η_t cross section, and similarly A/H limits at low masses, are dominated by systematic effects, especially the sensitivity at high A and H masses is limited by the statistics of the data. The increase in center-of-mass energy from 13 to 13.6 TeV will also help increase the cross section of high-mass signals, together making it possible to extend the probed A/H mass range to higher values.

Furthermore, concerning the limits on A and H derived here, the next step is to include these generic exclusion limits into concrete bounds on BSM models of interest. A particular such model, the production of heavy Axion-Like Particles coupling to top quarks, is studied on a phenomenological basis in the following chapter.

9 Investigation of Axion-Like Particles decaying to $t\bar{t}$

9.1 Introduction

In Chapter 8, an intriguing excess in $t\bar{t}$ events close to the $t\bar{t}$ threshold has been observed, and different scenarios, such as $t\bar{t}$ bound states or the potential existence of heavy BSM pseudoscalar particles, have been discussed to explain it.

This chapter is dedicated to another such interpretation that could explain the excess, but might also have the potential to shed light into other mysteries of the universe such as the origin of dark matter, and could further resolve some difficulties in the SM such as the strong \mathcal{CP} problem. Particles that might be key to deliver explanations in both fields are Axion-Like Particles (ALPs). In this chapter it is studied how they can be searched for in $t\bar{t}$ production.

As discussed in Sec. 2.4.3, the coupling structure of ALPs to top quarks is identical to those of the generic pseudoscalar A, such as e.g. in the 2HDM, if the basis for the ALP is chosen appropriately (cf. Eq. (2.34)). The difference comes from the gluon interaction term, which is absent for the model used for A in Chapter 8, and which results in an additional diagram where the ALP is produced through a contact interaction with the gluons.

If the coefficient $c_{\tilde{G}}$ of the ALP-gluon interaction term in Eq. (2.34) vanishes, the forms of the Lagrangians for ALP and A become identical, and the limits for A shown in Chapter 8 can be directly recasted. This is done in Sec. 9.2. If on the other hand $c_{\tilde{G}} \neq 0$, the kinematic distributions of the ALP will differ from those of A, and the experimental results are not easily translatable. This case is addressed in the scope of this work through an phenomenological study on simulation only. The technical setup of this study is described in Sec. 9.3, after which the distributions of ALP and A are compared for different benchmark points in Sec. 9.4. Projected exclusion limits for the $c_{\tilde{G}} \neq 0$ case are presented in Sec. 9.5, and a short summary is given in Sec. 9.6.

The results of this chapter have been originally published in *JHEP* as Ref. [10]. Since the results of Chapter 8 (Refs. [8, 211]) were not yet public at the time, the previous CMS result from Ref. [22] was used as a baseline. For this thesis, the translation of limits in Sec. 9.2 has been updated to reflect the results of Chapter 8.

All results presented in this chapter have been obtained as part of this thesis, except for the comparison to other final states in Sec. 9.5, which was performed by

the coauthors of Ref. [10] as indicated.

9.2 Translation of experimental limits

In the basis of Eq. (2.34), the ALP Lagrangian is identical in form to the Lagrangian of the generic pseudoscalar A given in Eq. (2.29) as long as the gluon interaction coefficient $c_{\tilde{G}}$ vanishes. For this case, one finds by comparing the coefficients that the phenomenology will be identical if

$$\frac{c_t}{f_a} = \frac{g_{A t \bar{t}}}{v} \quad (9.1)$$

where $v = 246$ GeV is the SM Higgs vacuum expectation value. Thus, the experimental results of Chapter 8, particularly the limits on $g_{A t \bar{t}}$ from the combination of dilepton and $\ell + \text{jets}$ decay channels as presented in Sec. 8.9.2, can be recasted into limits on the ALP coupling c_t/f_a for the case $c_{\tilde{G}} = 0$. This is shown in Fig. 9.1 for two different (fixed) ALP widths. The observed limits are shown with and without a $t\bar{t}$ bound state contribution, corresponding to the two scenarios in Fig. 8.30 and Fig. 8.32, and the same excess as in Chapter 8 is seen for at low ALP masses when the η_t contribution is not included. These results represent the first time limits on ALPs decaying to $t\bar{t}$ are set in the considered mass range.

In a similar fashion, the best-fit point for A as presented in Eq. (8.19) can be translated to an ALP (denoted a) for the case of $c_{\tilde{G}} = 0$, giving

$$m_a = 365 \text{ GeV}, \quad \Gamma_a/m_a = 2\%, \quad \text{and} \quad \frac{c_t}{f_a} = 3.2 \pm 0.2 \text{ TeV}^{-1}.$$

This represents a third alternative interpretation of the excess besides a $t\bar{t}$ bound state or a generic pseudoscalar A . The same caveats as for the A interpretation, as outlined in Sec. 8.7.4, apply; in particular, the mass of 365 GeV is the lowest mass point considered in the signal samples, and it is possible that lower masses closer to the $t\bar{t}$ threshold would result in a better fit.

9.3 Phenomenological setup

The remainder of this chapter is dedicated to exploring an ALP decaying to $t\bar{t}$ for the case $c_{\tilde{G}} \neq 0$, for which the results of Chapter 8 are not easily translatable since the distributions are expected to differ in shape. Due to time constraints, it was not possible as part of this work to investigate this case experimentally in the same fashion as done in Chapter 8. Instead, a phenomenological study is performed on MC simulation only, using a setup that approximates the workflow in Chapter 8.

To do so, MC samples for the signal are generated at LO in QCD with MG5_AMC@NLO for two different ALP masses (400 GeV and 800 GeV). For the ALP, an UFO model

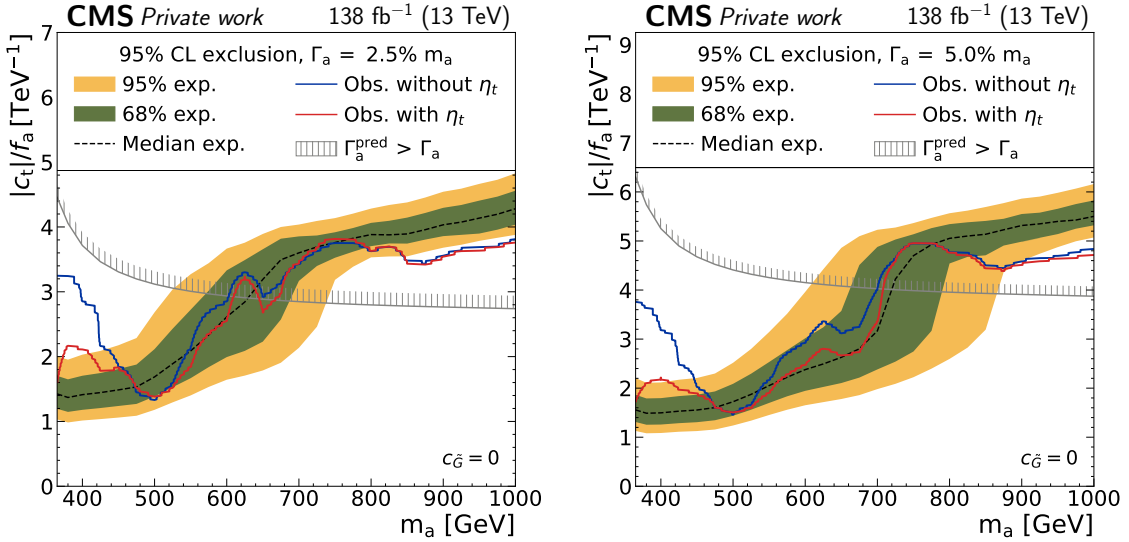


Figure 9.1: **ALP limits for $c_{\tilde{G}} = 0$.** Expected and observed limits on the ALP-top coupling c_t/f_a as a function of the ALP mass for the case $c_{\tilde{G}} = 0$ for the combined dilepton and $\ell + \text{jets}$ decay channels, translated from the results of Chapter 8. The expected limit (black line) is shown without contribution from $t\bar{t}$ bound states in the background modeling, while the observed limit is shown both without $t\bar{t}$ bound states (blue) and with η_t included as a floating background (red). The gray hatched line denotes the phase space region where the combined predicted partial width of $a \rightarrow t\bar{t}$, $a \rightarrow gg$, and $a \rightarrow \gamma\gamma$ exceeds the assumed total ALP width [10].

taken from Ref. [85] is used and modified to include the top quark loop form factor, considering finite mass effects, according to the expressions given in Ref. [274]. Both possible production diagrams, as shown in Fig. 2.10, as well as their interference with the SM are considered. A similar ME reweighting technique as in Sec. 8.4 is used to obtain samples for different widths and $c_{\tilde{G}}$ values. For the generic pseudoscalar A as well as the SM $t\bar{t}$ background, the same generators as in Sec. 8.2.1 are used (MG5_AMC@NLO and POWHEG v2 hvq, respectively, see also Sec. 4.1.2). For all samples, the NNPDF 3.1 PDF set [120] is used, and PYTHIA 8.2 is used to simulate initial and final state radiation [132].

Since the ALP always has a \mathcal{CP} -odd coupling to top quarks (cf. Eq. (2.34)), it is expected to decay to a $t\bar{t}$ system in the 1S_0 state, identically to A . This is true irrespective of the gluon coupling $c_{\tilde{G}}$ since the latter only affects the production, but not the decay $a \rightarrow t\bar{t}$, and the ALP as a colorless, spinless particle has no internal degrees of freedom. Thus, $m_{t\bar{t}}$ and c_{hel} are good discriminating variables, again similar to A , while c_{han} (optimal for \mathcal{CP} -even couplings) does not offer much additional discrimination and is not considered here. Because c_{hel} is easily experimentally

available only in the dilepton decay channel of $t\bar{t}$, only this decay channel is considered here.

No detector simulation is performed. Instead, the truth-level top quarks and leptons after parton showering are used, and efficiency, acceptance, and resolution corrections are applied to the $m_{t\bar{t}}$ distribution. The resolution correction is performed via a Gaussian smearing on a per-event basis, the standard deviation of which is derived from full detector simulation. Since this study was performed before the results of Chapter 8 were public, its predecessor Ref. [22] is used to extract the resolution by fitting to the $m_{t\bar{t}}$ distributions displayed therein. The result is $\sigma(m_{t\bar{t}})/m_{t\bar{t}} = 15\%$, which is somewhat lower than the widths found using the full detector simulation in Sec. 8.2.5 (c.f. Fig. 8.3). However, it should be cautioned that since the true $m_{t\bar{t}}$ smearing in the full detector simulation is not perfectly Gaussian, the results are not one-to-one comparable.

The experimental acceptance and efficiency, defined as the fraction of $t\bar{t} \rightarrow \ell\ell$ (ℓ being electrons, muons or leptonically decaying taus) events to survive all trigger and selection requirements, is estimated to be 10.6% for both signal and $t\bar{t}$ background, also based on Ref. [22]. This is lower compared to the updated analysis presented in Chapter 8, where values of 15–16% are achieved, varying slightly with the data-taking period. Thus, the projections in this chapter should be considered somewhat conservative.

For simplicity, instead of a multi-dimensional binning in $m_{t\bar{t}}$ and c_{hel} like in Chapter 8, a one-dimensional binning in $m_{t\bar{t}}$ only is used, and events are required to have $c_{\text{hel}} > 0.6$ to enhance the ALP signal over the background. A simplified version of the likelihood model from Chapter 8 is used, implemented in `pyhf` [154], in order to estimate projected significances and limits. Only sources of systematic uncertainty arising from theory are considered, namely:

- Missing higher orders in the matrix element, estimated from varying renormalization and factorization scale by factors of 2,
- The PDF uncertainty, estimated as the envelope of 100 pseudo-Hessian NNPDF 3.1 replicas [120],
- The total $t\bar{t}$ background production cross section, taken as a log-normal uncertainty of 6% following Ref. [22],
- The top quark mass in the $t\bar{t}$ background, varied in the range $m_t = 172.5 \pm 1 \text{ GeV}$.

It is clear that this simple treatment of systematic uncertainties can only give a rough estimate of the full likelihood as used in Chapter 8, which is sensitive mostly to the differences in shapes induced by the various systematic sources. In particular,

c_t/f_a [TeV $^{-1}$]	$c_{\tilde{G}}/f_a$ [TeV $^{-1}$]	A	$(\sigma^{\text{tot}} - \sigma^{\text{SM}})$ [pb]
3.0	+0.015	0.95	+6.7
3.0	-0.015	0.43	-2.7
1.0	+0.025	0.75	-1.7
1.0	-0.025	0.87	+2.0

Table 9.1: **Benchmark points for comparing ALP and A.** In addition to the ALP couplings c_t/f_a and $c_{\tilde{G}}/f_a$ for the benchmark points, also the difference in integrated cross section to the SM is shown, as well as a value of $g_{A t\bar{t}}$ corresponding to a generic pseudoscalar A with the same integrated cross section.

like in the experimental result, the variation of the top quark mass is important especially for ALPs with masses close to the $t\bar{t}$ threshold.

To illustrate the dependence on the likelihood model, the significances in the following results will be quoted for three different setups including different systematic uncertainties, namely all of the above, all of the above except for the top quark mass, and statistical uncertainties only. By comparing to the expected significance given in Ref. [22] for the best-fit point of the pseudoscalar A, it is found that the full setup overestimates the uncertainty, while the setup without the top quark mass slightly underestimates it.

9.4 Comparison of ALP and pseudoscalar A

To investigate the differences and possible discrimination between ALP and A, four different ALP benchmark points with $c_{\tilde{G}} \neq 0$ are defined for a mass of 400 GeV and a width of 2.5%. Each of the benchmarks is compared to a generic pseudoscalar A with its coupling $g_{A t\bar{t}}$ chosen such that the total integrated cross section of ALP and A are identical, i.e. that they cannot be distinguished by cross section information alone. The chosen couplings and resulting cross sections can be found in Tab. 9.1.

The expected $m_{t\bar{t}}$ distributions, including the smearing and acceptance described in Sec. 9.3, for the four benchmark points are shown in Fig. 9.2, together with the expected statistical uncertainty for both full Run 2 and the HL-LHC.

It can be seen that the shapes of the distributions differ qualitatively for the different benchmarks: For example, the case $c_t/f_a = 3.0$ TeV $^{-1}$ and $c_{\tilde{G}}/f_a = 0.015$ TeV $^{-1}$ (top left) shows a clear peak-dip structure similar to the A case, and as a result will likely not be distinguishable from it. In contrast, e.g. the case $c_t/f_a = 1.0$ TeV $^{-1}$ and $c_{\tilde{G}}/f_a = -0.025$ TeV $^{-1}$ (bottom right) shows a dip-peak structure instead, which cannot be reproduced by the peak-dip behavior of A production. This is possible because of the relative sign of the two couplings in this case, i.e. $c_t c_{\tilde{G}} < 0$, which

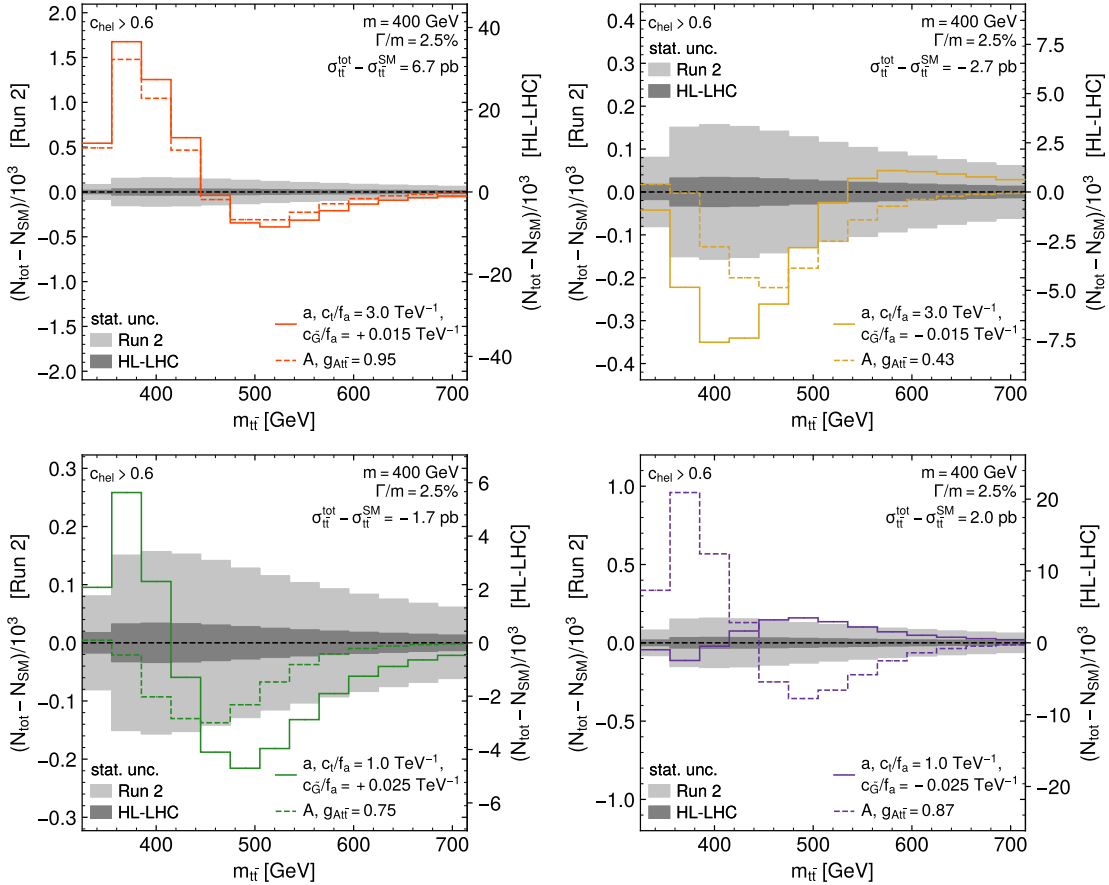


Figure 9.2: **Expected $m_{t\bar{t}}$ distributions for $pp \rightarrow a/A \rightarrow t\bar{t}$.** Shown are both ALP and A at a mass of 400 GeV for four benchmark points, with the SM subtracted. The couplings for A and a are adjusted such that the inclusive cross section is identical. The gray bands show the expected statistical uncertainty for Run 2 and HL-LHC [10].

flips the sign of the interference between the gluon interaction diagram in Fig. 2.10 (left) and the SM. In total, it is clear from all panels of Fig. 9.2 that the possibility of discriminating ALP and A depends strongly on the relative sign of c_t and $c_{\tilde{G}}$ as well as their numerical values.

By comparing the distributions to the expected statistical uncertainty, one can already estimate roughly whether discrimination of the signals with respect to the SM or with respect to each other is possible. To quantify this further, the expected significance to reject the SM-only hypothesis under the benchmark scenarios are reported in Tab. 9.2. They are computed with the likelihood model as defined in Sec. 9.3, and quoted both for the three different described uncertainty setups as well as for three different eras of the LHC, corresponding to different (expected)

c_t/f_a [TeV $^{-1}$]	$c_{\tilde{G}}/f_a$ [TeV $^{-1}$]	a	Significance (a vs. SM)			
			Luminosity	all syst.	no m_t	stats only
3.0	+0.015	Run 2	3.9	> 10	> 10	> 10
		Run 2+3	5.2	> 10	> 10	> 10
		HL-LHC	> 10	> 10	> 10	> 10
3.0	−0.015	Run 2	2.1	2.2	4.4	
		Run 2+3	3.0	3.0	6.5	
		HL-LHC	8.7	8.8	> 10	
1.0	+0.025	Run 2	1.1	2.6	4.0	
		Run 2+3	1.4	3.2	5.9	
		HL-LHC	3.9	8.2	> 10	
1.0	−0.025	Run 2	0.7	1.7	2.8	
		Run 2+3	0.9	2.2	4.1	
		HL-LHC	2.3	5.5	> 10	

Table 9.2: **Significances for detecting an ALP** with a mass of 400 GeV and a width of 2.5% for the benchmark scenarios considered in Fig. 9.2. Three different treatments of the uncertainties as defined in Sec. 9.3 are shown. For the HL-LHC projection, all systematic uncertainties are scaled by a factor of 0.5.

integrated luminosities: full Run 2 (138 fb $^{-1}$), Run 2+3 (300 fb $^{-1}$), and the HL-LHC (3 ab $^{-1}$). For the latter case, all systematic uncertainties are halved to account for the expected increase in data reconstruction quality and reduction in theoretical uncertainty.

Tab. 9.2 shows that for the HL-LHC all considered benchmark scenarios can be expected to be distinguished from the SM with $> 5\sigma$ significance if the top quark mass uncertainty is not considered in the model, that is, if experimentally it can be significantly reduced from the estimate used in this study.

If one such signal would be discovered in the future, it would be important to ascertain the particle it originates from. The $m_{t\bar{t}}$ distribution could then be used to distinguish between an ALP, exhibiting both couplings to top quarks and gluons, and the more restrictive case of A, in which only a top quark coupling is allowed. To quantify this, Tab. 9.3 now shows, for the four benchmark points, the expected significances for rejecting the A hypothesis assuming that the corresponding ALP model is realized in nature. Again, the three different uncertainty models and three LHC eras are considered. It can be seen that for all benchmarks, the HL-LHC data would make it possible to distinguish the two scenarios with $> 5\sigma$ significance in the case of an observation.

c_t/f_a [TeV $^{-1}$]	a	$c_{\tilde{G}}/f_a$ [TeV $^{-1}$]	A	$g_{A t \bar{t}}$	Luminosity	Significance (a vs. A)		
						all syst.	no m_t	stats only
3.0	+0.015	0.95	Run 2 Run 2+3 HL-LHC	0.95	1.3	1.9	3.3	
					1.8	2.3	4.9	
					5.3	5.7	> 10	
3.0	−0.015	0.43	Run 2 Run 2+3 HL-LHC	0.43	1.2	1.9	3.3	
					1.7	2.4	4.9	
					5.0	6.0	> 10	
1.0	+0.025	0.75	Run 2 Run 2+3 HL-LHC	0.75	1.5	2.3	2.7	
					2.0	3.1	3.9	
					5.8	8.8	> 10	
1.0	−0.025	0.87	Run 2 Run 2+3 HL-LHC	0.87	3.7	9.0	> 10	
					4.6	> 10	> 10	
					> 10	> 10	> 10	

Table 9.3: **Significances for the discrimination of an ALP and A** for the benchmark scenarios considered in Fig. 9.2. The uncertainties are treated as in Tab. 9.2.

9.5 Projected limits for ALPs

In case that no (additional) signal is seen in either Run 3 or at the HL-LHC, one would quantify the exclusion of ALP models based on limits in the plane of c_t/f_a and $c_{\tilde{G}}/f_a$. Projections for such expected 95% exclusion limits are presented in Fig. 9.3 for the three different considered luminosities as well as for ALP masses of 400 and 800 GeV. All systematic uncertainties except for the top quark mass are considered here, same as in the “no m_t ” column in Tab. 9.2, corresponding to the expectation that the top quark mass uncertainty can be significantly reduced in the future.

The figures show that strong limits can be set for values of $|c_{\tilde{G}}/f_a| \gtrsim 0.05$ TeV $^{-1}$ where the gluon-ALP interaction dominates and leads to signals with large cross sections, while the limits are weaker close to $c_{\tilde{G}} = 0$. Notably, the smallest signals are obtained for slightly negative values of $c_{\tilde{G}}/f_a$ due to destructive interference between the two production diagrams, leading to a slight tilt of the curve in the left panel of Fig. 9.3. Of the four considered benchmark points for a 400 GeV ALP, all can be safely expected to be excluded with HL-LHC data, while those with $c_t/f_a = 3$ TeV $^{-1}$ (red and yellow stars) as well as the scenario $c_t/f_a = 1$ TeV $^{-1}$ and $c_{\tilde{G}}/f_a = 0.025$ TeV $^{-1}$ (green star) might already be excluded by the combination of Run 2 and 3.

As part of the work of the coauthors in Ref. [10], the projected limits for Run 2 were compared with limits derived from existing analyses in other search channels, using `HiggsTools` [275]. These are reproduced briefly in the following in order to

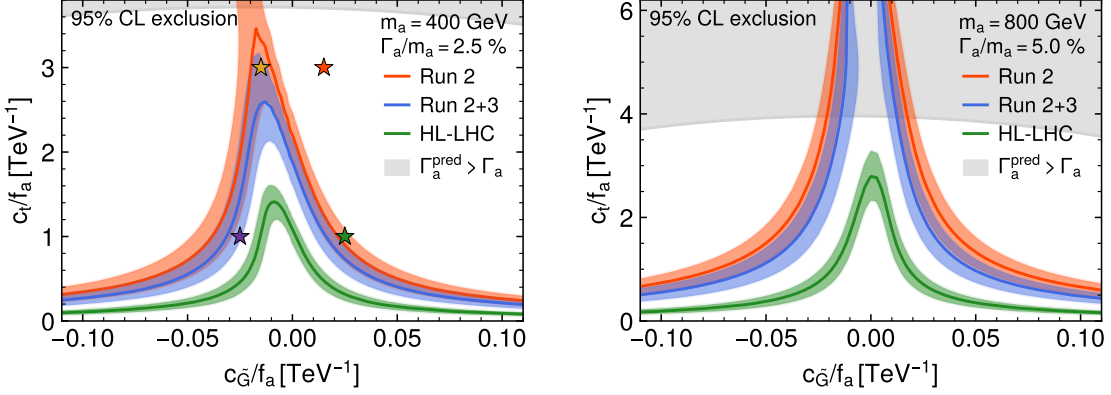


Figure 9.3: Projected ALP limits. Projected 95% exclusion limits in the plane of $c_{\tilde{G}}/f_a$ and c_t/f_a for a mass of 400 GeV and a width of 2.5% (left) as well as 800 GeV and 5.0% (right). The limits are shown for three different integrated luminosities, corresponding to Run 2, Run 2+3, and the HL-LHC, where for the latter the systematic uncertainties are halved. The gray area denotes the phase space region where the combined predicted partial width of $a \rightarrow t\bar{t}$, $a \rightarrow gg$, and $a \rightarrow \gamma\gamma$ exceeds the assumed total ALP width [10].

provide a point of reference; details can be found in Ref. [10]. The following search channels were found to be of relevance:

- $pp \rightarrow a \rightarrow \gamma\gamma$, from a generic narrow-resonance search in ATLAS [276],
- $pp \rightarrow a \rightarrow Zh$, from a search for pseudoscalars decaying into a Z boson and a SM Higgs boson in ATLAS [277],
- $pp \rightarrow t\bar{t}a \rightarrow t\bar{t}t\bar{t}$, from the CMS measurement of the four-top production cross section [261],
- interference effects between the ALP effective Lagrangian and SM Effective Field Theory (SMEFT), which would induce non-zero Wilson coefficients of SMEFT operators in electroweak precision observables such as e.g. the W boson mass, leading to indirect limits [278].

The comparison of all these limits to the projected limits from $pp \rightarrow a \rightarrow t\bar{t}$ derived in this work is shown in Fig. 9.4 in the c_t - $c_{\tilde{G}}$ plane for a 400 GeV ALP. For almost all points, $pp \rightarrow a \rightarrow t\bar{t}$ leads to stronger limits than all other direct search channels. Furthermore, for $|c_{\tilde{G}}|/f_a \gtrsim 0.03 \text{ TeV}^{-1}$ the projected limits are also stronger than the indirect ones from ALP-SMEFT interference, while this is not the case for smaller $|c_{\tilde{G}}|/f_a$. It should however be noted that the indirect limits are subject to more

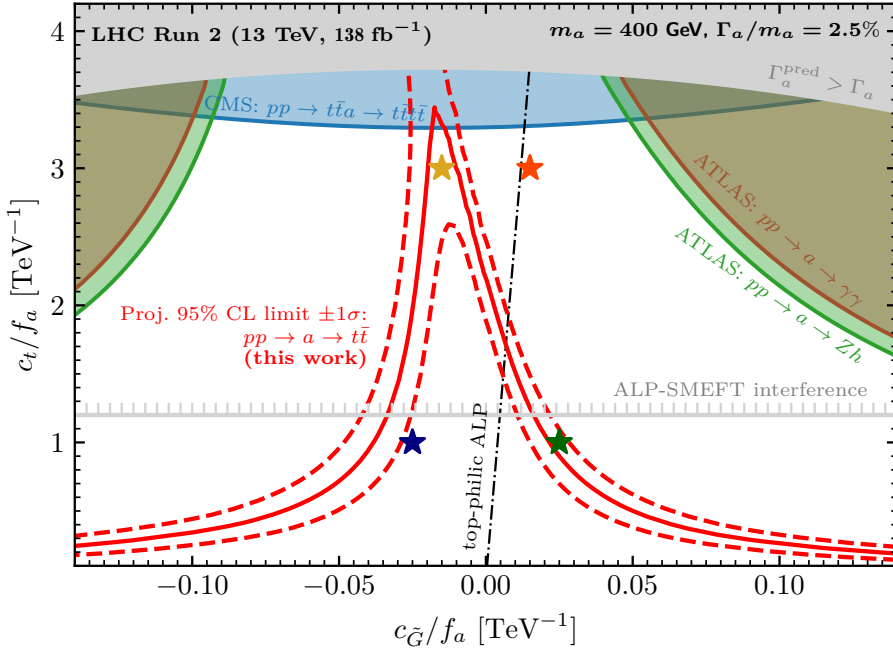


Figure 9.4: **Comparison of limits from different search channels.** 95% exclusion limits in the plane of $c_{\tilde{G}}/f_a$ and c_t/f_a for a mass of 400 GeV and a width of 2.5% (left) from different search channels. The projected limits from this work are overlaid in red [10].

assumptions, in particular, that the ALP is the only new physics contribution at the ALP scale ($\approx f_a$). For a more detailed discussion, see again Ref. [10].

9.6 Summary and Outlook

In this chapter, the $t\bar{t}$ final state is found to be an excellent channel for searching for heavy ALPs coupling to top quarks. Depending on the value of the explicit gluon-ALP coupling $c_{\tilde{G}}$, two scenarios are considered. For $c_{\tilde{G}} = 0$, the results of the experimental search for a generic pseudoscalar presented in Chapter 8, including the excess observed there, are directly translated into limits on the ALP-top coupling c_t/f_a .

For $c_{\tilde{G}} \neq 0$, on the other hand, a phenomenological study targeting the dilepton decay channel of $t\bar{t}$ is performed on simulation only, comparing ALPs to a generic pseudoscalar A which does not couple directly to gluons. It is found that ALP and A can lead to drastically different $m_{t\bar{t}}$ distributions depending on its mass as well as the strengths and signs of the couplings to top quarks and gluons. ALP and A could thus possibly be distinguished at the HL-LHC if a signal is observed. Furthermore, projected expected limits in the plane of the ALP couplings c_t/f_a and $c_{\tilde{G}}/f_a$ are set

for different integrated luminosities. They are more sensitive than other possible direct search channels in almost the whole parameter space.

The obvious continuation of this work would be to include the ALP signals for the $c_{\tilde{G}} \neq 0$ case into an experimental search like the one performed in Chapter 8. For the purpose of this thesis, this was not possible within the time constraints, and needs to be postponed to the future.

One could further investigate how the parameter space considered in this work - in particular, the very large ALP mass and comparatively strong top coupling - match to possible UV completions of the ALP effective Lagrangian. For example, Refs. [69, 70], which postulate extended color groups, seem to indicate that at least large ALP masses at the electroweak scale can be compatible with solutions of the strong \mathcal{CP} problem. It would be interesting to check whether the masses and coupling values considered in this work can be mapped into the phase spaces of such models.

10 Conclusions

10.1 Summary

In this work, key measurements and searches for new physics are performed in top quark pair ($t\bar{t}$) production with the CMS detector at the Large Hadron Collider (LHC). First, a measurement of the inclusive $t\bar{t}$ production cross section at a world-record center-of-mass energy of $\sqrt{s} = 13.6$ TeV was performed, using 1.21 fb^{-1} of early LHC Run 3 data. By combining the dilepton and $\ell+\text{jets}$ decay channels of $t\bar{t}$ for the first time and categorizing the events by their number of b tagged jets, the analysis is capable of constraining lepton and b tagging efficiencies directly *in situ*.

The result of $\sigma_{t\bar{t}} = 881 \pm 23 \text{ (stat+syst)} \pm 20 \text{ (lumi)} \text{ pb}$ is compatible with the SM prediction within one standard deviation. The measurement became public only two months after the analyzed data set was recorded, constituting the first physics result of LHC Run 3. Despite the small luminosity, the precision of the result is comparable with previous $\sigma_{t\bar{t}}$ measurements. At the time, it served as an important validation of the quality of CMS Run 3 data.

Second, essential studies on the modeling of $t\bar{t}$ production have been performed. In particular, off-shell $t\bar{t}$ production as well as interference between $t\bar{t}$ and tW production was studied in simulation using the Monte Carlo (MC) generator **bb41**, which generates the full $\text{pp} \rightarrow b\bar{b}\ell\ell\nu\bar{\nu}$ amplitude at next-to-leading order (NLO) in quantum chromodynamics (QCD). In this work, **bb41** matched to the parton shower in PYTHIA is implemented and validated in the CMS software stack for the first time and compared to several other $t\bar{t}$ MC generators. Good agreement between **bb41** and unfolded ATLAS data is found for the variable $m_{b\ell}^{\text{minimax}}$, which is sensitive to the $t\bar{t}/tW$ interference. Significant shifts in the reconstructed top mass line shape compared to other generators are observed. Additionally, a brief investigation of the matching procedure between **bb41** and PYTHIA is presented. These studies represent the starting point for future precision $t\bar{t}$ analyses in CMS using **bb41**, such as measurements of the top mass and width.

Finally, a search for spin-0 states decaying to $t\bar{t}$ in the dilepton channel has been presented. The search uses the full CMS Run 2 data set, corresponding to 138 fb^{-1} and $\sqrt{s} = 13$ TeV, and employs the invariant $t\bar{t}$ mass ($m_{t\bar{t}}$) as well as two $t\bar{t}$ spin correlation observables to gain sensitivity to the \mathcal{CP} structure of possible new intermediate states. An excess compared to the $t\bar{t}$ continuum prediction is observed for low $m_{t\bar{t}}$ events, consistent with spin correlations as expected from a pseudoscalar state. This excess is interpreted as a pseudoscalar $t\bar{t}$ bound state η_t , as predicted by

several calculations in non-relativistic QCD (NRQCD). The production cross section of η_t is measured using a simplified η_t model, resulting in $\sigma(\eta_t) = 8.7 \pm 1.1 \text{ pb}$, which is of the same order of magnitude as NRQCD-based estimates. The uncertainty is dominated by its systematic component, in particular the challenging modeling of the $t\bar{t}$ continuum. Several detailed cross-checks, such as bypassing the experimental $t\bar{t}$ reconstruction as well as using different MC generators, are discussed, and all confirm the presence of the excess. The significance of the result exceeds five standard deviations. The excess has furthermore been confirmed by the ATLAS Collaboration in a preliminary result.

Because possible BSM contributions to the excess cannot be ruled out with the current experimental precision, the same search is further interpreted in terms of new, generic pseudoscalar (A) or scalar (H) particles coupling to top quarks, as expected e.g. in Two-Higgs Doublet models (2HDMs). The interference between the new particles and the SM is taken into account. Besides an interpretation of the same excess at low $m_{t\bar{t}}$, exclusion limits on the couplings to the top quark are presented in two scenarios, assuming the excess to be either fully described by A and H or fully by a $t\bar{t}$ bound state. These limits are combined with a similar search in the $\ell+\text{jets}$ decay channels of $t\bar{t}$, giving the most stringent limits to date for the coupling of the scalar H to top quarks. Furthermore, exclusion regions are also provided for the simultaneous presence of A and H, for the first time in the $t\bar{t}$ final state.

For a third interpretation, Axion-Like Particles (ALPs) decaying to $t\bar{t}$ are considered. In the case of vanishing tree-level couplings between ALPs and gluons $c_{\tilde{G}}$, the results for the generic pseudoscalar A are directly translatable, and experimental limits on the coupling between ALP and top quark are presented. The more generic case of $c_{\tilde{G}} \neq 0$ is studied using simulated events, and projected significances and exclusion limits on such ALPs decaying to $t\bar{t}$ are derived for various phases of the LHC. It is found that at the high-luminosity LHC, ALPs and other pseudoscalars as e.g. in the 2HDM could be distinguishable based on their $m_{t\bar{t}}$ distribution. The resulting limits are expected to improve on limits from other final states in large areas of phase space.

10.2 Outlook

Branching out from the different aspects of this work, many directions of further study could be pursued. The most pressing one is certainly a further investigation of the excess at the $t\bar{t}$ production threshold observed here. Since the ATLAS experiment has confirmed the excess in a preliminary result, it would now be of great interest to scrutinize its origin, and to attempt to disentangle $t\bar{t}$ bound state effects from possible BSM contributions.

At the LHC, this will likely be challenging. For a direct measurement of the line shape, which could then be compared to predictions in the SM and for BSM models,

the $m_{t\bar{t}}$ resolution would need to be increased by orders of magnitude. Applying modern machine learning techniques such as transformers or normalizing flows to the reconstruction of top quarks could present a first step in this direction. These improvements would also benefit top quark physics in general, e.g. for precision measurements of the top quark mass.

At the same time, more precise calculations of the $t\bar{t}$ threshold are required. In particular, no fully differential Monte Carlo generator for the $t\bar{t}$ threshold in proton-proton collisions is in sight at the time of writing, which required the use of toy models for a $t\bar{t}$ bound state in this work. Replacing these by a rigorous first-principles calculation, which should simultaneously take into account bound state contributions and the $t\bar{t}$ continuum, is indispensable to separate out any possible BSM effects. It will further be necessary to study the interplay and possible admixture between the bound state and BSM contributions.

Simultaneously, one should search for possible signals at the same resonance mass in other decay channels. For a $t\bar{t}$ bound state, the decays to $\gamma\gamma$ and Zh could possibly be observed, either already with the full Run 3 data or only at the high-luminosity LHC, depending on the uncertain branching fractions. Measurements of the ratio of these branching fractions and the branching fraction to $t\bar{t}$ could then be compared to the predictions of specific BSM models, giving another handle for discriminating between $t\bar{t}$ bound state and BSM. Further such handles could be provided by measurements of orthogonal observables in $t\bar{t}$ events, e.g. color flow observables, for which machine learning-based reconstruction techniques are again crucial.

In the more distant future, a possible e^+e^- collider running at a center-of-mass energy close to the $t\bar{t}$ threshold would be invaluable to ascertain the nature of the excess. Due to the excellent energy resolution of lepton colliders, and the significantly cleaner environment due to reduced QCD effects, an energy scan of the $t\bar{t}$ production cross section around the threshold would directly measure the line shape of the expected bound state peak. At the same time, the theory predictions of this line shape are available at great precision in QCD already now, and so a comparison of the energy scan results to the calculations could immediately exclude or confirm the presence of possible BSM contributions to the excess. A fit of the position and line shape of the peak could further be used for a precise determination of the top quark mass, width and Yukawa coupling, as well as the strong coupling α_s .

It is not every day that such an excess is observed in high energy physics. Regardless of its origin, its study marks the begin of a new chapter in top quark physics.

A Bibliography

- [1] ATLAS Collaboration, “Observation of a new particle in the search for the standard model Higgs boson with the ATLAS detector at the LHC”, *Phys. Lett. B*, vol. 716, p. 1, 2012. DOI: 10.1016/j.physletb.2012.08.020. arXiv: 1207.7214 [hep-ex].
- [2] CMS Collaboration, “Observation of a new boson at a mass of 125 GeV with the CMS experiment at the LHC”, *Phys. Lett. B*, vol. 716, p. 30, 2012. DOI: 10.1016/j.physletb.2012.08.021. arXiv: 1207.7235 [hep-ex].
- [3] CMS Collaboration, “Observation of a new boson with mass near 125 GeV in pp collisions at $\sqrt{s} = 7$ and 8 TeV”, *JHEP*, vol. 06, p. 081, 2013. DOI: 10.1007/JHEP06(2013)081. arXiv: 1303.4571 [hep-ex].
- [4] CMS Collaboration, “The CMS Experiment at the CERN LHC”, *JINST*, vol. 3, S08004, 2008. DOI: 10.1088/1748-0221/3/08/S08004.
- [5] CMS Collaboration, “First measurement of the top quark pair production cross section in proton-proton collisions at $\sqrt{s} = 13.6$ TeV”, *JHEP*, vol. 08, p. 204, 2023. DOI: 10.1007/JHEP08(2023)204. arXiv: 2303.10680 [hep-ex].
- [6] T. Ježo, J. M. Lindert, P. Nason, C. Oleari, and S. Pozzorini, “An NLO+PS generator for $t\bar{t}$ and Wt production and decay including non-resonant and interference effects”, *Eur. Phys. J. C*, vol. 76, p. 691, 2016. DOI: 10.1140/epjc/s10052-016-4538-2. arXiv: 1607.04538 [hep-ph].
- [7] CMS Collaboration, “Simulation of on- and off-shell $t\bar{t}$ production with the Monte Carlo generator `b_bbar_4l` at CMS”, CERN, Geneva, Tech. Rep., 2023. [Online]. Available: <https://cds.cern.ch/record/2884265>.
- [8] CMS Collaboration, “Observation of a pseudoscalar excess at the top quark pair production threshold”, 2025, accepted by *Rep. Prog. Phys.* arXiv: 2503.22382 [hep-ex].
- [9] CMS Collaboration, “Search for heavy pseudoscalar and scalar bosons decaying to a top quark pair in proton-proton collisions at $\sqrt{s} = 13$ TeV”, 2025, submitted to *Rep. Prog. Phys.* arXiv: 2507.05119 [hep-ex].
- [10] A. Anuar et al., “ALP-ine quests at the LHC: hunting axion-like particles via peaks and dips in $t\bar{t}$ production”, *JHEP*, vol. 24, p. 197, 2024. DOI: 10.1007/JHEP12(2024)197. arXiv: 2404.19014 [hep-ph].
- [11] B. R. Martin and G. Shaw, *Particle Physics*. Wiley, 2008, ISBN: 978-0-470-03294-7.

- [12] M. D. Schwartz, *Quantum Field Theory and the Standard Model*. Cambridge University Press, Mar. 2014, ISBN: 978-1-107-03473-0, 978-1-107-03473-0.
- [13] R. L. Workman et al., “Review of Particle Physics”, *PTEP*, vol. 2022, p. 083C01, 2022. DOI: 10.1093/ptep/ptac097.
- [14] P. W. Higgs, “Broken symmetries, massless particles and gauge fields”, *Phys. Lett.*, vol. 12, pp. 132–133, 1964. DOI: 10.1016/0031-9163(64)91136-9.
- [15] F. Englert and R. Brout, “Broken Symmetry and the Mass of Gauge Vector Mesons”, *Phys. Rev. Lett.*, vol. 13, J. C. Taylor, Ed., pp. 321–323, 1964. DOI: 10.1103/PhysRevLett.13.321.
- [16] M. E. Peskin and D. V. Schroeder, *An Introduction to quantum field theory*. Reading, USA: Addison-Wesley, 1995, ISBN: 978-0-201-50397-5, 978-0-429-50355-9, 978-0-429-49417-8. DOI: 10.1201/9780429503559.
- [17] P. Skands, “Introduction to QCD”, in *Searching for New Physics at Small and Large Scales*, 2013, pp. 341–420. DOI: 10.1142/9789814525220_0008. arXiv: 1207.2389 [hep-ph].
- [18] CDF Collaboration, “Observation of top quark production in $\bar{p}p$ collisions”, *Phys. Rev. Lett.*, vol. 74, pp. 2626–2631, 1995. DOI: 10.1103/PhysRevLett.74.2626. arXiv: hep-ex/9503002.
- [19] D0 Collaboration, “Observation of the top quark”, *Phys. Rev. Lett.*, vol. 74, pp. 2632–2637, 1995. DOI: 10.1103/PhysRevLett.74.2632. arXiv: hep-ex/9503003.
- [20] ATLAS and CMS Collaborations, “Combination of Measurements of the Top Quark Mass from Data Collected by the ATLAS and CMS Experiments at $\sqrt{s} = 7$ and 8 TeV”, *Phys. Rev. Lett.*, vol. 132, no. 26, p. 261902, 2024. DOI: 10.1103/PhysRevLett.132.261902. arXiv: 2402.08713 [hep-ex].
- [21] Y. Kats and D. Uzan, “Prospects for measuring quark polarization and spin correlations in $b\bar{b}$ and $c\bar{c}$ samples at the LHC”, *JHEP*, vol. 03, p. 063, 2024. DOI: 10.1007/JHEP03(2024)063. arXiv: 2311.08226 [hep-ph].
- [22] CMS Collaboration, “Search for heavy Higgs bosons decaying to a top quark pair in proton-proton collisions at $\sqrt{s} = 13$ TeV”, *JHEP*, vol. 04, p. 171, 2020, [Erratum: JHEP 03, 187 (2022)]. DOI: 10.1007/JHEP04(2020)171. arXiv: 1908.01115 [hep-ex].
- [23] W. Bernreuther, A. Brandenburg, Z. G. Si, and P. Uwer, “Top quark pair production and decay at hadron colliders”, *Nucl. Phys. B*, vol. 690, pp. 81–137, 2004. DOI: 10.1016/j.nuclphysb.2004.04.019. arXiv: hep-ph/0403035.
- [24] F. Maltoni, C. Severi, S. Tentori, and E. Vryonidou, “Quantum detection of new physics in top-quark pair production at the LHC”, *JHEP*, vol. 03, p. 099, 2024. DOI: 10.1007/JHEP03(2024)099. arXiv: 2401.08751 [hep-ph].

- [25] K. Cheng, T. Han, and M. Low, “Optimizing entanglement and Bell inequality violation in top antitop events”, *Phys. Rev. D*, vol. 111, no. 3, p. 033 004, 2025. DOI: [10.1103/PhysRevD.111.033004](https://doi.org/10.1103/PhysRevD.111.033004). arXiv: 2407.01672 [hep-ph].
- [26] A. Czarnecki, M. Jezabek, and J. H. Kuhn, “Lepton Spectra From Decays of Polarized Top Quarks”, *Nucl. Phys. B*, vol. 351, pp. 70–80, 1991. DOI: [10.1016/0550-3213\(91\)90082-9](https://doi.org/10.1016/0550-3213(91)90082-9).
- [27] W. Bernreuther, A. Brandenburg, Z. G. Si, and P. Uwer, “Spin properties of top quark pairs produced at hadron colliders”, *Acta Phys. Polon. B*, vol. 34, K. Fialkowski, M. Jezabek, and M. Rozanska, Eds., pp. 4477–4490, 2003. arXiv: [hep-ph/0304244](https://arxiv.org/abs/hep-ph/0304244).
- [28] CMS Collaboration, “Measurements of t t-bar spin correlations and top quark polarization using dilepton final states in pp collisions at sqrt(s) = 8 TeV”, *Phys. Rev. D*, vol. 93, no. 5, p. 052 007, 2016. DOI: [10.1103/PhysRevD.93.052007](https://doi.org/10.1103/PhysRevD.93.052007). arXiv: 1601.01107 [hep-ex].
- [29] CMS Collaboration, “Measurement of the top quark polarization and t t-bar spin correlations using dilepton final states in proton-proton collisions at $\sqrt{s} = 13$ TeV”, *Phys. Rev. D*, vol. 100, no. 7, p. 072 002, 2019. DOI: [10.1103/PhysRevD.100.072002](https://doi.org/10.1103/PhysRevD.100.072002). arXiv: 1907.03729 [hep-ex].
- [30] CMS Collaboration, “Measurements of polarization and spin correlation and observation of entanglement in top quark pairs using lepton+jets events from proton-proton collisions at $\sqrt{s} = 13$ TeV”, *Phys. Rev. D*, vol. 110, no. 11, p. 112 016, 2024. DOI: [10.1103/PhysRevD.110.112016](https://doi.org/10.1103/PhysRevD.110.112016). arXiv: 2409.11067 [hep-ex].
- [31] CMS Collaboration, “Observation of quantum entanglement in top quark pair production in proton–proton collisions at $\sqrt{s} = 13$ TeV”, *Rept. Prog. Phys.*, vol. 87, no. 11, p. 117 801, 2024. DOI: [10.1088/1361-6633/ad7e4d](https://doi.org/10.1088/1361-6633/ad7e4d). arXiv: 2406.03976 [hep-ex].
- [32] ATLAS Collaboration, “Observation of quantum entanglement with top quarks at the ATLAS detector”, *Nature*, vol. 633, no. 8030, pp. 542–547, 2024. DOI: [10.1038/s41586-024-07824-z](https://doi.org/10.1038/s41586-024-07824-z). arXiv: 2311.07288 [hep-ex].
- [33] A. A. Anuar, “Top Quark Spin and Polarization Properties in Searches for New Phenomena with the CMS Detector at the LHC”, PhD thesis, DESY, Hamburg, 2019.
- [34] W. Bernreuther, P. Galler, Z.-G. Si, and P. Uwer, “Production of heavy Higgs bosons and decay into top quarks at the LHC. II: Top-quark polarization and spin correlation effects”, *Phys. Rev. D*, vol. 95, no. 9, p. 095 012, 2017. DOI: [10.1103/PhysRevD.95.095012](https://doi.org/10.1103/PhysRevD.95.095012). arXiv: 1702.06063 [hep-ph].

- [35] W. Bernreuther, D. Heisler, and Z.-G. Si, “A set of top quark spin correlation and polarization observables for the LHC: Standard Model predictions and new physics contributions”, *JHEP*, vol. 12, p. 026, 2015. DOI: 10.1007/JHEP12(2015)026. arXiv: 1508.05271 [hep-ph].
- [36] A. Deur, S. J. Brodsky, and G. F. de Teramond, “The QCD Running Coupling”, *Nucl. Phys.*, vol. 90, p. 1, 2016. DOI: 10.1016/j.ppnp.2016.04.003. arXiv: 1604.08082 [hep-ph].
- [37] V. S. Fadin and V. A. Khoze, “Threshold behavior of the cross section for the production of t quarks in e^+e^- annihilation”, *JETP Lett.*, vol. 46, p. 417, 11 1987.
- [38] N. Fabiano, G. Pancheri, and A. Grau, “Toponium from different potential models”, *Nuovo Cim. A*, vol. 107, pp. 2789–2804, 1994. DOI: 10.1007/BF02730956.
- [39] F. Maltoni, “Introduction to toponium physics”, Talk at the LHC Top Working Group Open Session, 2024. [Online]. Available: <https://indico.cern.ch/event/1444046/contributions/6216409>.
- [40] Y. Kiyo, J. H. Kuhn, S. Moch, M. Steinhauser, and P. Uwer, “Top-quark pair production near threshold at LHC”, *Eur. Phys. J. C*, vol. 60, pp. 375–386, 2009. DOI: 10.1140/epjc/s10052-009-0892-7. arXiv: 0812.0919 [hep-ph].
- [41] J.-H. Fu, Y.-J. Li, H.-M. Yang, Y.-B. Li, Y.-J. Zhang, and C.-P. Shen, “Toponium: The smallest bound state and simplest hadron in quantum mechanics”, *Phys. Rev. D*, vol. 111, no. 11, p. 114020, 2025. DOI: 10.1103/fqc9-k315. arXiv: 2412.11254 [hep-ph].
- [42] V. S. Fadin, V. A. Khoze, and T. Sjöstrand, “On the threshold behaviour of heavy top production”, *Z. Phys. C*, vol. 48, p. 613, 1990. DOI: 10.1007/BF01614696.
- [43] Y. Sumino and H. Yokoya, “Bound-state effects on kinematical distributions of top quarks at hadron colliders”, *JHEP*, vol. 09, p. 034, 2010, [Erratum: JHEP 06, 037 (2016)]. DOI: 10.1007/JHEP09(2010)034. arXiv: 1007.0075 [hep-ph].
- [44] M. V. Garzelli, G. Limatola, S. Moch, M. Steinhauser, and O. Zenaiev, “Updated predictions for toponium production at the LHC”, Dec. 2024. arXiv: 2412.16685 [hep-ph].
- [45] W.-L. Ju, G. Wang, X. Wang, X. Xu, Y. Xu, and L. L. Yang, “Top quark pair production near threshold: single/double distributions and mass determination”, *JHEP*, vol. 06, p. 158, 2020. DOI: 10.1007/JHEP06(2020)158. arXiv: 2004.03088 [hep-ph].

- [46] F. Maltoni, C. Severi, S. Tentori, and E. Vryonidou, “Quantum tops at circular lepton colliders”, *JHEP*, vol. 09, p. 001, 2024. DOI: 10.1007/JHEP09(2024)001. arXiv: 2404.08049 [hep-ph].
- [47] B. Fuks, K. Hagiwara, K. Ma, and Y.-J. Zheng, “Signatures of toponium formation in LHC run 2 data”, *Phys. Rev. D*, vol. 104, no. 3, p. 034023, 2021. DOI: 10.1103/PhysRevD.104.034023. arXiv: 2102.11281 [hep-ph].
- [48] J. A. Aguilar-Saavedra, “Toponium hunter’s guide”, *Phys. Rev. D*, vol. 110, no. 5, p. 054032, 2024. DOI: 10.1103/PhysRevD.110.054032. arXiv: 2407.20330 [hep-ph].
- [49] B. Fuks, K. Hagiwara, K. Ma, and Y.-J. Zheng, “Simulating toponium formation signals at the LHC”, *Eur. Phys. J. C*, vol. 85, no. 2, p. 157, 2025. DOI: 10.1140/epjc/s10052-025-13853-3. arXiv: 2411.18962 [hep-ph].
- [50] S.-J. Jiang, B.-Q. Li, G.-Z. Xu, and K.-Y. Liu, “Study on Toponium: Spectrum and Associated Processes”, Dec. 2024. arXiv: 2412.18527 [hep-ph].
- [51] T. Barnes, S. Godfrey, and E. S. Swanson, “Higher charmonia”, *Phys. Rev. D*, vol. 72, p. 054026, 2005. DOI: 10.1103/PhysRevD.72.054026. arXiv: hep-ph/0505002.
- [52] G. Bertone, D. Hooper, and J. Silk, “Particle dark matter: Evidence, candidates and constraints”, *Phys. Rept.*, vol. 405, pp. 279–390, 2005. DOI: 10.1016/j.physrep.2004.08.031. arXiv: hep-ph/0404175.
- [53] T. A. Porter, R. P. Johnson, and P. W. Graham, “Dark Matter Searches with Astroparticle Data”, *Ann. Rev. Astron. Astrophys.*, vol. 49, pp. 155–194, 2011. DOI: 10.1146/annurev-astro-081710-102528. arXiv: 1104.2836 [astro-ph.HE].
- [54] A. Arbey and F. Mahmoudi, “Dark matter and the early Universe: a review”, *Prog. Part. Nucl. Phys.*, vol. 119, p. 103865, 2021. DOI: 10.1016/j.ppnp.2021.103865. arXiv: 2104.11488 [hep-ph].
- [55] M. Dine and A. Kusenko, “The Origin of the matter - antimatter asymmetry”, *Rev. Mod. Phys.*, vol. 76, p. 1, 2003. DOI: 10.1103/RevModPhys.76.1. arXiv: hep-ph/0303065.
- [56] L. Canetti, M. Drewes, and M. Shaposhnikov, “Matter and Antimatter in the Universe”, *New J. Phys.*, vol. 14, p. 095012, 2012. DOI: 10.1088/1367-2630/14/9/095012. arXiv: 1204.4186 [hep-ph].
- [57] A. de Gouv  a, “Neutrino Mass Models”, *Ann. Rev. Nucl. Part. Sci.*, vol. 66, pp. 197–217, 2016. DOI: 10.1146/annurev-nucl-102115-044600.
- [58] A. Dev, “Neutrino Oscillations and Mass Models”, Oct. 2023. arXiv: 2310.17685 [hep-ph].

- [59] P. Nelson, “Naturalness in Theoretical Physics”, *American Scientist*, vol. 73, no. 1, pp. 60–67, 1985.
- [60] S. Koren, “New Approaches to the Hierarchy Problem and their Signatures from Microscopic to Cosmic Scales”, Ph.D. dissertation, UC Santa Barbara, 2020. arXiv: 2009.11870 [hep-ph].
- [61] N. Craig, “Naturalness: past, present, and future”, *Eur. Phys. J. C*, vol. 83, no. 9, p. 825, 2023. DOI: 10.1140/epjc/s10052-023-11928-7. arXiv: 2205.05708 [hep-ph].
- [62] R. D. Peccei and H. R. Quinn, “CP Conservation in the Presence of Instantons”, *Phys. Rev. Lett.*, vol. 38, pp. 1440–1443, 1977. DOI: 10.1103/PhysRevLett.38.1440.
- [63] R. D. Peccei and H. R. Quinn, “Constraints Imposed by CP Conservation in the Presence of Instantons”, *Phys. Rev. D*, vol. 16, pp. 1791–1797, 1977. DOI: 10.1103/PhysRevD.16.1791.
- [64] G. C. Branco, P. M. Ferreira, L. Lavoura, M. N. Rebelo, M. Sher, and J. P. Silva, “Theory and phenomenology of two-Higgs-doublet models”, *Phys. Rept.*, vol. 516, pp. 1–102, 2012. DOI: 10.1016/j.physrep.2012.02.002. arXiv: 1106.0034 [hep-ph].
- [65] K. Huitu, N. Koivunen, O. Lebedev, S. Mondal, and T. Toma, “Probing pseudo-Goldstone dark matter at the LHC”, *Phys. Rev. D*, vol. 100, p. 015009, 2019. DOI: 10.1103/PhysRevD.100.015009. arXiv: 1812.05952 [hep-ph].
- [66] M. Mühlleitner, M. O. P. Sampaio, R. Santos, and J. Wittbrodt, “Phenomenological comparison of models with extended Higgs sectors”, *JHEP*, vol. 08, p. 132, 2017. DOI: 10.1007/JHEP08(2017)132. arXiv: 1703.07750 [hep-ph].
- [67] J. Abdallah et al., “Simplified models for dark matter searches at the LHC”, *Phys. Dark Univ.*, vol. 9–10, p. 8, 2015. DOI: 10.1016/j.dark.2015.08.001. arXiv: 1506.03116 [hep-ph].
- [68] C. Arina et al., “A comprehensive approach to dark matter studies: Exploration of simplified top-philic models”, *JHEP*, vol. 11, p. 111, 2016. DOI: 10.1007/JHEP11(2016)111. arXiv: 1605.09242 [hep-ph].
- [69] S. Dimopoulos, A. Hook, J. Huang, and G. Marques-Tavares, “A collider observable QCD axion”, *JHEP*, vol. 11, p. 052, 2016. DOI: 10.1007/JHEP11(2016)052. arXiv: 1606.03097 [hep-ph].
- [70] T. Gherghetta, N. Nagata, and M. Shifman, “A Visible QCD Axion from an Enlarged Color Group”, *Phys. Rev. D*, vol. 93, no. 11, p. 115010, 2016. DOI: 10.1103/PhysRevD.93.115010. arXiv: 1604.01127 [hep-ph].

- [71] CMS Collaboration, “Search for dark matter produced in association with one or two top quarks in proton-proton collisions at $\sqrt{s} = 13$ TeV”, 2025, accepted by *JHEP*. arXiv: 2505.05300 [hep-ex].
- [72] T. D. Lee, “A Theory of Spontaneous T Violation”, *Phys. Rev. D*, vol. 8, G. Feinberg, Ed., pp. 1226–1239, 1973. DOI: 10.1103/PhysRevD.8.1226.
- [73] H. E. Haber and G. L. Kane, “The Search for Supersymmetry: Probing Physics Beyond the Standard Model”, *Phys. Rept.*, vol. 117, pp. 75–263, 1985. DOI: 10.1016/0370-1573(85)90051-1.
- [74] J. E. Kim, “Light Pseudoscalars, Particle Physics and Cosmology”, *Phys. Rept.*, vol. 150, pp. 1–177, 1987. DOI: 10.1016/0370-1573(87)90017-2.
- [75] S. Weinberg, “A New Light Boson?”, *Phys. Rev. Lett.*, vol. 40, pp. 223–226, 1978. DOI: 10.1103/PhysRevLett.40.223.
- [76] F. Wilczek, “Problem of Strong P and T Invariance in the Presence of Instantons”, *Phys. Rev. Lett.*, vol. 40, pp. 279–282, 1978. DOI: 10.1103/PhysRevLett.40.279.
- [77] L. Di Luzio, M. Giannotti, E. Nardi, and L. Visinelli, “The landscape of QCD axion models”, *Phys. Rept.*, vol. 870, pp. 1–117, 2020. DOI: 10.1016/j.physrep.2020.06.002. arXiv: 2003.01100 [hep-ph].
- [78] J. M. Pendlebury et al., “Revised experimental upper limit on the electric dipole moment of the neutron”, *Phys. Rev. D*, vol. 92, no. 9, p. 092003, 2015. DOI: 10.1103/PhysRevD.92.092003. arXiv: 1509.04411 [hep-ex].
- [79] C. Abel et al., “Measurement of the Permanent Electric Dipole Moment of the Neutron”, *Phys. Rev. Lett.*, vol. 124, no. 8, p. 081803, 2020. DOI: 10.1103/PhysRevLett.124.081803. arXiv: 2001.11966 [hep-ex].
- [80] J. E. Kim, “Weak Interaction Singlet and Strong CP Invariance”, *Phys. Rev. Lett.*, vol. 43, p. 103, 1979. DOI: 10.1103/PhysRevLett.43.103.
- [81] M. A. Shifman, A. I. Vainshtein, and V. I. Zakharov, “Can Confinement Ensure Natural CP Invariance of Strong Interactions?”, *Nucl. Phys. B*, vol. 166, pp. 493–506, 1980. DOI: 10.1016/0550-3213(80)90209-6.
- [82] M. Dine, W. Fischler, and M. Srednicki, “A Simple Solution to the Strong CP Problem with a Harmless Axion”, *Phys. Lett. B*, vol. 104, pp. 199–202, 1981. DOI: 10.1016/0370-2693(81)90590-6.
- [83] A. R. Zhitnitsky, “On Possible Suppression of the Axion Hadron Interactions”, *Sov. J. Nucl. Phys.*, vol. 31, p. 260, 1980.
- [84] H. Georgi, D. B. Kaplan, and L. Randall, “Manifesting the Invisible Axion at Low-energies”, *Phys. Lett. B*, vol. 169, pp. 73–78, 1986. DOI: 10.1016/0370-2693(86)90688-X.

- [85] I. Brivio et al., “ALPs Effective Field Theory and Collider Signatures”, *Eur. Phys. J. C*, vol. 77, no. 8, p. 572, 2017. DOI: 10.1140/epjc/s10052-017-5111-3. arXiv: 1701.05379 [hep-ph].
- [86] M. Bauer, M. Neubert, S. Renner, M. Schnubel, and A. Thamm, “The Low-Energy Effective Theory of Axions and ALPs”, *JHEP*, vol. 04, p. 063, 2021. DOI: 10.1007/JHEP04(2021)063. arXiv: 2012.12272 [hep-ph].
- [87] Q. Bonnely, C. Grojean, and J. Kley, “Shift-Invariant Orders of an Axionlike Particle”, *Phys. Rev. Lett.*, vol. 130, no. 11, p. 111803, 2023. DOI: 10.1103/PhysRevLett.130.111803. arXiv: 2206.04182 [hep-ph].
- [88] V. A. Rubakov, “Grand unification and heavy axion”, *JETP Lett.*, vol. 65, pp. 621–624, 1997. DOI: 10.1134/1.567390. arXiv: hep-ph/9703409.
- [89] B. Holdom and M. E. Peskin, “Raising the Axion Mass”, *Nucl. Phys. B*, vol. 208, pp. 397–412, 1982. DOI: 10.1016/0550-3213(82)90228-0.
- [90] “LHC Design Report Vol.1: The LHC Main Ring”, O. S. Bruning et al., Eds., Jun. 2004. DOI: 10.5170/CERN-2004-003-V-1.
- [91] CERN, *Overall view of the LHC*, 2014. [Online]. Available: <https://cds.cern.ch/record/1708849>.
- [92] ATLAS Collaboration, “The ATLAS Experiment at the CERN Large Hadron Collider”, *JINST*, vol. 3, S08003, 2008. DOI: 10.1088/1748-0221/3/08/S08003.
- [93] LHCb Collaboration, “The LHCb Detector at the LHC”, *JINST*, vol. 3, S08005, 2008. DOI: 10.1088/1748-0221/3/08/S08005.
- [94] ALICE Collaboration, “The ALICE experiment at the CERN LHC”, *JINST*, vol. 3, S08002, 2008. DOI: 10.1088/1748-0221/3/08/S08002.
- [95] I. Zurbano Fernandez et al., “High-Luminosity Large Hadron Collider (HL-LHC): Technical design report”, vol. 10/2020, I. Béjar Alonso, O. Brüning, P. Fessia, L. Rossi, L. Tavian, and M. Zerlauth, Eds., Dec. 2020. DOI: 10.23731/CYRM-2020-0010.
- [96] CMS Collaboration, “Technical Proposal for the Phase-II Upgrade of the CMS Detector”, Geneva, Tech. Rep., 2015. DOI: 10.17181/CERN.VU8I.D59J. [Online]. Available: <https://cds.cern.ch/record/2020886>.
- [97] CMS Collaboration, “Development of the CMS detector for the CERN LHC Run 3”, *JINST*, vol. 19, P05064, 2024. DOI: 10.1088/1748-0221/19/05/P05064. arXiv: 2309.05466 [physics.ins-det].
- [98] CMS Collaboration, *Placing the Tracker inside CMS*, 2007. [Online]. Available: <https://cds.cern.ch/record/1275108>.

- [99] CMS Collaboration, “Description and performance of track and primary-vertex reconstruction with the CMS tracker”, *JINST*, vol. 9, P10009, 2014. DOI: 10.1088/1748-0221/9/10/P10009. arXiv: 1405.6569 [physics.ins-det].
- [100] W. Adam et al., “The CMS Phase-1 Pixel Detector Upgrade”, *JINST*, vol. 16, no. 02, P02027, 2021. DOI: 10.1088/1748-0221/16/02/P02027. arXiv: 2012.14304 [physics.ins-det].
- [101] CMS Collaboration, *CMS Detector Slice*, 2016. [Online]. Available: <https://cds.cern.ch/record/2120661>.
- [102] “The CMS electromagnetic calorimeter project: Technical Design Report”, Tech. Rep., 1997.
- [103] CMS Collaboration, “Electron and photon reconstruction and identification with the CMS experiment at the CERN LHC”, *JINST*, vol. 16, no. 05, P05014, 2021. DOI: 10.1088/1748-0221/16/05/P05014. arXiv: 2012.06888 [hep-ex].
- [104] “The CMS hadron calorimeter project: Technical Design Report”, Tech. Rep., 1997.
- [105] “CMS Technical Design Report for the Phase 1 Upgrade of the Hadron Calorimeter”, Tech. Rep., Sep. 2012. DOI: 10.2172/1151651.
- [106] “The CMS muon project: Technical Design Report”, Tech. Rep., 1997.
- [107] N. Pozzobon, “The CMS Muon System performance during the LHC Run-2”, CERN, Geneva, Tech. Rep., 2019. DOI: 10.1088/1748-0221/14/11/C11031. [Online]. Available: <https://cds.cern.ch/record/2701333>.
- [108] V. Khachatryan et al., “The CMS trigger system”, *JINST*, vol. 12, no. 01, P01020, 2017. DOI: 10.1088/1748-0221/12/01/P01020. arXiv: 1609.02366 [physics.ins-det].
- [109] CMS Collaboration, “Performance of the CMS Level-1 trigger in proton-proton collisions at $\sqrt{s} = 13$ TeV”, *JINST*, vol. 15, no. 10, P10017, 2020. DOI: 10.1088/1748-0221/15/10/P10017. arXiv: 2006.10165 [hep-ex].
- [110] W. Adam et al., “The CMS high level trigger”, *Eur. Phys. J. C*, vol. 46, pp. 605–667, 2006. DOI: 10.1140/epjc/s2006-02495-8. arXiv: hep-ex/0512077.
- [111] S. Varghese, “CMS High Level Trigger Performance for Run 3”, *PoS*, vol. EPS-HEP2023, p. 517, 2023. DOI: 10.22323/1.449.0517.
- [112] CMS Collaboration, “Particle-flow reconstruction and global event description with the CMS detector”, *JINST*, vol. 12, P10003, 2017. DOI: 10.1088/1748-0221/12/10/P10003. arXiv: 1706.04965 [physics.ins-det].
- [113] D. Bertolini, P. Harris, M. Low, and N. Tran, “Pileup Per Particle Identification”, *JHEP*, vol. 10, p. 059, 2014. DOI: 10.1007/JHEP10(2014)059. arXiv: 1407.6013 [hep-ph].

- [114] CMS Collaboration, “Pileup mitigation at CMS in 13 TeV data”, *JINST*, vol. 15, no. 09, P09018, 2020. DOI: [10.1088/1748-0221/15/09/P09018](https://doi.org/10.1088/1748-0221/15/09/P09018). arXiv: 2003.00503 [hep-ex].
- [115] M. Cacciari, G. P. Salam, and G. Soyez, “The anti- k_t jet clustering algorithm”, *JHEP*, vol. 04, p. 063, 2008. DOI: [10.1088/1126-6708/2008/04/063](https://doi.org/10.1088/1126-6708/2008/04/063). arXiv: 0802.1189 [hep-ph].
- [116] E. Bols, J. Kieseler, M. Verzetti, M. Stoye, and A. Stakia, “Jet Flavour Classification Using DeepJet”, *JINST*, vol. 15, no. 12, P12012, 2020. DOI: [10.1088/1748-0221/15/12/P12012](https://doi.org/10.1088/1748-0221/15/12/P12012). arXiv: 2008.10519 [hep-ex].
- [117] CMS Collaboration, “Performance of missing transverse momentum reconstruction in proton-proton collisions at $\sqrt{s} = 13$ TeV using the CMS detector”, *JINST*, vol. 14, no. 07, P07004, 2019. DOI: [10.1088/1748-0221/14/07/P07004](https://doi.org/10.1088/1748-0221/14/07/P07004). arXiv: 1903.06078 [hep-ex].
- [118] C. Bierlich et al., “A comprehensive guide to the physics and usage of PYTHIA 8.3”, *SciPost Phys. Codeb.*, vol. 2022, p. 8, 2022. DOI: [10.21468/SciPostPhysCodeb.8](https://doi.org/10.21468/SciPostPhysCodeb.8). arXiv: 2203.11601 [hep-ph].
- [119] G. Altarelli and G. Parisi, “Asymptotic Freedom in Parton Language”, *Nucl. Phys. B*, vol. 126, pp. 298–318, 1977. DOI: [10.1016/0550-3213\(77\)90384-4](https://doi.org/10.1016/0550-3213(77)90384-4).
- [120] R. D. Ball et al., “Parton distributions from high-precision collider data”, *Eur. Phys. J. C*, vol. 77, p. 663, 2017. DOI: [10.1140/epjc/s10052-017-5199-5](https://doi.org/10.1140/epjc/s10052-017-5199-5). arXiv: 1706.00428 [hep-ph].
- [121] F. Maltoni and T. Stelzer, “MadEvent: Automatic event generation with MadGraph”, *JHEP*, vol. 02, p. 027, 2003. DOI: [10.1088/1126-6708/2003/02/027](https://doi.org/10.1088/1126-6708/2003/02/027). arXiv: hep-ph/0208156.
- [122] F. J. Tackmann, “Beyond Scale Variations: Perturbative Theory Uncertainties from Nuisance Parameters”, Nov. 2024. arXiv: 2411.18606 [hep-ph].
- [123] P. Nason and B. Webber, “Next-to-Leading-Order Event Generators”, *Ann. Rev. Nucl. Part. Sci.*, vol. 62, pp. 187–213, 2012. DOI: [10.1146/annurev-nucl-102711-094928](https://doi.org/10.1146/annurev-nucl-102711-094928). arXiv: 1202.1251 [hep-ph].
- [124] J. Alwall et al., “The automated computation of tree-level and next-to-leading order differential cross sections, and their matching to parton shower simulations”, *JHEP*, vol. 07, p. 079, 2014. DOI: [10.1007/JHEP07\(2014\)079](https://doi.org/10.1007/JHEP07(2014)079). arXiv: 1405.0301 [hep-ph].
- [125] C. Degrande, C. Duhr, B. Fuks, D. Grellscheid, O. Mattelaer, and T. Reiter, “UFO - The Universal FeynRules Output”, *Comput. Phys. Commun.*, vol. 183, pp. 1201–1214, 2012. DOI: [10.1016/j.cpc.2012.01.022](https://doi.org/10.1016/j.cpc.2012.01.022). arXiv: 1108.2040 [hep-ph].

- [126] P. Nason, “A new method for combining NLO QCD with shower Monte Carlo algorithms”, *JHEP*, vol. 11, p. 040, 2004. DOI: [10.1088/1126-6708/2004/11/040](https://doi.org/10.1088/1126-6708/2004/11/040). arXiv: [hep-ph/0409146](https://arxiv.org/abs/hep-ph/0409146).
- [127] S. Frixione, P. Nason, and C. Oleari, “Matching NLO QCD computations with parton shower simulations: The POWHEG method”, *JHEP*, vol. 11, p. 070, 2007. DOI: [10.1088/1126-6708/2007/11/070](https://doi.org/10.1088/1126-6708/2007/11/070). arXiv: [0709.2092 \[hep-ph\]](https://arxiv.org/abs/0709.2092).
- [128] S. Alioli, P. Nason, C. Oleari, and E. Re, “A general framework for implementing NLO calculations in shower Monte Carlo programs: The POWHEG BOX”, *JHEP*, vol. 06, p. 043, 2010. DOI: [10.1007/JHEP06\(2010\)043](https://doi.org/10.1007/JHEP06(2010)043). arXiv: [1002.2581 \[hep-ph\]](https://arxiv.org/abs/1002.2581).
- [129] S. Frixione, G. Ridolfi, and P. Nason, “A positive-weight next-to-leading-order Monte Carlo for heavy flavour hadroproduction”, *JHEP*, vol. 09, p. 126, 2007. DOI: [10.1088/1126-6708/2007/09/126](https://doi.org/10.1088/1126-6708/2007/09/126). arXiv: [0707.3088 \[hep-ph\]](https://arxiv.org/abs/0707.3088).
- [130] S. Frixione, E. Laenen, P. Motylinski, and B. R. Webber, “Angular correlations of lepton pairs from vector boson and top quark decays in Monte Carlo simulations”, *JHEP*, vol. 04, p. 081, 2007. DOI: [10.1088/1126-6708/2007/04/081](https://doi.org/10.1088/1126-6708/2007/04/081). arXiv: [hep-ph/0702198](https://arxiv.org/abs/hep-ph/0702198).
- [131] P. Artoisenet, R. Frederix, O. Mattelaer, and R. Rietkerk, “Automatic spin-entangled decays of heavy resonances in Monte Carlo simulations”, *JHEP*, vol. 03, p. 015, 2013. DOI: [10.1007/JHEP03\(2013\)015](https://doi.org/10.1007/JHEP03(2013)015). arXiv: [1212.3460 \[hep-ph\]](https://arxiv.org/abs/1212.3460).
- [132] T. Sjöstrand et al., “An introduction to PYTHIA8.2”, *Comput. Phys. Commun.*, vol. 191, p. 159, 2015. DOI: [10.1016/j.cpc.2015.01.024](https://doi.org/10.1016/j.cpc.2015.01.024). arXiv: [1410.3012 \[hep-ph\]](https://arxiv.org/abs/1410.3012).
- [133] S. Frixione and B. R. Webber, “Matching NLO QCD computations and parton shower simulations”, *JHEP*, vol. 06, p. 029, 2002. DOI: [10.1088/1126-6708/2002/06/029](https://doi.org/10.1088/1126-6708/2002/06/029). arXiv: [hep-ph/0204244](https://arxiv.org/abs/hep-ph/0204244).
- [134] M. L. Mangano, M. Moretti, F. Piccinini, and M. Treccani, “Matching matrix elements and shower evolution for top-quark production in hadronic collisions”, *JHEP*, vol. 01, p. 013, 2007. DOI: [10.1088/1126-6708/2007/01/013](https://doi.org/10.1088/1126-6708/2007/01/013). arXiv: [hep-ph/0611129](https://arxiv.org/abs/hep-ph/0611129).
- [135] R. Frederix and S. Frixione, “Merging meets matching in MC@NLO”, *JHEP*, vol. 12, p. 061, 2012. DOI: [10.1007/JHEP12\(2012\)061](https://doi.org/10.1007/JHEP12(2012)061). arXiv: [1209.6215 \[hep-ph\]](https://arxiv.org/abs/1209.6215).
- [136] J. Bellm et al., “HERWIG7.0/HERWIG++3.0 release note”, *Eur. Phys. J. C*, vol. 76, p. 196, 2016. DOI: [10.1140/epjc/s10052-016-4018-8](https://doi.org/10.1140/epjc/s10052-016-4018-8). arXiv: [1512.01178 \[hep-ph\]](https://arxiv.org/abs/1512.01178).

- [137] M. Bähr et al., “HERWIG++ physics and manual”, *Eur. Phys. J. C*, vol. 58, p. 639, 2008. DOI: [10.1140/epjc/s10052-008-0798-9](https://doi.org/10.1140/epjc/s10052-008-0798-9). arXiv: 0803.0883 [hep-ph].
- [138] P. Skands, S. Carrazza, and J. Rojo, “Tuning PYTHIA 8.1: the Monash 2013 Tune”, *Eur. Phys. J. C*, vol. 74, no. 8, p. 3024, 2014. DOI: [10.1140/epjc/s10052-014-3024-y](https://doi.org/10.1140/epjc/s10052-014-3024-y). arXiv: 1404.5630 [hep-ph].
- [139] CMS Collaboration, “Extraction and validation of a new set of CMS Pythia 8 tunes from underlying-event measurements”, *Eur. Phys. J. C*, vol. 80, p. 4, 2020. DOI: [10.1140/epjc/s10052-019-7499-4](https://doi.org/10.1140/epjc/s10052-019-7499-4). arXiv: 1903.12179 [hep-ex].
- [140] B. Andersson, G. Gustafson, G. Ingelman, and T. Sjostrand, “Parton Fragmentation and String Dynamics”, *Phys. Rept.*, vol. 97, pp. 31–145, 1983. DOI: [10.1016/0370-1573\(83\)90080-7](https://doi.org/10.1016/0370-1573(83)90080-7).
- [141] T. Sjostrand, “Jet Fragmentation of Nearby Partons”, *Nucl. Phys. B*, vol. 248, pp. 469–502, 1984. DOI: [10.1016/0550-3213\(84\)90607-2](https://doi.org/10.1016/0550-3213(84)90607-2).
- [142] S. Argyropoulos and T. Sjöstrand, “Effects of color reconnection on $t\bar{t}$ final states at the LHC”, *JHEP*, vol. 11, p. 043, 2014. DOI: [10.1007/JHEP11\(2014\)043](https://doi.org/10.1007/JHEP11(2014)043). arXiv: 1407.6653 [hep-ph].
- [143] J. R. Christiansen and P. Z. Skands, “String Formation Beyond Leading Colour”, *JHEP*, vol. 08, p. 003, 2015. DOI: [10.1007/JHEP08\(2015\)003](https://doi.org/10.1007/JHEP08(2015)003). arXiv: 1505.01681 [hep-ph].
- [144] CMS Collaboration, “Measurement of the top quark mass using a profile likelihood approach with the lepton + jets final states in proton–proton collisions at $\sqrt{s} = 13$ TeV”, *Eur. Phys. J. C*, vol. 83, no. 10, p. 963, 2023. DOI: [10.1140/epjc/s10052-023-12050-4](https://doi.org/10.1140/epjc/s10052-023-12050-4). arXiv: 2302.01967 [hep-ex].
- [145] ATLAS Collaboration, “Measurement of the top quark mass with the ATLAS detector using $t\bar{t}$ events with a high transverse momentum top quark”, *Phys. Lett. B*, vol. 867, p. 139608, 2025. DOI: [10.1016/j.physletb.2025.139608](https://doi.org/10.1016/j.physletb.2025.139608). arXiv: 2502.18216 [hep-ex].
- [146] CMS Collaboration, “Precision luminosity measurement in proton-proton collisions at $\sqrt{s} = 13$ TeV in 2015 and 2016 at CMS”, *Eur. Phys. J. C*, vol. 81, no. 9, p. 800, 2021. DOI: [10.1140/epjc/s10052-021-09538-2](https://doi.org/10.1140/epjc/s10052-021-09538-2). arXiv: 2104.01927 [hep-ex].
- [147] S. Agostinelli et al., “GEANT4 — a simulation toolkit”, *Nucl. Instrum. Meth. A*, vol. 506, p. 250, 2003. DOI: [10.1016/S0168-9002\(03\)01368-8](https://doi.org/10.1016/S0168-9002(03)01368-8).

- [148] G. Cowan, K. Cranmer, E. Gross, and O. Vitells, “Asymptotic formulae for likelihood-based tests of new physics”, *Eur. Phys. J. C*, vol. 71, p. 1554, 2011, [Erratum: Eur.Phys.J.C 73, 2501 (2013)]. DOI: 10.1140/epjc/s10052-011-1554-0. arXiv: 1007.1727 [physics.data-an].
- [149] S. S. Wilks, “The large-sample distribution of the likelihood ratio for testing composite hypotheses”, *Annals Math. Statist.*, vol. 9, no. 1, pp. 60–62, 1938. DOI: 10.1214/aoms/1177732360.
- [150] A. Wald, “Tests of statistical hypotheses concerning several parameters when the number of observations is large”, *Trans. Am. Math. Soc.*, vol. 54, no. 3, pp. 462–482, 1942. DOI: 10.1090/S0002-9947-1943-0012401-3.
- [151] T. Junk, “Confidence level computation for combining searches with small statistics”, *Nucl. Instrum. Meth. A*, vol. 434, p. 435, 1999. DOI: 10.1016/S0168-9002(99)00498-2. arXiv: hep-ex/9902006.
- [152] A. L. Read, “Presentation of search results: The CL_s technique”, *J. Phys. G*, vol. 28, p. 2693, 2002. DOI: 10.1088/0954-3899/28/10/313.
- [153] CMS Collaboration, “The CMS Statistical Analysis and Combination Tool: Combine”, *Comput. Softw. Big Sci.*, vol. 8, no. 1, p. 19, 2024. DOI: 10.1007/s41781-024-00121-4. arXiv: 2404.06614 [physics.data-an].
- [154] L. Heinrich, M. Feickert, G. Stark, and K. Cranmer, “Pyhf: Pure-Python implementation of HistFactory statistical models”, *Journal of Open Source Software*, vol. 6, no. 58, p. 2823, 2021. DOI: 10.21105/joss.02823. [Online]. Available: <https://doi.org/10.21105/joss.02823>.
- [155] CMS Collaboration, *Cumulative delivered and recorded luminosity versus time for 2022-2024 (pp data only)*, accessed on August 10th 2025, 2025. [Online]. Available: <https://twiki.cern.ch/twiki/bin/view/CMSPublic/LumiPublicResults>.
- [156] CMS Collaboration, “First measurement of the top quark pair production cross section in proton-proton collisions at $\sqrt{s} = 13.6\text{TeV}$ ”, CMS Physics Analysis Summary CMS-PAS-TOP-22-012, 2022. [Online]. Available: <https://cds.cern.ch/record/2834110>.
- [157] ATLAS Collaboration, “Measurement of the $t\bar{t}$ cross section and its ratio to the Z production cross section using pp collisions at $\sqrt{s} = 13.6\text{ TeV}$ with the ATLAS detector”, *Phys. Lett. B*, vol. 848, p. 138376, 2024. DOI: 10.1016/j.physletb.2023.138376. arXiv: 2308.09529 [hep-ex].
- [158] M. Czakon and A. Mitov, “TOP++: A program for the calculation of the top-pair cross-section at hadron colliders”, *Comput. Phys. Commun.*, vol. 185, p. 2930, 2014. DOI: 10.1016/j.cpc.2014.06.021. arXiv: 1112.5675 [hep-ph].

- [159] E. Re, “Single-top Wt -channel production matched with parton showers using the powheg method”, *Eur. Phys. J. C*, vol. 71, p. 1547, 2011. DOI: [10.1140/epjc/s10052-011-1547-z](https://doi.org/10.1140/epjc/s10052-011-1547-z). arXiv: [1009.2450 \[hep-ph\]](https://arxiv.org/abs/1009.2450).
- [160] S. Alioli, P. Nason, C. Oleari, and E. Re, “NLO single-top production matched with shower in POWHEG: s- and t-channel contributions”, *JHEP*, vol. 09, p. 111, 2009, [Erratum: *JHEP* 02, 011 (2010)]. DOI: [10.1088/1126-6708/2009/09/111](https://doi.org/10.1088/1126-6708/2009/09/111). arXiv: [0907.4076 \[hep-ph\]](https://arxiv.org/abs/0907.4076).
- [161] N. Kidonakis and N. Yamanaka, “Higher-order corrections for tW production at high-energy hadron colliders”, *JHEP*, vol. 05, p. 278, 2021. DOI: [10.1007/JHEP05\(2021\)278](https://doi.org/10.1007/JHEP05(2021)278). arXiv: [2102.11300 \[hep-ph\]](https://arxiv.org/abs/2102.11300).
- [162] J. Campbell, T. Neumann, and Z. Sullivan, “Single-top-quark production in the t -channel at NNLO”, *JHEP*, vol. 02, p. 040, 2021. DOI: [10.1007/JHEP02\(2021\)040](https://doi.org/10.1007/JHEP02(2021)040). arXiv: [2012.01574 \[hep-ph\]](https://arxiv.org/abs/2012.01574).
- [163] S. Camarda et al., “DYTURBO: Fast predictions for Drell–Yan processes”, *Eur. Phys. J. C*, vol. 80, p. 251, 2020. DOI: [10.1140/epjc/s10052-020-7757-5](https://doi.org/10.1140/epjc/s10052-020-7757-5). arXiv: [1910.07049 \[hep-ph\]](https://arxiv.org/abs/1910.07049).
- [164] M. Grazzini, S. Kallweit, and M. Wiesemann, “Fully differential NNLO computations with MATRIX”, *Eur. Phys. J. C*, vol. 78, p. 537, 2018. DOI: [10.1140/epjc/s10052-018-5771-7](https://doi.org/10.1140/epjc/s10052-018-5771-7). arXiv: [1711.06631 \[hep-ph\]](https://arxiv.org/abs/1711.06631).
- [165] CMS Collaboration, “Performance of the CMS muon detector and muon reconstruction with proton-proton collisions at $\sqrt{s} = 13$ TeV”, *JINST*, vol. 13, no. 06, P06015, 2018. DOI: [10.1088/1748-0221/13/06/P06015](https://doi.org/10.1088/1748-0221/13/06/P06015). arXiv: [1804.04528 \[physics.ins-det\]](https://arxiv.org/abs/1804.04528).
- [166] CMS Collaboration, “Identification of heavy-flavour jets with the CMS detector in pp collisions at 13 TeV”, *JINST*, vol. 13, no. 05, P05011, 2018. DOI: [10.1088/1748-0221/13/05/P05011](https://doi.org/10.1088/1748-0221/13/05/P05011). arXiv: [1712.07158 \[physics.ins-det\]](https://arxiv.org/abs/1712.07158).
- [167] CMS Collaboration, “Jet energy scale and resolution in the CMS experiment in pp collisions at 8 TeV”, *JINST*, vol. 12, P02014, 2017. DOI: [10.1088/1748-0221/12/02/P02014](https://doi.org/10.1088/1748-0221/12/02/P02014). arXiv: [1607.03663 \[hep-ex\]](https://arxiv.org/abs/1607.03663).
- [168] CMS Collaboration, “Determination of Jet Energy Calibration and Transverse Momentum Resolution in CMS”, *JINST*, vol. 6, P11002, 2011. DOI: [10.1088/1748-0221/6/11/P11002](https://doi.org/10.1088/1748-0221/6/11/P11002). arXiv: [1107.4277 \[physics.ins-det\]](https://arxiv.org/abs/1107.4277).
- [169] CDF Collaboration, “Measurement of $\sigma \cdot B(W \rightarrow e\nu)$ and $\sigma \cdot B(Z^0 \rightarrow e^+e^-)$ in $p\bar{p}$ Collisions at $\sqrt{s} = 1.8$ TeV”, *Phys. Rev. Lett.*, vol. 76, pp. 3070–3075, 1996. DOI: [10.1103/PhysRevLett.76.3070](https://doi.org/10.1103/PhysRevLett.76.3070). arXiv: [hep-ex/9509010](https://arxiv.org/abs/hep-ex/9509010).

- [170] CDF Collaboration, “Measurement of the W boson mass with the Collider Detector at Fermilab”, *Phys. Rev. D*, vol. 64, p. 052001, 2001. doi: 10.1103/PhysRevD.64.052001. arXiv: hep-ex/0007044.
- [171] CMS Collaboration, “Search for dark matter particles produced in association with a top quark pair at $\sqrt{s} = 13$ TeV”, *Phys. Rev. Lett.*, vol. 122, no. 1, p. 011803, 2019. doi: 10.1103/PhysRevLett.122.011803. arXiv: 1807.06522 [hep-ex].
- [172] CMS Collaboration, “Luminosity monitoring with z counting in early 2022 data”, CMS Detector Performance Note CMS-DP-2023-003, 2023. [Online]. Available: <https://cds.cern.ch/record/2851655>.
- [173] CMS Collaboration, “Luminosity measurement in proton-proton collisions at 13.6 TeV in 2022 at CMS”, CERN, Geneva, CMS Physics Analysis Summary, 2024. [Online]. Available: <http://cds.cern.ch/record/2890833>.
- [174] M. Cacciari, S. Frixione, M. L. Mangano, P. Nason, and G. Ridolfi, “The $t\bar{t}$ cross-section at 1.8 and 1.96 TeV: A study of the systematics due to parton densities and scale dependence”, *JHEP*, vol. 04, p. 068, 2004. doi: 10.1088/1126-6708/2004/04/068. arXiv: hep-ph/0303085.
- [175] J. Butterworth et al., “PDF4LHC recommendations for LHC Run II”, *J. Phys. G*, vol. 43, p. 023001, 2016. doi: 10.1088/0954-3899/43/2/023001. arXiv: 1510.03865 [hep-ph].
- [176] CMS Collaboration, “Investigations of the impact of the parton shower tuning in PYTHIA 8 in the modelling of $t\bar{t}$ at $\sqrt{s} = 8$ and 13 TeV”, CMS Physics Analysis Summary CMS-PAS-TOP-16-021, 2016. [Online]. Available: <https://cds.cern.ch/record/2235192>.
- [177] CMS Collaboration, “Measurements of $t\bar{t}$ differential cross sections in proton-proton collisions at $\sqrt{s} = 13$ TeV using events containing two leptons”, *JHEP*, vol. 02, p. 149, 2019. doi: 10.1007/JHEP02(2019)149. arXiv: 1811.06625 [hep-ex].
- [178] CMS Collaboration, “Measurement of normalized differential $t\bar{t}$ cross sections in the dilepton channel from pp collisions at $\sqrt{s} = 13$ TeV”, *JHEP*, vol. 04, p. 060, 2018. doi: 10.1007/JHEP04(2018)060. arXiv: 1708.07638 [hep-ex].
- [179] CMS Collaboration, “Measurement of differential cross sections for top quark pair production using the lepton+jets final state in proton-proton collisions at 13 TeV”, *Phys. Rev. D*, vol. 95, no. 9, p. 092001, 2017. doi: 10.1103/PhysRevD.95.092001. arXiv: 1610.04191 [hep-ex].
- [180] M. Czakon, D. Heymes, A. Mitov, D. Pagani, I. Tsirikos, and M. Zaro, “Top-pair production at the LHC through NNLO QCD and NLO EW”, *JHEP*, vol. 10, p. 186, 2017. doi: 10.1007/JHEP10(2017)186. arXiv: 1705.04105 [hep-ph].

- [181] R. Barlow and C. Beeston, “Fitting using finite Monte Carlo samples”, *Comput. Phys. Commun.*, vol. 77, p. 219, 1993. DOI: 10.1016/0010-4655(93)90005-W.
- [182] CMS Collaboration, “Measurement of the $t\bar{t}$ production cross section, the top quark mass, and the strong coupling constant using dilepton events in pp collisions at $\sqrt{s} = 13$ TeV”, *Eur. Phys. J. C*, vol. 79, p. 368, 2019. DOI: 10.1140/epjc/s10052-019-6863-8. arXiv: 1812.10505 [hep-ex].
- [183] ATLAS Collaboration, “Measurement of the $t\bar{t}$ production cross-section in the lepton+jets channel at $\sqrt{s} = 13$ TeV with the ATLAS experiment”, *Phys. Lett. B*, vol. 810, p. 135 797, 2020. DOI: 10.1016/j.physletb.2020.135797. arXiv: 2006.13076 [hep-ex].
- [184] CMS Collaboration, “Measurement of the $t\bar{t}$ production cross section in the all-jet final state in pp collisions at $\sqrt{s} = 7$ TeV”, *JHEP*, vol. 05, p. 065, 2013. DOI: 10.1007/JHEP05(2013)065. arXiv: 1302.0508 [hep-ex].
- [185] CMS Collaboration, “Measurement of the $t\bar{t}$ production cross section in the all-jets final state in pp collisions at $\sqrt{s} = 8$ TeV”, *Eur. Phys. J. C*, vol. 76, p. 128, 2016. DOI: 10.1140/epjc/s10052-016-3956-5. arXiv: 1509.06076 [hep-ex].
- [186] CMS Collaboration, “Measurements of the $t\bar{t}$ production cross section in lepton+jets final states in pp collisions at 8 TeV and ratio of 8 to 7 TeV cross sections”, *Eur. Phys. J. C*, vol. 77, p. 15, 2017. DOI: 10.1140/epjc/s10052-016-4504-z. arXiv: 1602.09024 [hep-ex].
- [187] CMS Collaboration, “Measurement of the $t\bar{t}$ production cross section in the $e\mu$ channel in proton-proton collisions at $\sqrt{s} = 7$ and 8 TeV”, *JHEP*, vol. 08, p. 029, 2016. DOI: 10.1007/JHEP08(2016)029. arXiv: 1603.02303 [hep-ex].
- [188] CMS Collaboration, “Measurement of the top quark pair production cross section in dilepton final states containing one τ lepton in pp collisions at $\sqrt{s} = 13$ TeV”, *JHEP*, vol. 02, p. 191, 2020. DOI: 10.1007/JHEP02(2020)191. arXiv: 1911.13204 [hep-ex].
- [189] CMS Collaboration, “Measurement of differential $t\bar{t}$ production cross sections in the full kinematic range using lepton+jets events from proton-proton collisions at $\sqrt{s} = 13$ TeV”, *Phys. Rev. D*, vol. 104, p. 092013, 2021. DOI: 10.1103/PhysRevD.104.092013. arXiv: 2108.02803 [hep-ex].
- [190] CMS Collaboration, “Measurement of the inclusive $t\bar{t}$ production cross section in proton-proton collisions at $\sqrt{s} = 5.02$ TeV”, *JHEP*, vol. 04, p. 144, 2022. DOI: 10.1007/JHEP04(2022)144. arXiv: 2112.09114 [hep-ex].
- [191] M. Czakon, P. Fiedler, and A. Mitov, “Total top-quark pair-production cross section at hadron colliders through $\mathcal{O}(\alpha_S^4)$ ”, *Phys. Rev. Lett.*, vol. 110, p. 252 004, 2013. DOI: 10.1103/PhysRevLett.110.252004. arXiv: 1303.6254 [hep-ph].

- [192] A. H. Hoang, “What is the Top Quark Mass?”, *Ann. Rev. Nucl. Part. Sci.*, vol. 70, pp. 225–255, 2020. DOI: [10.1146/annurev-nucl-101918-023530](https://doi.org/10.1146/annurev-nucl-101918-023530). arXiv: [2004.12915 \[hep-ph\]](https://arxiv.org/abs/2004.12915).
- [193] R. Tarrach, “The Pole Mass in Perturbative QCD”, *Nucl. Phys. B*, vol. 183, pp. 384–396, 1981. DOI: [10.1016/0550-3213\(81\)90140-1](https://doi.org/10.1016/0550-3213(81)90140-1).
- [194] M. C. Smith and S. S. Willenbrock, “Top quark pole mass”, *Phys. Rev. Lett.*, vol. 79, pp. 3825–3828, 1997. DOI: [10.1103/PhysRevLett.79.3825](https://doi.org/10.1103/PhysRevLett.79.3825). arXiv: [hep-ph/9612329](https://arxiv.org/abs/hep-ph/9612329).
- [195] ATLAS Collaboration, “Probing the quantum interference between singly and doubly resonant top-quark production in pp collisions at $\sqrt{s} = 13\text{TeV}$ with the ATLAS detector”, *Phys. Rev. Lett.*, vol. 121, p. 152002, 2018. DOI: [10.1103/PhysRevLett.121.152002](https://doi.org/10.1103/PhysRevLett.121.152002). arXiv: [1806.04667 \[hep-ex\]](https://arxiv.org/abs/1806.04667).
- [196] T. Ježo, J. M. Lindert, and S. Pozzorini, “Resonance-aware NLOPS matching for off-shell $t\bar{t} + tW$ production with semileptonic decays”, *JHEP*, vol. 10, p. 008, 2023. DOI: [10.1007/JHEP10\(2023\)008](https://doi.org/10.1007/JHEP10(2023)008). arXiv: [2307.15653 \[hep-ph\]](https://arxiv.org/abs/2307.15653).
- [197] T. Ježo and P. Nason, “On the treatment of resonances in next-to-leading order calculations matched to a parton shower”, *JHEP*, vol. 12, p. 065, 2015. DOI: [10.1007/JHEP12\(2015\)065](https://doi.org/10.1007/JHEP12(2015)065). arXiv: [1509.09071 \[hep-ph\]](https://arxiv.org/abs/1509.09071).
- [198] <https://powhegbox.mib.infn.it>.
- [199] S. Frixione, E. Laenen, P. Motylinski, B. R. Webber, and C. D. White, “Single-top hadroproduction in association with a W boson”, *JHEP*, vol. 07, p. 029, 2008. DOI: [10.1088/1126-6708/2008/07/029](https://doi.org/10.1088/1126-6708/2008/07/029). arXiv: [0805.3067 \[hep-ph\]](https://arxiv.org/abs/0805.3067).
- [200] T. M. P. Tait, “The tW^- mode of single top production”, *Phys. Rev. D*, vol. 61, p. 034001, 1999. DOI: [10.1103/PhysRevD.61.034001](https://doi.org/10.1103/PhysRevD.61.034001). arXiv: [hep-ph/9909352](https://arxiv.org/abs/hep-ph/9909352).
- [201] J. M. Campbell, R. K. Ellis, P. Nason, and E. Re, “Top-pair production and decay at NLO matched with parton showers”, *JHEP*, vol. 04, p. 114, 2015. DOI: [10.1007/JHEP04\(2015\)114](https://doi.org/10.1007/JHEP04(2015)114). arXiv: [1412.1828 \[hep-ph\]](https://arxiv.org/abs/1412.1828).
- [202] S. Ferrario Ravasio, T. Ježo, P. Nason, and C. Oleari, “A theoretical study of top-mass measurements at the LHC using NLO+PS generators of increasing accuracy”, *Eur. Phys. J. C*, vol. 78, p. 458, 2018. DOI: [10.1140/epjc/s10052-018-5909-7](https://doi.org/10.1140/epjc/s10052-018-5909-7). arXiv: [1906.09166 \[hep-ph\]](https://arxiv.org/abs/1906.09166).
- [203] C. Bierlich et al., “Robust independent validation of experiment and theory: Rivet version 3”, *SciPost Phys.*, vol. 8, p. 026, 2020. DOI: [10.21468/SciPostPhys.8.2.026](https://doi.org/10.21468/SciPostPhys.8.2.026). arXiv: [1912.05451 \[hep-ph\]](https://arxiv.org/abs/1912.05451).
- [204] M. Cacciari and G. P. Salam, “Pileup subtraction using jet areas”, *Phys. Lett. B*, vol. 659, pp. 119–126, 2008. DOI: [10.1016/j.physletb.2007.09.077](https://doi.org/10.1016/j.physletb.2007.09.077). arXiv: [0707.1378 \[hep-ph\]](https://arxiv.org/abs/0707.1378).

- [205] M. Cacciari, G. P. Salam, and G. Soyez, “The Catchment Area of Jets”, *JHEP*, vol. 04, p. 005, 2008. DOI: 10.1088/1126-6708/2008/04/005. arXiv: 0802.1188 [hep-ph].
- [206] ATLAS Collaboration, “Studies of $t\bar{t}/tW$ interference effects in $b\bar{b}\ell^+\ell^-\nu\bar{\nu}'$ final states with POWHEG and MG5_AMC@NLO setups”, ATLAS PUB Note ATL-PHYS-PUB-2021-042, 2021. [Online]. Available: <https://cds.cern.ch/record/2792254>.
- [207] D. Boer et al., “Gluons and the quark sea at high energies: Distributions, polarization, tomography”, Aug. 2011. arXiv: 1108.1713 [nucl-th].
- [208] ATLAS Collaboration, “Search for Heavy Higgs Bosons A/H Decaying to a Top Quark Pair in pp Collisions at $\sqrt{s} = 8$ TeV with the ATLAS Detector”, *Phys. Rev. Lett.*, vol. 119, no. 19, p. 191803, 2017. DOI: 10.1103/PhysRevLett.119.191803. arXiv: 1707.06025 [hep-ex].
- [209] ATLAS Collaboration, “Search for heavy neutral Higgs bosons decaying into a top quark pair in 140 fb^{-1} of proton-proton collision data at $\sqrt{s} = 13$ TeV with the ATLAS detector”, *JHEP*, vol. 08, p. 013, 2024. DOI: 10.1007/JHEP08(2024)013. arXiv: 2404.18986 [hep-ex].
- [210] ATLAS Collaboration, “Observation of a cross-section enhancement near the $t\bar{t}$ production threshold in $\sqrt{s} = 13$ TeV pp collisions with the ATLAS detector”, ATLAS Conference Note ATLAS-CONF-2025-008, 2025. [Online]. Available: <https://cds.cern.ch/record/2937636>.
- [211] CMS Collaboration, “Search for heavy pseudoscalar and scalar bosons decaying to top quark pairs in proton-proton collisions at $\sqrt{s} = 13$ TeV”, CMS Physics Analysis Summary CMS-PAS-HIG-22-013, 2024. [Online]. Available: <https://cds.cern.ch/record/2911775>.
- [212] J. Rübenach, “Search for Heavy Higgs Bosons in Conjunction with Neural-Network-Driven Reconstruction and Upgrade of the Fast Beam Condition Monitor at the CMS Experiment”, PhD thesis, DESY, Hamburg, May 2023.
- [213] CMS Collaboration, “Simulation of the silicon strip tracker pre-amplifier in early 2016 data”, CMS Detector Performance Note CMS-DP-2020-045, 2020. [Online]. Available: <https://cds.cern.ch/record/2740688>.
- [214] P. F. Monni, P. Nason, E. Re, M. Wiesemann, and G. Zanderighi, “MiNNLO_{PS}: a new method to match NNLO QCD to parton showers”, *JHEP*, vol. 05, p. 143, 2020, [Erratum: JHEP 02, 031 (2022)]. DOI: 10.1007/JHEP05(2020)143. arXiv: 1908.06987 [hep-ph].
- [215] P. F. Monni, E. Re, and M. Wiesemann, “MiNNLO_{PS}: optimizing $2 \rightarrow 1$ hadronic processes”, *Eur. Phys. J. C*, vol. 80, no. 11, p. 1075, 2020. DOI: 10.1140/epjc/s10052-020-08658-5. arXiv: 2006.04133 [hep-ph].

- [216] M. Aliev, H. Lacker, U. Langenfeld, S. Moch, P. Uwer, and M. Wiedermann, “HATHOR: Hadronic top and heavy quarks cross section calculator”, *Comput. Phys. Commun.*, vol. 182, p. 1034, 2011. DOI: [10.1016/j.cpc.2010.12.040](https://doi.org/10.1016/j.cpc.2010.12.040). arXiv: [1007.1327 \[hep-ph\]](https://arxiv.org/abs/1007.1327).
- [217] P. Kant et al., “HatHor for single top-quark production: Updated predictions and uncertainty estimates for single top-quark production in hadronic collisions”, *Comput. Phys. Commun.*, vol. 191, pp. 74–89, 2015. DOI: [10.1016/j.cpc.2015.02.001](https://doi.org/10.1016/j.cpc.2015.02.001). arXiv: [1406.4403 \[hep-ph\]](https://arxiv.org/abs/1406.4403).
- [218] K. Melnikov and F. Petriello, “Electroweak gauge boson production at hadron colliders through $\mathcal{O}(\alpha_S^2)$ ”, *Phys. Rev. D*, vol. 74, p. 114017, 2006. DOI: [10.1103/PhysRevD.74.114017](https://doi.org/10.1103/PhysRevD.74.114017). arXiv: [hep-ph/0609070](https://arxiv.org/abs/hep-ph/0609070).
- [219] Y. Li and F. Petriello, “Combining QCD and electroweak corrections to dilepton production in FEWZ”, *Phys. Rev. D*, vol. 86, p. 094034, 2012. DOI: [10.1103/PhysRevD.86.094034](https://doi.org/10.1103/PhysRevD.86.094034). arXiv: [1208.5967 \[hep-ph\]](https://arxiv.org/abs/1208.5967).
- [220] T. Gehrmann et al., “ W^+W^- Production at Hadron Colliders in Next to Next to Leading Order QCD”, *Phys. Rev. Lett.*, vol. 113, no. 21, p. 212001, 2014. DOI: [10.1103/PhysRevLett.113.212001](https://doi.org/10.1103/PhysRevLett.113.212001). arXiv: [1408.5243 \[hep-ph\]](https://arxiv.org/abs/1408.5243).
- [221] J. M. Campbell and R. K. Ellis, “MCFM for the Tevatron and the LHC”, *Nucl. Phys. B Proc. Suppl.*, vol. 205–206, J. Blümlein, S.-O. Moch, and T. Riemann, Eds., pp. 10–15, 2010. DOI: [10.1016/j.nuclphysbps.2010.08.011](https://doi.org/10.1016/j.nuclphysbps.2010.08.011). arXiv: [1007.3492 \[hep-ph\]](https://arxiv.org/abs/1007.3492).
- [222] CMS Collaboration, “Measurement of the differential cross section for top quark pair production in pp collisions at $\sqrt{s} = 8$ TeV”, *Eur. Phys. J. C*, vol. 75, no. 11, p. 542, 2015. DOI: [10.1140/epjc/s10052-015-3709-x](https://doi.org/10.1140/epjc/s10052-015-3709-x). arXiv: [1505.04480 \[hep-ex\]](https://arxiv.org/abs/1505.04480).
- [223] L. Sonnenschein, “Analytical solution of ttbar dilepton equations”, *Phys. Rev. D*, vol. 73, p. 054015, 2006, [Erratum: *Phys. Rev. D* 78, 079902 (2008)]. DOI: [10.1103/PhysRevD.78.079902](https://doi.org/10.1103/PhysRevD.78.079902). arXiv: [hep-ph/0603011](https://arxiv.org/abs/hep-ph/0603011).
- [224] I. Korol, “Measurement of double differential $t\bar{t}$ production cross sections with the CMS detector”, CERN-THESIS-2016-060, DESY-THESIS-2016-011, Ph.D. dissertation, Universität Hamburg, 2016. DOI: [10.3204/DESY-THESIS-2016-011](https://doi.org/10.3204/DESY-THESIS-2016-011).
- [225] J. H. Kühn, A. Scharf, and P. Uwer, “Electroweak corrections to top-quark pair production in quark-antiquark annihilation”, *Eur. Phys. J. C*, vol. 45, p. 139, 2006. DOI: [10.1140/epjc/s2005-02423-6](https://doi.org/10.1140/epjc/s2005-02423-6). arXiv: [hep-ph/0508092](https://arxiv.org/abs/hep-ph/0508092).
- [226] J. H. Kühn, A. Scharf, and P. Uwer, “Electroweak effects in top-quark pair production at hadron colliders”, *Eur. Phys. J. C*, vol. 51, p. 37, 2007. DOI: [10.1140/epjc/s10052-007-0275-x](https://doi.org/10.1140/epjc/s10052-007-0275-x). arXiv: [hep-ph/0610335](https://arxiv.org/abs/hep-ph/0610335).

- [227] J. H. Kühn, A. Scharf, and P. Uwer, “Weak interactions in top-quark pair production at hadron colliders: An update”, *Phys. Rev. D*, vol. 91, p. 014020, 2015. DOI: 10.1103/PhysRevD.91.014020. arXiv: 1305.5773 [hep-ph].
- [228] CMS Collaboration, “Combined measurements of Higgs boson couplings in proton–proton collisions at $\sqrt{s} = 13$ TeV”, *Eur. Phys. J. C*, vol. 79, no. 5, p. 421, 2019. DOI: 10.1140/epjc/s10052-019-6909-y. arXiv: 1809.10733 [hep-ex].
- [229] CMS Collaboration, “CMS pythia 8 colour reconnection tunes based on underlying-event data”, *Eur. Phys. J. C*, vol. 83, no. 7, p. 587, 2023. DOI: 10.1140/epjc/s10052-023-11630-8. arXiv: 2205.02905 [hep-ex].
- [230] ATLAS Collaboration, “Measurement of the inclusive cross-sections of single top-quark and top-antiquark t -channel production in pp collisions at $\sqrt{s} = 13$ TeV with the ATLAS detector”, *JHEP*, vol. 04, p. 086, 2017. DOI: 10.1007/JHEP04(2017)086. arXiv: 1609.03920 [hep-ex].
- [231] CMS Collaboration, “Measurement of the single top quark and antiquark production cross sections in the t channel and their ratio in proton-proton collisions at $\sqrt{s} = 13$ TeV”, *Phys. Lett. B*, vol. 800, p. 135042, 2020. DOI: 10.1016/j.physletb.2019.135042. arXiv: 1812.10514 [hep-ex].
- [232] CMS Collaboration, “Measurement of the production cross section for single top quarks in association with W bosons in proton-proton collisions at $\sqrt{s} = 13$ TeV”, *JHEP*, vol. 10, p. 117, 2018. DOI: 10.1007/JHEP10(2018)117. arXiv: 1805.07399 [hep-ex].
- [233] CMS Collaboration, “Measurement of the cross section for top quark pair production in association with a W or Z boson in proton-proton collisions at $\sqrt{s} = 13$ TeV”, *JHEP*, vol. 08, p. 011, 2018. DOI: 10.1007/JHEP08(2018)011. arXiv: 1711.02547 [hep-ex].
- [234] ATLAS Collaboration, “Measurement of the $t\bar{t}Z$ and $t\bar{t}W$ cross sections in proton-proton collisions at $\sqrt{s} = 13$ TeV with the ATLAS detector”, *Phys. Rev. D*, vol. 99, p. 072009, 2019. DOI: 10.1103/PhysRevD.99.072009. arXiv: 1901.03584 [hep-ex].
- [235] ATLAS Collaboration, “Measurements of top-quark pair to Z-boson cross-section ratios at $\sqrt{s} = 13, 8, 7$ TeV with the ATLAS detector”, *JHEP*, vol. 02, p. 117, 2017. DOI: 10.1007/JHEP02(2017)117. arXiv: 1612.03636 [hep-ex].
- [236] CMS Collaboration, “CMS luminosity measurement for the 2017 data-taking period at $\sqrt{s} = 13$ TeV”, CMS Physics Analysis Summary CMS-PAS-LUM-17-004, 2018. [Online]. Available: <https://cds.cern.ch/record/2621960>.
- [237] CMS Collaboration, “CMS luminosity measurement for the 2018 data-taking period at $\sqrt{s} = 13$ TeV”, CMS Physics Analysis Summary CMS-PAS-LUM-18-002, 2019. [Online]. Available: <https://cds.cern.ch/record/2676164>.

- [238] CMS Collaboration, “Measurement of the inelastic proton-proton cross section at $\sqrt{s} = 13$ TeV”, *JHEP*, vol. 07, p. 161, 2018. DOI: [10.1007/JHEP07\(2018\)161](https://doi.org/10.1007/JHEP07(2018)161). arXiv: [1802.02613 \[hep-ex\]](https://arxiv.org/abs/1802.02613).
- [239] W. S. Cleveland, “Robust locally weighted regression and smoothing scatterplots”, *Journal of the American Statistical Association*, vol. 74, no. 368, pp. 829–836, 1979. DOI: [10.1080/01621459.1979.10481038](https://doi.org/10.1080/01621459.1979.10481038).
- [240] W. S. Cleveland and S. J. Devlin, “Locally weighted regression: An approach to regression analysis by local fitting”, *Journal of the American Statistical Association*, vol. 83, no. 403, pp. 596–610, 1988. DOI: [10.1080/01621459.1988.10478639](https://doi.org/10.1080/01621459.1988.10478639).
- [241] CMS Collaboration, “Measurement of differential cross sections for the production of top quark pairs and of additional jets in lepton+jets events from pp collisions at $\sqrt{s} = 13$ TeV”, *Phys. Rev. D*, vol. 97, no. 11, p. 112003, 2018. DOI: [10.1103/PhysRevD.97.112003](https://doi.org/10.1103/PhysRevD.97.112003). arXiv: [1803.08856 \[hep-ex\]](https://arxiv.org/abs/1803.08856).
- [242] CMS Collaboration, “Development and validation of HERWIG 7 tunes from CMS underlying-event measurements”, *Eur. Phys. J. C*, vol. 81, no. 4, p. 312, 2021. DOI: [10.1140/epjc/s10052-021-08949-5](https://doi.org/10.1140/epjc/s10052-021-08949-5). arXiv: [2011.03422 \[hep-ex\]](https://arxiv.org/abs/2011.03422).
- [243] B. R. Webber, “A QCD Model for Jet Fragmentation Including Soft Gluon Interference”, *Nucl. Phys. B*, vol. 238, pp. 492–528, 1984. DOI: [10.1016/0550-3213\(84\)90333-X](https://doi.org/10.1016/0550-3213(84)90333-X).
- [244] F. J. Llanes-Estrada, “Ensuring that toponium is glued, not nailed”, Nov. 2024. arXiv: [2411.19180 \[hep-ph\]](https://arxiv.org/abs/2411.19180).
- [245] D. d’Enterria and K. Kang, “Exclusive photon-fusion production of even-spin resonances and exotic QED atoms in high-energy hadron collisions”, Mar. 2025. arXiv: [2503.10952 \[hep-ph\]](https://arxiv.org/abs/2503.10952).
- [246] A. Djouadi, J. Ellis, A. Popov, and J. Quevillon, “Interference effects in $t\bar{t}$ production at the LHC as a window on new physics”, *JHEP*, vol. 03, p. 119, 2019. DOI: [10.1007/JHEP03\(2019\)119](https://doi.org/10.1007/JHEP03(2019)119). arXiv: [1901.03417 \[hep-ph\]](https://arxiv.org/abs/1901.03417).
- [247] A. Djouadi, J. Ellis, and J. Quevillon, “Contrasting pseudoscalar Higgs and toponium states at the LHC and beyond”, *Phys. Lett. B*, vol. 866, p. 139583, 2025. DOI: [10.1016/j.physletb.2025.139583](https://doi.org/10.1016/j.physletb.2025.139583). arXiv: [2412.15138 \[hep-ph\]](https://arxiv.org/abs/2412.15138).
- [248] B. A. Betchart, R. Demina, and A. Harel, “Analytic solutions for neutrino momenta in decay of top quarks”, *Nucl. Instrum. Meth. A*, vol. 736, p. 169, 2014. DOI: [10.1016/j.nima.2013.10.039](https://doi.org/10.1016/j.nima.2013.10.039). arXiv: [1305.1878 \[hep-ph\]](https://arxiv.org/abs/1305.1878).

- [249] R. Demina, A. Harel, and D. Orbaker, “Reconstructing $t\bar{t}$ events with one lost jet”, *Nucl. Instrum. Meth. A*, vol. 788, p. 128, 2015. DOI: 10.1016/j.nima.2015.03.069. arXiv: 1310.3263 [hep-ex].
- [250] G. J. Feldman and R. D. Cousins, “Unified approach to the classical statistical analysis of small signals”, *Phys. Rev. D*, vol. 57, p. 3873, 1998. DOI: 10.1103/PhysRevD.57.3873. arXiv: physics/9711021.
- [251] R. D. Cousins and V. L. Highland, “Incorporating systematic uncertainties into an upper limit”, *Nucl. Instrum. Meth. A*, vol. 320, pp. 331–335, 1992. DOI: 10.1016/0168-9002(92)90794-5.
- [252] HEPData record for analysis “Search for heavy pseudoscalar and scalar bosons decaying to a top quark pair in proton-proton collisions at $\sqrt{s} = 13$ TeV” (CMS-HIG-22-013), 2025. DOI: 10.17182/hepdata.159298.
- [253] H. Brooks and P. Skands, “Coherent showers in decays of colored resonances”, *Phys. Rev. D*, vol. 100, no. 7, p. 076006, 2019. DOI: 10.1103/PhysRevD.100.076006. arXiv: 1907.08980 [hep-ph].
- [254] ATLAS Collaboration, “Measurement of the $t\bar{t}$ production cross-section and lepton differential distributions in $e\mu$ dilepton events from pp collisions at $\sqrt{s} = 13$ TeV with the ATLAS detector”, *Eur. Phys. J. C*, vol. 80, no. 6, p. 528, 2020. DOI: 10.1140/epjc/s10052-020-7907-9. arXiv: 1910.08819 [hep-ex].
- [255] CMS Collaboration, “Differential cross section measurements for the production of top quark pairs and of additional jets using dilepton events from pp collisions at $\sqrt{s} = 13$ TeV”, *JHEP*, vol. 02, p. 064, 2025. DOI: 10.1007/JHEP02(2025)064. arXiv: 2402.08486 [hep-ex].
- [256] ATLAS Collaboration, “Inclusive and differential cross-sections for dilepton $t\bar{t}$ production measured in $\sqrt{s} = 13$ TeV pp collisions with the ATLAS detector”, *JHEP*, vol. 07, p. 141, 2023. DOI: 10.1007/JHEP07(2023)141. arXiv: 2303.15340 [hep-ex].
- [257] J. Gallicchio and M. D. Schwartz, “Seeing in Color: Jet Superstructure”, *Phys. Rev. Lett.*, vol. 105, p. 022001, 2010. DOI: 10.1103/PhysRevLett.105.022001. arXiv: 1001.5027 [hep-ph].
- [258] ATLAS Collaboration, “Measurement of colour flow using jet-pull observables in $t\bar{t}$ events with the ATLAS experiment at $\sqrt{s} = 13$ TeV”, *Eur. Phys. J. C*, vol. 78, no. 10, p. 847, 2018. DOI: 10.1140/epjc/s10052-018-6290-2. arXiv: 1805.02935 [hep-ex].
- [259] J. A. Raine, M. Leigh, K. Zoch, and T. Golling, “Fast and improved neutrino reconstruction in multineutrino final states with conditional normalizing flows”, *Phys. Rev. D*, vol. 109, no. 1, p. 012005, 2024. DOI: 10.1103/PhysRevD.109.012005. arXiv: 2307.02405 [hep-ph].

- [260] CMS Collaboration, “High-precision measurement of the W boson mass with the CMS experiment at the LHC”, Dec. 2024. arXiv: 2412.13872 [hep-ex].
- [261] CMS Collaboration, “Observation of four top quark production in proton-proton collisions at $\sqrt{s} = 13$ TeV”, *Phys. Lett. B*, vol. 847, p. 138 290, 2023. DOI: 10.1016/j.physletb.2023.138290. arXiv: 2305.13439 [hep-ex].
- [262] ATLAS Collaboration, “Observation of four-top-quark production in the multilepton final state with the ATLAS detector”, *Eur. Phys. J. C*, vol. 83, no. 6, p. 496, 2023, [Erratum: Eur.Phys.J.C 84, 156 (2024)]. DOI: 10.1140/epjc/s10052-023-11573-0. arXiv: 2303.15061 [hep-ex].
- [263] O. Brunner et al., “The CLIC project”, Mar. 2022. arXiv: 2203.09186 [physics.acc-ph].
- [264] L. Evans and S. Michizono, “The International Linear Collider Machine Staging Report 2017”, Nov. 2017. arXiv: 1711.00568 [physics.acc-ph].
- [265] M. Benedikt et al., “Future Circular Collider Feasibility Study Report: Volume 1, Physics, Experiments, Detectors”, Apr. 2025. DOI: 10.17181/CERN.9DKX.TDH9. arXiv: 2505.00272 [hep-ex].
- [266] W. Abdallah et al., “CEPC Technical Design Report: Accelerator”, *Radiat. Detect. Technol. Methods*, vol. 8, no. 1, pp. 1–1105, 2024, [Erratum: Radiat.Detect.Technol.Methods 9, 184–192 (2025)]. DOI: 10.1007/s41605-024-00463-y. arXiv: 2312.14363 [physics.acc-ph].
- [267] M. Beneke, Y. Kiyo, P. Marquard, A. Penin, J. Piclum, and M. Steinhauser, “Next-to-Next-to-Next-to-Leading Order QCD Prediction for the Top Antitop S-Wave Pair Production Cross Section Near Threshold in e^+e^- Annihilation”, *Phys. Rev. Lett.*, vol. 115, no. 19, p. 192 001, 2015. DOI: 10.1103/PhysRevLett.115.192001. arXiv: 1506.06864 [hep-ph].
- [268] A. H. Hoang and M. Stahlhofen, “The Top-Antitop Threshold at the ILC: NNLL QCD Uncertainties”, *JHEP*, vol. 05, p. 121, 2014. DOI: 10.1007/JHEP05(2014)121. arXiv: 1309.6323 [hep-ph].
- [269] M. Martinez and R. Miquel, “Multiparameter fits to the t anti-t threshold observables at a future e+ e- linear collider”, *Eur. Phys. J. C*, vol. 27, pp. 49–55, 2003. DOI: 10.1140/epjc/s2002-01094-1. arXiv: hep-ph/0207315.
- [270] T. Horiguchi et al., “Study of top quark pair production near threshold at the ILC”, Oct. 2013. arXiv: 1310.0563 [hep-ex].
- [271] K. Seidel, F. Simon, M. Tesar, and S. Poss, “Top quark mass measurements at and above threshold at CLIC”, *Eur. Phys. J. C*, vol. 73, no. 8, p. 2530, 2013. DOI: 10.1140/epjc/s10052-013-2530-7. arXiv: 1303.3758 [hep-ex].
- [272] P. Bambade et al., “The International Linear Collider: A Global Project”, Mar. 2019. arXiv: 1903.01629 [hep-ex].

- [273] D. Attié et al., “A Linear Collider Vision for the Future of Particle Physics”, Mar. 2025. arXiv: 2503.19983 [hep-ex].
- [274] J. Bonilla, I. Brivio, M. B. Gavela, and V. Sanz, “One-loop corrections to ALP couplings”, *JHEP*, vol. 11, p. 168, 2021. DOI: 10.1007/JHEP11(2021)168. arXiv: 2107.11392 [hep-ph].
- [275] H. Bahl et al., “HiggsTools: BSM scalar phenomenology with new versions of HiggsBounds and HiggsSignals”, *Comput. Phys. Commun.*, vol. 291, p. 108 803, 2023. DOI: 10.1016/j.cpc.2023.108803. arXiv: 2210.09332 [hep-ph].
- [276] ATLAS Collaboration, “Search for resonances decaying into photon pairs in 139 fb^{-1} of pp collisions at $\sqrt{s}=13 \text{ TeV}$ with the ATLAS detector”, *Phys. Lett. B*, vol. 822, p. 136 651, 2021. DOI: 10.1016/j.physletb.2021.136651. arXiv: 2102.13405 [hep-ex].
- [277] ATLAS Collaboration, “Search for heavy resonances decaying into a Z or W boson and a Higgs boson in final states with leptons and b -jets in 139 fb^{-1} of pp collisions at $\sqrt{s} = 13 \text{ TeV}$ with the ATLAS detector”, *JHEP*, vol. 06, p. 016, 2023. DOI: 10.1007/JHEP06(2023)016. arXiv: 2207.00230 [hep-ex].
- [278] A. Biekötter, J. Fuentes-Martín, A. M. Galda, and M. Neubert, “A global analysis of axion-like particle interactions using SMEFT fits”, *JHEP*, vol. 09, p. 120, 2023. DOI: 10.1007/JHEP09(2023)120. arXiv: 2307.10372 [hep-ph].

This was a triumph.

I'm making a note here: HUGE SUCCESS.

It's hard to overstate my satisfaction.

— GLaDOS

B Acknowledgments

I wish to thank, first and foremost, my excellent PhD supervisors: Christian Schwanenberger and Alexander Grohsjean. You gave me feedback when I needed it, left me space when I did not, and always had my back in our common (mis-)adventures in the wide and wonderful and sometimes wondrous world that is Experimental Particle Physics. You also gave me great (and honest) advice and support for my further career, for which I am extremely thankful. Working with you has been a pleasure.

I am also deeply grateful to the many colleagues, postdocs and other PhD students, who taught me the intricacies of CMS and provided technical and moral support: Afiq Anuar, for unleashing $A/H \rightarrow t\bar{t}$ in the first place, and for always distracting me with interesting physics; Evan Ranken, who for some reason agreed to help perform a measurement in only two months; Jonas Rübenach and Dominic Stafford, for collectively sparing me from ROOT with their framework; again Jonas, for setting up the A/H analysis and giving me an excess to interpret; and again Dominic, for tolerating me as an office mate. Thanks to all of you.

Furthermore, I would like to thank my additional collaborators and supervisors on the different projects I worked on: Maria Aldaya and Andreas Meyer for the $t\bar{t}$ cross section in Run 3; Simone Amoroso for **bb4l**; as well as Georg Weiglein, Sven Heinemeyer, and the Biekötter Cousins for ALPs $\rightarrow t\bar{t}$.

Finally, I wish to give a huge thanks to the DESY CMS group for being a great place to work.

C Appendix

C.1 Sample normalizations in the matrix element reweighting

In this section, a derivation of the optimal way to combine multiple independent origin samples for the purpose of matrix element reweighting, as described in Sec. 8.4 is given. In particular, Eq. (8.16) is proven for the case that the cross section corresponding to the target hypothesis is known from an external calculation.

The notation used is the same as in Sec. 8.4. Let $\hat{w}_{i,j}$ be the weight of event i in origin sample j after reweighting, i.e. the product of ME weight and generator weight of the origin sample, and v_j the per-sample normalization that is to be determined. The per-event weight after normalization is $v_j \hat{w}_{i,j}$.

First, consider the case that the total cross section σ is known for the target hypothesis, meaning that the ME reweighting needs to only predict the shapes of the distributions. In Sec. 8.4, this is achieved by explicitly calculating σ with MG5_AMC@NLO for each target A/H hypothesis. The goal is now to minimize the total variance of the sample, given by

$$V = \sum_{i,j} v_j^2 \hat{w}_{i,j}^2, \quad (\text{C.1})$$

under the constraint that the total yield is

$$N = \sum_{i,j} v_j \hat{w}_{i,j} \equiv \sigma L, \quad (\text{C.2})$$

where L is the integrated luminosity. This is done with the method of Lagrange multipliers, giving the Lagrange function

$$\mathcal{L}(v_j, \lambda) = \sum_{i,j} v_j^2 \hat{w}_{i,j}^2 + \lambda \left(\sum_{i,j} v_j \hat{w}_{i,j} - \sigma L \right) \quad (\text{C.3})$$

which needs to be minimized simultaneously over v_j and λ . Differentiating by v_j gives

$$\frac{\partial \mathcal{L}}{\partial v_j} = 2v_j \sum_i \hat{w}_{i,j}^2 + \lambda \sum_i \hat{w}_{i,j} \equiv 0 \quad \Rightarrow \quad v_j = -\frac{\lambda}{2} \frac{\sum_i \hat{w}_{i,j}}{\sum_i \hat{w}_{i,j}^2}. \quad (\text{C.4})$$

By substituting this into Eq. (C.2) to find λ , one obtains

$$v_j = \sigma L \left(\sum_k \frac{\sum_i \hat{w}_{i,k}}{\sum_i \hat{w}_{i,k}^2} \right)^{-1} \frac{\sum_i \hat{w}_{i,j}}{\sum_i \hat{w}_{i,j}^2} \quad (\text{C.5})$$

which has the form of Eq. (8.16).

Alternatively, one might consider the case that the cross section σ is not known and should be predicted by the reweighting. In this case, one should require that the normalizations v_j do not change the total yield in the limit of large statistics, implying $\sum_j v_j = 1$. This leads to the Lagrange function

$$\mathcal{L}(v_j, \lambda) = \sum_{i,j} v_j^2 \hat{w}_{i,j}^2 + \lambda \left(\sum_j v_j - 1 \right) \quad (\text{C.6})$$

from which one finds through an analogous calculation

$$v_j = \left(\sum_k \frac{1}{\sum_i \hat{w}_{i,k}^2} \right)^{-1} \frac{1}{\sum_i \hat{w}_{i,j}^2}. \quad (\text{C.7})$$